Etching nanopores in single-layer graphene with a sub-angstrom resolution in molecular sieving

"Engineers create the world that never has been."

-- Theodore von Kármán

Acknowledgment

First of all, I would like to express my heartfelt thanks to my thesis supervisor Prof. Kumar Varoon Agrawal, for accepting me as his first Ph. D. student and guiding me to a fantastic research world. I am deeply inspired by his enthusiasm for science and insightful thoughts on research. His optimism and determination during failure always encourage me to roll with the punches. Thanks for all of his great supports in my study and thoughtful suggestions on my career. I appreciate his guidance and mentoring during my Ph. D, and this will go a long way for my life. I would also like to extend my gratitude to Prof. Paul Dyson, Prof. Wendy Lee Queen, Prof. Kang Li, and Prof. Chih-Jen Shih for serving as the jury committee of my thesis.

I feel grateful and fortunate to work with my brilliant and friendly colleagues in LAS. They are all fantastic researchers in science as well as warm friends in life. I would like to especially thank Dr. Guangwei He and Dr. Luis Francisco Villalobos for the beneficial scientific discussion and fruitful collaborations. Both of them are excellent and experienced scholars and have always helped me out of trouble. Also, I want to thank Dr. Jing Zhao, Dr. Deepu J. Babu, and Mostapha Dakhchoune for their enthusiastic help with my work, and their cautionary attitude towards science impact me a lot. I also got extensive help from my subgroup-mates, and here I would like to express my gratitude to Wan-Chi Lee, Shaoxian Li, and Kuang-Jung Hsu for the numerous brainstorms and useful discussions. Besides, I must thank our hospitable secretary Catherine Marie Regamey, who gives me a lot of warm help for my life in Swiss. I had a great time interacting with Heng-yu Chi, Dr. Qi Liu, Dr. Jian Hao, Dr. Mina Moradi, Mojtaba Rezaei, Mohammad Tohidi Vahdat, Dr. Majharul Haque Khan, Dr. Kangning Zhao, Dr. Marina Micari, and Dr. Cédric Van Goethem. Thank all of you.

This dissertation could not be completed without professional help from excellent scientists and engineers from EPFL. Here, I would like to address my thanks to Dr. Emad Oveisi, Dr. Mounir Driss Mensi, Dr. Wen Luo, Mo Li, Stéphane Voeffray and Benjamin Charles Le Geyt for their great contributions to my works.

Throughout the years spent in Switzerland, I feel grateful to have many friends in my life. I always gain courage from my best friend, Junhong; Meihui and Mengjiao

consistently support me when I am down. I also appreciate the encouragement and accompany from Yingdi and Lu. Thank all of you for helping me go through hard time of my life and back me up in all situations. Also, I want to thank Yan, Mo and Kun, all of them offered me useful suggestions when I met troubles.

Finally, I would like to address my big thanks to my family. Their unconditional love and substantial support shaped me as I am. No matter when or where I am, my heart is always with them.

Abstract

Single-layer graphene (SLG) membranes, hosting molecular-sieving nanopores have been regarded as the ultimate gas separation membranes, attributing to the fact that they are the thinnest possible molecular barrier. However, the expected attractive performance for gas separation from one-atom-thick graphene membranes has rarely been demonstrated experimentally. There are two major bottlenecks to realize this high-performance graphene membrane: 1) crack-free fabrication of large membrane area; 2) incorporation of high-density nanopores with a narrow pore-size distribution in the otherwise impermeable graphene lattice.

This dissertation focuses on the development of a crack-free transfer method and highly-precise pore-etching chemistry to realize high-performance single-layer graphene membranes for gas separation. A novel nanoporous carbon-assisted transfer method was developed to mechanically reinforce the atom-thick graphene layer during its transfer from catalytic Cu foil to a porous substrate, yielding a relatively large area (millimeter-scale) crack-free graphene membrane. This enabled, for the first time, the observation of the gas-sieving behavior through the intrinsic defects in the chemical vapor deposition (CVD) derived polycrystalline SLG. Attractive H_2 permeance and molecular-sieving selectivity between H_2 (kinetic diameter of 2.89 Å) and CH_4 (kinetic diameter of 3.80 Å) were achieved by the graphene film.

A scalable gas-phase millisecond ozone-based carbon gasification chemistry was developed to realize a controllable etching of graphene lattice. High-density (10^{12} cm^{-2}) gas-sieving nanopores with narrow pore-size distribution were observed by scanning tunneling microscopy and aberration-corrected high-resolution transmission electron microscopy. A model based on the kinetics of ozone etching was built to optimize the incorporation of CO_2-sieving pores on graphene. The nanoporous single-layer graphene (N-SLG) membranes accomplished an effective separation between CO_2 (3.30 Å) and O_2 (3.46 Å), corresponding to 0.2 Å molecular sieving resolution. Furthermore, ozone-based pore-edge functionalization chemistry and oxygen-based slow etching method were developed to adjust the molecular cut-off within the sub-angstrom for tuning the gas separation performance. The resulting N-SLG membrane reached O_2/N_2 selectivity of 3.4

with corresponding O_2 permeance of 1300 gas permeation units (GPU; 1 GPU = 3.35×10^{-10} mol m^{-2} s^{-1} Pa^{-1}), and CO_2/N_2 selectivity of 21.7 with corresponding CO_2 permeance of 11850 GPU. These are, so far, the best membrane performance for the post-combustion carbon capture, and will likely tilt the capture technology toward the membrane-based process.

The developed transfer method and ozone-based pore-edge functionalization chemistry are universal tools for high-performance carbon-based membrane fabrication. Accordingly, a sub-200 nm defect-free carbon molecular sieve membrane was successfully fabricated with a tunable pore-size distribution, resulting in attractive gas separation performance as well.

Résumé

Les membranes de graphène monocouches (SLG), qui contiennent des nanopores à taille moléculaire, sont considérées comme les membranes de séparation des gaz les plus performantes, car elles constituent la barrière moléculaire la plus fine possible. Cependant, les performances attractives attendues pour la séparation des gaz par des membranes de graphène d'un atome d'épaisseur ont rarement été démontrées expérimentalement. Il existe deux principaux obstacles à la réalisation de cette membrane de graphène à haute performance: 1) la fabrication sans fissures d'une grande surface de membrane; 2) l'incorporation de nanopores avec une haute densité et une distribution de la taille étroite dans le réseau de graphène imperméable autrement.

Cette thèse se concentre sur le développement d'une méthode de transfert sans fissure et d'une chimie de gravure des pores très précise pour réaliser des membranes de graphène monocouche à haute performance pour la séparation des gaz. Une nouvelle méthode de transfert nanoporeux assistée par carbone a été mise au point pour renforcer mécaniquement la couche de graphène d'épaisseur atomique lors de son transfert d'une feuille catalytique de cuivre à un substrat poreux, donnant une membrane de graphène sans fissure de surface relativement importante (à l'échelle du millimètre). Cela a permis, pour la première fois, d'observer le comportement de séparation des gaz à travers les défauts intrinsèques du SLG polycristallin dérivé du dépôt chimique en phase vapeur (CVD). Une perméance du H_2 et une sélectivité de taille moléculaire attrayantes entre H_2 (diamètre cinétique de 2,89 Å) et CH_4 (diamètre cinétique de 3,80 Å) a pu être obtenue avec la membrane de graphène.

Une chimie de gazéification en milliseconde du carbone en phase gazeuse, basée sur l'ozone, a été mise au point pour réaliser une gravure contrôlable du réseau de graphène. Des nanopores à haute densité (10^{12} cm^{-2}) avec une distribution étroite de la taille des pores pour la séparation des gaz ont été observés par microscopie à effet tunnel à balayage et par microscopie électronique à transmission à haute résolution avec correction des aberrations. Un modèle basé sur la cinétique de la gravure à l'ozone a été construit pour optimiser l'incorporation des pores pour la séparation du CO_2. La membrane dérivée a permis une séparation efficace entre le CO_2 (3,30 Å) et l'O_2 (3,46 Å), correspondant à une

résolution de tamisage moléculaire de 0,2 Å. En outre, une chimie de fonctionnalisation de la bordure des pores basée sur l'ozone et une méthode de gravure lente basée sur l'oxygène ont été développées pour ajuster la coupure moléculaire dans le sous-angstrom afin d'ajuster la performance de séparation des gaz. La membrane résultante a atteint une sélectivité O_2/N_2 de 3,4 avec une perméance à l'O_2 correspondante de 1300 unités de perméation de gaz (GPU ; 1 GPU = 3,35× 10^{-10} mol m^{-2} s^{-1} Pa^{-1}), et une sélectivité CO_2/N_2 de 21,7 avec une perméance au CO_2 correspondante de 11850 GPU. A l'heure actuelle, ce sont les meilleures performances pour le captage du carbone en postcombustion avec une membrane, et elles feront probablement pencher la technologie de captage vers les procédés à base de membrane.

La méthode de transfert développée et la chimie de fonctionnalisation des pores à base d'ozone sont des outils universels pour la fabrication de membranes à base de carbone à haute performance. Ainsi, une membrane de tamis moléculaire en carbone sans défaut de moins de 200 nm a été fabriquée avec succès avec une distribution de taille de pore accordable, ce qui a également permis d'obtenir des performances intéressantes en matière de séparation des gaz.

Mots clés: graphène nanoporeux monocouche; membrane; défauts de vacuité; séparation des gaz; capture du carbone

List of Abbreviation

2D	Two-dimensional
AAO	Anodic aluminum oxide
AC-HRTEM	Aberration-corrected (Cs) high-resolution transmission electron microscopy
AFM	Atomic force microscopy
CMS	Carbon molecular sieve
CVD	Chemical vapor deposition
DFT	Density functional theory
DMAc	Dimethylacetamide
DMF	Dimethylformamide
DNA	Deoxyribonucleic acid
FIB	Focused ion beam
FWHM	Full width at half maximum
GPU	Gas permeation unit
HOPG	Highly oriented pyrolytic graphite
HRTEM	High-resolution transmission electron microscopy
LPCVD	Low pressure chemical vapor deposition
MD	Molecular dynamics
MFC	Mass flow controller
MGR	Millisecond gasification reactor
MLV	Millisecond leak valve
MOF	Metal-organic framework
MS	Mass spectrometer
MSR	Molecular sieving resolution

NIPS	Non-solvent induced phase separation process
NPC	Nanoporous carbon
N-SLG	Nanoporous single-layer graphene
PBI	Polybenzimidazole
PCTE	Polycarbonate track etch
PES	Polyethersulphone
PMMA	Poly(methyl methacrylate)
PSD	Pore-size distribution
PS-P4VP	polystyrene-co-poly(4-vinylpyridine)
PVA	Polyvinyl alcohol
SAED	Selected area electron diffraction
SEM	Scanning electron microscope
SLG	Single-layer graphene
SLT	Selective layer thickness
STM	Scanning tunneling microscope
TEM	Transmission electron microscopy
UHV	Ultrahigh vacuum
UV	Ultraviolet
vdW-DF2	Van der Waals density functional
W foil	Tungsten foil
XPS	X-ray photoelectron spectroscopy
XRD	X-ray diffraction

List of Symbols

D	Diameter
E_{act}	Activation energy
$E_{app\text{-}act}$	Apparent activation energy
$erfc$	Error function
E_{sur}	Adsorption energy
H_{sur}	Henry coefficient
k	Rate constant
k_B	Boltzmann constant
m	Mass
P	Pressure
R	Resistance of gas transport
r	Radius
T	Temperature
t_d	Delay time
θ	Coverage
τ	Opening time of MLV

Table of Contents

Chapter 1 Introduction

1. Challenges and opportunity for membrane separation

Separation, as the most critical and energy-intensive manufacturing process, takes 10 – 15% of the world's energy utilization.[1] The increasing demand for energy-efficient industrial production has stimulated vigorous research to reduce the energy consumption of the separation process.
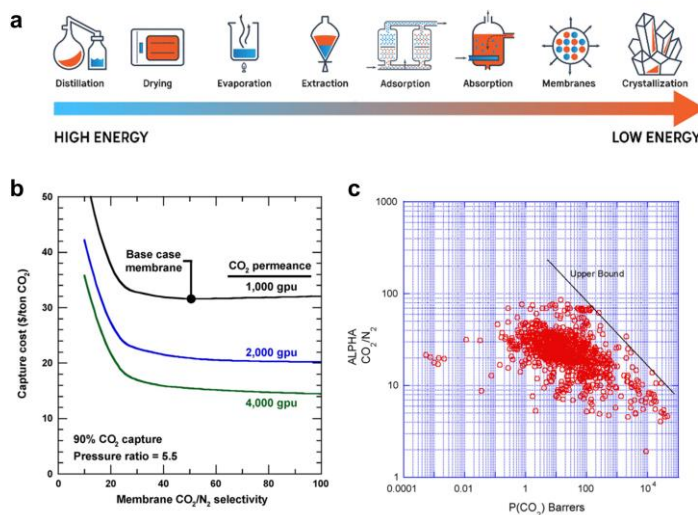
Figure 1.1 a) The energy consumptions of different separation processes (left to right: high energy use to low energy use). Reprinted with permission from National Academies Press.[2] b) The cost of capturing 90% CO_2 in the flue gas by membrane as a function of membrane CO_2/N_2 selectivity and CO_2 permeance.[3] c) Upper bound of polymeric membranes for CO_2/N_2 separation. Reprinted with permission from Elsevier B.V.

Membrane separation, as one of the most energy-efficient ways[2] (**Figure 1.1**), is predicted to reduce energy consumption by 90% in the separation field.[1] For example, it

is estimated that the high-performance membrane separation could reduce the capture cost to $15 – 32$ ton^{-1} CO_2 for post-combustion capture, compared with the existing state-of-the-art amine-adsorption capture cost of $\$ 60 – 100$ ton^{-1} CO_2.[3,4] However, the commercial polymeric membrane sufferers a trade-off between permeance (gas flux per unit area) and gas pair selectivity, limiting the applications of membrane separation.[5] Hence, developing a high gas permeance membrane combined with a moderate gas pair selectivity is highly attractive for the separation field.
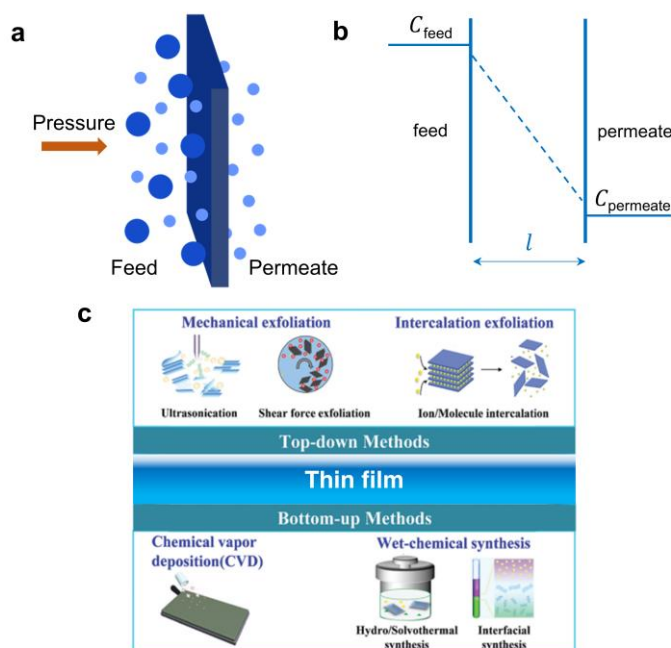
Figure 1.2 a) Schematic of the transport of molecules through a membrane. b) The concentration profile of a permeating molecule across the membrane. c) Representative top-down and bottom-up methods to synthesize 2D membranes.[6] Reprinted with permission from The Royal Society of Chemistry (RSC).

The membrane separation process is driven by the concentration (pressure) difference to differentiate the molecules in the feed mixture, transporting the permeable molecule across the membrane, and retaining non-permeable ones. In most cases of gas separation, the transport resistance of the molecule through the membrane is proportional to the membrane thickness (**Figure 1.2 a-b**). Thin-film with a well-defined pore structure provides a short and selective transport path, resulting in high gas flux along with molecular-sieving selectivity. Two-dimensional (2D) membranes, assembled with 2D-

nanosheet from top-down (exfoliation from bulk) or bottom-up (direct synthesis) process, possess a prominent advantage to reduce the molecular transport path, attributing to its ultrathin thickness.[6–8] Graphene oxide,[9–11] MXene nanosheet,[12–14] exfoliated nanosheets of zeolite,[15–17] and metal-organic framework (MOF) nanosheet [18,19] have been studied extensively for membrane fabrication in the last decade. The ultrathin 2D membranes display the great potential to realize high-throughput membrane separation and open a new direction to fabricate a high-performance membrane (**Figure 1.3**).
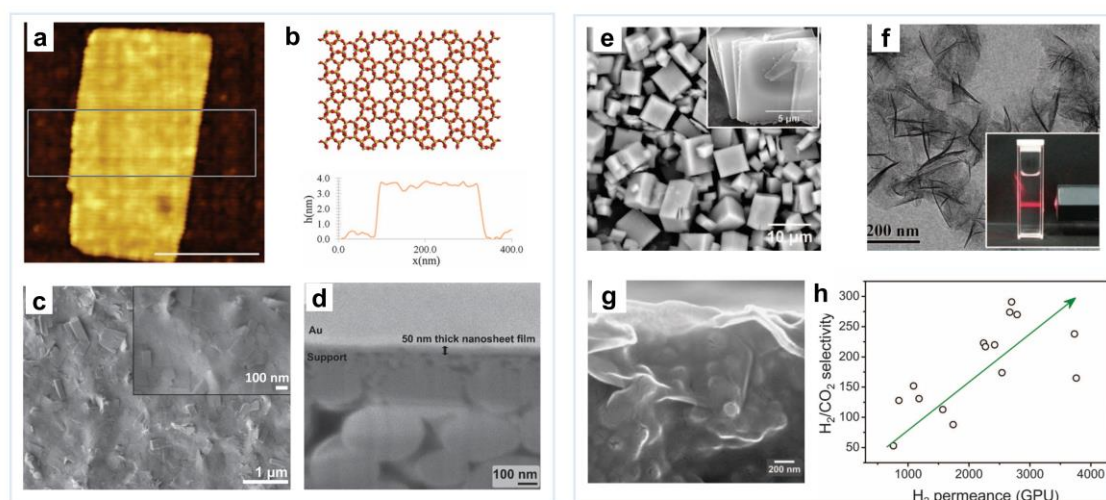
Figure 1.3 Representative 2D membranes assembled by 2D nanosheets. a-d) Oriented MFI membranes fabricated by 2D MFI nanosheet.[16,17] Reprinted with permission from The American Association for the Advancement of Scienc (AAAS) and John Wiley and Sons. e-h) Ultrathin MOF membrane obtained by stacking layered metal-organic frameworks.[19] Reprinted with permission from AAAS.

2. Nanoporous single-layer graphene (N-SLG) membrane

Single-layer graphene

What is the perfect material for membrane-based separation? From the point-of-view of the mass transport mechanism of the membrane process, the lower the transport resistance experienced by the molecule, the faster the transport will be, thus resulting in a high-throughput membrane process. The ultimate thickness of the membrane that we could imagine is the thickness of one atom layer, which would provide the lowest possible transport resistance during separation. Besides, to endure high-temperature, long-time pressure, and harsh chemical environment during the membrane operation, the one-atom-thick film has to be mechanically robust, thermally stable, and chemically inert.

Single-layer graphene with one-atom-thick honeycomb lattice,[20] was first successfully isolated by Andre Geim and Kostya Novoselov in 2004.[21] The magic material with the thinnest layer has drawn unprecedented attention from the scientific community in the last 15 years.[22–24] In the 1930s, Landau and Peierls predicted that the two-dimensional crystals were supposed not to exist at any finite temperature, due to the thermodynamical instability in the low-dimensional crystal lattice.[21,25] Unlike the presumption, the atomic-thick graphene lattice exhibits extraordinary mechanical and thermal stability. The Young's modulus and intrinsic strength reach 1 TPa[26–28] and 130 TPa[28] for monolayer graphene, establishing the graphene as the strongest material ever measured. Meanwhile, the suspended single-layer graphene also exhibits exceptional thermal properties; it could conduct heat rapidly with 5000 W mK^{-1} thermal conductivity, [29,30] and could be heated up and remain stable at 2600 K.[31] The atomic-thickness and excellent inherent physical properties indicate that graphene would be an ideal membrane material for the membrane separation process.
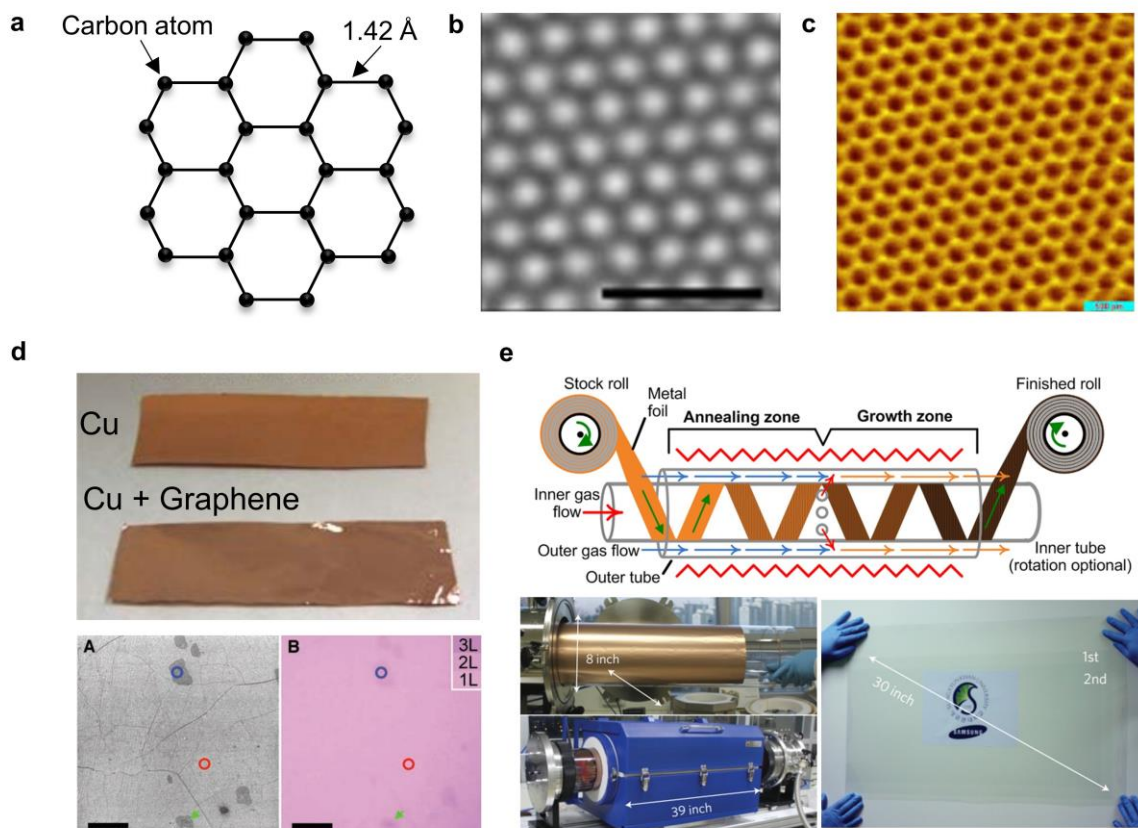
Figure 1.4 Graphene structure and synthesis. a) Schematic of the graphene honeycomb structure constructed by sp^2 carbon atoms; b) Abbreaction-corrected high-resolution transmission electron

microscopy (Ac-HRTEM) image of the hexagon structure of graphene, the scale bar is 1 nm;[32] reprinted with permission from Springer Nature. c) Scanning tunneling microscopy (STM) image of graphene on graphite, the scale bar is 0.5 nm;[33] reprinted with permission from American Physical Society (APS). d) Single-layer graphene synthesized by chemical vapor deposition method on the copper surface with 95% area predominated with single-layer;[34] reprinted with permission from AAAS. e) Schematic and instrument of roll-to-roll manufacturing large-area graphene,[35,36] reprinted with permission from Springer Nature.

Moreover, compared with other two-dimensional materials, such as the materials mentioned previously, graphene oxide, zeolite, and MOF nanosheets, which are mainly exfoliated from the bulk crystal, and limited to the micron-size nanosheet, it is possible to realize single-layer graphene at the meter-scale by the well-established chemical vapor deposition (CVD) method. The first successful CVD single-layer graphene synthesized via CH_4 precursor on the catalytic copper surface was reported in 2009 by Ruoff's group (**Figure 1.4**).[34] Followed by this, 30-inch roll-to-roll continuous CVD graphene synthesis was demonstrated by Bae et al.[35] In addition, the vacuum deposition condition of CVD enabled high-throughput single-layer graphene production via gapless stacking of the catalytic substrates.[37] These developments throw light on the road to fabricate large-area graphene membrane with meter-scale and atomic thickness.

Incorporation of nanopores on graphene lattice

The pristine graphene is a honeycomb lattice constructed by sp^2-hybridized carbon, where the density-gap of the lattice prevents even the smallest gas molecule, helium, permeating through the lattice.[38,39] Perforation of the graphene lattice would be an essential step to break the energy barrier for molecular translocation. Meanwhile, the membrane separation via the size-sieving mechanism, requires precise nanopores with high-resolution to differentiate the molecules in the mixture based on their sizes. Hence, incorporating well-defined nanopore with a narrowly distributed pore size on graphene would be favorable for the gas separation application. Previous works have demonstrated several pore-etching methods for nanopore creation on the graphene lattice, including the bottom-up methods (synthesize the nanoporous graphene inherently) and the top-down methods (start with pristine graphene, and incorporate nanopores by post-treatment). However, due to an inherent trade-off between the pore density and pore-size-distribution, the efficient approach to realize high-density, narrowly-distributed-nanopores on graphene

remains elusive.

Bottom-up synthesis of inherently nanoporous graphene was demonstrated by pre-patterning the substrate or self-assembling the porous nanoribbons. Barrier-guided chemical vapor deposition would assist the synthesis of perforated graphene by pre-patterning the substrate with nanostructures such as Al_2O_3 nanoparticle,[40] self-assembled silica[41] or tungsten nanoparticles[42] before the chemical vapor deposition. The pattern nanostructures hindered the graphene growth below it, generating 25 – 200 nm nanopores inherently during graphene synthesis (**Figures 1.5b-c**). But the incorporated pore size heavily depended on the patterned nanoparticle size, which is difficult to incorporate sub-nanometer pores for gas and ion separation. An ordered array of sub-nanometer pores in graphene could be realized by compacting the nanoribbons (**Figure 1.5a**).[43] However, this process is complicated to implement and could only be achieved in nano-meter size.
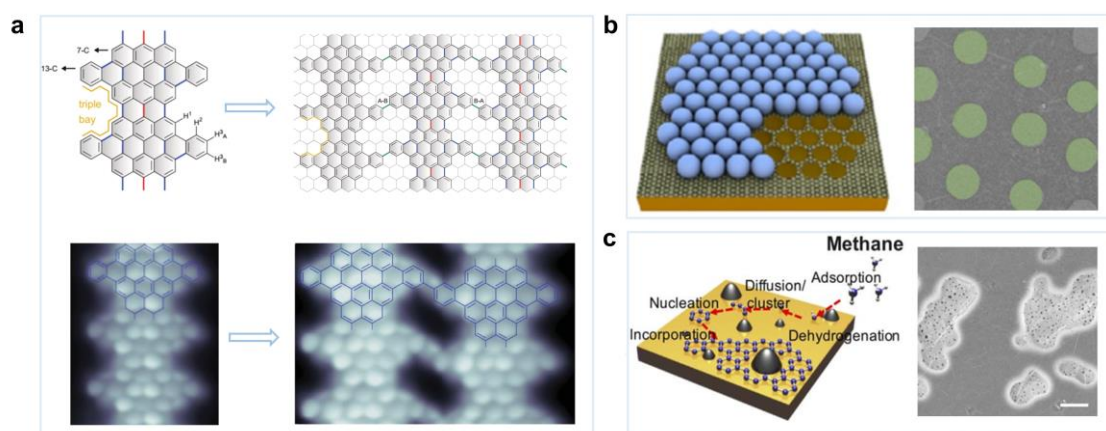
Figure 1.5 Bottom-up methods of nanoporous graphene synthesis. (a) Nanometer-size nanoporous graphene sheet synthesized by comprising an ordered array of pores separated by ribbons.[43] Reprinted with permission from AAAS.(b) Barrier-guided chemical vapor deposition to synthesize nanoporous graphene by patterning with silica particles, the diameter of nanopores are around 300 nm.[41] Reprinted with permission from American Chemical Society (ACS). (c) Porous graphene film obtained by forming a catalytically inactive material cluster on the copper catalyst surface before chemical vapor deposition, the scale bar in (c) is 500 nm. Reprinted with permission from AAAS.

Electron beam and focused ion beam (FIB)

The top-down pore creation methods include physical bombardment and chemical etching on pristine graphene. The physical bombardment applies high-energy electrons or ions to break the sp^2 C-C bonds, and removes the carbon atoms by the colliding with the

high-energy particles. Smith et al. estimated around 86 keV incident electron energy is required to break three C-C bonds and knock out one carbon atom from the pristine graphene.[44] J. Warner et al. applied 80 keV electron-beam-induced sputtering on few-layer graphene to selective remove carbon atoms from the top monolayer graphene.[32,45] Schneider et al. and Garaj et al. drilled 2 – 40 nm nanometer-scale pores on graphene lattice with 200 – 300 keV electron beam bombardment (**Figure 1.6a**).[46,47] High-energy electron beam facilitates to knock out the carbon atoms on the basal plane and nucleate the vacancy defect. Meanwhile, the excited state electrons initiate fast etching around the defective edge and trigger complicated vacancy migration. The knock-out threshold of carbon atom drops to 15 eV when it is adjacent to vacancy defects,[48] and the migration energy barrier of the single vacancy is only 1.3 eV. [49,50] The much lower energy barrier benefits the fast expansion of the nanopore rather than the initialization of new pits, making it difficult to control the pore size and pore size distribution. A. Zettl and co-workers have observed the rearrangement of the carbon atoms of the nanopore edge and the nanopore growth via an aberration-corrected transmission electron microscope,[51] depicting the complexity of the process.

Except for the high-energy electron beam, focused ion beam (FIB) such as Ar^+, He^+, and Ga^+ bombardment were extensively explored to create nanopores on graphene. The working mechanism is the same as the electron beam bombardment that the energy transferred by the collision of the high-energy particle break the carbon-carbon bonds. The displacement energy of a carbon atom of pristine graphene sheet is around 23 eV, the minimum energy of the ions to knock out the carbon atom by a head-on collision could be estimated by kinematical relationship[52]:

$$E_{\min} = \frac{E_d (m_c + M)^2}{4 m_c M}$$

Where E_d is the displacement energy of carbon atom, m_c and M indicated the mass of the carbon atom and ion mass. Lehtinen et al. calculated the number of removing carbon atoms per ion impingement as a function of ion energy. The results indicated the heavier ions, such as Xe^+, Kr^+, could sputter out more carbon atoms than the lighter ion as He^+ under the same voltage.[52] Russo et al. nucleated the vacancy defect with 1 – 2 missing carbon atoms via 3 keV Ar^+ bombarding.[53] To avoid fast expansion of the pore edge under

Ar$^+$ beam, they applied weak electron recoil sputtering for further removal of 10 carbon atoms on graphene lattice (**Figure 1.6b**).[53] Deng et al.[54] reported another interesting phenomenon that the etching rate of the beam center is much faster than the periphery. The ion beam center will generate maximum intensity due to the intensity of the ion beam follows the Gaussian distribution. The calculated the He$^+$ beam with 11 nm mean diameter would generate an 11 nm nanopore within 1.07 s, and then the pore expansion rate of the nanopore would experience exponentially decay to 1.3 nm s^{-1} due to the weak intensity of the beam periphery. Similar pore size was also reported by Celebi et al. that nanopores with 7.6 nm mean pore-size were obtained by perforating bilayer graphene lattice with He-based FIB (**Figure 1.6b**). [55] Hence, the properties of the incorporated nanopore would be mainly limited by the diameter of the ion beam.

Indeed, the microscopy-derived technology provided an interesting platform to perforate the nanopores and observe the morphology of nanopores simultaneously, which greatly contributes to the fundamental study of nanopore on graphene. However, the micrometer working area under microscopy and the low throughput of the beam-fabrication limits the application in the membrane field.
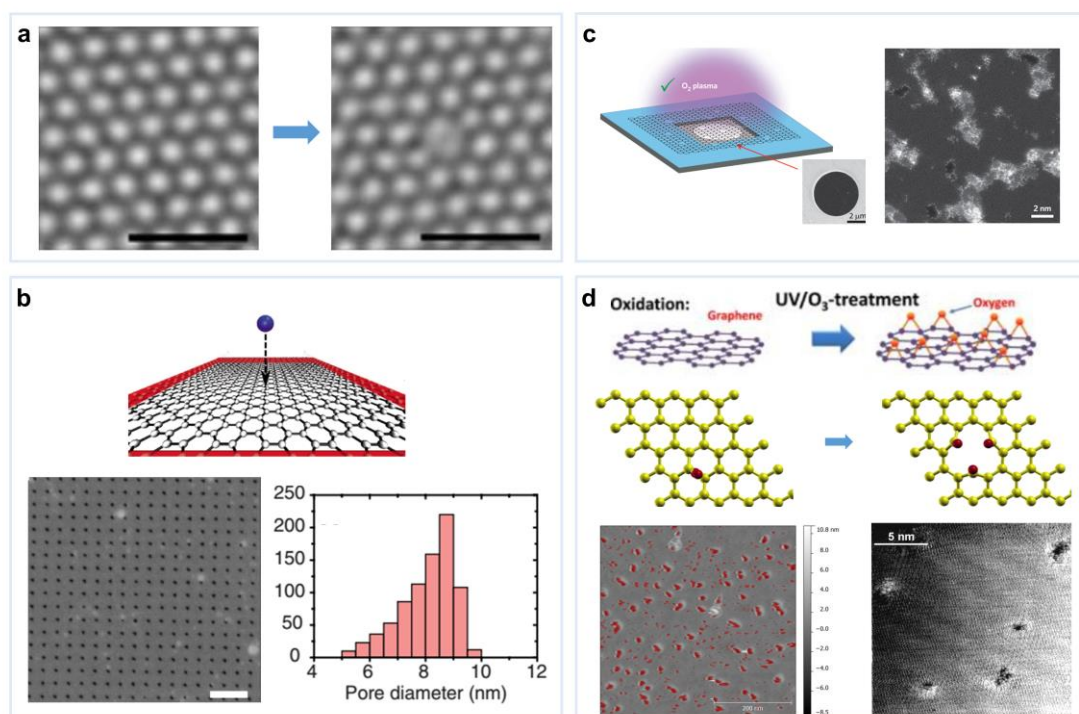
Figure 1.6 Top-down methods of nanoporous graphene synthesis. (a) Single-vacancy defect creation in graphene lattice by transmission electron microscopy.[32] Reprinted with permission from Springer

Nature. (b) Schematic of vacancy defect formed by focus ion beam (FIB)[52] and nanoporous graphene perforated by He-based FIB with 7.6 nm nanopores.[55] Reprinted with permission from APS and AAAS. (c) Nanoporous graphene with 1 nm nanopores formed oxygen plasma.[56] Reprinted with permission from Springer Nature. (d) Schematic of ozone treatment on graphene and nanopore formation,[57,58] The atomic force microscopy (AFM) image[56] and scanning tunneling microscopy (STM) image[59] of nanoporous graphene generated by ozone. Reprinted with permission from American Institute of Physics and Springer Nature.

Oxygen plasma

Oxygen plasma treatment is another popular method to incorporate nanopores in the graphene lattice. The oxygen atoms excited to higher energy states as atomic oxygen (O) and charged molecular ion (O_2^+),[60] are effective in breaking the C-C bonding on the graphene lattice. Surwade et al. investigated the relationship between the plasma dose and nanopore size, and obtained the optimal condition to generate nanometer-sized pores (~ 1 nm) on 5 μm monolayer graphene (**Figure 1.6c**).[56] Bai et al. created a template mask on graphene before plasma treatment by the block copolymer lithography approach, leading a nanoporous graphene mesh with 5 – 20 nm pores.[61] Jang et al. initialized the defects with ion bombardment, guiding the plasma etching to realize a narrow pore-size distribution (0 – 1 nm).[62]

In fact, the etching mechanism behind oxygen plasma etching is quite sophisticated. The effective oxidative species are different with the type of plasma, for example, charged molecular ion (O_2^+) is responsible for removing carbon atoms in dielectric barrier discharge (DBD)-generated plasma; while atomic oxygen (O) and O_2^+ co-exist in radiofrequency (RF) and microwave (MW) plasma.[63] Because the mechanism of the DBD is similar to ion bombardment, here we mainly discuss the O and O_2^+ mixture etching in the graphene. Koizumi et al. reported atomic O would like to be adsorbed on the defective graphene surface and form a lactone group, while O_2^+ just bombarded vacant sites with dangling bonds.[60] Martínez-Alonso and co-workers demonstrated a similar mechanism, but they explained the impingement energy of the O_2^+ in MW plasma (10 – 20 eV) would be less than the minimum energy of carbon displacement, so the main etchant in MW plasmas is atomic oxygen.[64] The etching in the oxygen plasma would start with the stochastical chemisorption of atomic O on the graphene surface, generating disorder in the adjacent C-C, which will finally knock out the carbon atoms. Although the mechanism is similar to chemical etching, yet the highly mobile and active atomic O would like to etch

both defective sites and the perfect graphene lattice. The work from Dong and co-workers also observed similar results that oxygen plasma is anisotropic vertical (top surface) etching rather than anisotropic horizontal (edges) etching.[65]

Hence, achieving a precise oxygen plasma etching is not trivial but sophisticated.[66] The random nucleation, caused by the highly reactive and mobile atomic oxygen, makes it difficult to form ordered vacancy defects. Meanwhile, the condition of the oxygen plasma could be significantly affected by various factors, including electrical, thermopower properties, and even the position of the electrodes. Compared with electron/ion bombardment, oxygen plasma treatment could work with a relatively large area. Still, it is challenging to realize a controllable etching with a sub-nanometer resolution.

Chemical etching

Chemical etching would provide an alternative way to incorporate nanopores on graphene lattice **(Figure 1.6c)**. Especially, the gas-phase reaction is promising to apply to the relative-large area. The reactive etching mediums such as ozone (O_3),[59,64,67] oxygen (O_2),[68–70] and nitric oxide (NO),[69,71] are great candidates that have been extensively investigated to form etching pits on the graphite surface.

The successful attack on the graphene basal plane by NO and O_2 were observed when the reaction temperature was above 700 °C.[71] Below such temperature, the chemical etching of NO and O_2 was inclined to enlarge the pre-existing vacancies rather than nucleate new pits. The reason for the preferential etching is the huge energy barrier for O_2 (200 kJ mol^{-1}) and NO (167 kJ mol^{-1}) to initialize nucleation on the basal plane of graphene. The sluggish etching reaction would prefer to take place around pre-existing defective sites by overcoming a lower energy barrier at the defective edge (127 kJ mol^{-1} for O_2). Chang et al. observed the etching pits growth around the pre-existing defect in the oxygen atmosphere at 650 °C without new nucleation formation in the basal plane,[68] and Chu et al. reported the same pore expansion rate of the defective top layer and second layer graphene.[70] The results indicated that the oxygen etching on graphene lattice is sensitive to defective area, following anisotropically horizontal etching (edge) mode.[65]

Ozone, as a reactive component, is regarded as an effective etchant to remove carbon

atom from graphene lattice. Koenig et al. applied UV-ozone oxidation on 5 μm bilayer graphene balloon incorporating 3.4 Å nanopore on graphene lattice.[72] C. M. Sotomayor-Torres and co-workers also observed cavities formation on graphene after treating with UV-O$_3$ by STM.[73] The effective etchant in UV-O$_3$ etching is not only ozone. UV light dissociates the oxygen molecule to create atomic oxygen (O), which attaches to other oxygen molecules to form ozone. Therefore, the atomic oxygen and ozone co-exist in the UV-O$_3$, and both of them could etch the lattice. Especially, the atomic oxygen has a much lower energy barrier (8 – 10 kJ mol^{-1}) to etch graphene lattice than ozone (80 kJ mol^{-1}).[59,74] In the UV-O$_3$ process, atomic oxygen would nucleate the vacancy defect stochastically, and ozone enlarges the defect in the process. Solís-Fernández et al. has observed a similar experimental phenomenon that the UV-O$_3$ would create a number of atomic vacancies and subsequently enlarge them to nano-meter pits. Hence, the UV-O$_3$ etching method is a combination of atomic oxygen etching and ozone etching.

The DFT has simulated the pure ozone chemical etching, without atomic oxygen. It starts with epoxy formation by overcoming a 0.74 eV energy barrier,[75] followed by epoxy group diffusion to form a cluster with ether group (0.73 -0.76 eV).[76] Eventually, a carbon atom will be removed because of the lattice strain induced by bucking of the lattice. The experimental data demonstrated that high reactivity of ozone enabled the functional groups' formation on the basal plane at room temperature.[77] The ozone etching starts with chemisorption of the etchants, which are more likely to form ordered nuclei on the graphene surface, compared with the stochastical etching of physical bombardment and oxygen plasma. The DFT also predicted that the unzipped linear functional group pair would be formed on graphene via ozone etching.[78] Because the energy barrier for O diffusion to extend linear functional group on graphene (0.60 eV) is energetically more favorable than the creation of a pair of next nearest-neighbor functional groups (0.71 eV) **(Figure 1.7)**. Tracz et al. observed a critical distance between the etching pits formed by ozonized air on HOPG, which indicated the ordered structure is possible. It was found the distance between the two etching pits was no more than 14 nm. They believed that any ozone molecule adsorbed on the surface larger than the distance would nucleate new pits. Otherwise, the ozone molecule would diffuse to the pre-existing vacancy to enlarge the defect due to the surface concentration gradient.[59] Direct experimental data are rarely reported to validate the nucleation mechanism of ozone, due to the difficulty of probing

the nucleation stage. The simulations and previous work suggests that ozone is a promising etchant to form ordered nuclei on graphene lattice.
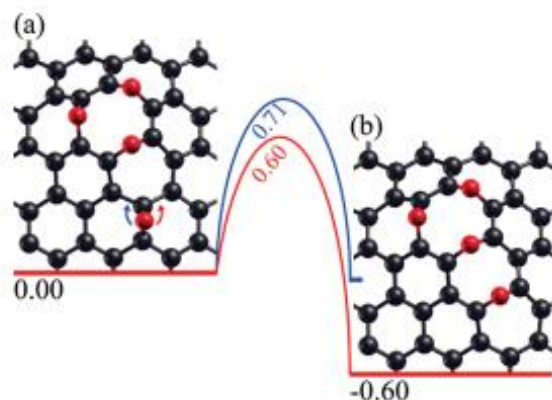
Figure 1.7 The energy barrier for the O diffusion to form extended defects. The blue and red arrow in (a) indicated two paths to extend the cluster, and the corresponding energy barrier is shown in blue and red curves.[78] Reprinted with permission of ACS.

Most of the ozone etching studies on graphite focus on the expansion stage of the nanopore. Hennig et al. measured the parallel expansion rate of the pre-existing defect in ozone at different temperatures. The activation energy of pore growth in ozone was extracted as 16.7 kcal mol^{-1}.[67] Compared with the simulated nucleation energy of ozone (0.74 eV)[75], it is interesting to find that the energy barrier to nucleate the sp^3 site is just slightly higher than the energy barrier of expansion. The energy barrier difference between nucleation and expansion of ozone is much lower than other chemical etchants, such as O_2 (73 kJ mol^{-1}). Hence, ozone is a promising etchant to realize a controllable etching of graphene lattice. It is important to mention that most of the mechanism of ozone etching relies on simulation due to the lack of experimental data. As a consequence, the effective ozone etching method to incorporate sub-nanometer pores in graphene lattice remains elusive.

Compared with physical bombardment and oxygen plasma, chemical etching seems to be a promising approach to controllably etch high-density sub-nanometer pores in a large area. But as we have mentioned, the etchant such as O_2 and NO has a sluggish nucleation rate, causing preferential chemical etching on defective sites and making it difficult to form high-density nanopores. O_3 seems to be a promising etchant to realize a controllable ordered etching based on the simulation prediction. However, due to the lack

of experiment data, the controllable etching methods and etching mechanism of ozone remain elusive.

Application of nanoporous single-layer graphene membrane

Attributing to the atomic-thick lattice, nanoporous graphene provides the thinnest possible transport barrier for molecules. The transport of biomolecules, water, ions, and gas through the film can be ultrafast, compared with the transport where the transport path is typically 20 – 1000 nm long of the traditional membrane. This ultrashort transport path could be attractive for the field of molecular separation to realize a high-throughput process. Besides, compared with the conventional porous materials that hold a well-defined pore structure, the pore-structure of nanoporous graphene is highly tunable to adapt to the specific separation. The unique post-incorporated pore formation would enable nanoporous graphene to hold different pore-structures to realize versatile separations. Combined with its excellent mechanical and thermal stability, nanoporous graphene has drawn a lot of attention from the separation field. This chapter will discuss the application of nanoporous graphene for biomolecules sensor, water, and ion separation, the details of gas separation will be discussed separately in the next section.

The one-atom-thick length of the pore channel significantly enhances the resolution of deoxyribonucleic acid (DNA) sequencing through the nanopore, by avoiding a large number of molecules present along the pore channel. In a typical DNA detector, the nanopore on the perforated film maintains a stable ion current through the porous area as background. When the DNA attempts to translocate through the pore, it blocks the ion transport, causing a sharp signal of current fluctuation. To obtain a high-resolution signal from the molecule translocation, the film that only allows single-molecule transport through the pore would be ideal for this application. The ultrashort pore channel of nanoporous graphene could avoid the noise from molecules along the passage, and the small area of nanopore on the lattice makes it easy to focus the signal, enabling a very high resolution and high throughput detection of single-molecule DNA through the nanopore.[46,47] In 2010, Merchant et al. reported 1 – 5 nm thick graphene membranes incorporated with nanopores of diameter 5 to 10 nm, and observed high-resolution signal, compared to that from the nanopore in traditional 30 nm-thick SiN_x substrates (**Figures 1.8a-b**).[79] Almost at the same time, both Garaj et al. and Schneider et al. also fabricated

nanoporous graphene sensor with 5 nm pore and found the tiny features reflected by the high-resolution current profiles.[46,47] The features could even identify the configuration of DNA as folded, non-folded, or partially folded during translocation (**Figures 1.8c-d**). Nanoporous graphene provided a great platform and pushed the field to generate more accurate high-resolution single-molecule DNA detection or screening.
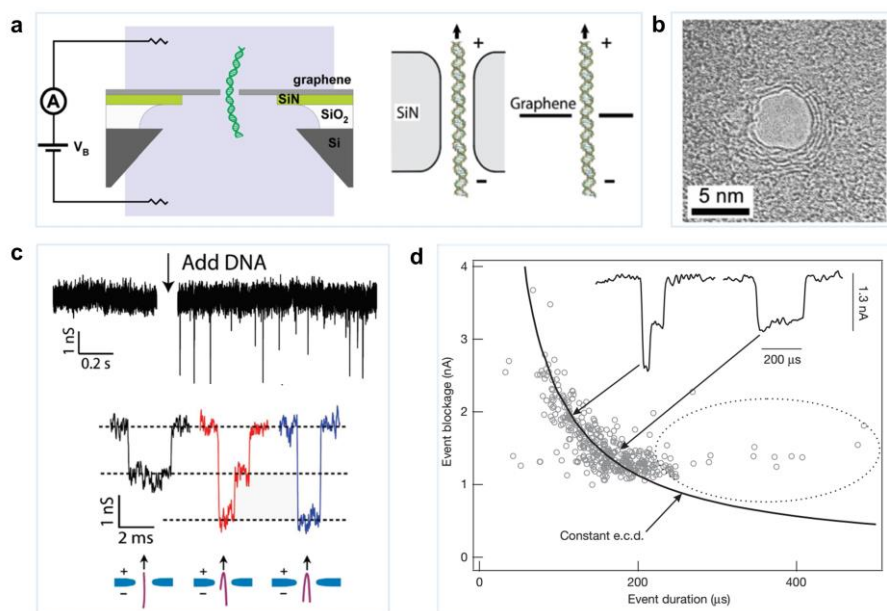
Figure 1.8 (a) Schematic of the DNA translocation through the device fabricated with nanoporous graphene, and the comparison of the translocation of DNA through SiN substrate and single-layer graphene.[47,79] (b) The HRTEM image of the 5 nm nanopore on the graphene lattice of the DNA sensor.[47] (c) The current profiles obtained by the DNA translocation with different DNA configurations.[47]. (d) The blockage current vs. the blockage duration during DNA translocation, which could distinguish the DNA configuration by the event duration.[46] Reprinted with permission from ACS and Springer Nature.

The transport of water molecules (molecule size of 2.65 Å) through the nanoporous graphene is another exciting field. Cohen-Tanugi and Grossman have predicted the ultra-high water flux through nanoporous graphene of $10^4 \, L \, m^{-2} \, h^{-1} \, bar^{-1}$ by molecular dynamics simulation, which would greatly benefit the water desalination and water purification applications. In 2014, Celebi et al. fabricated a double-layer nanoporous graphene membrane hosting 3.6 – 11.5% porosity comprised of 7.6 – 50 nm nanopores sculpted by He focused ion beam. The observed water flux could reach $10^{-13} \, L \, s^{-1} \, bar^{-1}$ per pore, consistent with the theoretical prediction from Sampson's formula for an infinitesimally

thin porous membrane.[55] Followed work from the same group reflected that the water permeance through nanoporous graphene could reach 5.58 L s^{-1} bar^{-1} m^{-2} when the porosity is increased to 14 – 18%. Their flow rate is one to two orders of magnitude higher than the commercially available ultrafiltration membranes (such as PCTE, MF-Millipore) with a similar size cut-off.[42] Besides the ultrahigh high water-flux, the nanoporous graphene membrane also demonstrated excellent separation performance for water purification. Surwade et al. incorporated plasma-etched 1 nm nanopore in 5 μm suspended graphene, exhibiting rapid water flux 10^3 L m^{-2} s^{-1} with a nearly 100% salt rejection rate. Yang et al. developed nanoporous graphene/carbon-nanotube hybrid membranes, and it reached 97% KCl rejection rate with water permeance of 20.6 L m^{-2} h^{-1} bar^{-1}.[80] Karnik and the co-workers combined the ion bombardment and oxygen plasma etching to incorporate high-density ($\sim 10^{13}$ cm^{-2}) nanopores, realizing size-selectivity between salt (KCl) and small molecules (Allura Red) in water-based systems (**Figures 1.9a-c**).[81,82] The ultrahigh water flux and excellent rejection rate, demonstrated a great potential to conduct high throughput water purification by applying nanoporous graphene membranes.

Several simulation works[83,84] also predicted the effective ion separation could be achieved by nanoporous graphene, and the revealed mechanism was more complicated than just based on the size-sieving. Two research groups reported the bio-inspired nanoporous graphene for sieving K$^+$ and Na$^+$, as Na$^+$ encountered a much higher energy barrier than K$^+$, although Na$^+$ posses a smaller radius than K$^+$. It was also found that the presence of charge or functional group around the surface would heavily affect the ion-transport from nanoporous graphene.[85] The experiments of ions separation by nanoporous graphene are few. Jain et al.[86] observed the selectivity of the monovalent cation (K$^+$) and divalent cations (Mg^{2+}) from sub-2 nm nanopore on graphene lattice. Rollings et al. [87] demonstrated a selectivity of 100 between K$^+$ and Cl$^-$ from even 20 nm graphene nanopore (**Figure 1.9d**). These interesting selectivity derived from nanopore, whose diameter is much bigger than the ion radius, suggests the mechanism of ion-transport is much more complicated than we understand now. There are still several mysterious mechanisms and interactions between ions and nanoporous graphene to explore.
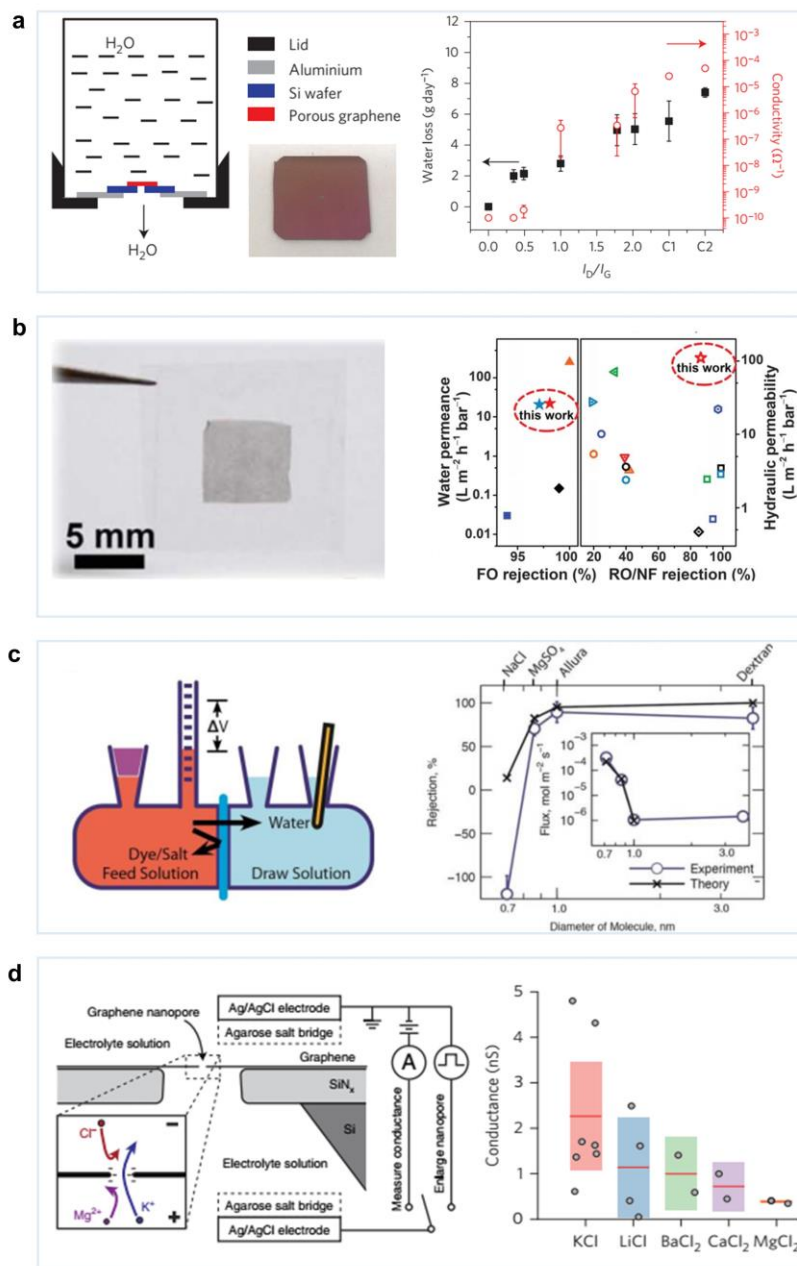
Figure 1.9 (a) The device for water transport measurements of 5 μm suspended nanoporous graphene on SiN substrate and the water loss through the nanoporous graphene as a function of the I_D/I_G ratio.[56] Reprinted with permission from Springer Nature. (b) The photo of nanoporous graphene/carbon nanotube hybrid membrane, and the water-permeability and salt-rejection performance of the membrane.[80] Reprinted with permission from AAAS. (c) Experimentally measured rejection and molar flux (inset) of solutes and predicted performance by the theoretical continuum model.[88] Reprinted with permission from ACS. (d) Schematic of the ion transport through nanoporous graphene and the obtained hydration-based cation selectivity.[86,87] Reprinted with permission from Springer Nature.

3. Nanoporous single-layer graphene for gas separation

Mechanism of gas transport through nanoporous single-layer graphene

Single-layer graphene, incorporated with high-density gas-sieving pores, has been regarded as the ultimate gas separation membranes, capable of yielding ultrahigh gas permeance and an attractive molecular selectivity. The gas transport through nanoporous graphene can be described by the two types of transport models. Strano, Blankschtein, and their co-workers focused on the analytical expression of various limits of gas diffusion, surface adsorption, or pore translocation as the rate-limiting step. They considered the limit steps are analogous to the reactant adsorption, diffusion, and reaction in the catalytic reaction.[89–91] Another model considered gas transport more from steric considerations, which was developed by Hadjiconstantinou,[92] Karnik,[93] Bai,[94] and their co-workers. They calculated the ideal flux from all the directions and calibrated the molecular flux of the steric considerations by calculating the fraction of trajectories with molecular centers that intersect the graphene membrane within the pore diameter.[92,93] Here, we discuss our gas transport model based on the two established models,[95] to elucidate the gas transport mechanism through the nanoporous graphene membrane.
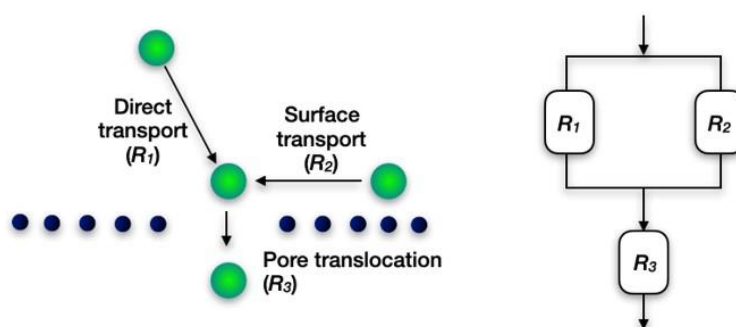
Figure 1.10 Schematic of gas molecules transport through the nanoporous graphene and the resistance model of the whole transport process.[95] Reprinted with permission from Wiley-VCH GmbH.

Let's consider a scenario where nanoporous graphene acts as a barrier to separate the gas molecules with a feed pressure of P, and the permeate side (vacuum) is kept as a vacuum. The gas molecules in the feed are driven to permeate side due to the pressure difference across the membrane. In this case, only the porous area would allow the molecules to pass through the membrane, analogous to the "active sites" in the reaction

process. The gas molecules reach these "active sites" (pore mouth) by either direct impingement or surface diffusion. The direct impingement flux is the ideal gas flux arriving at the pore from the bulk (gas) phase. The surface diffusion flux is the adsorbed gas molecules diffusing to the pore mouth. After the gas molecule reaches the pore mouth, it experiences an energy barrier to translocate the pore to the permeate side, similar to the activation energy encountered in the reaction. Below, we use the resistance model to express transport behavior, as shown in **Figure 1.10**.

The total resistance of the gas transport process through the nanoporous graphene is R, which could be calculated as follows,

$$R = R_3 + \frac{1}{R_1^{-1} + R_2^{-1}} \tag{1.1}$$

Where R_1, R_2, and R_3 represent the resistances corresponding to the direct impingement, surface diffusion, and translocation, respectively. R_1 and R_2 are in parallel, and their combination is in series with R_3 to obtain the total resistance R.

The net permeation rate through the nanopore is as follows,

$$N_p = \frac{\Delta P}{R} \tag{1.2}$$

Where N_p is net permeation rate through the nanopore, ΔP is the transmembrane pressure difference. R^{-1} is also the pressure-normalized permeation rate here, defined as the gas permeability coefficient of the nanopore.

For a given nanopore with an effective diameter, D_p, the resistances can be written as

$$R_1^{-1} = \sqrt{\frac{\pi}{2mk_BT}} \frac{D_p^2}{4} \tag{1.3}$$

$$R_2^{-1} = \sqrt{\frac{\pi k_B T}{2m}} D_p H_{sur} \tag{1.4}$$

$$R_3^{-1} = \frac{A_{pore}}{2\sqrt{2\pi mk_BT}} \text{erfc}\left(\sqrt{\frac{E_{act}}{k_BT}}\right) \tag{1.5}$$

where m is the molecular mass, T is temperature, k_B is the Boltzmann constant, H_{sur} is Henry's coefficient for the adsorption of the gas molecule on graphene basal plane, and E_{act} is the energy barrier for the translocation event.

The resistance of direct gas impingement, surface diffusion, and translocation would change with the pore diameters. For the pore diameter close to gas kinetic diameter, the gas molecules experience high energy barriers to translocate through the pore, where the translocation resistance R_3 would be the dominating resistance for the total; we called this is in the activated regime. In this regime, different gas molecules encounter different activation energy generated by the size-sieving effects, resulting in gas selectivity of the nanoporous graphene. For the relatively bigger pore, the translocation resistance becomes negligible, and it is mainly generated by direct impingement and surface diffusion. In this case, the selectivity would be generated from the surface interaction of the nanoporous graphene and gas molecules. **Figure 1.11** displays the inverse transport resistance of direct impingement, surface diffusion and translocation of the nanopores graphene as a function of the pore diameters.
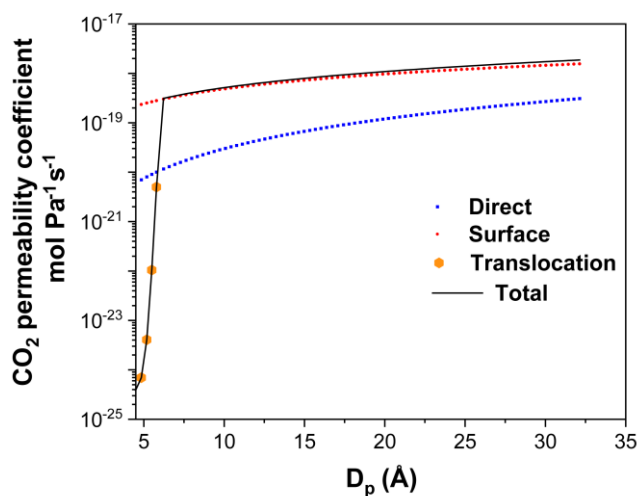
Figure 1.11 The inverse transport resistance of CO_2 from direct impingement, surface diffusion, and translocation of the nanopores graphene as a function of the pore diameter.[56] Reprinted with permission from Wiley-VCH GmbH.

From the mechanism of gas transport through the nanoporous graphene, we could see the selectivity obtained from the membrane heavily depends on the pore-size-distribution in the nanoporous graphene. Incorporating sub-nanometer nanopores with a sub-angstrom resolution is the critical step to fabricate a high-performance membrane for gas separation.

Gas separation through nanoporous single-layer graphene

As discussed in the previous work on transport mechanism, the nanoporous graphene with suitable pore-size would generate high gas pair selectivity via the size-sieving effect, attributing to the hindrance of the diffusion of the slightly larger molecules. The gas flux and selectivity through the nanopore are highly dependent on the relative size of the molecule with respect to the pore diameter. With the help of the computation method, based on DFT and MD simulations, the gas flux and selectivity of the gas pairs could be estimated by calculating the energy barrier described by the enthalpic and entropic penalties between the gas molecule and nanopore. Jiang et al.[96–98] carried out a series of simulations on gas flux and selectivity through the nanopore of ten carbon atoms missing (3.0×3.8 Å) on graphene lattice, showing the pore could separate the H_2/CH_4, CO_2/N_2 with over 300 selectivities and 10^5 GPU permeance (**Figure 1.12a**). Schrier et al.[99–101] showed the hydrogen-terminated nanopore with six carbon atom missing on graphene could confine the He^3 and He^4, realizing the quantum separation of fermionic He from bosonic He (**Figure 1.12b**). Those simulations established the great potential of the size-sieving effect from the nanoporous graphene.
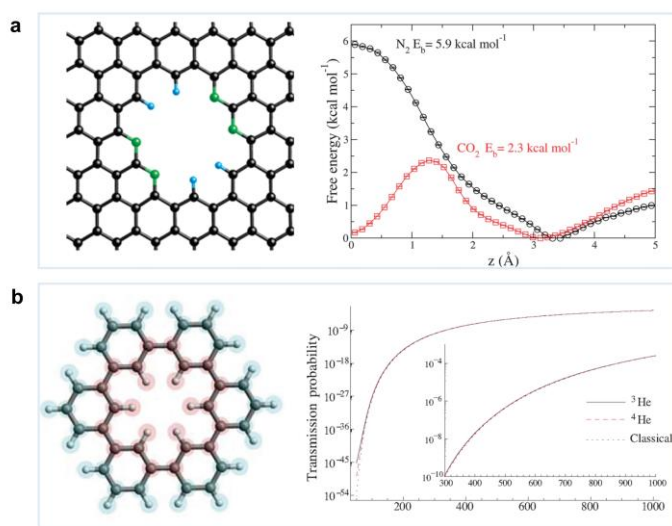
Figure 1.12 (a) Schematic of 3.0 x 3.8 Å nanopore with ten carbon atoms missing on graphene lattice and the free profiles for a gas molecule permeating through the nanoporous graphene at 20 atm.[98] (b) Schematic of the nanopore structure on graphene lattice and potential energy for ^3He and ^4He transmission.[100] [88] Reprinted with permission from ACS.

The transport mechanism also reveals that the surface diffusion and the direct impingement could dominate the transport when the nanopore is much larger than the kinetic diameter of the gas. Here, the translocation energy barrier is zero, and the net flux is equivalent to the flux of the gas molecules arriving at the pore mouth. In that case, surface modification on the graphene surface would promote the selectivity of the nanopores by tuning the surface diffusion rate. Schrier et al.[102] investigated Henry's constant of various gases molecules on the fluorinated nanoporous graphene, showing the possibility to obtain adsorption selectivity from the gas pairs on graphene lattice. Jiang et al.[103] implemented the ionic liquid [emim][BF_4] on the nanoporous graphene surface to tune the adsorption energies of gas on the graphene surface. The calculation displayed the adsorption selectivity of 4.6 and 2.7 for CO_2/N_2 and CO_2/CH_4 (**Figure 1.13**) could be obtained from 6 Å nanopore, which is much bigger than the kinetic diameters of the gas molecules.
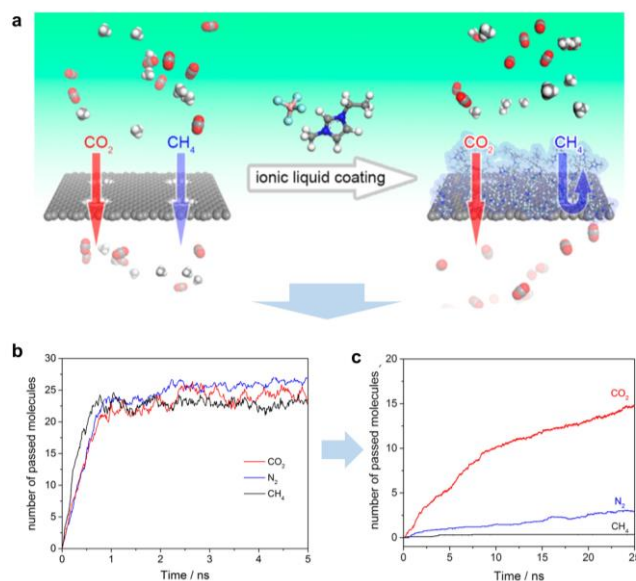
Figure 1.13 (a) Schematic of ionic liquid gated single-layer graphene. The number of gas molecules passed through nanoporous graphene (b) and nanoporous graphene with ionic liquid (c).[103] Reprinted with permission from ACS.

These simulation studies depict the potential of nanoporous graphene in gas separation applications and highlight key strategies to synthesize gas-sieving nanoporous graphene membrane:

1) Manipulate the pore-size of the nanopore in graphene to achieve the size-sieving separation. All the previous models and simulations stated the relative size of the molecule with respect to the pore diameter determines the gas flux and selectivity. A narrow pore-size distribution is necessary to realize effective molecular sieving with sub-angstrom resolution.

2) Incorporate high-density nanopores to realize the great potential of the nanoporous graphene for separation. Most of the simulation calculations predicted high gas permeance of the nanoporous graphene membrane based on the multiplication of pore density and permeance coefficient (gas permeance per pore). Hence, high-density gas-sieving nanopores are required to achieve a high-flux membrane.

3) Modify the graphene surface to promote the adsorption selectivity of gas pairs. When the translocation barrier is close to zero (the nanopore located in the Knudsen regime), the resistance of the surface diffusion dominated the whole transport resistance based on the gas transport model. The DFT simulation works exhibited the effusive nanopore could generate adsorption selectivity, which is derived from the different adsorption energies of gases on the nanoporous graphene surface. It is possible to increase the separation performance of the nanoporous graphene membrane by creating a competitive adsorption environment for the gas mixture.

A few experimental studies have been reported, demonstrating gas separation through nanopore on graphene; however, it has remained a challenging task to achieve high-performance nanoporous graphene membrane. A proof-concept of gas separation was demonstrated by Koenig et al. with 5 μm suspended exfoliated graphene treated by UV-treatment.[72] The double-layer graphene was pressurized as a micron-size balloon filled with a specific gas, then the deflation rate of the gas was monitored via the pressure change. The different deflation rates of H_2, CO_2, Ar, N_2, CH_4 through micro-size balloon reflected the gas pair selectivity from the graphene nanopore, indicating the nanoporous graphene could reach highly selective separation (**Figure 1.14a**). However, the micrometer-sized exfoliated graphene nanosheet limited the scalability of the device. Followed by this, Celebi et al.[55] transferred 2500 μm^2 CVD derived graphene on SiN_x porous substrate and drilled arrays of nanopores with 7.6 nm by FIB on the graphene lattice (**Figure 1.14b**).

The resulting membrane displayed ultra-high gas flux ($\sim 10^{-3}$ mol Pa^{-1} s^{-1} m^{-2}) but effusive gas transport with the nanometer-sized pores. Boutilier et al. fabricated a centimeter-scale single-layer graphene membrane with oxygen plasma. However, the cracks induced during the transfer process suppressed the gas separation performance, limiting the H_2/CH_4 selectivity (3.2) close to the Knudsen selectivity (2.8) (**Figure 1.14c**).[104] Similarly, Yuan et al. observed gas mixture permeances of the order of 10^{-6} to 10^{-5} mol m^{-2} s^{-1} Pa^{-1} with slightly higher gas pair selectivity ($He/SF_6 = 9.3$) than Knudsen selectivity (6.0) (**Figure 1.14d**).[105]

Overall, the expected attractive performance for gas separation from the one-atom-thick nanoporous graphene membranes with a sufficiently large area has never been demonstrated experimentally.
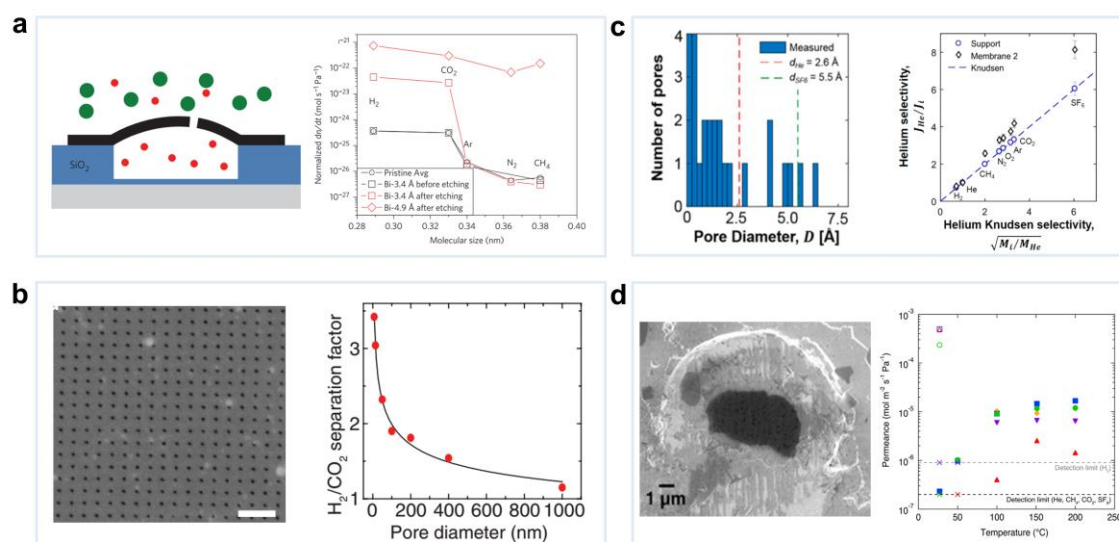
Figure 1.14 (a) Schematic of a microscopic graphene membrane on 5 μm a silicon oxide substrate and leak rate of different gas through the UV-ozone treated nanoporous graphene.[72] Reprinted with permission from Springer Nature. (b) Nanoporous graphene with 7.6 nm nanopores induced by FIB, and the gas permeance and selectivity through the film.[55] Reprinted with permission from AAAS. (c) The gas separation performance and pore-size distribution obtained by the nanoporous graphene treated by oxygen plasma.[104] (d) SEM image of the 5 μm suspended graphene and gas separation performance from the intrinsic defect during graphene synthesis.[105] Reprinted with permission from ACS.

Existing bottlenecks of nanoporous graphene for gas separation

Previous studies revealed the great potential of the nanoporous graphene for gas separation, but there are at least two bottlenecks hindering the realization of the high-performance gas separation through the atom-thick graphene membrane. a) Crack-free transfer of relatively large-area graphene onto porous supports. The previous works either showed a 5 μm membrane area or poor gas selectivity due to the cracks introduced during the transfer. b) Incorporate high-density gas-sieving nanopores with a narrow pore-size-distribution (PSD). The incorporated nanopore aperture needs to differentiate the gas molecules with sub-angstrom size differences to realize effective separation. For example, the kinetic diameter of CO_2 and N_2 is 0.33 nm and 0.364 nm, respectively, so the size difference between the two gas molecules is only 0.03 nm. Besides, the high pore density is also required to realize a high flux from the nanoporous graphene membrane, attributing to the fact that permeance of the membrane is the sum-up of gas flux through all nanopores. The incorporation of high-density, narrowly-distributed nanopores, is the most critical step to realize the high-permeance nanoporous graphene membrane. However, the current pore-fabrication method is challenging to achieve this due to the inherent trade-off between pore density and pore-size distribution. In this part, we will discuss the two bottlenecks in detail.

Chemical vapor deposition-derived single-layer graphene is suitable for scalable single-layer graphene membrane fabrication. However, the one-atom-thick layer needs to be transferred from the impermeable metal foil (such as Cu foil) to porous support for membrane fabrication. Wet-transfer has been investigated as an effective and widely used method to transfer single-layer graphene to the targeted substrate. Typically, a thin-layer of poly(methyl methacrylate) (PMMA) was coated on graphene/copper as the reinforcement during the transfer. The layer of graphene with PMMA floated on the etching bath after removing the copper substrate. Subsequently, the floating film would be scooped by the substrate after several times of rinsing. Finally, the PMMA layer would be washed out by the solvent, leaving the graphene on the target substrate. Conventionally, wet-transfer works effectively for the transfer of graphene onto a non-porous substrate.

However, for the porous substrate, the different evaporation rate of the solvent on the open surface and porous area would generate significant capillary force, inducing tears,

and cracks in graphene film during the solvent drying step. This could be mitigated by using a solvent with low surface tension, such as $C_4F_9OCH_3$.[106] But for gas separation, even nanometer-size defect on single-layer graphene could contribute several orders of magnitude gas permeance (ca. 10^{-18} mol Pa^{-1} s^{-1} m^{-2} for effusive nanopore), compared with the gas-sieving pore (ca. 10^{-22} mol Pa^{-1} s^{-1} m^{-2}).[55,72] As a result, the non-selective effusive gas flux generated from the defects would dominate the gas transport, leading to poor gas pair selectivity of the membrane. The existing PMMA-assisted wet-transfer method inevitably induces crack when the transfer area exceeds tens of micrometers. Recently, phase-inversion casting to transfer single-layer graphene on the porous substrate was implemented to fabricate the relatively large-area membrane.[80,104,107–109] Yet this method still generates cracks after the metal removing step, because of the variable pore structures of the membrane substrate. Hence, crack-free single-layer graphene membrane and effective gas separation through the nanopore is rarely demonstrated, remaining as a hurdle for investigation of gas transport through the nanopores on graphene. Also, it is a starting point to scale up the crack-free membrane area to meter-size for practical industrial applications. Overall, realizing the crack-free transfer is the precondition for developing effective gas-sieving nanoporous graphene membranes.

How to incorporate high-density gas-sieving nanopores with a narrow pore-size distribution in graphene film is another dilemma for graphene membrane fabrication. Gas separation requires sub-nanometer pores even sub-angstrom resolution of the pore aperture to differentiate the gas molecules with similar gas kinetic diameters (k.d.), such as gas pair H_2 (k.d. 2.89Å) and CH_4 (k.d. 3.80Å), or CO_2 (k.d. 3.30Å) and N_2 (k.d. 3.64Å). The small kinetic diameter difference of the gas pair makes it extremely difficult for gas-sieving through nanoporous graphene, which inherently lacks ordered and uniform pore aperture. As mentioned above, there are several methods to incorporate the nanopores in the graphene lattice, but there is no effective approach to fabricate high-density nanopores to realize high-resolution gas separation.

The existing pore-fabrication method could not overcome the trade-off between the pore density and pore size. The carbon etching chemistry on graphene lattice is analogous to the crystal nucleation and growth, and the nucleation in the basal plane requires much higher energy than removing a carbon atom near the pore-edge. For the perfect sp^2 carbon

structure, removing one carbon atom requires 20 – 24 eV energy to break the three C-C bonds. Subsequently, the energy barrier of cleaving carbon atom around the nuclei would drop to 14 eV, attributing to the less-bonded carbon near the defective site.[53] Due to the huge energy barrier difference, the expansion rate could be several orders of magnitude higher than that of the nucleation rate. Moreover, in most of the nanopore etching processes, the two steps happened simultaneously and are difficult to decouple. This dilemma leads to the trade-off between pore size distribution and pore density, namely higher pore density always along with broad pore-size distribution and vice versa. As a consequence, it is challenging to incorporate gas-sieving pores in single-layer graphene to achieve sub-angstrom molecular sieving resolution.

4. Thesis outline

This dissertation focuses on addressing the existing bottlenecks of nanoporous single-layer graphene membrane for gas separation, exploring the potential of the atom-thick layer to be an ultrahigh throughput gas-sieving film. Chapter 1 summarizes the development of nanoporous graphene and its application for separation. It also discusses the existing problems to be solved. Chapter 2 demonstrates a novel nanoporous carbon-assisted transfer method to fabricate the defect-free single-layer graphene membrane on a porous substrate for the first time and investigates the gas transport through the CVD-derived graphene membrane. Chapter 3 describes a novel millisecond ozone etching method to incorporate high-density (10^{12} cm^{-2}) nanopores in single-layer graphene with a narrow pore-size distribution, working against the trade-off between pore-density and pore-size distribution. Chapter 4 applies the transfer method and ozone-functionalization tools for other carbon-based membranes, fabricating sub-200 nm high-performance carbon molecular sieve membrane. Chapter 5 summarizes the current work and proposes the future direction of this topic. Below are the details of each chapter.

Chapter 1 introduces the importance of the high-performance membrane for the development of energy-efficient membrane separation, discusses current etching method and difficulty of sub-nanopore incorporation, demonstrates the great potential as well as challenges of the nanoporous graphene membrane in the gas separation field.

Chapter 2 describes a novel nanoporous carbon (NPC)-assisted transfer method to

fabricate crack-free, suspended single-layer CVD graphene films with millimeter-scale, which enables us to observe and understand the gas transport through the intrinsic defects in CVD-derived graphene. The single-layer graphene membrane with a minuscule porosity of 0.025% displayed attractive H_2 permeance and H_2/CH_4 selectivities. Followed by the exploration of ozone functionalization on graphene lattice, it demonstrates the improvements in the H_2 permeance and H_2/CH_4 selectivity by ozone-functionalization.

Chapter 3 describes an ozone-based carbon gasification chemistry applied in the custom-made millisecond gasification reactor (MGR), which works against the existing trade-off between pore density and pore-size distribution. Rapid and controllable etching on the graphene lattice incorporated high-density (10^{12} cm^{-2}) of nanopores with a narrow pore-size distribution of sub-angstrom resolution (0.2 Å). The molecular cut-off could be further adjusted with slow oxygen etching, yielding attractive CO_2/CH_4, CO_2/N_2, O_2/N_2 separation performances. The film with 1% porosity realized a high-performance membrane for CO_2 capture and reached the U.S. Department of Energy (DOE) target, attributing to the ultrashort and selective diffusion path.

Chapter 4 fabricates a high-performance ultrathin carbon molecular sieve (CMS) membrane by applying transfer and masking methods, cutting down the thicknesses of CMS films from several micrometers to less than 200 nm. The room-temperature ozone treatment is applied to shrink CMS pores by a fraction of an angstrom, improving H_2/CH_4 and H_2/CO_2 selectivities by several folds.

Chapter 5 summarizes the development of the methods to fabricate a high-performance single-layer graphene membrane and possible future directions for the development of the nanoporous graphene membrane.

Chapter 2 Single-layer graphene membranes by crack-free transfer for gas mixture separation

Adapted with permission from <u>Shiqi Huang</u>, Mostapha Dakhchoune, Wen Luo, Emad Oveisi, Guangwei He, Mojtaba Rezaei, Jing Zhao, Duncan T. L. Alexander, Andreas Züttel, Michael S. Strano & Kumar Varoon Agrawal, Single-layer graphene membranes by crack-free transfer for gas mixture separation, **Nature Communications**, 9, 2632 (2018), DOI:10.1038/s41467-018-04904-3. Copyright © 2018, Springer Nature*

Abstract

The single-layer graphene film, when incorporated with molecular-sized pores, is predicted to be the ultimate membrane. However, the major bottlenecks have been (a) crack-free transfer of large-area graphene on a porous support and, (b) incorporation of molecular-sized nanopores. Herein, we report a nanoporous-carbon-assisted transfer technique, yielding a relatively large area (1 mm^2), crack-free, suspended graphene films. Gas-sieving (H_2/CH_4 selectivity up to 25) is observed from the intrinsic defects generated during the chemical vapor deposition of graphene. Despite the ultralow porosity of 0.025%, attractive H_2 permeance (up to 4.1 x 10^{-7} mol m^{-2} s^{-1} Pa^{-1}) is observed. Finally, we report an ozone-functionalization based etching and pore-modification chemistry to etch hydrogen-selective pores, and to shrink the pore-size, improving H_2 permeance (up to 300%) and H_2/CH_4 selectivity (up to 150%). Overall, the scalable transfer, etching and functionalization methods developed herein is expected to bring nanoporous graphene membranes a step closer to reality.

1. Introduction

Atom-thick graphene film is the thinnest possible molecular barrier and therefore incorporated with molecular-sized pores, it can be regarded as the ultimate membrane[93]. Several molecular simulations have shown that the two-dimensional nanopores in graphene can yield high gas permeance, orders of magnitude higher than that attainable with the conventional membranes[92,96,97,100,102,110–114]. Such high-flux membranes can considerably reduce the needed membrane area for separating a volume of a molecular

mixture, addressing the problem of scale-up, a longstanding issue with the inorganic membranes. The thermal and chemical robustness and the high mechanical strength of the graphene lattice, even with porosity as high as 5%[115,116], makes it highly attractive for the gas separation. Recently, several etching methods for incorporating sub-nanometer pores in graphene lattice have been developed, leading to promising sieving performances for liquids and dissolved ions[46,55,81,86]. However, the demonstration of gas mixture separation from the single-layer graphene membrane has remained a challenging task[104,117]. A proof-of-concept was demonstrated by measuring the deflation rate of a bilayer graphene microballoon, where pores were incorporated by multiple ultraviolet treatment[72]. In general, the molecular transport studies through single-layer graphene have been primarily carried out on micron-sized domains, attributing to the poor scalability of the micromechanical exfoliation, and the challenging transfer of the chemical vapor deposition derived graphene. Celebi et al. reported a 2500 μm^2-sized bilayer graphene membrane by masking cracks in a graphene film by another graphene film[55]. Using focused ion beam, an array of nanopores (>7.6 nm in diameter) were incorporated, leading to an effusive gas transport. Recently, a centimeter-scale single-layer graphene membrane hosting molecular-sized pores was reported, however, the cracks generated during the transfer limited the separation selectivity close to that expected from the Knudsen diffusion (H_2/CH_4 and He/SF_6 selectivities of 3.2 and 8.0, respectively, were reported)[104]. Overall, the demonstration of gas mixture separation from a sufficiently-scaled single-layer graphene membrane has remained elusive. To develop graphene membranes, one needs to a) transfer large-area graphene onto porous supports without generating cracks and tears, and b) generate molecular-sized pores with a narrow pore-size-distribution (PSD). Development of such method would also allow one to study the gas transport mechanism (activated vs. surface vs. Knudsen transport), and effect of the competitive adsorption through the graphene nanopores.

Herein, we report a novel nanoporous-carbon-assisted graphene transfer technique that enables the transfer of relatively large area (1 mm^2) single-layer CVD graphene onto a macroporous support (pore-opening of 5 μm) without generating cracks or tears, allowing observation of gas-sieving from the intrinsic defects of CVD graphene. An attractive H_2 permeance (up to 4.1 x 10^{-7} mol m^{-2} s^{-1} Pa^{-1}) is obtained despite the ultralow-density of the intrinsic defects (porosity of 0.025%). Activated gas transport is observed

with the average activation energy for H_2 transport across eight membranes being 20.2 ± 2.7 kJ/mole. The molecular-sized intrinsic defects yield an attractive separated selectivity, including those from the mixed gas feed (H_2/CH_4 separation factor up to 18). The membrane performance remains stable during several heating and cooling cycles (25-150 °C), and at least up to 7 bar of the transmembrane pressure difference. Finally, in the pursuit to increase the density of gas-selective pores, we also report an ozone-functionalization based etching and pore-modification chemistry, increasing the nanopore density and/or reducing the effective pore-size. A combination of higher selectivity, higher permeance, and higher selectivity/higher permeance is observed.

2. Methods

2.1 Graphene growth

Single-layer graphene was synthesized by the low-pressure chemical vapor deposition (LPCVD) on a Cu foil (25 μm, 99.999% purity, Alfa-Aesar). Before CVD, the foil was placed in the fused quartz tube and annealed at 1000 °C in a CO_2 atmosphere at 700 Torr for 30 min to remove organic contaminents[118]. Then CO_2 was switch off and the chamber was evacuated. Following this, 8 sccm of H_2 was introduced to purge out CO_2 and to subsequently anneal the copper surface at 1000 °C. To initiate graphene nucleation, 24 sccm of CH_4 was added at total pressure of 460 mTorr. After 30 min growth, the CH_4 flow was switched off and the chamber was rapidly cooled down to the room temperature.

2.2 Nanoporous carbon-assisted graphene transfer

To deposit the nanoporous carbon (NPC) film on graphene, 0.1g block-copolymer (poly (styrene-b-4-vinyl pyridine), Polymer Source) and 0.2 g turanose (Sigma-Aldrich) were dissolved in DMF (Sigma-Aldrich). After heat treatment of the solution at 180 °C, the solution was spin-coated onto the as-synthesized CVD graphene supported on the Cu foil. Pyrolysis of the polymer film was conducted at 500 °C in a H_2/Ar atmosphere for 1 h, forming the NPC film on top of graphene. The NPC/graphene/Cu was floated on a $Na_2S_2O_8$ bath (0.2 M in water) to etch the Cu foil. After Cu etching, the floating NPC/graphene film was rinsed in deionized water to remove the residues. Finally,

NPC/graphene was scooped on the porous tungsten support.

The standalone NPC film was fabricated and tested as the control experiment[119]. The precursor polymer solution was coated on bare copper foil, then transferred to a TEM grid and a porous tungsten substrate by the same method as that used for the transfer of the graphene membrane. Image analysis of the pore-size-distribution revealed pores with a diameter between 20-30 nm. Gas permeance test on porous W supported NPC film exhibited gigantic H_2 permeance 1.9 x 10^{-3} mol m^{-2} s^{-1} Pa^{-1} (**Table 2.1**)[119]. The high-permeance of the NPC film ensures that the NPC film does not restrict the gas permeance from the pores in the single-layer graphene.

The macroporous substrate was fabricated by drilling an array of 5 μm holes (2500 holes) in 1 mm^2 area of a 50-μm-thick tungsten foil. Laser drilling was carried out by Potomac Photonics Inc. A tungsten foil was chosen as membrane support due to its rigidity, mechanical and thermal stability. More importantly, the W support enabled metal-to-metal sealing, which was gas-tight. Hydrogen permeances through these 5 μm holes exceeded 10^{-2} mol m^{-2} s^{-1} Pa^{-1}. Therefore, like NPC film, the W support also does not restrict the gas-transport through the single-layer graphene membrane.

Table 2.1 Gas permeance through the NPC film

Gas	Permeance (mol m^{-2} s^{-1} Pa^{-1})
H_2	1.9 x10^{-3}
He	1.1 x10^{-3}
CH_4	7.8 x10^{-4}
N_2	6.0 x10^{-4}
CO_2	4.4 x10^{-4}

2.3 In-situ ozone functionalization

Ozone functionalization on the suspended graphene film was conducted in-situ in the membrane module. The gas permeation module was leak-proof based on the metal-metal

(Swagelok VCR fittings) seal. The membrane was sandwiched as a gasket in the VCR based module, making a leak-tight fitting. Before, ozone functionalization, the membrane was heated to 150 °C to remove adsorbed atmospheric contaminations and to allow measurement of the gas separation performance. Then, the membrane was cooled to the functionalization temperature. Subsequently, a mixture of O_2 and O_3 (21% in O_3) generated by the ozone generator (Absolute Ozone® Atlas 30) was exposed to the permeate side of graphene. After a certain time, argon was used to sweep-out the residual ozone.

2.4 Gas permeation test

The single-component and mixture gas permeation tests were carried out in a homemade permeation setup (**Fig. 2.1a**). Permeation tests were conducted in the open-end mode. All equipment used in the permeation setup (the mass flow controllers (MFCs) and mass spectrometer (MS)) were calibrated within 5% error. The gas permeation module based on the metal-metal (Swagelok VCR fittings) seal was leak-proof. The porous tungsten support was sandwiched as a gasket in the VCR based module, making a leak-tight fitting (**Fig. 2.1b**). To ensure temperature uniformity and accuracy, the feed and the sweep lines were preheated, and the membrane module was heated inside an oven with the temperature accuracy of ± 1 ºC.

A pre-calibrated MFC regulated the flow rate of feed gas, and the feed pressure was controlled by adjusting the back-pressure regulator installed at the downstream. Another pre-calibrated MFC controlled the flow rate of sweep gas (Ar), which carried the permeate gas to the pre-calibrated MS for real-time analysis of the permeate concentration (**Figure 2.1**). The MS was capable to read an extremely low concentration in the permeate stream. To reduce errors, MS was calibrated at low concentration of H_2, He, CO_2 and CH_4 in Ar, similar to those in the permeate stream.

The transmembrane pressure difference was varied between 1.5 to 7.0 bar. Before testing, all membranes were heated to 150 ºC to remove the contaminations on the graphene surface. For the mixture permeation tests, an equimolar gas mixture was used on the feed side. The gas flux was calculated once the steady-state was established (typically 30 minutes after changing the permeation conditions). The measurements were

carried out at continuously, in real-time, and only the steady-state data are reported
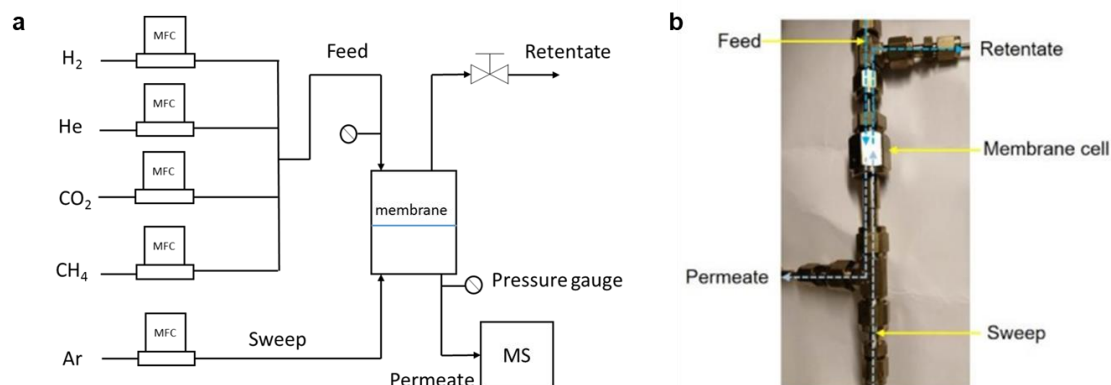
Figure 2.1 a) Schematic of the setup for gas permeance test. b) photograph of membrane cell with leak-tight VCR fitting.

2.5 Characterization

Electron microscopy

Scanning electron microscopy (SEM) was carried out by using FEI Teneo SEM at 0.8-2.0 kV and working distances of 2.5-9.0 mm. No conductive coating was applied on the substrates prior to SEM. Transmission electron microscopy (TEM) imaging and electron diffraction of the NPC film and the composite graphene/NPC film were conducted by FEI Tecnai G2 Spirit Twin with 120 keV incident electron beam.

For high-resolution TEM (HRTEM), graphene was transferred on a quantifoil TEM grid by the traditional wet-transfer technique[120]. Briefly, a thin poly(methyl methacrylate) or PMMA film was spin-coated on top of graphene. Following this, Cu was etched in a sodium persulfate bath. After rinsing the floating graphene/PMMA film with deionized water, the composite film was transferred to the TEM grid. Subsequently, PMMA was removed by heating the sample to 400 °C in a reducing atmosphere of H_2/Ar.

Aberration-corrected (Cs) HRTEM was performed using a double-corrected Titan Themis 60-300 (FEI) equipped with a Wein-type monochromator. To reduce the electron radiation damage, an 80 keV incident electron beam was used for all experiments. The

incident electron beam was monochromated ("rainbow" mode illumination) to reduce the effects of chromatic aberration, and a negative Cs of ~15–20 μm and slight over-focus were used to give a "bright atom" contrast in the images. HRTEM images were post-treated using a combination of Bandpass and Gaussian filters to reduce noise and improve contrast.

Raman Spectroscopy

Raman characterization was carried on graphene transferred onto the SiO_2/Si wafer by the wet-transfer method[120]. Single-point data collection and mapping were performed using Renishaw micro-Raman spectroscope (532 nm, 2.33 eV, 100x objective). Analysis of the Raman data was carried out using MATLAB. For calculation of the D and the G peak height, the background was subtracted from the Raman data using the least-squares curve fitting tool (lsqnonlin).

X-ray photoelectron spectroscopy (XPS)

The X-ray photoelectron spectroscopy (XPS) analysis was conducted on the graphene mounted on Cu foil using an Mg Kα X-ray source (1253.6 eV) and Phoibos 100 (SPECS) hemispherical electron analyzer with multichanneltron detector. The XPS spectra were recorded in fixed analyzer transmission (FAT) mode using pass energies of 90 eV for the survey and 20 eV for the narrow scans. The samples did not show electrostatic charging thus the binding energies are presented without any correction (Bonding energy of C-C: 284.4 eV; C-O: 285.7 eV; C=O: 286.8 eV; O-C=O: 288.5 eV). Because the carbonyl group (C=O) is part of (O-C=O), O-C=O was counted in C=O in the summation of the functional group. The XPS spectra were processed with CasaXPS, with background subtraction by the Shirley method.

3. Results and discussions

3.1 Crack-free transfer of CVD graphene

CVD derived single-layer graphene is well-suited for the fabrication of large-area membranes attributing to the scalability of the CVD process[35,36]. Post-CVD, graphene needs to be transferred from the catalytic metal foil to a porous support for the membrane fabrication. However, the conventional transfer techniques invariably introduce cracks

and tears in the graphene film[121], and therefore, so far the suspended, crack- and tear-free, single-layer graphene membranes have been limited to a few μm^2 in area[56,86,122].
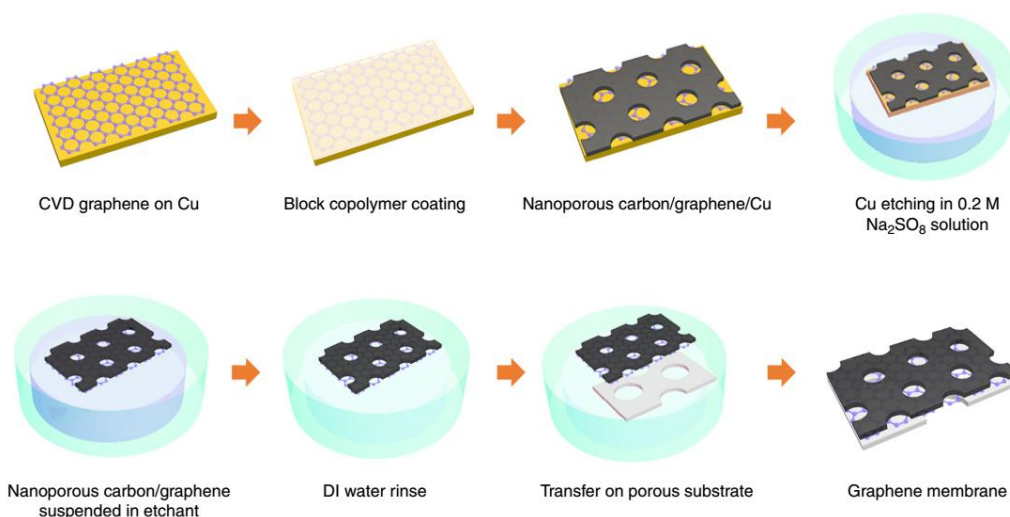
**Figure 2.2** Schematic of fabrication of large-area graphene membrane by the nanoporous carbon (NPC) film-assisted transfer method. A block copolymer solution was spin-coated onto the CVD graphene supported on the Cu foil; pyrolysis was conducted to form NPC film on top of graphene. The copper was etched by 0.2 M sodium sulfate, after which the floating graphene/NPC film was rinsed with DI water. Finally, the NPC/graphene film was transferred onto the porous tungsten support.

Among several transfer techniques developed so far, the wet-transfer technique has been investigated the most attributing to its versatility allowing the transfer of graphene on a wide-range of substrates[120,123–125]. Briefly, the exposed surface of graphene lying on a metal foil is coated with a sacrificial mechanically reinforcing polymer film (typically 100-200 nm thick poly(methyl methacrylate) (PMMA) film). Subsequently, the metal foil is removed by etching the metal in an etchant bath, leaving the polymer-coated graphene floating on the bath. Finally, the floating film is scooped on top of the desired substrate, and the polymer film is dissolved away to expose the surface of graphene. This wet-transfer process has been proven to be quite successful in fabricating graphene-based devices on smooth non-porous substrates[121]. However, significant cracks and tears develop in the graphene film when a porous support is used, primarily because of a strong capillary force on the suspended graphene film during the solvent drying stage[126].

This issue can be mitigated if the mechanically reinforcing film is not removed, and yet somehow the graphene surface is exposed. Motivated by this, we developed a nanoporous carbon (NPC) film-assisted transfer method (**Figure 2.2**), where at the end of the graphene transfer, the NPC film is left on top of the graphene film. Briefly, a solution of turanose and polystyrene-co-poly(4-vinylpyridine) (PS-P4VP) was spin-coated on top of the as-synthesized CVD graphene. The block-copolymer film undergoes phase separation into hydrophobic and hydrophilic domains upon drying[127]. Subsequently, the film was pyrolyzed at 500 °C in the flow of H_2/Ar, leading to the formation of the NPC film on top of graphene. Scanning electron microscope images of the NPC/graphene film on Cu, and transmission electron microscopy images of the transferred NPC/graphene film on a TEM grid revealed that the NPC film was 100 nm thick, and comprised of 20 – 30 nm sized nanopores (**Figure 2.3a-c**), which should expose at least 50% of the graphene surface. Selected area electron diffraction (SAED) of the composite NPC/graphene film (**Figure 2.3d**), displayed the typical diffraction peaks of a suspended single-layer graphene, representing periodicities of 0.213 and 0.123 nm[128]. NPC film (**Table 2.1**) contributed to the SAED with broad rings, a characteristic of the amorphous structure (**Figure 2.4**). We could not find any area representing only the NPC film, indicating that graphene and NPC film bonded strongly during the pyrolysis step and that the graphene did not peel off from the NPC film during the etching of the metal foil. This is highly important for crack-free transfer of graphene, otherwise poor interactions of graphene with a support film can lead to severe cracks and tears during the transfer step[129]. The NPC coated graphene was transferred from the Cu foil to custom-made macroporous support (porous area of 1 mm^2, **Figure 2.3e-f**). The support was fabricated by laser drilling an array of 5 μm pores in a 50 μm thick W foil[122]. The inspection of the transferred film by the SEM confirmed that there were no visible tears or cracks in the transferred film (**Figure 2.3g**). Interestingly, even a macroscopic fold as shown in **Figure 2.3g** did not break the membrane, making this process highly promising for the scale-up of single-layer graphene membrane.
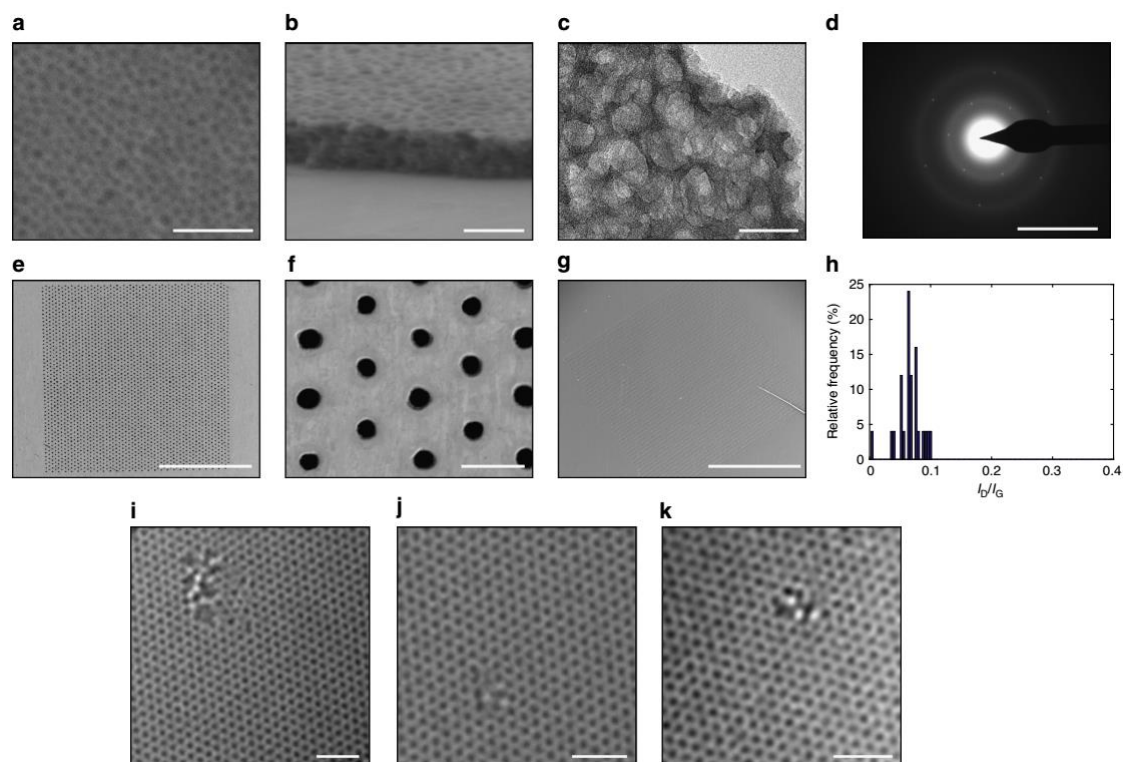
Figure 2.3 Synthesis, transfer, and characterization of low-pressure chemical vapor deposition (LPCVD) derived graphene. a) Scanning electron microscopy (SEM) image of the nanoporous carbon (NPC) film coated on top of graphene. b) Cross-sectional SEM image of the composite NPC film and graphene. c) Transmission electron microscopy (TEM) image of the composite NPC film/graphene. d) The electron diffraction pattern from the composite film shown in (c). e) SEM image of porous tungsten support. f) SEM image of porous tungsten support. g) SEM image of the transferred graphene on the tungsten support. h) Histogram of I_D/I_G from LPCVD graphene. i-k) High-resolution TEM (HRTEM) images of the intrinsic defects in graphene lattice.. Scale bars in (a), (b), and (c) are 200, 100 and 50 nm, respectively. Scale bar in (d) is 10 nm^{-1}. Scale bars in (e), (f), and (g) are 500, 20 and 500 μm, respectively. Scale bars in (i), (j) and (k) are 1 nm.
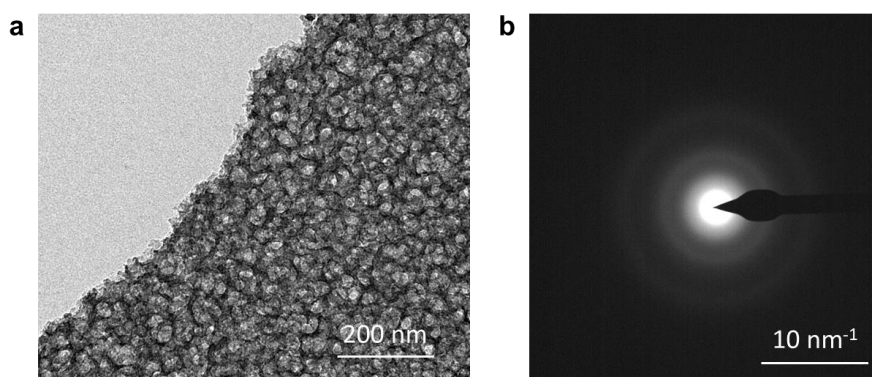
Figure 2.4 a) TEM image and b) SAED of the standalone NPC film.

3.2 Gas transport through intrinsic defects of graphene

Using a scanning tunneling microscope directly on the as-synthesized graphene supported on the Cu foil, we recently imaged the low-density of intrinsic defects in the CVD graphene[122]. These defects are essentially molecular-sized pores (missing 10-16 carbon atoms), formed by etching of the graphene lattice in the presence of residual oxygen in the CVD chamber, and are promising for the gas separation. In the current study, the density of defects, estimated by the carbon amorphization trajectory[130] (I_D/I_G of 0.07 ± 0.02, **Figure 2.3h, Figure 2.5**), was 5.4 x 10^{10} cm^{-2} corresponding to a porosity of 0.025%. A survey of the graphene lattice by aberration-corrected high-resolution TEM (HRTEM) revealed several sub-1-nm nanopores with a pore-density of 2.8 x10^{11} cm^{-2} (**Figure 2.3i-k**). This small disagreement between the HRTEM survey and the estimate from the amorphization trajectory is expected, especially at a low defect density. Nevertheless, the successful crack-free transfer of the CVD graphene allowed us to study the transport behavior of the intrinsic defects.
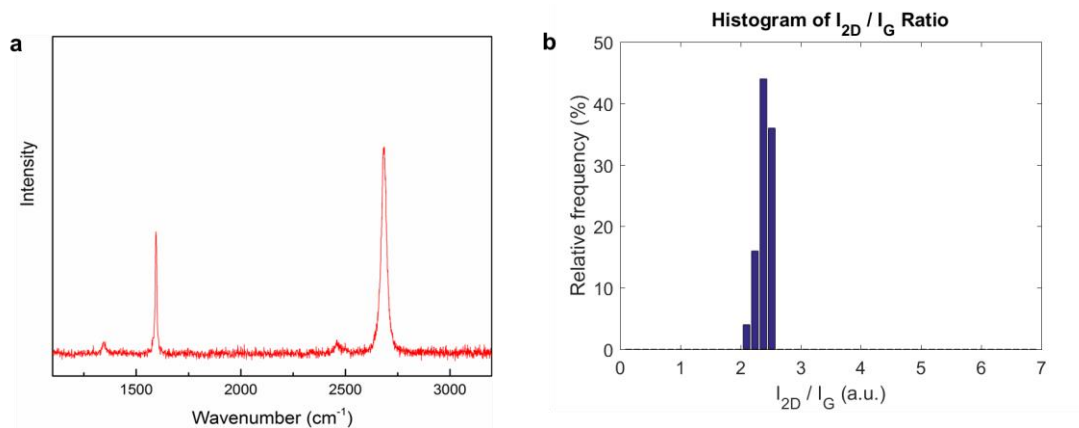
Figure 2.5 a) Raman spectrum of LPCVD graphene. b) Histogram of I_{2D}/I_G of LPCVD graphene from Raman mapping.

Graphene membranes were sealed in a homemade permeation cell using a metal face seal directly on top of the W support, ensuring a leak-proof measurement of the gas transport (details in **section 2.4**). Typically, the feed side (a pure gas feed or a mixture feed) was pressurized to 1.5 – 7.0 bar, whereas the permeate side connected to a pre-calibrated

mass spectrometer was maintained at 1 bar with an argon sweep (**Figure 2.1**). The temperature of the membrane was varied between 25 – 250 °C. Single-component gas transport study from eight separate membranes revealed H_2 permeance in the range of 5.2 x 10^{-9} – 7.2 x 10^{-8} mol m^{-2} s^{-1} Pa^{-1} (15 - 215 gas permeation units, GPU) with H_2/CH_4, H_2/CO_2, and He/H_2 ideal selectivities ranging between 4.8-13.0, 3.1-7.2, and 0.7-2.0, respectively, at 25 °C (**Figs. 2.6 a-d, Appendix-II**). The H_2 permeance corresponded to a permeation coefficient of 1.0 x 10^{-23} – 1.3 x 10^{-22} mol s^{-1} Pa^{-1} based on the defect density of 5.4 x 10^{10} cm^{-2}. This permeation coefficient is consistent with that of Bi-3.4 Å membrane reported by Koenig et al. (4.5 x 10^{-23} mol s^{-1} Pa^{-1})[72]. The H_2/CH_4 selectivity was lower than that from Bi-3.4 Å membrane[72], indicating a wider PSD of intrinsic defects in CVD graphene, compared to PSD from pores incorporated in micromechanically exfoliated graphene. Based on the achieved H_2/CH_4 selectivities, the estimated percentage of larger nanopores yielding non-selective effusive gas transport is less than 25 ppm (Table 2.2). Interestingly, the H_2/CO_2 selectivity was higher than that of the Bi-3.4 membrane, where a selectivity of ca. 1.5 was reported. Membrane M8 displayed the best molecular sieving performance and was the only membrane displaying He/H_2 selectivity greater than 1, implying that the mean pore-size in M8 was less than the kinetic diameter of H_2 (0.289 nm).
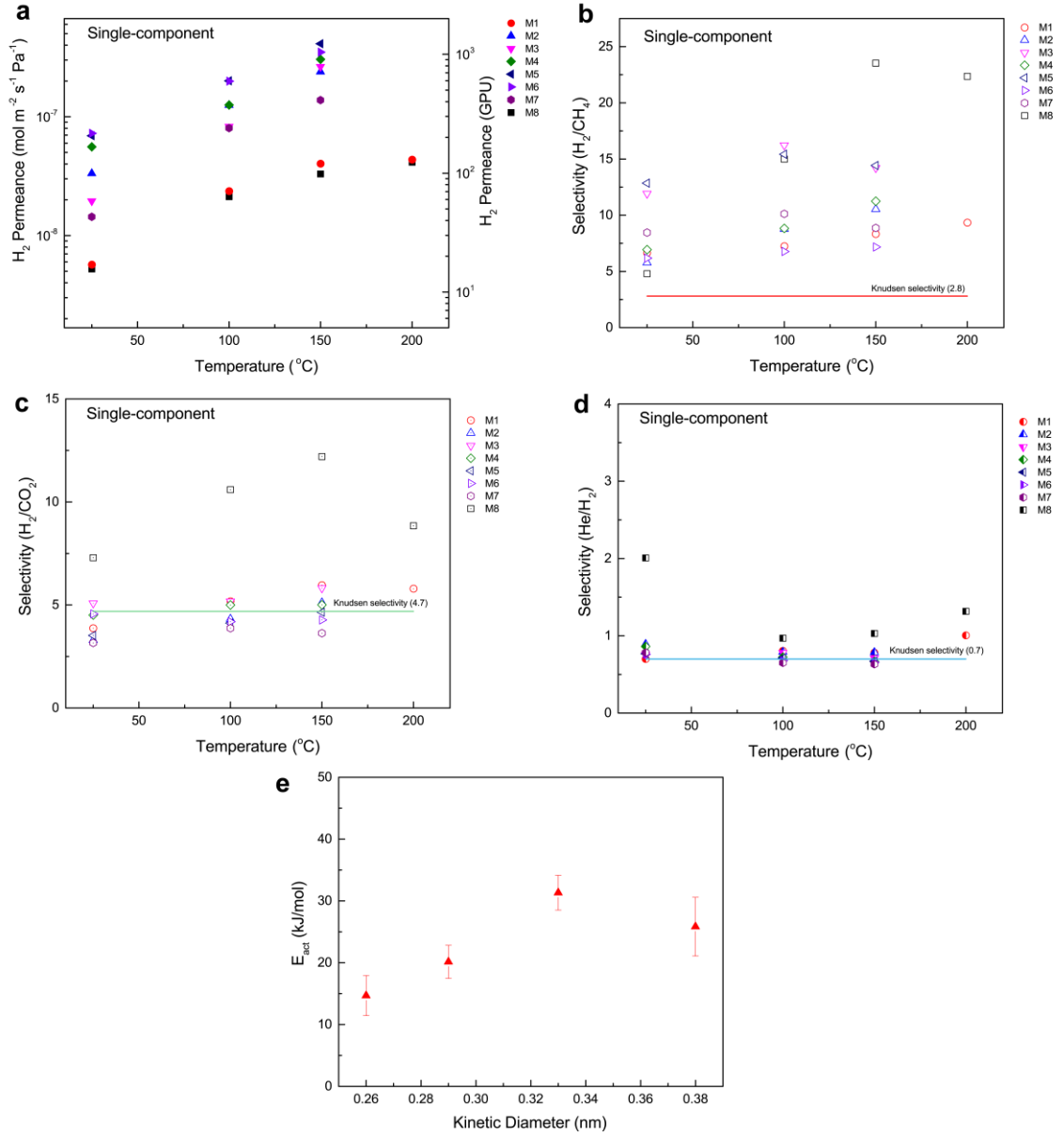
Figure 2.6 Gas separation performance of the intrinsic defects in graphene. a) H_2 permeance across eight graphene membranes (M1-M8) as a function of temperature when using a single-component feed. b-d) Ideal selectivities for various gas pairs from the eight membranes as a function of temperature; b) H_2/CH_4, c) H_2/CO_2, and d) He/H_2. e) Extracted activation energies (average across all 8 membranes) are plotted as a function of the kinetic diameters of various gases.

The method of estimation non-selective nanopores in the graphene membrane was as follows. Given that the transmission coefficient for H_2 and CH_4 from a large nanopore (effusive transport, ca. 10^{-18} mol s^{-1} Pa^{-1}) is several orders of magnitude higher than that from a molecular-selective pore (activated transport, 10^{-22} - 10^{-23} mol s^{-1} Pa^{-1} for H_2, and

10^{-26} mol s^{-1} Pa^{-1} for CH$_4$),[55,72,90,93] we expect that the percentage of pores hosting an electron-density-gap larger than the size of CH$_4$ (kinetic diameter of 0.38 nm) in our graphene membrane is quite low, otherwise H$_2$/CH$_4$ selectivities greater than 2.8 could not be achieved.

Typically, the H$_2$ and CH$_4$ permeances from the graphene membrane of can be written as

$$Permeance_{H_2} = C_e\ N_{e,H_2} +\ C_a\ N_{a,H_2} \tag{2.1}$$

$$Permeance_{CH_4} = C_e\ N_{e,CH4} +\ C_a\ N_{a,CH_4} \tag{2.2}$$

where N_{e,H_2} and $N_{e,CH4}$ correspond to the permeation coefficient of H$_2$ and CH$_4$, respectively for the effusive transport. N_{a,H_2} and N_{a,CH_4} correspond to the permeation coefficient of H$_2$ and CH$_4$, respectively for the activated transport. C_e and C_a correspond to the pore-density (number of pores per unit area) of pores corresponding to the effusive and the activated transport, respectively. The selectivity of gas, α_{H_2/CH_4}, is simply the ratio of the two permeances.

$$\alpha_{H2/CH4} = \frac{Permeance_{H_2}}{Permeance_{CH_4}} = \frac{C_e\ N_{e,H_2} + C_a\ N_{a,H_2}}{C_e\ N_{e,CH_4} + C_a\ N_{a,CH_4}} \tag{2.3}$$

Rearranging above, we get

$$\alpha_{H2/CH4} = \left(\frac{N_{a,H_2}}{N_{a,CH_4}}\right) \left(\frac{1 + \frac{C_e}{C_a}\ \frac{N_{e,H_2}}{N_{a,H_2}}}{1 + \frac{C_e}{C_a}\ \frac{N_{e,CH_4}}{N_{a,CH_4}}}\right) \tag{2.4}$$

Taking N_{a,H_2} and N_{a,CH_4} to be 10^{-22} and 10^{-26} mol s^{-1} Pa^{-1}, respectively,[72] and N_{e,H_2} and N_{e,CH_4} to be 10^{-18} mol s^{-1} Pa^{-1},[55] we get

$$\alpha_{H_2/CH_4} = 10^4\ \left(\frac{1 + 10^4\frac{C_e}{C_a}}{1 + 10^8\frac{C_e}{C_a}}\right) \tag{2.5}$$

Rearranging, we get

$$\frac{C_e}{C_a} = 10^{-4}\left(\frac{1 - 10^{-4}\alpha_{H_2/CH_4}}{\alpha_{H_2/CH_4} - 1}\right) \tag{2.6}$$

Based on above, we list the percentage of large pores in the CVD graphene (**Table 2.2**).

Table 2.2   Estimated density of large, non-selective pores in graphene as a function of α_{H_2/CH_4}.

α_{H_2/CH_4}	C_e / C_a	PPM of nanopores (with respect to all nanopores) with an electron density gap larger than 0.38 nm
5	2.5×10^{-5}	25.0
10	1.1×10^{-5}	11.1
15	7.1×10^{-6}	7.1
20	5.3×10^{-6}	5.3
25	4.2×10^{-6}	4.2

The graphene membranes did not rupture during heating to up to 250 °C. The permeance of He, H_2, CO_2 and CH_4 increased with temperature, indicating that its transport was in the activated transport regime. At 150 °C, the H_2 permeance increased to $3.3 \times 10^{-8} - 4.1 \times 10^{-7}$ mol m^{-2} s^{-1} Pa^{-1} (100 – 1220 GPU), with H_2/CH_4, and H_2/CO_2 selectivities increasing to 7.1 – 23.5 and 3.6 – 12.2, respectively. We note that this H_2/CH_4 separation performance from single-layer graphene with 0.025% porosity approaches the 2008 Robeson upper bound for polymers[5] (assuming 1-μm-thick selective skin layer of the polymer membrane, **Figure 2.7**).
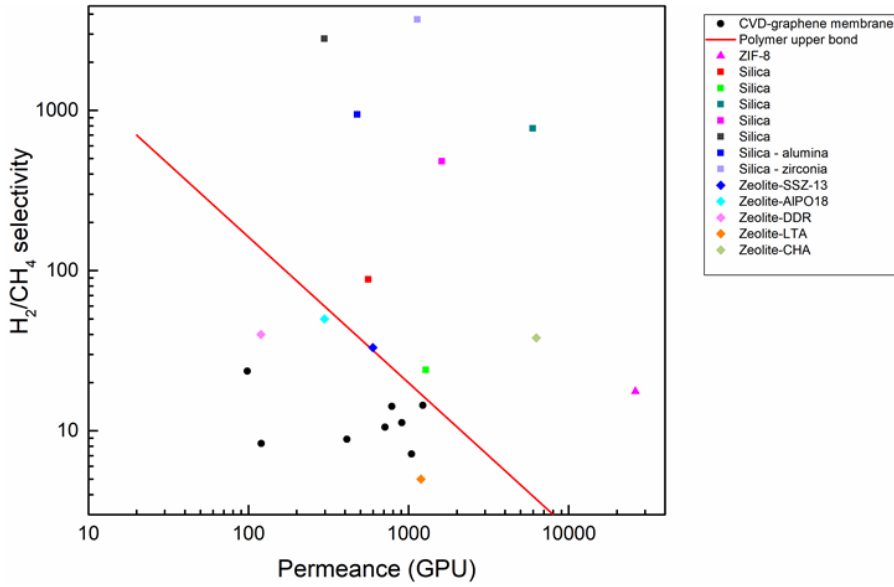
Figure 2.7 A comparison of single-layer graphene films (all eight membranes) with a low-density of intrinsic defects (0.025%) with membranes in the literature in terms of the H_2/CH_4 separation performances. The red line is the polymer upper bond assuming 1 μm-thick skin layer[5], ZIF-8[131], silica[132–138] and zeolite membranes (SSZ-13[139], AlPO-18[140], DDR[141], LTA[142], CHA[143]).

To understand the transport behavior, the activation energy for gas diffusion across the nanopores was extracted from the temperature-dependent gas flux using an adsorbed phase transport model developed using the concepts of adsorption and diffusion[90,91,144,145] (**Appendix-I**).

$$\text{Flux} \; = \; C_o \; A_{act} \; A_{sur} \; exp\left(-\frac{(E_{act} + \; \Delta E_{sur})}{RT}\right)\left(f(P_A) - f(P_R)\right) \quad (2.7)$$

$$\text{where } f(P_x) = \; \frac{P_x}{1 + \; A_{sur} \; exp\left(\frac{-\Delta E_{sur}}{RT}\right) \; P_x}$$

Here, C_O is the pore-density, E_{act} is the activation energy for the gas diffusion across the nanopores, and ΔE_{sur} is the adsorption energy of gas on to the graphene nanopore. A_{act} is the pre-exponential factor for the gas diffusion across the nanopores. A_{sur} is the pre-exponential factor for the adsorption event, representing changes in the overall entropy. T is the temperature, and P_A and P_R are the gas partial pressures on the feed and permeate sides, respectively. A comparison of E_{act} for the four gases can indicate the ease with which the molecules diffuse across the nanopores, while a comparison of the pre-exponential factor, $C_o A_{act} A_{sur}$, can indicate the relative number of pores

participating in the molecular diffusion. Average E_{act} across eight membranes for He, H_2, CO_2, and CH_4 were 14.7 ± 3.2, 20.2 ± 2.7, 31.3 ± 2.8, and 25.8 ± 4.8 kJ mol^{-1}, respectively, increasing as a function of kinetic diameter (**Figure 2.6e**, **Table 2.3**). A slightly smaller E_{act} for CH_4 in comparison to CO_2 can be explained by the fact that diffusion of CH_4 takes place from a smaller number of pores (average $C_o A_{act} A_{sur}$ for He, H_2, CO_2, and CH_4 were 1.5 x 10^{-5}, 2.6 x 10^{-5}, 3.8 x 10^{-6} and 1.3 x 10^{-6}, respectively, **Table 2.4**), assuming $A_{act} A_{sur}$ do not change significantly for CO_2 and CH_4[90]. The activation energy for H_2 was similar to that from hydrogen-functionalized pore-10 reported by Jiang et al. (0.22 eV)[96], providing an indication that the average pore in this study is close to that made from missing 10 carbon atoms, which is supported by the HRTEM images (**Figure 2.3i-k**) and our previous STM findings[122]. We note that while the gas permeance varied across the eight membranes, the activation energies for diffusion across the nanopores were consistent across the membranes. This indicates that, while the PSD was uniform across the membranes, the density of the intrinsic defects varied across the membranes.

Table 2.3 E_{act} for gas diffusion across the intrinsic defects in graphene

| E_{act} (kJ/mol)	He	H_2	CO_2	CH_4
M1	16.3	20.6	30.0	27.8
M2	15.3	20.5	29.8	24.4
M3	20.8	25.2	37.2	32.4
M4	11.4	17.6	29.6	22.7
M5	13.6	18.7	29.4	26.5
M6	11.8	17.1	30.7	24.8
M7	17.5	23.3	34.9	31.6
M8	10.8	18.2	29.1	16.5

Table 2.4 $C_o A_{act} A_{sur}$ of pristine graphene membranes extracted by adsorption model fitting

$C_o A_{act} A_{sur}$	He	H$_2$	CO$_2$	CH$_4$
M1	3.05×10^{-6}	4.70×10^{-6}	2.82×10^{-7}	3.52×10^{-7}
M2	1.51×10^{-5}	2.49×10^{-5}	1.85×10^{-6}	5.74×10^{-7}
M3	6.13×10^{-5}	9.14×10^{-5}	1.24×10^{-5}	3.73×10^{-6}
M4	4.55×10^{-6}	1.24×10^{-5}	1.85×10^{-6}	3.74×10^{-7}
M5	1.24×10^{-5}	2.49×10^{-5}	3.05×10^{-6}	1.24×10^{-6}
M6	6.33×10^{-6}	1.37×10^{-5}	4.12×10^{-6}	1.37×10^{-6}
M7	1.24×10^{-5}	3.72×10^{-5}	6.79×10^{-6}	3.05×10^{-6}
M8	7.52×10^{-7}	1.76×10^{-6}	1.02×10^{-7}	4.59×10^{-9}

Separation of a gas mixture can elucidate the contribution of competitive adsorption on the overall separation performance from the nanoporous graphene membrane. To the best of our knowledge, gas mixture separation through a single-layer graphene membrane has not been reported. Here, the large-area of the graphene membrane enabled measurements of He, H$_2$, CO$_2$ and CH$_4$ permeances from an equimolar gas mixture. The competitive adsorption[91,96,98,102] is expected to yield a reduced He/H$_2$, H$_2$/CO$_2$ and H$_2$/CH$_4$ separation factor (SF) compared to the corresponding ideal selectivities (IS). However, the separation factors were similar (He/H$_2$ and H$_2$/CO$_2$) or higher (H$_2$/CH$_4$) compared to the corresponding ideal selectivities (**Figure 2.8**). For example, for membrane M2, the H$_2$/CH$_4$ separation factor was higher than ideal selectivity (10.8 vs. 5.7 at 25 °C and 12.2 vs. 11.2 at 150 °C), while the H$_2$ permeance (3.3×10^{-8} – 2.2×10^{-7} mol m^{-2} s^{-1} Pa^{-1} between 25 – 150 °C) in the mixture case was similar to the single-component case (**Figure 2.6a**). Similarly, the H$_2$ permeance did not reduce for the membrane M3 for the mixture case, while the H$_2$/CH$_4$ SF increased to 18.0 from an ideal selectivity of 14.2. For other membranes (M1, M4, M5, and M6), the H$_2$ permeance and the H$_2$/CH$_4$ selectivity in the mixture case were similar to those in the single-component case. These results indicate that the competitive adsorption of gases on the basal plane of graphene does not play a significant role in overall transport especially when the transport is in the activated regime,

and when the feed pressure is moderate (up to 8 bar in this study). We expect the competitive adsorption to play a role at a higher feed pressure (30 – 50 bar, refer to **Appendix-I**) which will be investigated in future studies.
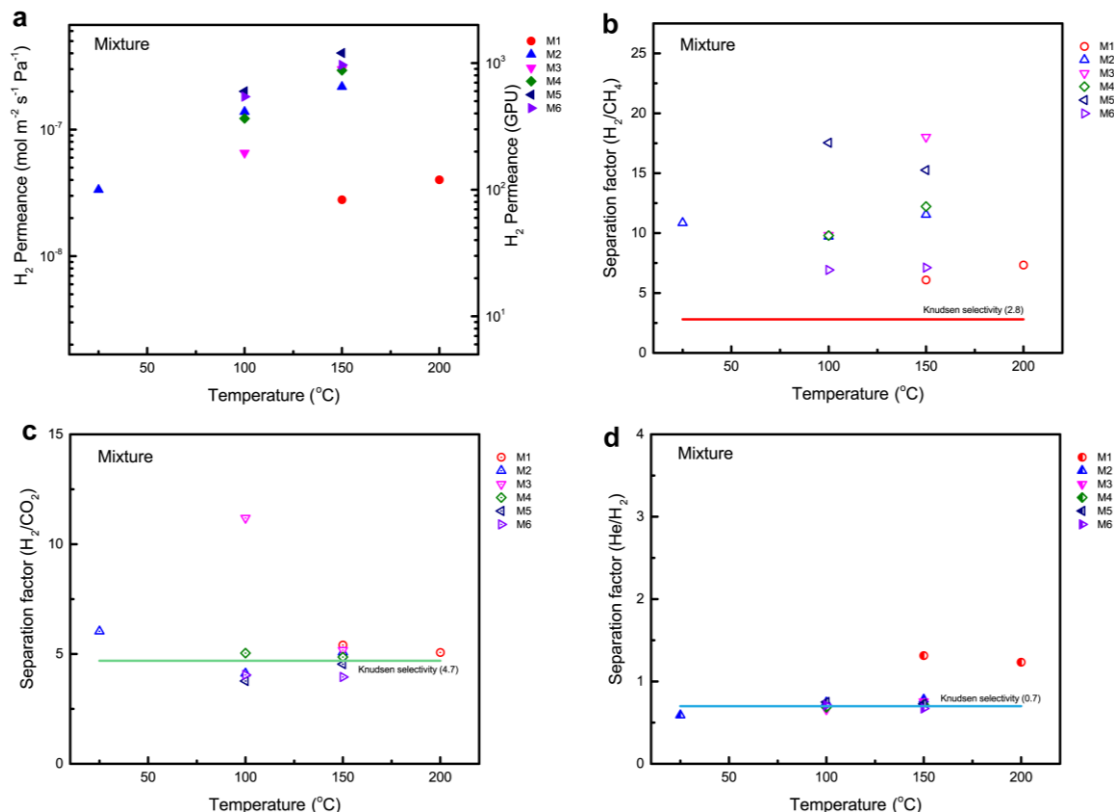
Figure 2.8 The gas mixture separation performance of the intrinsic defects in graphene.   a) H_2 permeance from six membranes (M1-M6) as a function of temperature when using an equimolar mixture gas feed. H_2/CH_4, H_2/CO_2, and He/H_2 separation factors as a function of temperature are shown in (b), (c), and (d), respectively.

The graphene membranes were thermally stable (**Figure 2.9a**). In general, all membranes were stable at least up to 150 °C. For instance, the performance of membrane M2, tested under three consecutive temperature cycles from 25 °C to 150 °C, did not change significantly. From cycle one to cycle three at 150 °C, the H_2 permeance decreased marginally (3.3 x 10^{-7} to 2.3 x 10^{-7} mol m^{-2} s^{-1} Pa^{-1}), while the H_2/CH_4 selectivity increased marginally (8.3 to 10.5). Moreover, the graphene membranes were also stable at least up to 8 bar of mixture feed at 100 °C (permeate pressure 1 bar, **Figures 2.9 b and c**), where the H_2 permeance and the H_2/CH_4 separation factor did not change significantly.
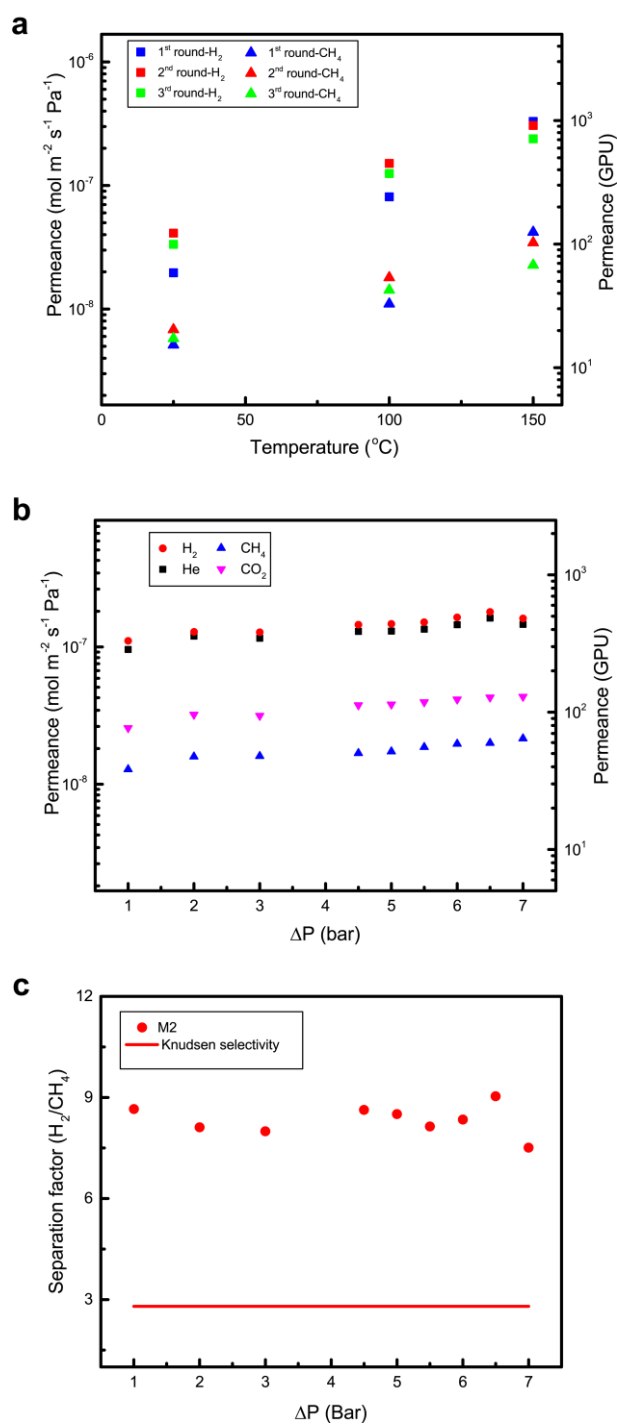
**Figure 2.9** Stability test of graphene membrane. a) H_2 and CH_4 permeances of the membrane M2 with three consecutive temperature cycles. Gas permeance (b) and H_2/CH_4 separation factor (c) from membrane M2 as a function of transmembrane pressure difference at 100 ºC.

3.3 Ozone-functionalization based etching and pore-modification chemistry

The porosity of graphene lattice yielding the attractive H_2 permeance was only 0.025%. Theoretically, the H_2 permeance can be further increased beyond 10^5 GPU by increasing the defect-density to $10^{12} – 10^{13}$ cm^{-2}. On the other hand, the gas-selectivity can be improved by constricting the nanopores. One way to achieve this is the chemical functionalization of the pore-edge. Although there are several potential chemical and physical routes to open pores in graphene, the development of an in-situ etching method (inside membrane module), allowing a high degree of control is highly attractive. In this pursuit, we report a scalable ozone-functionalization based pore-etching and pore-edge-functionalization chemistry, improving the performance of the single-layer graphene membranes. We demonstrate that a controlled temperature-dependent oxidative functionalization of the graphene lattice with ozone-derived epoxy and carbonyl groups can be used to either etch molecular-sized pores in the CVD derived graphene or constrict the existing pores.

Oxidative treatment of graphene has been shown to incorporate sp^3-hybridized sites (epoxy and carbonyl groups) on the basal plane of graphene[57,77,146]. When the functionalization density is high, such as that in graphene oxide, one can introduce nanopores in the lattice by thermal annealing[10,147–149]. Typically, the functional groups migrate and rearrange, forming larger groups (such as lactone), and finally desorb as CO or CO_2 leading to a vacancy[149]. Ozone, in the gas phase, can be conveniently used to oxidize graphene lattice. To understand the evolution of functionalization, CVD graphene supported on a Cu foil was exposed to ozone at various temperatures (25 °C, 80 °C, and 100 °C) and time (1 min to 7 min). The evolution of oxidative groups on graphene was probed by micro-Raman and X-ray photoelectron spectroscopy (XPS).
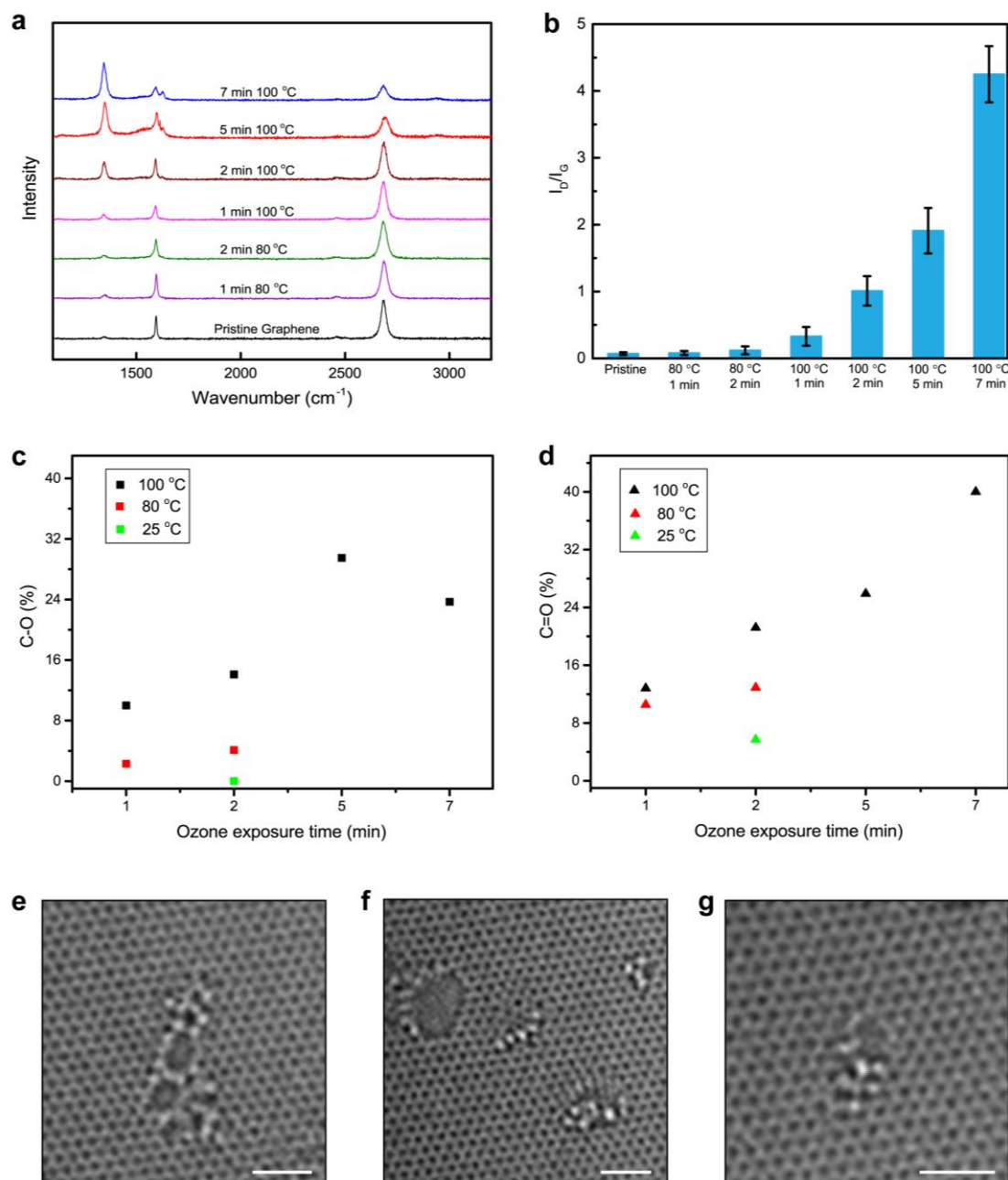
Figure 2.10 Characterization of the ozone-treated graphene. a) Raman spectra of functionalized graphene under different functionalization conditions. b) I_D/I_G for various ozone treatment. c-d) C-O (c) and C=O (d) content of the graphene as a function of the functionalization time and temperature. e-g) High-resolution transmission electron microscopy (HRTEM) images of the nanopores in the ozone functionalized graphene (2 min at 80 °C). The scale bar is 1 nm.

The relative intensity of the D peak with respect to the G peak (I_D/I_G), which marks the extent of disorder in graphene[150], increased from 0.07 to 4.0, while the intensity of the 2D peak decreased in intensity with the increasing reaction time and temperature, indicating that the sp^3-hybridized sites in graphene increased after ozone treatment (**Figure 2.10a-b**). XPS indicated that C-O and C=O were the major functional groups on the functionalized graphene (**Figure 2.10c-d** and **Figure 2.11**). The number density of functional groups increased with the reaction temperature and time, in agreement with the Raman spectroscopy. In general, the density of C=O groups was higher than that of the C-O groups, even when the functionalization was carried out at room temperature for a short exposure of 2 minutes. At 100 ºC, the degree of oxidation approached that of graphene oxide (35, 56, and 65% of the oxidized carbon lattice with exposure times of 2, 5 and 7 min, respectively). Overall, the functionalization was reproducible and was simple to implement. HRTEM images of the ozone-functionalized graphene (80 ºC for 2 min) indeed revealed a higher pore-density (4.2 x10^{11} cm^{-2}) compared to that in as-synthesized graphene (**Figure 2.10e-g**). Moreover, the population of the sub-1-nm pores (87%) increased compared to that in the as-synthesized graphene (76%).

Statistics summary on the pores characterized by HRTEM were based on the pores located at a minimum distance of 2 nm away from the PMMA contaminations. 31 sub-1-nm nanopores and 10 bigger pores (1 – 5 nm) were found in the CVD graphene (survey area of 14200 nm^2), corresponding to a pore-density of 2.8 x 10^{11} cm^{-2}. We found 67 sub-1-nm nanopores and 10 bigger pores (1 – 5 nm) in the ozone-treated graphene in (survey area of 18200 nm^2), corresponding to a pore-density of 4.2 x 10^{11} cm^{-2}.
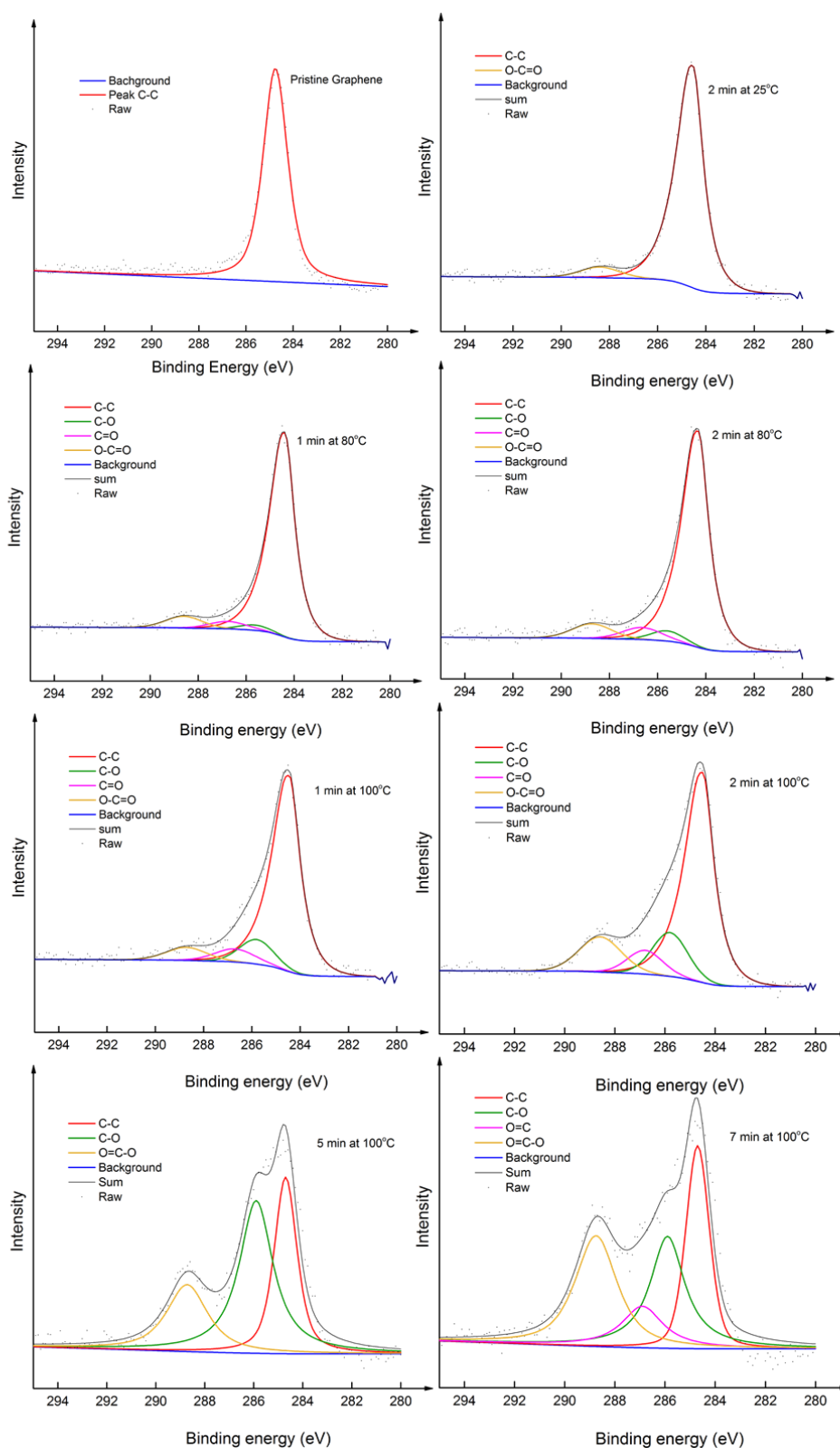
Figure 2.11 X-ray photoelectron spectroscopy (XPS) spectra of functionalized graphene with different ozone treatments.
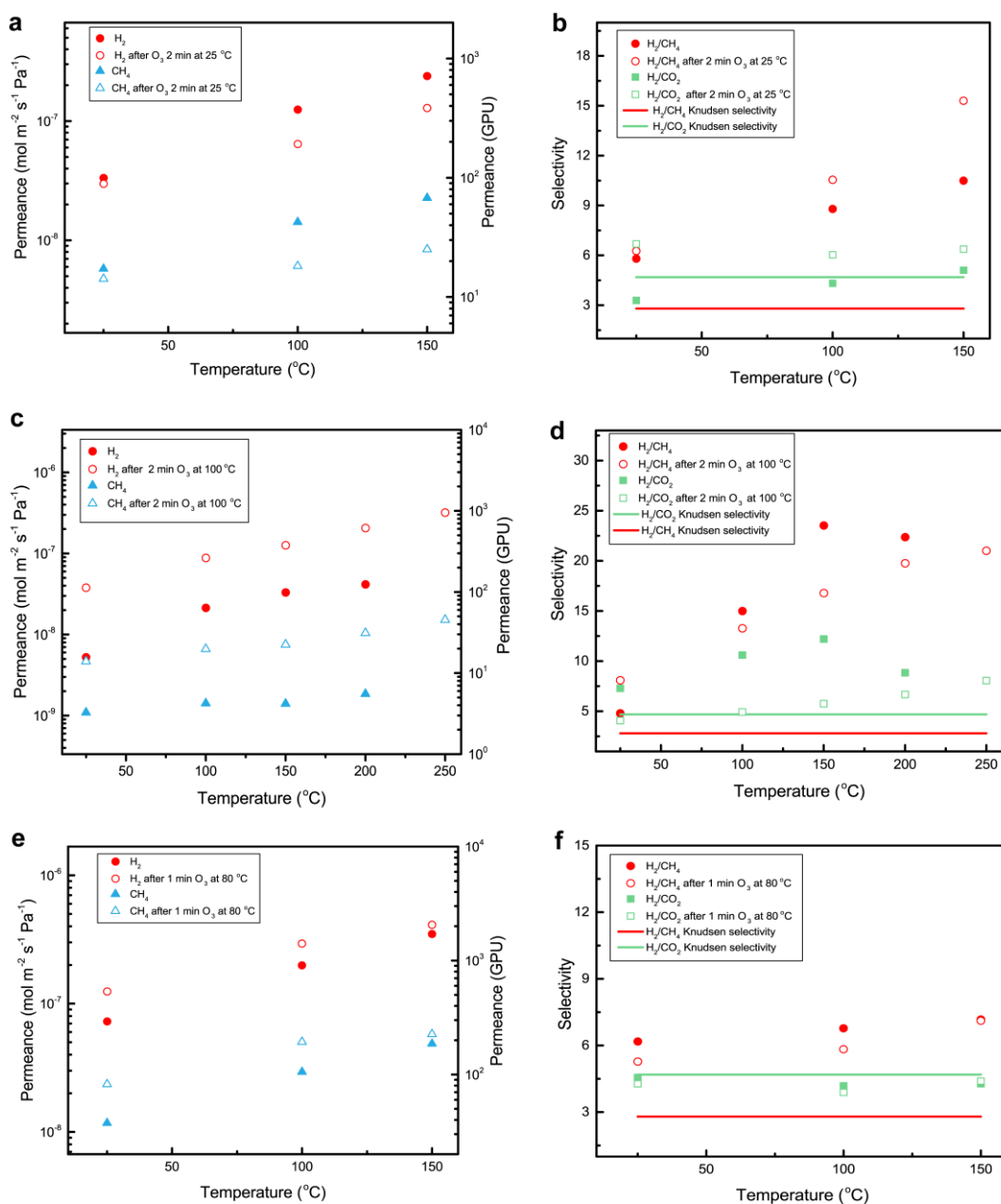
Figure 2.12 Gas separation performance of ozone-treated graphene membranes. a-b) Gas separation performance of M2 treated by 2 min O_3 at 25 °C, a) gas permeance of H_2 and CH_4, b) gas selectivity of H_2/CH_4 and H_2/CO_2. c-d) Gas separation performance of M8 treated by 2 min O_3 at 100 °C, c) gas permeance of H_2 and CH_4, d) gas selectivity of H_2/CH_4 and H_2/CO_2. e-f) Gas separation performance of M6 treated by 1 min O_3 at 80 °C, e) gas permeance of H_2 and CH_4, f) gas selectivity of H_2/CH_4 and H_2/CO_2.

To understand the effect of functionalization on the performance of graphene membrane, the graphene membrane was exposed to ozone, in-situ, in the permeation setup after probing the gas transport from the intrinsic defects. With this strategy, the gas transport before and after the functionalization could be compared. Overall, the separation

performance of the graphene membranes improved, reflected by an increase in the H_2 permeance or an increase in the H_2/CH_4 selectivity or an increase in the permeance as well as the selectivity (**Figure 2.12 and Figure 2.13**). When functionalization was carried out at 25 ^{o}C for 2 min, the H_2 permeance decreased from 2.3 x 10^{-7} to 1.2 x 10^{-7} mol m^{-2} s^{-1} Pa^{-1}, while the H_2/CH_4 and the H_2/CO_2 selectivities increased from 10.0 to 15.0 and 5.1 to 6.4, respectively at 150 ^{o}C (M2, **Figure 2.12 a-b**), indicating pore-shrinkage. Interestingly, both $E_{act-app}$ (defined as $E_{act} + \Delta E_{sur}$) and $C_o A_{act} A_{sur}$ decreased after the functionalization (**Tables 2.5 and Appendix-I**). While the changes in $E_{act-app}$ are complex to interpret because of relative changes in E_{act} (higher activation energy due to pore-shrinking) and ΔE_{sur} (increase in binding energy with functionalized pores), a 20-fold decrease in $C_o A_{act} A_{sur}$ for CH_4 (5.7 x 10^{-7} to 2.8 x 10^{-8}, **Table 2.6**) as a result of functionalization indicates reduced pore-density for the diffusion of CH_4. We envision the functionalized pore-edges would shrink in size, providing higher resistance to CH_4 for the diffusion, and therefore resulting in a higher gas selectivity[122]. In contrast, functionalization at 100 ^{o}C led to an increase in gas permeance by 3-fold, while the gas selectivity change slightly (**Figure 2.12 c-d**). Here, $E_{act-app}$ did not change significantly after functionalization (**Table 2.7**), while $C_o A_{act} A_{sur}$ for gases increased by an order magnitude (**Table 2.8**) indicating an increase in the pore-density. Given that the high-temperature functionalization leads to a higher coverage of the C-O and C=O groups, it is highly likely that these functional groups formed new pores as indicated by the HRTEM analysis.

Table 2.5 $E_{act-app}$ of M2 before and after ozone functionalization (2 min at 25 ^{o}C)

$E_{app-act}$ (kJ/mol)	He	H_2	CO_2	CH_4
Intrinsic defects	15.3	16.5	12.8	11.4
Post-functionalization	12.9	11.8	12.4	5.0

Table 2.6 $C_o A_{act} A_{sur}$ of M2 before and after ozone functionalization (2 min at 25 °C)

$C_o A_{act} A_{sur}$	He	H_2	CO_2	CH_4
Intrinsic defects	1.5×10^{-5}	2.5×10^{-5}	1.9×10^{-6}	5.7×10^{-7}
Post-functionalization	4.1×10^{-6}	3.4×10^{-6}	6.8×10^{-7}	2.8×10^{-8}

Table 2.7 $E_{act-app}$ of M8 before and after ozone functionalization (2 min at 100 °C)

$E_{app-act}$ (kJ/mol)	He	H_2	CO_2	CH_4
Intrinsic defects	10.8	14.2	12.1	3.5
Post-functionalization	12.9	12.0	8.2	6.3

Table 2.8 $C_o A_{act} A_{sur}$ of M8 before and after ozone functionalization (2 min at 100 °C)

$C_o A_{act} A_{sur}$	He	H_2	CO_2	CH_4
Intrinsic defects	7.5×10^{-7}	1.8×10^{-6}	1.0×10^{-7}	4.6×10^{-9}
Post-functionalization	7.5×10^{-6}	4.5×10^{-6}	2.5×10^{-7}	5.6×10^{-8}

We constructed a separation performance trajectory (**Figure 2.13**), comparing the separation selectivity and hydrogen permeance before and after the ozone functionalization. The overall trajectory trends clearly show that the gas separation performance of graphene membranes can be tuned by the ozone functionalization. Higher gas permeance (up to 300%) was achieved by generating new nanopore by ozone functionalization at 80 – 100 °C (membranes M7 and M8, **Figure 2.14 and Figure 2.12c-d**). A higher separation selectivity (up to 150%) was achieved by functionalization at 25 °C (M2, **Figure 2.12a-b**). In one case, an increase in permeance, as well as separation selectivity, was obtained after ozone treatment at 80 °C for 1 min (M5, **Figure 2.15**).

Therefore, one can use ozone-functionalization as a post-synthetic performance tuning method to enhance the separation performance of nanoporous single-layer graphene membranes.
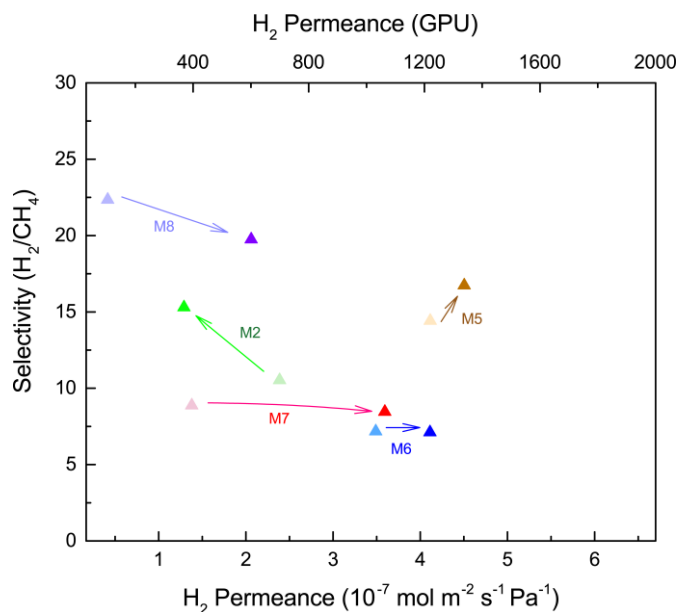
Figure 2.13 The evolution of gas separation performance after different ozone treatments. Permeance data for membrane M8 is at 200 °C, and all other (M2, M5, M6, and M7) is at 150 °C. Light and dark markers represent the gas performance from the intrinsic defects and the ozone-treated graphene, respectively.
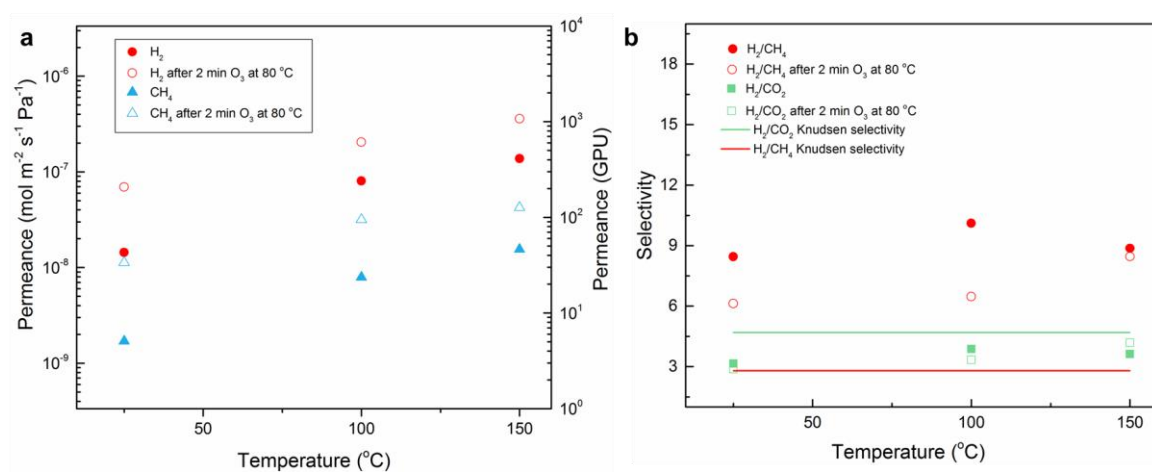
Figure 2.14 Gas separation performance of M7 treated by 2 min O_3 at 80 °C, a) gas permeance of H_2 and CH_4, b) gas selectivity between H_2/CH_4 and H_2/CO_2.
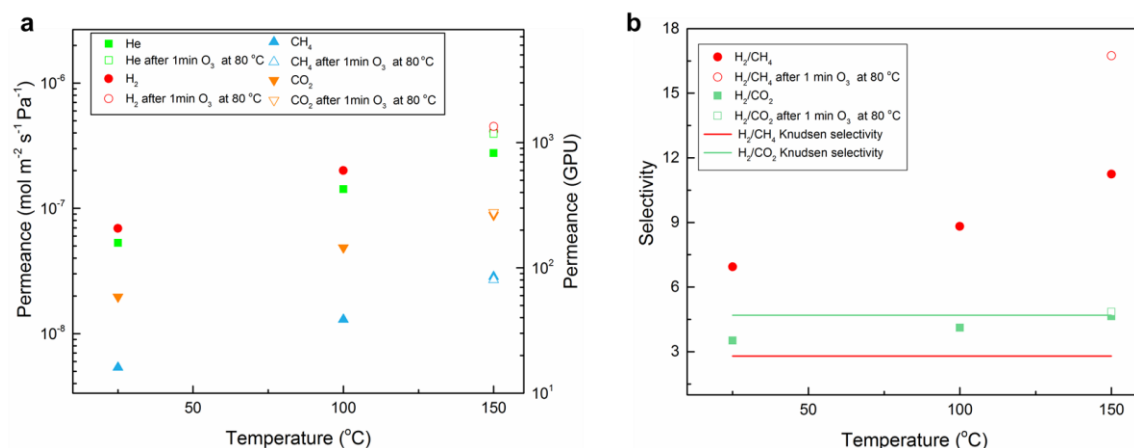
Figure 2.15 Gas separation performance of M5 treated by 1 min O_3 at 80 °C, a) gas permeance of H_2 and CH_4, b) gas selectivity between H_2/CH_4 and H_2/CO_2.

4. Conclusions

We developed a scalable NPC film-assisted transfer method to fabricate crack- and tear-free, millimeter-scale suspended single-layer CVD graphene films, allowing us to observe and understand the temperature-dependent single-component and mixture gas transport through the intrinsic defects in graphene.   Graphene films with a minuscule porosity of 0.025% displayed attractive H_2 permeance and H_2/CH_4 selectivities approaching the performance of 1-µm-thick state-of-the-art polymer membranes. Improvements in the H_2 permeance and/or H_2/CH_4 selectivity were demonstrated by ozone-functionalization. Overall, the methods developed here bring deployment of the single-layer nanoporous graphene membranes for gas separation a step closer to reality.

Appendix I

Gas transport model

The adsorbed phase transport of gases through pores on the graphene can be summarized in the following steps as described by the previous works[91,144,145].

<u>Single-component feed</u>

1) Gas adsorption on the graphene lattice;

$$l + A \quad \overset{k_1}{\Leftrightarrow} A_l \tag{1}$$

Adsorption rate:

$$k_1 P_A[l] - k_{-1}[A_l] \tag{2}$$

2) 2D diffusion of adsorbed gas towards the pores on graphene;

$$A_l + \ B_l \overset{k_2}{\Leftrightarrow} AB_l + l \tag{3}$$

Pore-association rate:

$$k_2[A_l][B_l] - k_{-2}[AB_l][l] \tag{4}$$

3) Gas diffusion across the pore;

$$AB_l \quad \overset{k_3}{\Leftrightarrow} RB_m \tag{5}$$

Diffusion rate:

$$k_3[AB_l] - k_{-3}[RB_m] \tag{6}$$

4) Dissociation of the molecule from the pore and 2D diffusion of the molecule away from the pore (permeate side).

$$RB_m + m \overset{k_4 = \ k_{-2}}{\Longleftrightarrow} R_m + B_m \tag{7}$$
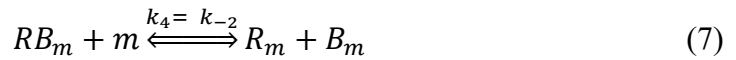
Dissociation rate:

$$k_4[RB_m][m] - k_{-4}[R_m][B_m] \tag{8}$$

5) Desorption of molecular from the graphene lattice (permeate side).

$$R_m \overset{k_5 = k_{-1}}{\rlongleftrightarrow} R + m \tag{9}$$

Desorption rate:

$$k_5[R_m] - k_{-5} \, P_R[m] \tag{10}$$

A: Feed gases with P_A; R: permeate gases with P_R

l: Available adsorption sites of the graphene lattice (feed side);

m: Available adsorption sites of the graphene lattice (permeate side);

A_l: Gas adsorbed on graphene (feed side);

R_m: Gas adsorbed on graphene (permeate side);

B_l: Empty holes on graphene (feed side);

B_m: Empty holes on graphene (permeate side);

AB_l: Gas associated with hole (feed side);

RB_m: Gas associated with hole (permeate side);

k_i: rate constant for step i; k_{-i}: backward rate constant for step i.

Typically, the rate-limiting step is the diffusion step (step 3), while all other steps can be considered at the equilibrium.

Adsorption equilibrium:

$$K_1 = \frac{k_1}{k_{-1}} = \frac{[A_l]}{P_A[l]} \tag{11}$$

Association equilibrium:

$$K_2 = \frac{k_2}{k_{-2}} = \frac{[AB_l][l]}{[A_l][B_l]} \tag{12}$$

Dissociation rate:

$$K_4 = \frac{k_4}{k_{-4}} = \frac{[R_m][B_m]}{[RB_m][m]} \tag{13}$$

Desorption rate:

$$K_5 = \frac{k_5}{k_{-5}} = \frac{P_R[m]}{[R_m]} \tag{14}$$

Total sites of adsorption sites can be fixed as C_l,

$$C_l = [A_l] + [l] = [m] + [R_m] \tag{15}$$

Langmuir adsorption was assumed to describe the adsorption of gases on the graphene lattice, fraction of sites occupancy could be expressed as $\theta_A = \frac{K_1 P_A}{1 + K_1 P_A}$.

$$[A_l] = \frac{C_l K_1 P_A}{1 + K_1 P_A} \tag{16}$$

$$[l] = \frac{C_l}{1 + K_1 P_A} \tag{17}$$

Assumed total pore sites is fixed as C_o

$$C_o = [AB_l] + [B_l] = [B_m] + [RB_m] \tag{18}$$

$$[AB_l] = \frac{C_o K_1 K_2 P_A}{1 + K_1 K_2 P_A} \tag{19}$$

Overall transport rate = rate of molecular diffusion through the pores

$$k_3[AB_l] - k_{-3}[RB_m] = C_o \frac{k_1}{k_{-1}} \frac{k_2}{k_{-2}} k_3 \left(\frac{p_A}{1 + \frac{k_1}{k_{-1}} \frac{k_2}{k_{-2}} p_A} - \frac{p_R}{1 + \frac{k_1}{k_{-1}} \frac{k_2}{k_{-2}} p_R} \right) \tag{20}$$

From classical transition state theory,

$$\frac{k_1}{k_{-1}} \frac{k_2}{k_{-2}} = A_{sur} exp(-\frac{\Delta E_{sur}}{RT}) \tag{21}$$

$$k_3 = A_{act} exp(-\frac{E_{act}}{RT}) \tag{22}$$

$$Flux = C_o A_{act} A_{sur} exp(-\frac{E_{act}+\Delta E_{sur}}{RT})(f(P_A) - f(P_R)) \qquad (23)$$

$$* f(P_x) = \frac{P_x}{1 + A_{sur} exp(-\frac{\Delta E_{sur}}{RT})P_x}$$

A_{act}, A_{sur} are the pre-exponential factors; E_{act} is the activation energy to diffuse across the pores; E_{sur} is the energy of adsorption on the graphene pore.

Mixture feed

The kinetic notations for the component i can be written as

1) Gas adsorption on the graphene lattice;

$$l + A_i \overset{k_1}{\Leftrightarrow} A_{i,l} \qquad (24)$$
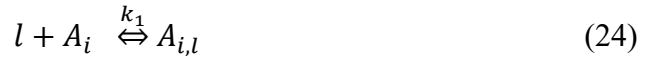
Adsorption rate:

$$k_1 P_{i,A}[l] - k_{-1}[A_{i,l}] \qquad (25)$$

2) 2D diffusion of adsorbed gas towards the pores on graphene;

$$A_{i,l} + B_l \overset{k_2}{\Leftrightarrow} A_i B_l + l \qquad (26)$$

Pore-association rate:

$$k_2[A_{i,l}][B_l] - k_{-2}[A_i B_l][l] \qquad (27)$$

3) Gas diffusion across the pore;

$$A_i B_l \overset{k_3}{\Leftrightarrow} R_i B_m \qquad (28)$$

Diffusion rate:

$$k_3[A_i B_l] - k_{-3}[R_i B_m] \qquad (29)$$

4) Dissociation of the molecule from the pore and 2D diffusion of the molecule away from the pore (permeate side).

$$R_i B_m + m \xrightleftharpoons{\quad k_4 = \ k_{-2} \quad} R_{i,m} B_m \tag{30}$$

Dissociation rate:

$$k_4 [R_i B_m][m] - k_{-4}[R_{i,m}][B_m] \tag{31}$$

5) Desorption of molecular from the graphene lattice (permeate side).

$$R_{i,m} \xrightleftharpoons{\quad k_5 = \ k_{-1} \quad} R_i + m \tag{32}$$

Desorption rate:

$$k_5 [R_{i,m}] - k_{-5} \ P_{i,R}[m] \tag{33}$$

Total sites of adsorption sites can be fixed as C_l,

$$C_l = \sum [A_{i,l}] + [l] = [m] + \sum [R_{i,m}] \tag{34}$$

Assumed total pore sites is fixed as C_o

$$C_o = \sum [A_i B_l] + [B_l] = [B_m] + \sum [R_i B_m] \tag{35}$$

Therefore, combining Eq. S25-S35, one can arrive to

$$\text{Flux}_i \ = \ C_o \ A_{act,i} \ A_{sur,i} \ exp\left(-\frac{(E_{act,i} + \ \Delta E_{sur,i})}{RT}\right)\left(g(P_{i,A}) - g(P_{i,R})\right) \tag{36}$$

$$* \ g(P_x) = \ \frac{P_x}{1 + \sum_1^n A_{sur} \ exp\left(\frac{-\Delta E_{sur}}{RT}\right) \ P_x}$$

The transport model was fitted to the temperature dependent experimental permeation data to obtain apparent activation energy $E_{app-act} = E_{act} + E_{sur}$ and products of pore density and pre-exponential factors $C_o A_{act} A_{sur}$. Based on previous work[102], $E_{CO2,sur}$= -17 kJ/mol, $E_{CH4,sur}$= -13 kJ/mol, $E_{H2,sur}$= -4 kJ/mol, $E_{He,sur}$= 0 kJ/mol, the E_{act} could be calculated by the equation $E_{act} = E_{act-app} - E_{sur}$.

Appendix II

Table 2.9 He permeance* through the intrinsic defects of M1-M8

Temperature (°C)	M1	M2	M3	M4	M5	M6	M7	M8
25	4.0×10^{-9}	3.0×10^{-8}	1.5×10^{-8}	4.8×10^{-8}	5.3×10^{-8}	5.5×10^{-8}	1.1×10^{-8}	1.0×10^{-8}
100	1.9×10^{-8}	9.9×10^{-8}	6.4×10^{-8}	9.1×10^{-8}	1.4×10^{-7}	1.4×10^{-7}	5.2×10^{-8}	2.1×10^{-8}
150	3.2×10^{-8}	1.9×10^{-7}	1.9×10^{-7}	2.0×10^{-7}	2.8×10^{-7}	2.3×10^{-7}	8.7×10^{-8}	3.4×10^{-8}
200	4.4×10^{-8}							5.5×10^{-8}

* Unit of permeance is mol m^{-2} s^{-1} Pa^{-1}

Table 2.10 CO_2 permeance* through the intrinsic defects of M1-M8

Temperature (°C)	M1	M2	M3	M4	M5	M6	M7	M8
25	1.5×10^{-9}	1.0×10^{-8}	3.8×10^{-9}	1.2×10^{-8}	2.0×10^{-8}	1.6×10^{-8}	4.6×10^{-9}	7.2×10^{-10}
100	4.6×10^{-9}	2.9×10^{-8}	1.6×10^{-8}	2.5×10^{-8}	4.9×10^{-8}	4.8×10^{-8}	2.1×10^{-8}	2.0×10^{-9}
150	6.7×10^{-9}	4.7×10^{-8}	4.5×10^{-8}	6.1×10^{-8}	8.9×10^{-8}	8.2×10^{-8}	3.8×10^{-8}	2.7×10^{-9}
200	7.5×10^{-9}							4.7×10^{-9}

* Unit of permeance is mol m^{-2} s^{-1} Pa^{-1}

Table 2.11 CH_4 permeance* through the intrinsic defects of M1-M8

Temperature (°C)	M1	M2	M3	M4	M5	M6	M7	M8
25	8.6×10^{-10}	5.8×10^{-9}	1.6×10^{-9}	8.1×10^{-9}	5.4×10^{-9}	1.2×10^{-8}	1.7×10^{-9}	1.1×10^{-9}
100	3.3×10^{-9}	1.4×10^{-8}	5.1×10^{-9}	1.4×10^{-8}	1.3×10^{-8}	2.9×10^{-8}	7.9×10^{-9}	1.4×10^{-9}
150	4.8×10^{-9}	2.3×10^{-8}	1.9×10^{-8}	2.7×10^{-8}	2.9×10^{-8}	4.9×10^{-8}	1.6×10^{-8}	1.4×10^{-9}
200	4.7×10^{-9}							1.9×10^{-9}

* Unit of permeance is mol m^{-2} s^{-1} Pa^{-1}

Chapter 3 Millisecond lattice gasification for high-density CO_2- and O_2-sieving nanopores in single-layer graphene

Adapted with permission from <u>Shiqi Huang</u>, Shaoxian Li, Luis Francisco Villalobos, Deepu J. Babu, Mohammad Tohidi Vahda, Emad Oveisi, Kumar Varoon Agrawal[*], Millisecond lattice gasification for high-density CO_2- and O_2-sieving nanopores in single-layer graphene, a manuscript in submission.

Abstract

Etching single-layer graphene to incorporate a high pore density with sub-Å precision in molecular differentiation is critical to realize the promising high-flux separation of similar-sized gas molecules, e.g., CO_2 from N_2. However, rapid etching kinetics needed to achieve the high pore density is challenging to control for such precision. Herein, we report a millisecond carbon gasification chemistry incorporating high-density ($>10^{12}$ cm^{-2}) CO_2-sieving vacancy defects under the controlled and predictable gasification conditions. A statistical distribution of nanopore lattice isomers is observed, in good agreement with the theoretical solution to the isomer cataloging problem. The gasification technique is scalable, and a centimeter-scale membrane is demonstrated. Finally, molecular cutoff could be adjusted by 0.1 Å by an in situ expansion of the vacancy defects in an O_2 atmosphere. Large CO_2 and O_2 permeances (>10000 and 1000 GPU, respectively) are demonstrated accompanying attractive CO_2/N_2 and O_2/N_2 selectivities.

1. Introduction

Molecular separation, a key component of industrial processes and at the heart of environmental issues like carbon capture, is highly energy-intensive. The energy-efficiency and capital cost of the separation processes can be substantially reduced by using high-performance molecular-sieving membranes separating gases based on their kinetic diameter[151–154]. Specifically, significant improvement in energy-efficiency of separation processes such as postcombustion carbon capture can be achieved by increasing

the CO_2 permeance[3,155] Gas-sieving nanoporous single-layer graphene (N-SLG), prepared by incorporating vacancy defects in the single-layer graphene (SLG) lattice[156,157], can be highly attractive for high-flux CO_2 and O_2 separation because the diffusion resistance is controlled by a single transition state at the nanopore[9,55,92,96].

While molecular simulations have predicted that graphene nanopores can indeed separate industrially-relevant mixtures containing similar-sized molecules such as CO_2/N_2[158], CO_2/CH_4[90], O_2/N_2[159], etc., it has remained challenging to incorporate these nanopores in graphene with a narrow-enough pore-size-distribution (PSD) to obtain the needed sub-Å resolution in molecular differentiation.[72,93,160] Further, for developing practical membranes, the lattice transformation must take place uniformly over a macroscopically-large area. The state-of-the-art nanofabrication routes, e.g., involving high-energy electron or ion bombardment have inherent limitations in achieving these requirements. This is mainly because displacing a carbon atom from the basal plane (nucleation event) has an energy barrier of 20-23 eV, [53,161,162] much higher than that needed to displace a carbon atom from the pore edge (pore growth, ca. 14 eV).[53] As a result, pore expansion takes place at a much faster rate than that for pore nucleation and tight control of PSD becomes challenging. In principle, CO_2-selective nanopores can be obtained by slowing down the etching kinetics by chemical etching technique involving O_2[156,163], UV/O_3[72], or O_3[59,160], e.g., using a low temperature or a small concentration of etchant[72]. However, approaches based on sluggish kinetics would not achieve the meaningful pore density needed to realize the primary objective of high-flux separation. Therefore, the development of methods involving rapid etching kinetics coupled with short but controllable pore expansion time is critically needed. Herein, by using a custom-made millisecond gasification reactor (MGR), we could control the expansion time of vacancy defects to a few milliseconds. High pore density ($>10^{12}$ cm^{-2}) combined with a narrow PSD consisting of missing 1-20 carbon atoms led to attractive CO_2/N_2 and CO_2/CH_4 selectivities. The gasification technique is highly scalable by design and could be used to produce centimeter-scale N-SLG membranes. Further, we show that molecular cut-off can be adjusted by 0.1 Å by a slow expansion of nanopores in situ inside the membrane module. The resulting membranes yielded attractive sieving performances with large CO_2 and O_2 permeances (>10000 and 1000 GPU, respectively), making these membranes highly promising for energy-efficient carbon capture.

2. Methods

2.1 Graphene Synthesis

Annealing of commercial Cu foil

The commercial Cu foil (Alfa-Aesar, 99.8% purity, 25 μm, or Strem Chemicals Inc., 99.9% purity, 50 μm) was thermally annealed in a furnace equipped with a high-purity alumina tube (99.8% purity). The high-purity alumina tube reduced the silica contaminations on the Cu foil. The annealing was done in three steps. First, the Cu foil was placed inside the furnace and heated to 1000 °C in a CO_2 atmosphere at 700 Torr to remove the organic contamination[118]. Second, CO_2 was purged out and a H_2/Ar mixture (10/90 ratio) was filled to a pressure of 700 Torr. Third, the temperature of the furnace was increased to 1075 °C and was maintained at this temperature for 1 h. Subsequently, the furnace was cooled down to 1000 °C at a rate of 0.1 °C min^{-1}, and then to room temperature by natural convection.

Graphene growth on Cu foil

SLG was synthesized in an LPCVD setup on the surface of the annealed Cu foil[34,35]. Briefly, the foil was heated to 1000 °C in a CO_2 atmosphere at 700 Torr and kept there for 30 min to remove the organic contaminations. Then, the CO_2 flow was stopped and the chamber was evacuated. Following this, a flow of 8 sccm of H_2 was introduced for 30 min. Finally, a flow of 24 sccm of CH_4 was added maintaining a total pressure of 460 mTorr for 30 min leading to the growth of polycrystalline SLG film. Finally, the growth chamber was cooled rapidly to room temperature while maintaining the H_2 flow.

2.2 Etching nanopores in single-layer graphene

Etching of graphene in MGR

The as-synthesized SLG supported on the Cu foil was etched in the home-made MGR setup (**Figure 3.1**). The MGR consisted of a 10-cm-long temperature-controlled reaction zone with three inlets and an outlet. One inlet was connected to a reservoir storing pressurized O_3/O_2 mixture. The reservoir, in turn, was connected to an O_3 generator (Atlas 30, Absolute Ozone®) supplying 9 mol% O_3 in O_2. The second inlet of MGR was

connected to purge gas supply (Ar or liquid-nitrogen-cooled He). Two millisecond leak valve (MLVs atomic layer deposition valve, Swagelok Corp) controlled a synchronized injection of O_3 and the purge gas to the MGR. The O_3 dose was controlled by opening the MLV for a short time and purging the MGR after a short delay (**Figure 3.1**). The third inlet of MGR was connected to H_2/Ar supply. The role of this supply was to maintain a reducing atmosphere in the reactor before and after the gasification. The outlet of MGR was connected to a vacuum pump via an outlet valve. The MGR was heated using a heating tape wrapped around the reaction zone and the heating was controlled using a feedback controller using input from a thermocouple placed inside the gasification zone.
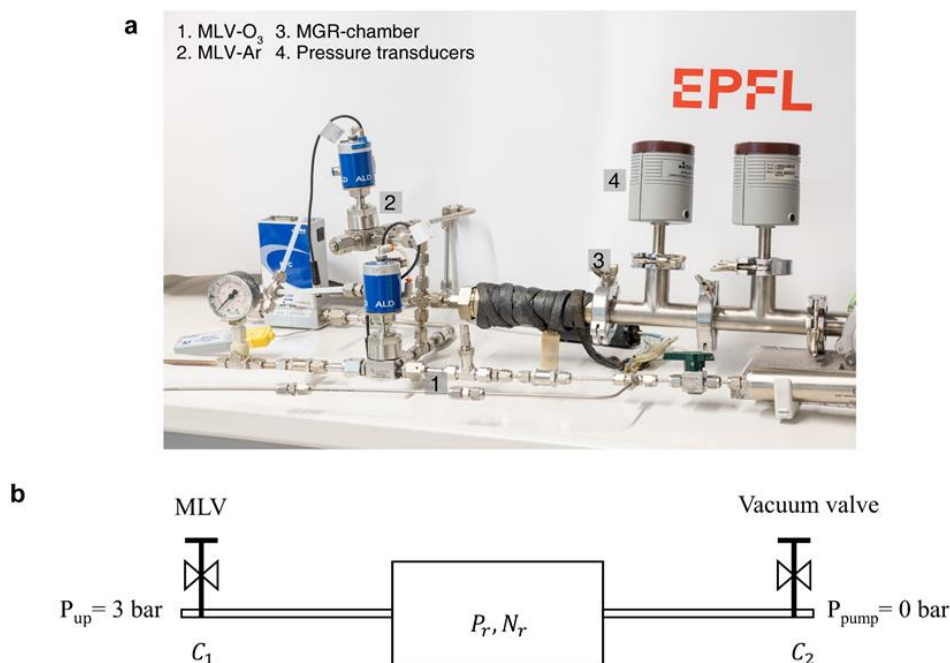
Figure 3.1 Photo a) and schematic b) of MGR equipped with O_3 supply via a millisecond leak valve (MLV).

For the etching of SLG, the following procedure was used. As-synthesized SLG was heated inside the reaction zone of MGR in a H_2 atmosphere. Before etching, H_2 was purged out with Ar while maintaining a chamber pressure of 0.8 Torr. A custom LabVIEW program was used to open the O_3 MLV for a short time (0.01 to 0.2 s), and optionally, to open the purge valve after a certain delay (0 to 1 s). Post etching, the sample was cooled

down to room temperature in an Ar atmosphere. We noticed oxidation of Cu during etching, and therefore, for further use, the sample was annealed at 300 °C in a H_2 atmosphere to reduce the oxidized Cu.

In-situ oxygen etching

O_2 etching was conducted on the suspended N-SLG membrane inside the membrane module. A metal-metal (Swagelok VCR fittings) seal, where the membrane was sandwiched in the VCR-based module, was used to ensure a leak-proof system. Before the oxygen etching, the membrane module with the membrane inside was heated to 100 °C to remove the adsorbed atmospheric contaminations and the gas separation performance was measured. Following this, the membrane was heated to 200 °C using Ar as the sweep and a CO_2/N_2 mixture in the feed side. The online MS monitored the CO_2 and N_2 concentration in the permeate side continuously. To start the in situ etching, the Ar flow in the sweep (permeate side of the membrane) was swapped with an O_2 flow. The permeate concentration was monitored as a function of time to evaluate the effect of the etching on the gas-sieving property of the membrane. After the etching reaction, the sweep was swapped back to Ar and the steady-state membrane performance was measured.

2.3 Fabrication of membrane

The fabrication of the 1-mm^2-sized graphene membrane on macroporous tungsten support was similar to the previously reported method[164]. Briefly, a nanoporous carbon (NPC) film was deposited on N-SLG as a mechanically-reinforcing layer. The NPC/N-SLG/Cu was floated on a $Na_2S_2O_8$ solution (20 wt.% in water) to etch the Cu foil. After Cu etching, the floating NPC/N-SLG film was rinsed in deionized water to remove the residues. Finally, the floating NPC/N-SLG film was scooped on the macroporous tungsten support hosting laser-drilled 5-μm pores.

The N-SLG membrane prepared using poly[1-(trimethylsilyl)-1-propyne] (PTMSP) reinforcement was fabricated in quite similar way as above. First, a 1.25 wt% of PTMSP solution in toluene was used to spin coat a PTMSP layer on N-SLG surface (1000 rpm for 30 s, and then 2000 rpm for 30 s). Next, the PTMSP/N-SLG/Cu was inserted in a vacuum oven at 25 °C for 12 h to completely remove the solvent from PTMSP. Subsequently, the PTMSP/N-SLG/Cu was floated on a 1 M $FeCl_3$ solution to etch the Cu foil. Finally, the

floating PTMSP/ N-SLG film was scooped on the macroporous tungsten support and smoothened macroporous metal-mesh support to fabricate the centimeter-scale N-SLG membrane.

2.4 Gas permeation test

The single-component and mixture gas permeation tests were carried out in a home-made permeation module. All the permeation tests were conducted in the open-end mode. All equipment used in the permeation setup (the MFCs, oven and mass spectrometer MS) were calibrated within a 5% error. The N-SLG membrane was sandwiched in the VCR-based module (Swagelok VCR fittings), making a leak-tight fitting. The feed and the sweep lines were preheated inside the oven to prevent temperature fluctuation. An MFC regulated the flow rate of the feed gas, where the feed pressure (1.5 – 2.0 bar) was adjusted by the back-pressure regulator. Another MFC controlled the flow rate of sweep gas (Ar) with 1 bar pressure. The sweep gas carried the permeate gas to the MS for real-time analysis of the permeate concentration. The MS was calibrated for the concentration range measured in the permeate stream for He, H_2, CO_2, O_2, N_2, CH_4, and C_3H_8 in Ar. Before testing, all membranes were heated to 100 °C to remove the atmospheric contaminations on the graphene surface. For the mixture permeation tests, an equimolar gas mixture (or a 20/80 mixture of CO_2/N_2 whenever specified) was used on the feed side. The performance of the membranes was tracked continuously in real-time. The gas flux and was calculated once the steady-state was established. Only the steady-state permeation data was reported.

2.5 Characterization of nanoporous graphene

Raman characterization

Raman characterization was carried on graphene transferred onto the SiO_2/Si wafer by the wet-transfer method. Single-point data collection and mapping were performed using Renishaw micro-Raman spectroscope equipped with a blue laser (λ_L = 457 nm, E_L = 2.71 eV) and a green laser (λ_L = 532 nm, E_L = 2.33 eV). Analysis of the Raman data was carried out using MATLAB. For calculation of the D and the G peak height, the background was subtracted from the Raman data using the least-squares curve fitting tool (lsqnonlin).

Sample preparation for transmission electron microscopy

The transfer-induced contaminations on the N-SLG surface were minimized by fabricating a thin porous polybenzimidazole (PBI) film and then transferring graphene on a transmission electron microscopy (TEM) grid with the help of this film (**Figure 3.2**). The porous PBI was prepared separately and adhered on top of graphene, which allowed us to avoid polymer-solution-induced contaminations on the surface of N-SLG. Such contaminations are difficult to avoid when directly forming the porous film on top of graphene[160,165] or when using a poly(methylmethacrylate) (PMMA)-based transfer approach[166]. The N-SLG domain resting in the micrometer-sized open areas of the porous PBI film was easy to find in the imaging conditions of AC-HRTEM (**Figure 3.2**).
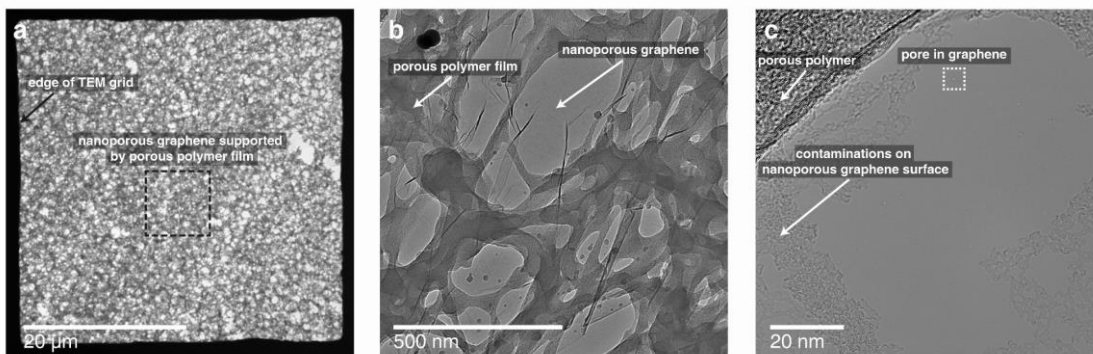
Figure 3.2 Porous PBI-reinforced N-SLG for TEM imaging. a) A bright-field TEM image of one of the holes of the TEM grid completely covered by the porous-PBI-reinforced N-SLG. b) Bright-field TEM image showing the open spaces in the polymer film where nanoporous graphene is exposed for imaging. c) An HRTEM image of N-SLG.

The porous PBI reinforcement layer was made of a thermally resistant PBI (fumion® AM provided by FUMATECH BWT GmbH, Germany), which can be carbonized once it sits on top of N-SLG to form a thermally conductive carbon porous reinforcement ideal for AC-HRTEM imaging.

A thin porous PBI film was prepared using the non-solvent induced phase separation process (NIPS). Briefly, a drop of a 1.5 wt.% solution of PBI in Dimethylacetamide (DMAc) was spread on top of a 25-µm-thick Cu foil by gently pressing it with a glass slide. The wet coating was immersed in an isopropanol bath to initiate phase separation, which led to a thin porous polymer film. After drying the resulting film, the Cu foil was

etched, and the floating porous PBI film was transferred to a water bath to rinse the residues from the etching step. Finally, the floating film was scooped out of the water bath using as-prepared N-SLG on Cu foil. After drying the porous PBI film, a drop of isopropanol was poured on it, which enhanced the adhesion of the film to the N-SLG surface upon the evaporation of isopropanol. Subsequently, the porous PBI film resting on N-SLG/Cu was pyrolyzed at 500 °C in the flow of H_2/Ar, leading to the formation of porous carbon. Next, the Cu foil was etched, and the resulting reinforced N-SLG was washed with water and transferred to a 400-mesh gold TEM grid (**Figure 3.2a**).
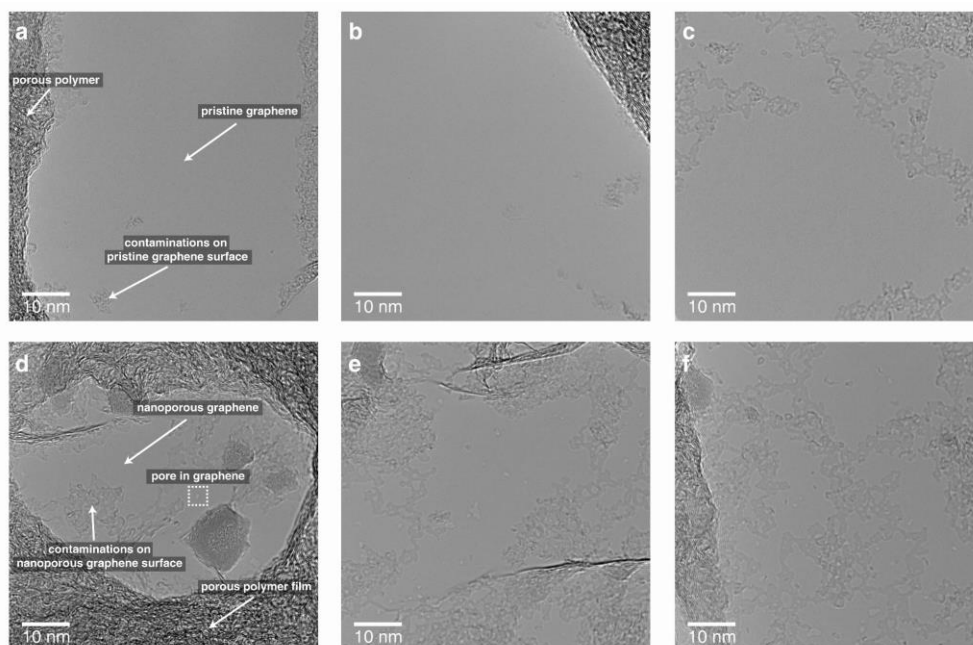
Figure 3.3 SLG after 900 ºC treatment in the H_2 atmosphere to remove contaminations on its surface. a-c) HRTEM of as-synthesized SLG after the heat treatment. No nanopores were observed on SLG. d-f) HRTEM of N-SLG prepared by gasification in MGR after the heat treatment. Several nanopores could be observed in this case.

Before AC-HRTEM, the TEM grid was cleaned inside activated carbon in a H_2 atmosphere 900 °C for 1 h to remove the contaminations covering the nanopores. The cleaning was carried out in a temperature- and environment-controlled furnace taking the following precautions to avoid the presence of O_2 in the system which could enlarge the pores: (i) the adsorbed gases on the N-SLG surface were removed by evacuating the system at 2 mTorr at 200 °C for 2 h; (ii) a positive pressure was maintained in the furnace (850 Torr of H_2) while heating the sample to 900 °C to avoid O_2 leak in the system. A

control sample consisting of as-synthesized SLG (without the gasification step) was loaded in the furnace together with the N-SLG sample. The analysis of the control sample confirmed that the sample preparation did not nucleate vacancy defects in the graphene lattice (**Figure 3.3**).

HRTEM imaging

HRTEM imaging was performed using a Talos F200X (FEI) microscope operated at an acceleration voltage of 80 kV. The dose rate was maintained at ca. 500 e^- s^{-1} $Å^{-2}$ during imaging. To reveal the nanopores and to verify that the pores did not expand during imaging, the procedure was followed: i) 30 consecutive images were taken with an exposure time of 2 s each; ii) the first and last images were compared to verify that no pore expansion occurred during imaging; iii) the first 5 to 8 images were integrated to form the final image. Typically, during HRTEM imaging of the nanoporous graphene samples in Talos the pores experienced a dose of ca. 8×10^3 e^- $Å^{-2}$ during focusing and imaging.
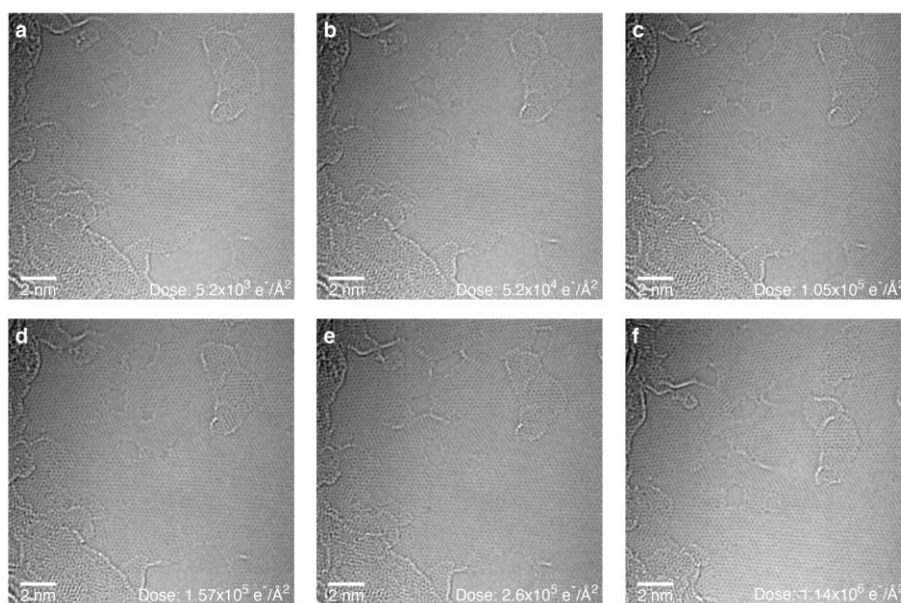
AC-HRTEM imaging

AC-HRTEM was performed using a double-corrected Titan Themis 60-300 (FEI) equipped with a Wein-type monochromator. An 80 keV incident electron beam was used for all experiments to reduce the electron radiation damage. The incident electron beam was monochromated ("rainbow" mode illumination) to reduce the effects of chromatic aberration, and a negative Cs of ~17–21 μm with a slight over-focus was used to give a "bright atom" contrast in the images. The dose rate was maintained at ca. 2×10^4 e^- s^{-1} $Å^{-2}$ during imaging, and a slit was used to expose only the area of the sample being imaged to the electron beam.

The maximum energy that can be transferred to a carbon atom by an 80 keV incident electron is 15.8 eV which is below the knock-on energy threshold for carbon atoms in the basal plane of graphene (17 eV)[51]. In agreement, we did not observe any knock-on from pristine areas during imaging. Similar to the literature[51], we observed reconfiguration of the pore edge in the scale of seconds, and on occasions, in less than a second. The knock-on of edge atoms (i.e. the expansion of vacancy defects) was observed only after a longer exposure time (**Figure 3.4**). The pores imaged to construct the pore library of the graphene samples prepared by MGR were exposed to doses that were low enough to avoid the

expansion. Typically, during imaging of the N-SLG samples, the lattice experienced a dose of ca. 2×10^5 e⁻ Å^{-2} during focusing and imaging. The first 5-10 frames (each frame corresponds to a dose of ca. 5×10^3 e⁻ Å^{-2}) were integrated into the final image. When needed, the images were processed with a combination of Gaussian, average and/or Bandpass filters to make the lattice clearer.

Analysis of AC-HRTEM images

The graphene lattice surrounding the vacancy defects was manually fitted with a hexagonal lattice to locate the missing carbon atoms. Dangling bonds and Stone-Wales defects were ignored. Such analysis is a powerful tool to quantify the number of missing atoms and to draw the shape of the defects in a large library of structures (49 distinct structures). We note the uncertainty in the edge configuration of the vacancy defect, because edge reconfiguration was present at the imaging conditions (80 keV, **Figure 3.4**). A total of 118 defects from three independently prepared samples were analyzed. The library containing the raw and the fitted images of all the defects is available in **Appendix-II**.

Figure 3.4 Stability of graphene nanopores during AC-HRTEM imaging. Structure of graphene nanopores after different doses of 80 keV electron beam. A continuous series of images were taken using an exposure time of 0.25 s per image (ca. 5.2×10^3 e⁻ Å^{-2}) to analyze the interaction of the e⁻ with the nanopores. The panels a, b, c, d, e and f correspond to the 1st, 10th, 20th, 30th, 50th, and 220th images of the series, respectively.

The diameter of the defects was determined using the ImageJ software. The diameter was calculated by fitting the largest possible circle that fitted inside the defect, as shown in **Figure 3.5**. Only pores surrounded by the graphene lattice were used for the analysis (i.e., pores touching contamination were ignored).
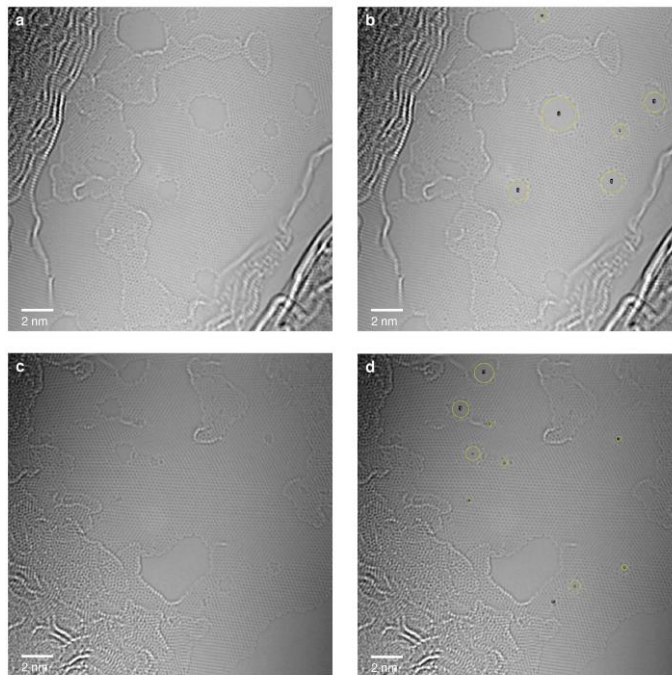
Figure 3.5 Pore diameter analysis from AC-HRTEM images. **(**a, c) AC-HRTEM images showing several nanopores in the graphene lattice. (b, d) Corresponding images after fitting the largest possible circle that could fit inside the nanopores. Pores near contaminations were ignored in the analysis. The images correspond to the graphene treated with the following MGR conditions: 250 °C, ozone dose: 1.6 x 10^{17} molecular cm^{-3} s, (τ =0.1 s, t_d = 0.5 s).

Scanning tunneling microscope imaging

Scanning tunneling microscope (STM) imaging was carried by using a low-temperature scanning tunneling microscope (CreaTec Fischer & Co. GmbH). To remove contamination from the graphene surface, the N-SLG samples were reduced under 50 sccm H_2 flow, at 800 Torr and 900 °C for 3 h in a quartz tube furnace. Immediately after, the sample was transferred to the ultrahigh vacuum (UHV) chamber of the STM. The N-SLG samples were again heated inside the UHV chamber at 900 °C for 3 hours to clean the surface from residual contamination. STM imaging was performed at 77 K and a pressure of 2×10^{-10} mbar. The STM probe was prepared by cutting a commercial Pt/Ir wire (Pt: 90 wt%, diameter: 0.25 mm, Alfa Aesar). The tilt in the acquired STM images

was reduced by flattening in the WSxM software.

Other characterizations

Scanning electron microscopy (SEM) imaging was carried out by using FEI Teneo scanning electron microscope at 1.0 – 2.0 kV and working distances of 4.0 – 9.0 mm. No conductive coating was applied to the substrates prior to SEM. X-ray diffraction (XRD) measurements were carried out in a Bruker D8 Discover X-ray diffractometer which was equipped with a laser-based sample alignment system.

**2.6 Density functional theory calculations for the heat of adsorption**

The density functional theory (DFT) calculations were performed using the Quantum Espresso package[167,168] to study the potential energy surface of H_2, N_2, CO_2, and CH_4 on the N-SLG lattice hosting two types of vacancy defects (P-13$_i$ and P-16$_i$). To represent the plane wave charge density, an energy cut-off of 70 Ry was used. The defects were incorporated in large enough graphene lattice in order to mimic an infinite sheet to avoid any interactions among pores during the calculations. The Brillouin zone was expressed with a uniform 3×3×1 k-point grids. To prevent interactions between the adjacent lattice, a vacuum region of 40 Å was employed in the z-direction. Calculations were performed by ultrasoft pseudopotentials[169,170], vdW-DF2 dispersion correction was used to correct noncovalent forces[171].

3. Results and discussion

3.1 Millisecond gasification reaction of single-layer graphene

The trade-off between pore density and pore-size distribution is the most challenging bottleneck of the state-of-the-art etching chemistry, due to the orders of magnitude etching rate difference between carbon atoms located in the basal plane and pore edge. We have observed in Chapter 2 that the quality of the CVD-derived graphene would indeed influence the incorporated pore-size distribution by the post-etching method. The as-received commercial copper foils displayed polycrystalline copper grids, deriving the fluctuating I_{2D}/I_G (**Figure 3.6 a-f**) and large quantities of intrinsic defects (**Table 3.1**). The previous works demonstrated the Cu (111) would benefit the quality of graphene

growth.[62,172] Hence, the Cu foils were thermally annealed with a slow programmed cooling rate to obtain Cu (111) to improve the uniformity of graphene and to reduce the density of intrinsic vacancy defects (**Figure 3.6 g-i and Table 3.1**)[164]. High-quality SLG (I_{2D}/I_G ratio of 4.8 ± 0.25) with a low density of intrinsic defects (I_D/I_G ratio of 0.04 ± 0.02) was synthesized by low-pressure chemical vapor deposition on an annealed Cu foil.
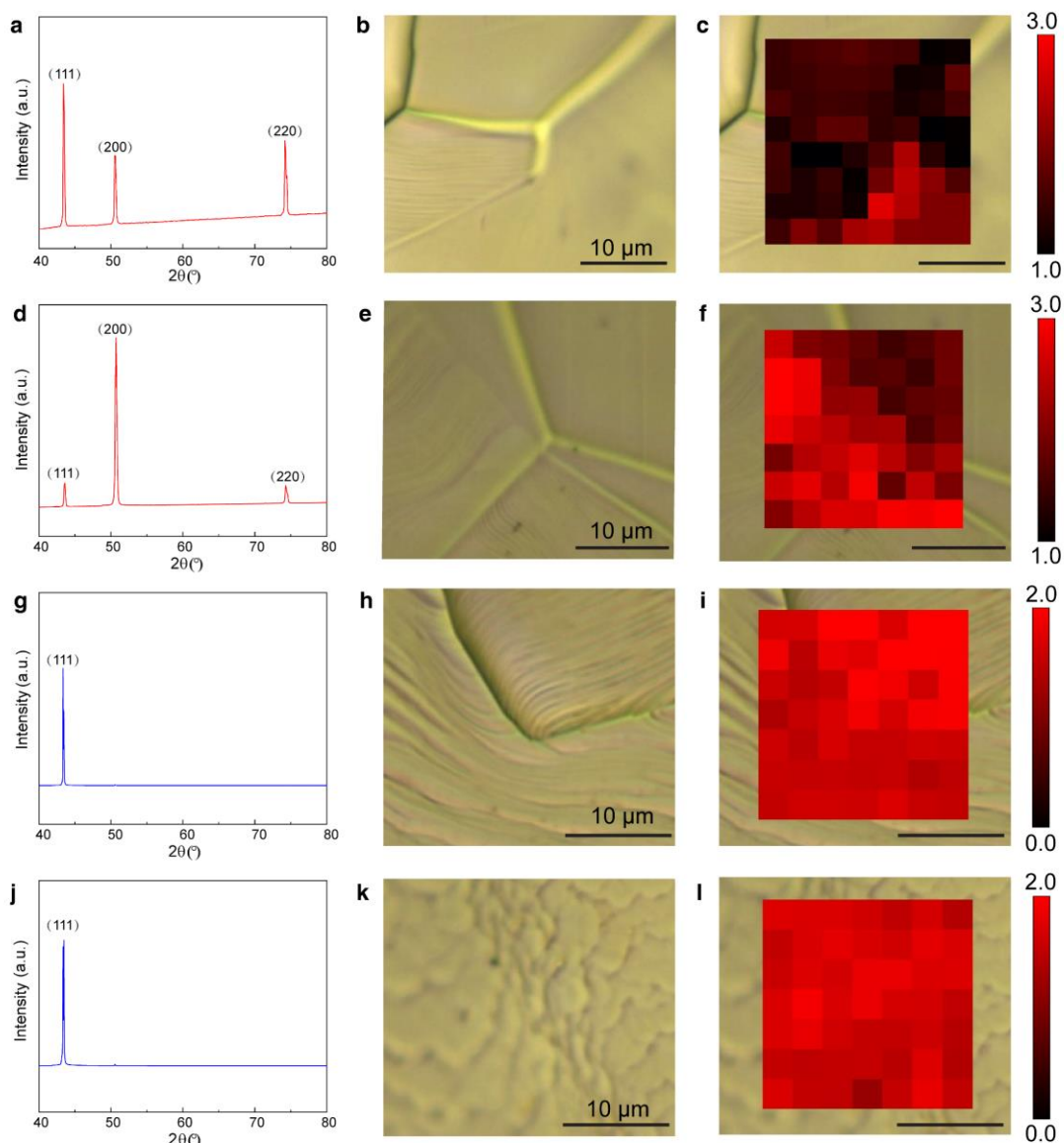
Figure 3.6 Cu (111) obtained by annealing commercial polycrystalline Cu foil from two separate suppliers and the resulting SLG. a-f) Characterization of as-received Cu foil without the annealing step and the resulting SLG. g-l) Characterization of the annealed Cu foil and the resulting SLG. XRD data on the as-received and annealed Cu foils are shown as following: Alfa-Aesar (a, g); Strem (d, j). Optical images from SLG on these foils are shown as following: Alfa-Aesar (b, h); Strem (e, k). The corresponding Raman mapping data (I_{2D}/I_G ratio) from SLG are shown as following: Alfa-Aesar (c, i); Strem (f, l). Overall, while the quality of graphene grown on as-received Cu is not uniform across the

grain, much more uniform quality graphene could be synthesized on the annealed Cu foil, irrespective of the supplier.

Table 3.1 Gas performance through intrinsic defect of as-synthesized CVD graphene with the various commercial copper substrates before and after the annealing step. The gas permeation data is reported at 150 ºC.

Cu supplier	Foil condition	H_2 permeance (mol m^{-2} s^{-1} Pa^{-1})	H_2/CH_4 separation factor
Alfa-Aesar	As-received	3.9×10^{-7}	3.6
Strem	As-received	1.7×10^{-7}	7.4
Alfa-Aesar	Annealed	8.3×10^{-8}	24.4
Strem	Annealed	9.5×10^{-8}	10.3
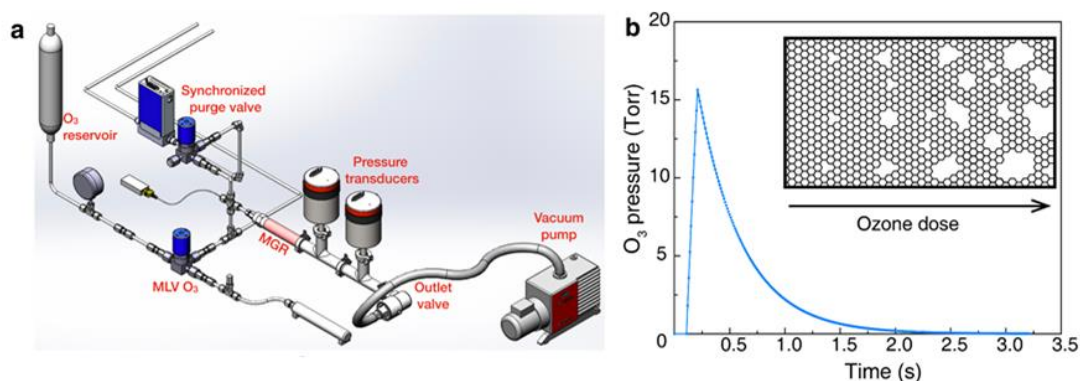
Figure 3.7 Controlled incorporation of vacancy defects by millisecond gasification. a) Schematic of the MGR setup. b) Profile of the O_3 pulse in MGR.

To overcome the trade-off of the etching method, we designed a millisecond gasification reactor (MGR) for a rapid ozone treatment to realize high-density, narrowly distributed nanopores on graphene lattice. The MGR is composed of an ozone (etchant) supply to a hot chamber (120 – 290 ºC) via a millisecond leak valves (MLV) (**Figure 3.1 and Figure 3.7**). To initiate the etching, the as-synthesized SLG was heated to the reaction temperature inside an evacuated MGR, and MLV was opened for 0.01 – 0.2 s, allowing a short O_3 pulse (FWHM of 0.3 s, **Figure 3.8**) with peak O_3 pressure in the range of 3 – 27 Torr. The concentrated etchant at elevated temperature promotes the nucleation rate, resulting in high pore density. Meanwhile, the unique design controls the expansion time of vacancy defects to a few milliseconds, generating nanopores with a narrow pore-size

distribution. Optionally, a purge (Ar or He) was opened after a synchronized delay time (t_d) to facilitate the rapid removal of O_3 (**Figure 3.8b**).
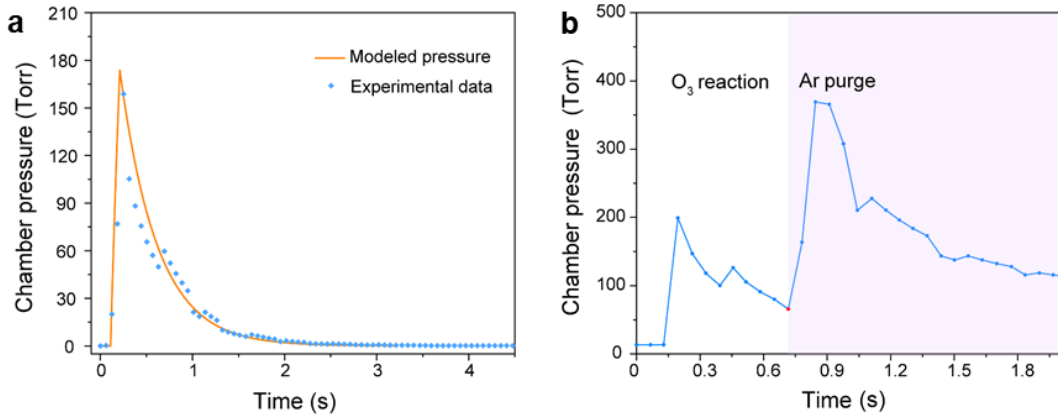
Figure 3.8 a) Total pressure (O_2/O_3) profile in MGR when operated using τ of 0.1 s and Pup of 3 bar. Blue markers represent experimental data and the orange profile represents the model detailed in as follows. b) Experimental chamber pressure profile obtained by using τ of 0.1 s, P_{up} of 3 bar, and t_d of 0.5 s.

The ozone pressure profile determines the resolution of the derived nanopore in graphene lattice. To understand and monitor the pressure profile of the MGR, a mathematical model was built to investigate the pressure profile of ozone when MLV is opened and closed. The photo and schematic of the MGR setup are shown in **Figure 3.1** and **Figure 3.7.** The inlet of the reactor is connected with an MLV, which connects with the O_2/O_3 reservoir, where the pressure of the reservoir is P_{up}. The outlet of the MGR is connected with a vacuum pump via an outlet valve, maintaining a P_{pump} of 0 bar. The total pressure of O_2/O_3 mixture in MGR, P_r, is initially 0.

Briefly, MLV is opened at t = 0 s and it is closed at t = τ. During $0 < t < \tau$, the O_2/O_3 mixture is delivered in the MGR chamber. We define C_1 as a transport coefficient of MLV, $\frac{dN}{dt}|_{in}$ as the inward flow rate of gas in the MGR.

$$\frac{dN}{dt}\Big|_{in} = C_1 \left(P_{up} - P_r \right) \tag{3.1}$$

We define C_2 as a transport coefficient of the outlet valve, $\frac{dN}{dt}|_{out}$ as the flow rate of gas pumped out from the MGR.

$$\frac{dN}{dt}\Big|_{out} = C_2 \left(P_r - P_{pump} \right) = C_2 P_r \tag{3.2}$$

Hence, the amount of gas accumulated in the MGR, $\frac{dN}{dt}$ is calculated as follows:

$$\frac{dN}{dt} = C_1 \left(P_{up} - P_r \right) - C_2 P_r \tag{3.3}$$

Therefore, during $0 < t < \tau$, the pressure change in the reactor is

$$\frac{dP}{dt} = \frac{RT}{V_r} (C_1 (P_{up} - P_r) - C_2 P_r) \tag{3.4}$$

where V_r is the reactor volume (150 cm^3).

When $t > \tau$, the MLV is closed, and the O_2/O_3 mixture is pumped out by the vacuum pump leading to the exponential decay of the pressure. The corresponding change in pressure profile is captured by the following:

$$\frac{dN}{dt} = -C_2 P_r \tag{3.5}$$

$$\frac{dP_r}{dt} = -\frac{RT}{V_r} C_2 P_r \tag{3.6}$$

After solving eqs. 3.4 and 3.6, we could calculate the pressure of the reactor.

$0 < t < \tau$

$$P_r = P_0 \, exp \, (-\frac{RT(C_1 + C_2)}{V_r} t) + \frac{C_1}{C_1 + C_2} \, P_{up}[1- \, exp \, (-\frac{RT(C_1 + C_2)}{V_r} t)] \tag{3.7}$$

When $t = \tau$, $P_r = P_{r-\tau}$

$t > \tau$

$$P_r = P_{r-\tau} \, exp \, (\frac{RTC_2}{V_r}(t - \tau)) \tag{3.8}$$

By fitting the experimental data of MLV open for $\tau = 0.1$ s (**Figure 3.7b** and **Figure 3.8a**), C_1 and C_2 were extracted as 5.5×10^{-8} and 1.7×10^{-7} mol s^{-1} Pa^{-1}, respectively.

With the ozone pressure file in the MGR, the O_3 dosage is proposed here to characterize the rapid ozone flow in the MGR chamber quantitively. It is calculated by the area under the curve of O_3 pressure as a function of time, was controlled by varying the

MLV opening time (τ) and O$_3$ supply pressure (P_{up}) (**Table 3.2**), calculated as follows:

$$\text{Dose} = \int_{t_o}^{t_f} [O_3] \, dt = \int_{t_o}^{t_f} N_A \frac{P}{RT} \, dt \tag{3.9}$$

where $[O_3]$ is the concentration of O$_3$, P is the partial pressure of O$_3$, N_A is Avogadro number 6.023×10^{23} mol^{-1}, R = 8.314 J mol^{-1} K^{-1}. t_0 is the etching start time (when MLV opens), and t_f is the time at which the etching finishes. Without the Ar purge, t_f is the time that the ozone pressure reduces to zero. With Ar purge, t_f corresponds to the time when Ar purge starts. The dose reported here was calculated by taking the average value of the integration of multiple pressure profiles (**Table 3.2**). Overall, O$_3$ dosage of 3.2×10^{16} to 3.5×10^{17} molecules cm^{-3} s was delivered while keeping the etching time well below 1 s.

Table 3.2 MGR parameters used in this study and the resulting ozone dose.

| τ	P_{up}	Purge gas	t_d	Ozone dose
(s)	(bar)		(s)	(molecules cm^{-3} s)
0.01	3	no purge	-	4.8×10^{16}
0.05	3	no purge	-	1.2×10^{17}
0.1	3	no purge	-	2.2×10^{17}
0.2	3	no purge	-	3.5×10^{17}
0.05	5	Ar	0.5	1.8×10^{17}
0.1	3	Ar	0	3.2×10^{16}
0.1	5	Ar	0	7.7×10^{16}
0.1	3	Ar	0.5	1.6×10^{17}
0.1	5	Ar	0.5	2.9×10^{17}
0.1	3	Ar	1	2.0×10^{17}
0.2	5	Ar	0	1.4×10^{17}
0.2	3	Ar	0.5	2.7×10^{17}
0.05	5	He	0.2	1.2×10^{17}
0.1	5	He	0.2	2.1×10^{17}

3.2 Nanopores incorporated by MGR

The evolution of nanopores incorporated in graphene with different ozone doses was probed by Raman spectroscopy. The graphene exposed to increasing O_3 dose between 4.8×10^{16} to 3.5×10^{17} molecules cm^{-3} s revealed significant D and D' peaks (**Figure 3.9a**). The increasing I_D/I_G ratio and decreasing I_{2D}/I_G ratio indicated the disorders propagation with increasing ozone dose. The $I_D/I_{D'}$ ratios were well below 7 reaching 3, indicating that most of the defects were edge-like defects of graphite[173]. The uniform I_D/I_G mapping indicated that the defects generated uniformly over a large area by MGR (**Figure 3.9c**). Optionally, the Raman spectrum of the N-SLG with a synchronized Ar purge showed much higher I_{2D}/I_G ratio ($I_{2D}/I_G = 0.9$) than the one without Ar purge ($I_{2D}/I_G = 1.8$) (**Figure 3.9d**), indicating a purge (Ar or He) after a synchronized delay time would quench the reaction and reduce the reaction time.
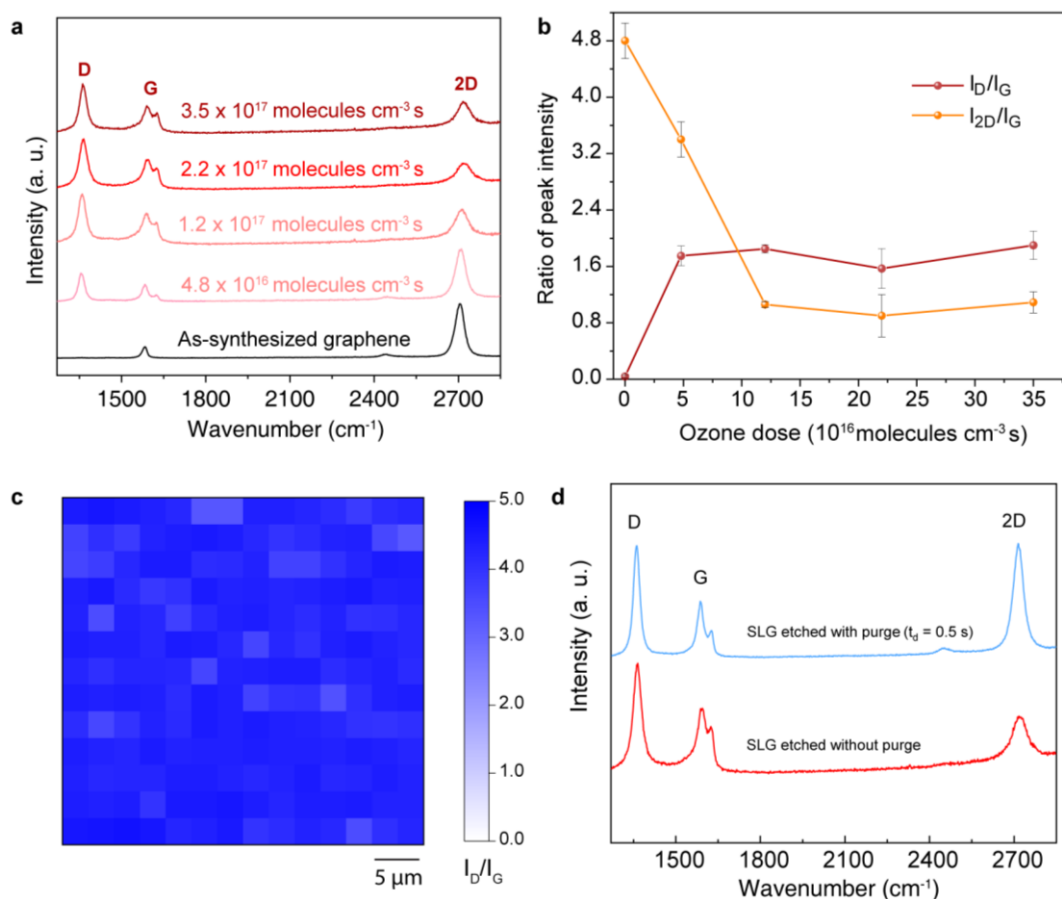
Figure 3.9 a) Raman spectroscopy of the evolution of vacancy defects by millisecond gasification. b) I_D/I_G, I_{2D}/I_G ratios ($\lambda_L = 457$ nm) from N-SLG as a function of the ozone dose. c) Raman map of the I_D/I_G ratio ($\lambda_L = 532$ nm) on a sample using ozone dose of 1.6×10^{17} molecules cm^{-3} s) at 250 °C. d)

Raman spectra (λ_L = 457 nm) of N-SLG prepared by MGR (τ = 0.1, P_{up} = 3 bar) with and without Ar purge.

Aberration-corrected HRTEM (AC-HRTEM) were carried out to understand pore-size distribution, pore density, and pore structure of N-SLG. To prevent cracks during the transfer of N-SLG to the TEM grid, a porous polybenzimidazole film was deposited on top of N-SLG as a mechanical reinforcement. The grid was annealed at 900 °C in a reducing atmosphere to remove contaminants that mask the SLG lattice (**Figure 3.2**). Control experiments on as-synthesized SLG proved that grid preparation steps did not lead to the incorporation of nanopores (**Figure 3.3**). Imaging was carried out using a stable 80 keV beam that did not nucleate or expand nanopores (**Figure 3.4**). Overall, a pore density of 1.6×10^{12} cm^{-2} was observed when SLG was etched with an O_3 dosage of 1.6×10^{17} molecules cm^{-3} s (τ = 0.1 s, t_d = 0.5 s) at 250 °C. About 49 distinct nanopore lattice structures, missing 1-20 carbon atoms (**Appendix-II**), were identified out of which 33 are reported in **Figure 3.10**. The structure of the vacancy defect imaged by AC-HRTEM was fitted to match the graphene lattice surrounding the pore and pore edge, to identify the pore structure and the missing carbon atoms.
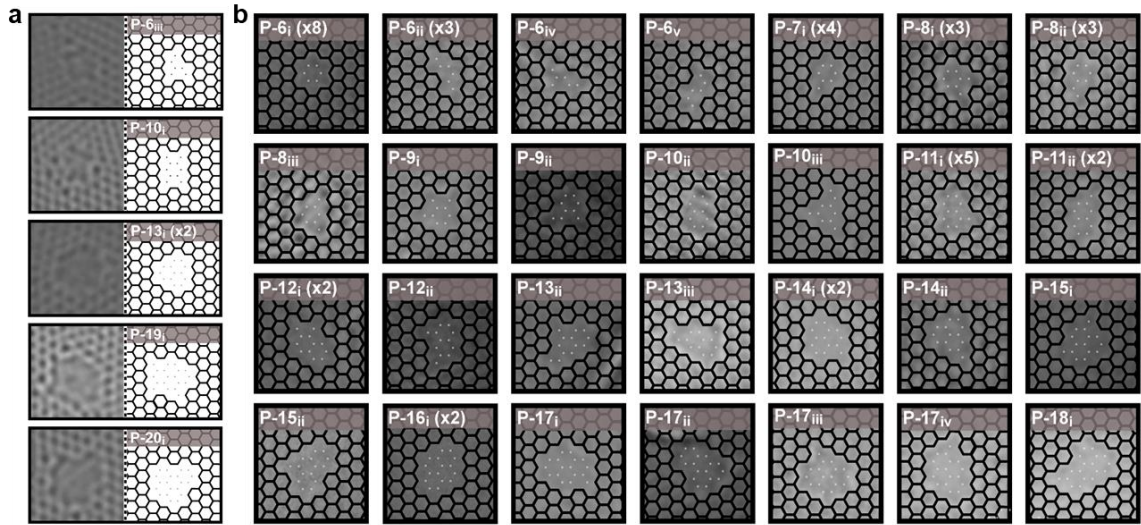
Figure 3.10 a-b) AC-HRTEM images of the vacancy defects and corresponding lattice-fitted structures (dots indicate missing carbon atoms).

Several nanopore isomers, defined as pores of different structures formed by removing exactly V number of atoms, were observed. These isomers are referred to as P-V_j. For example, P-10$_i$, P-10$_{ii}$, and P-10$_{iii}$ are made by removing 10 carbon atoms but host

different structures (**Figure 3.10**). The frequency of occurrence of this structure was labeled as "P-V$_j$ (×n)". For example, P-7$_i$ (×4), refers to the structure of P-7$_i$ which was observed 4 times. The relative population of isomers was consistent with the isomer cataloging of vacancy defects[174]. For example, P-11$_i$ and P-7$_i$, predicted to be the most probable isomers of P-11 and P-7, respectively, were indeed observed most frequently. No other isomer of P-7$_i$ were observed, perhaps attributing to the extremely high probability of P-7$_i$ (42%) and low probability of other P-7 isomers (<10%). Several high-probability isomers such as P-6$_{iii}$, P-8$_{ii}$, P-11$_i$, P-12$_i$, P-16$_i$, and P-17$_i$ were observed, filling the gap between the observed and simulation-predicted gas-sieving nanopores[174] (**Figure 3.10**, **Appendix-II**). Nanopores such as P-10$_i$, P-13$_i$, and P-16$_i$, which have drawn vast attention for gas-sieving, were also observed, albeit they constitute only a small fraction of nanopore population. Higher incidences of nanopore isomers with no repetition were observed when the number of missing carbon atoms was large. For example, six isomers of P-20 were observed without any repetition. This is consistent with the prediction that the diversity of the isomers would exponentially increase as one removes a large number of carbon atoms[174]. Pore-size distribution (PSD) based on the number of missing carbon atoms had a log-normal distribution with a majority of nanopores smaller than P-16 (**Figure 3.15**). In the tail, several nanopores had elongated structure, while several nanopores appeared to be formed by coalescence of smaller pores (**Figure 3.11**).
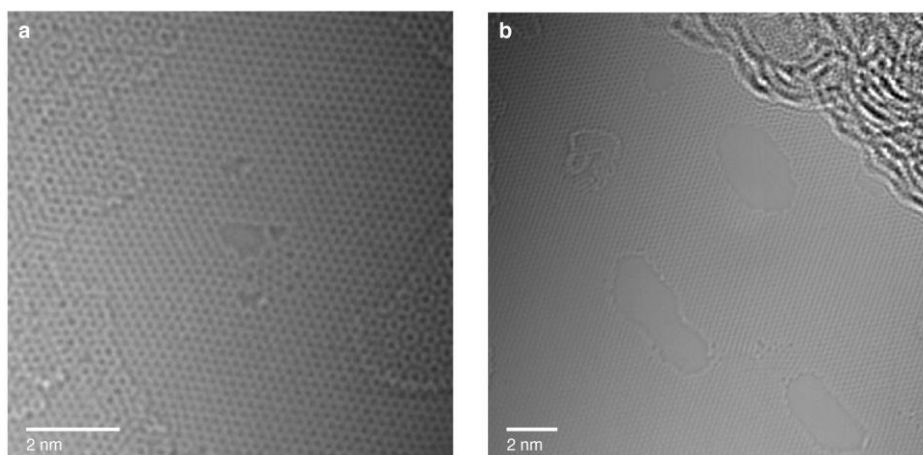
Figure 3.11 AC-HRTEM images of elongated pore generated by MGR. a) AC-HRTEM image of a vacancy defect surrounded by several small vacancy defects on the N-SLG sample prepared by MGR. b) The elongated vacancy defects found in N-SLG sample.

Scanning tunneling microscopy (STM) was carried out directly on N-SLG resting over the Cu foil without the need of transferring graphene (**Figure 3.12**). SLG etching was carried out by the exact same condition as that for AC-HRTEM. While we faced difficulty in lattice-resolved STM imaging because of partial oxidization of Cu foil during the O_3 treatment, images based on scan size of 100 nm × 100 nm revealed that a high density of vacancy defects ($\sim10^{12}$ cm^{-2}) was incorporated in the lattice. The size of the vacancy defect is in agreement with the HRTEM observations (**Figure 3.12c**). Occasionally, several nanopores appeared to be aligned and appear to be distributed more uniformly than anticipated from a purely stochastic etching (**Figure 3.12b**). This unique arrangement has likely origin in the cooperative linear clustering of epoxy groups (O atoms bridging C-C bonds) formed by chemisorption of O_3 on graphene [147]. The linear clustering is driven by the low-energy configuration of epoxy groups and is facilitated by a low barrier of diffusion of epoxy groups[76], which is predicted by the DFT simulation. Etching experiments carried out at 150 ºC with the same O_3 dose as above yielded much lower pore density compared to that at 250 ºC (**Figure 3.13**), consistent with the thermally-activated clustering of epoxy groups[59,76,147].
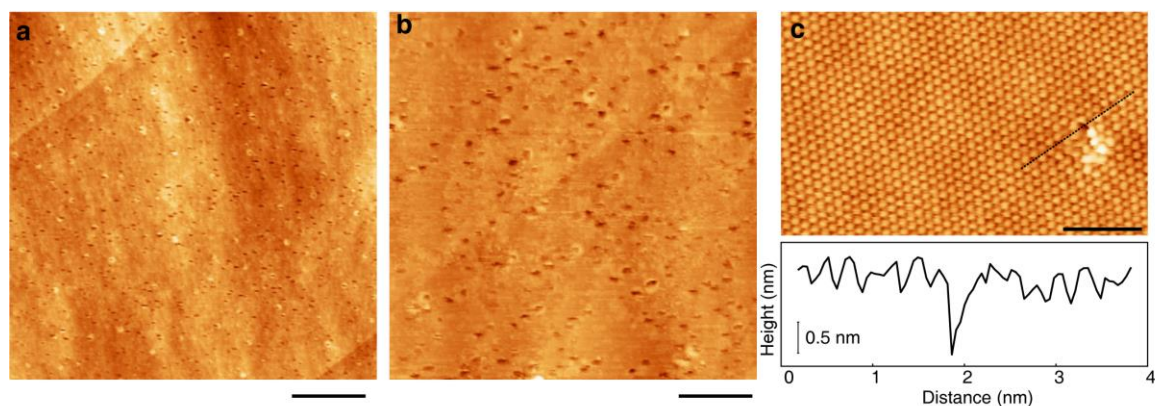
Figure 3.12 a-b) STM images of as-prepared N-SLG on Cu foil, c) lattice-resolved STM image of a vacancy defect with its height profile. Scale bars in a), b) and c) are 100, 40, and 1 nm, respectively.
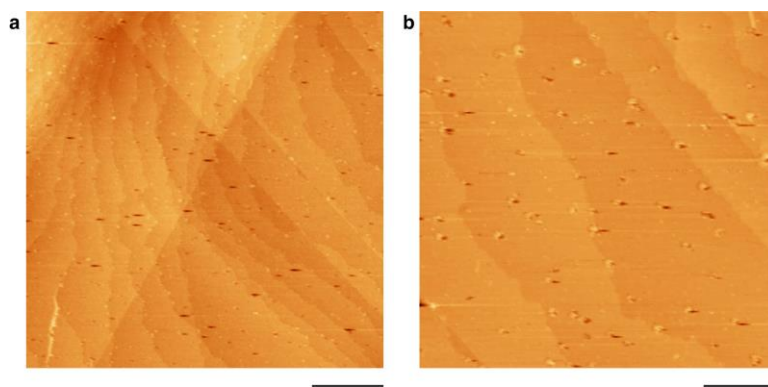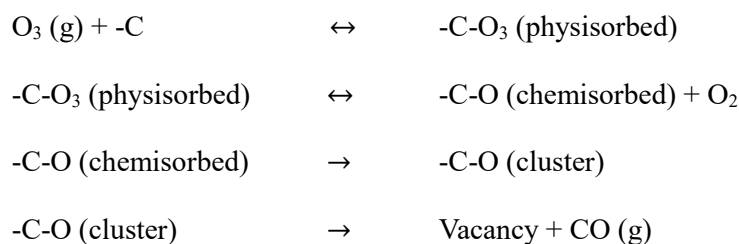
Figure 3.13. STM images of N-SLG on the copper substrate prepared by 150 °C MGR treatment. The bias voltage was −0.3 V. Tunneling currents for a) and b) were 0.5 nA. Scale bars of a) and b) are 100 nm and 40 nm, respectively. Ozone dose is 1.6×10^{17} molecules cm^{-3} s ($\tau = 0.1$ s, $t_d = 0.5$ s).

3.3 Kinetic models to predict PSD of MGR-treated N-SLG

To understand the evolution of nanopores and the resulting pore-size didtribution (PSD), we used kinetic models to simulate pore nucleation and expansion. As suggested by DFT simulation, ozone initialized sp^3 sites on graphene lattice with epoxy groups, and then it would evolve to ether and lactone group, followed by one carbon atom removing and vacancy formation. Herein, we assume the etching process started the epoxy group formation on graphene lattice, called nucleation. Subsequently, more carbon atoms were cleaved from the nuclei by propagated etching, creating nanopores on graphene lattice, called pore expansion. Based on the etching kinetics of ozone on graphene, we have built mathematical models as follows to predict the pore-size distribution of the incorporated nanopores on graphene lattice by MGR.

Nucleation

As we mentioned, the etching would begin with nucleating the reactive sites on graphene, so the nucleation density is expected to be proportional to the density of the chemisorbed functional group, which eventually yields a vacancy defect.

$$O_3 \text{ (g)} + \text{-C} \quad\leftrightarrow\quad \text{-C-}O_3 \text{ (physisorbed)}$$

$$\text{-C-}O_3 \text{ (physisorbed)} \quad\leftrightarrow\quad \text{-C-O (chemisorbed)} + O_2$$

$$\text{-C-O (chemisorbed)} \quad\rightarrow\quad \text{-C-O (cluster)}$$

$$\text{-C-O (cluster)} \quad\rightarrow\quad \text{Vacancy} + CO \text{ (g)}$$

In the beginning, ozone physisorption would take place on the surface of graphene lattice. Subsequently, the physisorbed ozone will be converted to chemisorption to generate the epoxy group. The epoxy groups would rearrange as ether or lactone groups to form clusters, eventually yield a vacancy defect. The formation of vacancy defects, by the release of CO, has a relatively lower energy barrier compared to that for the formation of the epoxy group clusters[75,175,176]. Physisorption is an equilibrium step, determined by Henry's coefficient for physisorption of ozone on graphene. Chemisorption to the epoxy group can be considered to be at equilibrium with physisorption. Since, physisorption is at an equilibrium step, we can write

$$\frac{d\theta_v}{dt} = \frac{d}{dt}\left[\text{-C-O(cluster)}\right] = k_c\left[\text{-C-O(physisorbed)}\right] \tag{3.10}$$

$$\left[\text{-C-O(physisorbed)}\right] = HP \tag{3.11}$$

where θ_v is the fractional occupancy of the single vacancy defects or nucleation site for the nanopores. P is the ozone pressure. H is the Henry's coefficient for physisorption of ozone on graphene. k_c is the effective rate constant for the formation of epoxy group cluster combining the chemisorption constant. Therefore,

$$\frac{d\theta_v}{dt} = k_c HP \tag{3.12}$$

Since both H and k_c are functions of temperature, the fractional occupancy of the nucleation site is expected to be proportional to ozone pressure at a given temperature.

In an elemental time Δt, the number of fresh nucleation sites is related to ozone pressure.

$$\theta_v = k_c HP\Delta t \tag{3.13}$$

Hence, the nucleation density between time period t_0 and t_n could be calculated as follows:

$$\theta_v = k_c H \int_{t_0}^{t_n} P\, dt \tag{3.14}$$

For ozone dose of 1.6×10^{17} molecules cm^{-3} s, $\int_{t_0}^{t_n} P\, dt = 4.9$ Torr s

Based on eq. 3.14 and the observed nucleation density at 250 ℃, $k_c H$ was calculated as 3.2×10^{-4} monolayer Torr^{-1} s^{-1}.

Pore expansion

At the same time, the pore started to expand after the nuclei formation. We define dC as the total number of carbon atom removed by pore expansion from N vacancy defects during an elemental time, dt. Since the number of missing carbon atoms in a vacancy defect is related to the area of the defect, we can write:

$$\frac{dC}{dt} = N C_{\text{density}} \frac{dA}{dt} \tag{3.15}$$

Where C_{density} is the density of carbon atoms in the graphene lattice, and is equal to 38 nm^{-2}, A is the area of the existing vacancy defect, N is the density of vacancy defects.

Based on the reported carbon etching parameters of graphite etched with ozone[59], we have extracted the nucleation density (pit density) and $\dfrac{dC}{dt}$ as follows (**Table 3.3**),

The correlation of $\dfrac{dC}{dt}$ with P as shown in **Figure 3.14** with power-law dependence:

$$\frac{dC}{dt} = k_e P^{0.47} \tag{3.16}$$

where k_e is the rate constant of pore expansion by O_3. The above relationship of the expansion rate of the graphitic pore with respect to the O_3 pressure is not surprising because the pore expansion takes place with O_3 reacting with edge carbon atoms where one O_3 molecule can graft more than one epoxy group[177].

The rate constant for etching k_e, can be expressed in the Arrhenius form as follows:

$$k_e = A_e \exp\left(\frac{-E_{act-e}}{RT}\right) \tag{3.17}$$

Where E_{act-e} is the activation energy, and A_e is the pre-exponential factor.

Table 3.3 Carbon etching rate with different temperature and ozone pressure

Temperature (K)	O_3 pressure, P (Torr)	Pit density (cm^{-2})	$\dfrac{dC}{dt}$ (atoms cm^{-2} min^{-1})
633	2.66×10^{-5}	1.3×10^{10}	1.75×10^{13}
633	9.88×10^{-5}	7.0×10^{10}	9.40×10^{13}
633	7.60×10^{-4}	1.4×10^{11}	1.88×10^{14}
723	7.60×10^{-5}	8.0×10^{9}	5.73×10^{14}
643	6.84×10^{-4}	1.96×10^{11}	2.92×10^{14}
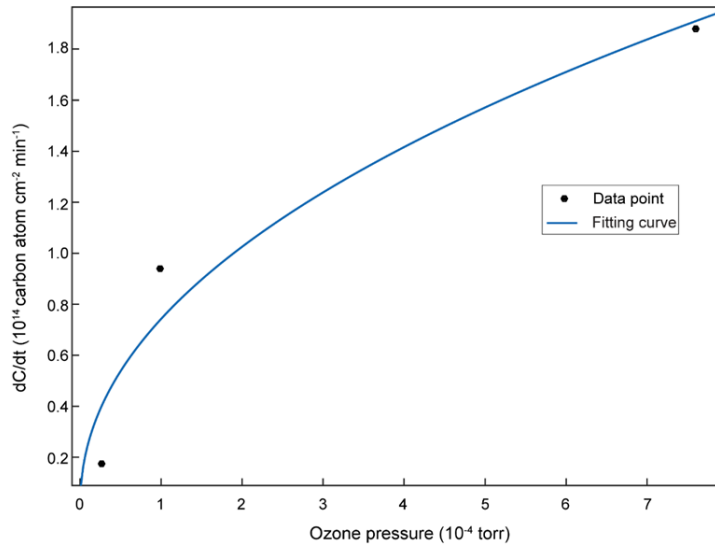
Figure 3.14 The correlation of carbon etching rate $\dfrac{dC}{dt}$ and ozone pressure, P, extracted from the literature[59] for etching at 633 K.

Based on data at 633 and 723 K, we could extract the activation energy for pore expansion is $E_{act-e} = 81.6$ kJ/mol and $A_e = 3.9 \times 10^{22}$ atoms cm^{-2} min^{-1} $Torr^{-0.47}$.

At 250 °C, the total number of missing carbon atoms during time interval $[t_{i-1}, t_i]$ is:

$$\Delta C_i = \int_{t_{i-1}}^{t_i} k_{523} P^{0.47} dt \tag{3.18}$$

Calculation of the pore-size distribution (PSD)

To estimate PSD, we tracked the expansion of pores nucleated during a certain time interval as a function of time. Briefly, the O_3 exposure was divided into n equal time intervals, Δt. At the end of O_3 exposure, the number of the missing carbon atom, v_i, for those pores which nucleated during a time step t_i, could be calculated as follows:

We define the following parameters to calculate the PSD:

t_0 = etching start time = 0

t_f = etching end time

Δt = elemental time interval obtained by dividing etching time in n equal steps = $(t_f - t_0)/n$

This implies

$t_1 = \Delta t$

$t_2 = t_1 + \Delta t = 2\Delta t$

....

$t_i = i\Delta t$

We also define the etching of carbon atoms in each of the elemental time steps as following,

ΔC_i = total carbon atom etched, and N_i = number of nuclei created during $t_{i-1} < t < t_i$ where i varies from 1 to n.

For estimating PSD, we define missing carbon atom per pore $v_i^{t_j}$ for those pore which nucleated in time duration of $t_{i-1} < t < t_i$ at the end of a particular etching period (time from t_0, $t_j = j*\Delta t$) with the condition that $j > i$.

$$v_i^{t_j} = \sum_{m=i}^{m=j} \frac{\Delta C_m}{\sum_{k=1}^{m} N_k} = \frac{\Delta C_i}{N_1 + N_2 + ...N_i} + ... + \frac{\Delta C_j}{N_1 + N_2 + ... + N_j} \qquad (3.19)$$

For example, if we consider pores that nucleated during $t_2 < t < t_3$, i.e. $i = 3$, and look at their expansion up to time $t_5 = 5\Delta t$ ($j = 5$), the number of the missing carbon atom of

the pore $v_3^{t_5}$ is as follows,

$$v_3^{t_5} = \sum_{m=3}^{m=5} \frac{\Delta C_m}{\sum_{k=1}^{m} N_k} = \frac{\Delta C_3}{N_1+N_2+N_3} + \frac{\Delta C_4}{N_1+N_2+N_3+N_4} + \frac{\Delta C_5}{N_1+N_2+N_3+N_4+N_5}$$

Our interest is to calculate PSD at the end of etching. So, we look at the evolution of pores and get to pore size at t_n. PSD corresponds to the contribution of all nuclei generated from t_1 to t_n. The number of missing carbon atom $v_i^{t_n}$ of the nuclei formed at t_i, could be calculated as follows,

$$v_i^{t_n} = \sum_{m=i}^{m=n} \frac{\Delta C_m}{\sum_{k=1}^{m} N_k} = \frac{\Delta C_i}{N_1+N_2+...+N_i} + ... + \frac{\Delta C_n}{N_1+N_2+......+N_n} \qquad (3.20)$$

For example, contribution from nuclei generated during $t_2 < t < t_3$, i.e. $i = 3$, to the end of the etching, is $v_3^{t_n}$

$$v_3^{t_n} = \sum_{m=3}^{m=n} \frac{\Delta C_m}{\sum_{k=1}^{m} N_k} = \frac{\Delta C_3}{N_1+N_2+N_3} + \frac{\Delta C_4}{N_1+N_2+N_3+N_4} + \frac{\Delta C_n}{N_1+N_2+......+N_n}$$

Overall, to calculate PSD for MGR condition used for the AC-HRTEM sample, the following steps were taken: i) the ozone pressure profile was obtained by model fitting (**Figure 3.8a**). The Δt was set as 0.01 s, the number of newly-generated nuclei during each Δt could be calculated by eq.3.13, and the carbon etching rate could be calculated during each Δt by eq. 3.18. Following this, the number of the missing carbon atom $v_i^{t_n}$ of the nuclei formed at t_i could be calculated by eq. 3.20.

Based on the model, we have calculate the missing carbon atoms per defect at the end of reaction is v_i by eq.3.21.

$$v_i = \sum_{m=i}^{m=n} \frac{\Delta C_m}{\sum_{k=1}^{m} N_k} = \frac{\Delta C_i}{N_1+N_2+...N_i} + ... + \frac{\Delta C_n}{N_1+N_2+......+N_n} \qquad (3.21)$$

where N_i is the number of new nuclei generated during a time step i, and ΔC_i is the total number of carbon atoms etched from the existing defects in time step i. The PSD

extracted by the model agrees well with that from the HRTEM observations (**Figure 3.15**). The calculation results are listed in **Table 3.11 (Appendix- I).**
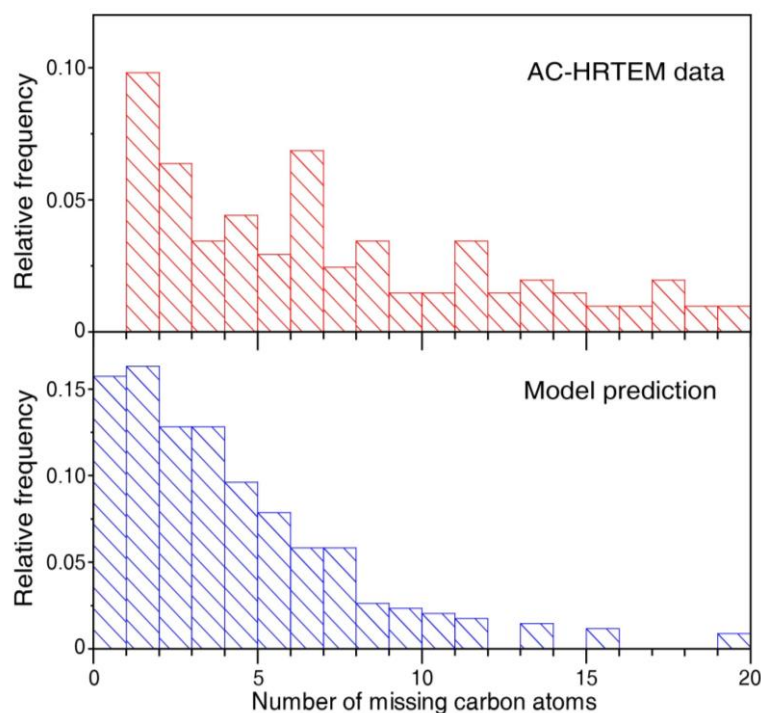

Figure 3.15 Top: distribution of the number of missing carbon atoms in the vacancy defects based on the AC-HRTEM; bottom: the predicted distribution of the missing carbon atoms using the gasification kinetics model.

3.4 Gas transport through nanoporous single-layer graphene

The N-SLG was transferred to the porous membrane support by the nanoporous carbon-assisted transfer method. The gas transport measurement was conducted in a leak-proof homemade permeation setup equipped with a mass spectrometer. Observation of gas flux through 1-mm^2-sized N-SLG membranes, prepared using O_3 dosage of 4.8×10^{16} to 3.5×10^{17} molecules cm^{-3} s ($\tau = 0.01 - 0.2$ s), revealed that N-SLG could separate H_2 and CO_2 from CH_4, with H_2 and CO_2 permeances increasing monotonically by 30-fold at the highest O_3 dose (**Figure 3.16 and Table 3.8**). It indicated more nanopores incorporated in the graphene with increased ozone dose, consistent with the observation of the Raman spectrum. The H_2/CH_4 and CO_2/CH_4 selectivities ($9.7 - 19.9$ and $6.1 - 18.4$, respectively), were much higher than the corresponding Knudsen selectivities (2.8 and 0.6, respectively),

confirming that the incorporated vacancy defects could indeed sieve similarly-sized molecules.
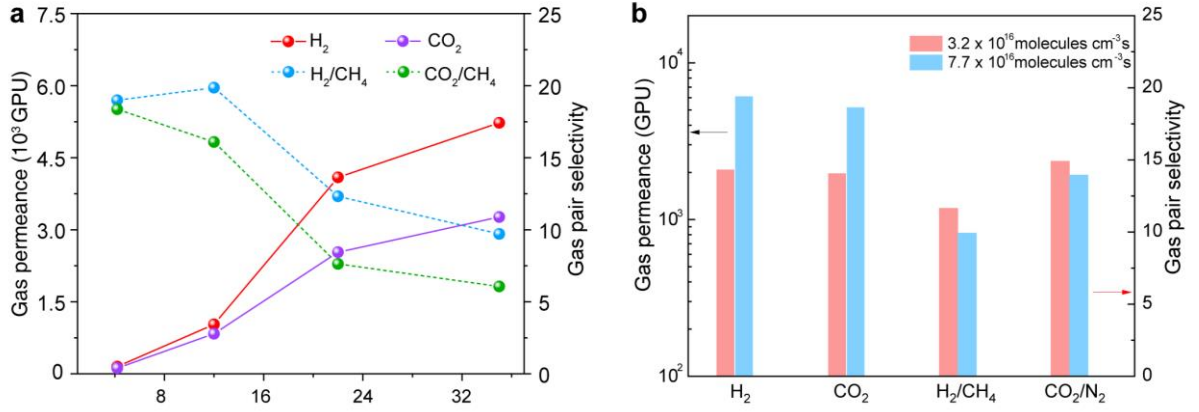
Figure 3.16 a) Gas permeance and gas pair selectivity through N-SLG with MGR with different ozone dose without Ar purge. b) Gas separation performance of N-SLG membranes prepared by MGR with 0 s Ar delay with different ozone dose.

The gas transport across size-sieving graphene nanopore takes place via the activated transport mechanism. The corresponding apparent activation energy $E_{app\text{-}act}$ could be extracted from the experimental data by fitting the temperature-dependent gas flux with an Arrhenius relationship[164]

$$\text{Flux} \propto C_0 A_p \exp(-\frac{E_{app\text{-}act}}{RT}) \qquad (3.22)$$

where

$$E_{app\text{-}act} = E_{act} + E_{sur} \qquad (3.23)$$

Here, A_p is the pre-exponential factor for the Arrhenius term, C_0 is the pore density, E_{act} is the activation energy to translocate the pores. E_{sur} is the adsorption energy of gas molecules on the graphene pore, and was estimated by the DFT calculation on porous graphene lattice (P-13$_i$ and P-16$_i$). Briefly, to study the interaction energy of gas molecules at different distances from the N-SLG lattice, gas molecules were relaxed in all directions except in the perpendicular direction to the lattice. The effective interaction energy between the gas molecule and the N-SLG lattice was calculated as follows:

$$E_{sur} = E_{gas+pore} - (E_{gas} + E_{pore}) \tag{3.24}$$

where $E_{gas+pore}$ is the total energy of gas molecules when it interacts with the nanopore, E_{gas} and E_{pore} are the energy of the gas and N-SLG lattice when gas molecule is far away from the lattice and does not interact with it. The minima in E_{sur}, when the molecule is close to the pore, was extracted as the adsorption energy of the gas molecule, and is listed below **Table 3.4**:

Table 3.4 Adsorption energy of the gas molecule on nanopore by DFT calculation

Gas molecule	E_{sur} (kJ/mole)		Average E_{sur} (kJ/mole)
	P-13$_i$	P-16$_i$	
H_2	-2.9	-2.5	-2.7
CO_2	-10.8	-9.0	-9.9
N_2	-6.6	-5.7	-6.1
CH_4	-8.5	-8.1	-8.3
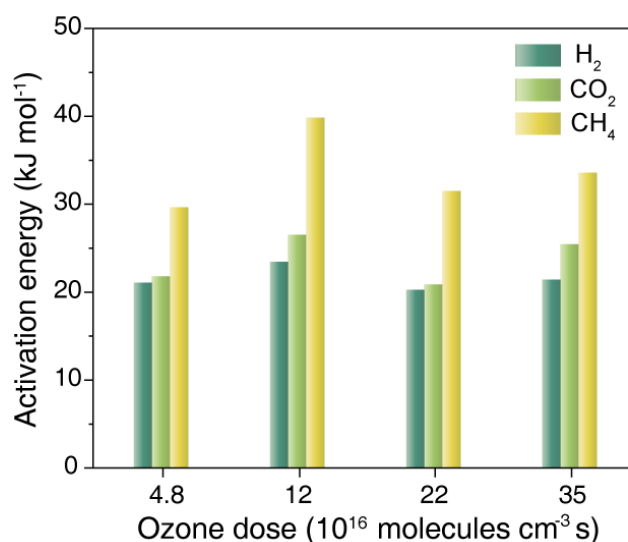
Figure 3.17 Activation energy extracted for gas molecules transport through N-SLG with different ozone dose treatment.

The calculated adsorption energies are consistent with the literature[90]. Since the

adsorption energy does not change significantly between these two pores, we used the average adsorption energy for the calculation of E_{act}. Interestingly, the activation energy for H_2, CO_2, and $CH_4$, extracted by subtracting their heat of adsorption (2.7, 9.9, and 8.3 kJ mol^{-1}, respectively) from the observed apparent activation energy, did not change significantly (**Figure 3.17**). The decrease in selectivity at higher dosage can be attributed to the coalescence of adjacent pores, which is expected to promote the effusive transport[160].

To improve the sieving resolution of the nanopore generated at higher ozone dose, pressurized Ar was synchronized to conduct a fast quench. Hindering the etching reaction with the synchronized Ar purge ($t_d = 0 – 1.0$ s) improved the CO_2-sieving performance (**Figure 3.18 and Table 3.7**). CO_2 permeance of 2620 GPU with corresponding CO_2/N_2 and CO_2/CH_4 selectivities of 27.6 and 20.0 could be achieved at O_3 dose of 1.6×10^{17} molecules cm^{-3} s ($\tau = 0.1$ s, $t_d = 0.5$ s), proving that the collection of nanopores observed by AC-HRTEM is indeed attractive for CO_2-sieving. The rapid removal of residual O_3 by the Ar purge was also reflected in the fact that a relatively lower structural disorder was observed by the Raman spectroscopy (**Figure 3.9**d). The use of purge improved CO_2/CH_4 selectivity without a significant loss in CO_2 permeance (**Figure 3.18**). We note that the sieving of CO_2 from N_2 corresponds to MSR of 0.3 Å. In fact, we could also achieve CO_2/O_2 selectivity of 12.6, respectively, corresponding to MSR of 0.2 Å.
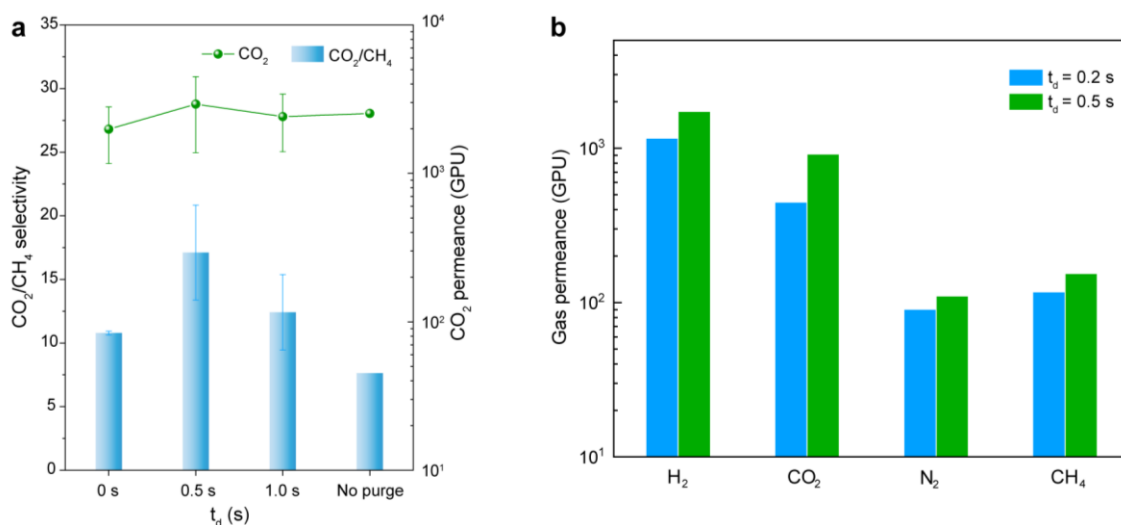
Figure 3.18 a) Gas separation performance of N-SLG etched at 250 ºC ($\tau = 0.1$ s) with varying Ar delay time td. b) Gas permeance through N-SLG membranes prepared by MGR at 290 ºC using τ of 0.05 s with P_{up} of 5 bar and using the He purge. Two separate td of 0.2 and 0.5 s were used (blue and green bars, respectively).

The etching kinetics could be controlled to yield attractive CO_2/CH_4 selectivities at a wide range of temperatures (120 – 290 ºC) with optimized O_3 dosages (**Figure 3.19b**). For a given ozone dose ($\tau = 0.1$ s, $t_d = 0.5$ s), we observed increasing gas permeance and decreasing selectivity as a function of the etching temperature, attributing to a faster etching kinetics at the higher temperature. This was evident in HRTEM-derived PSD where the mean pore size (edge to edge gap) increased by ca. 0.2 nm at 290 ºC (**Figure 3.19c**). We could shift back the mean pore size at 290 ºC by optimizing the O_3 dose involving reducing t_d from 0.5 to 0.2 s and using a cooled He purge. This was reflected in the improvements in the H_2/N_2 and CO_2/N_2 selectivities (**Figure 3.19c**).

The controlled gasification of graphene by millisecond etching is highly scalable attributing to the highly uniform etching of graphene under the partial vacuum in MGR. To demonstrate this, we gasified 2 cm × 1.5 cm sized SLG, and subsequently transferred it to a smoothened metal-mesh support hosting 20 μm pore opening. Attributing to the higher roughness of the metal-mesh compared to the drilled W foil, the transfer became more challenging, and therefore, the mechanical reinforcement was switched from the NPC film to a nanoporous polymer film, poly[1-(trimethylsilyl)-1-propyne] or PTMSP.[95,165] Briefly, the mechanically-reinforcing PTMSP layer was coated on N-SLG before its transfer to the porous support. The resulting centimeter-scale PTMSP-reinforced N-SLG membrane (**Fig. 3.19d**) yielded CO_2/N_2 selectivity of 17.4 at 25 ºC, close to double than that (8-10) expected from the standalone PTMSP film[178,179] and similar to that from millimeter-scale PTMSP-reinforced N-SLG membrane (22.5) as well as that from the NPC-reinforced N-SLG membranes prepared on the drilled W support, confirming that the gasification technique reported here is scalable.
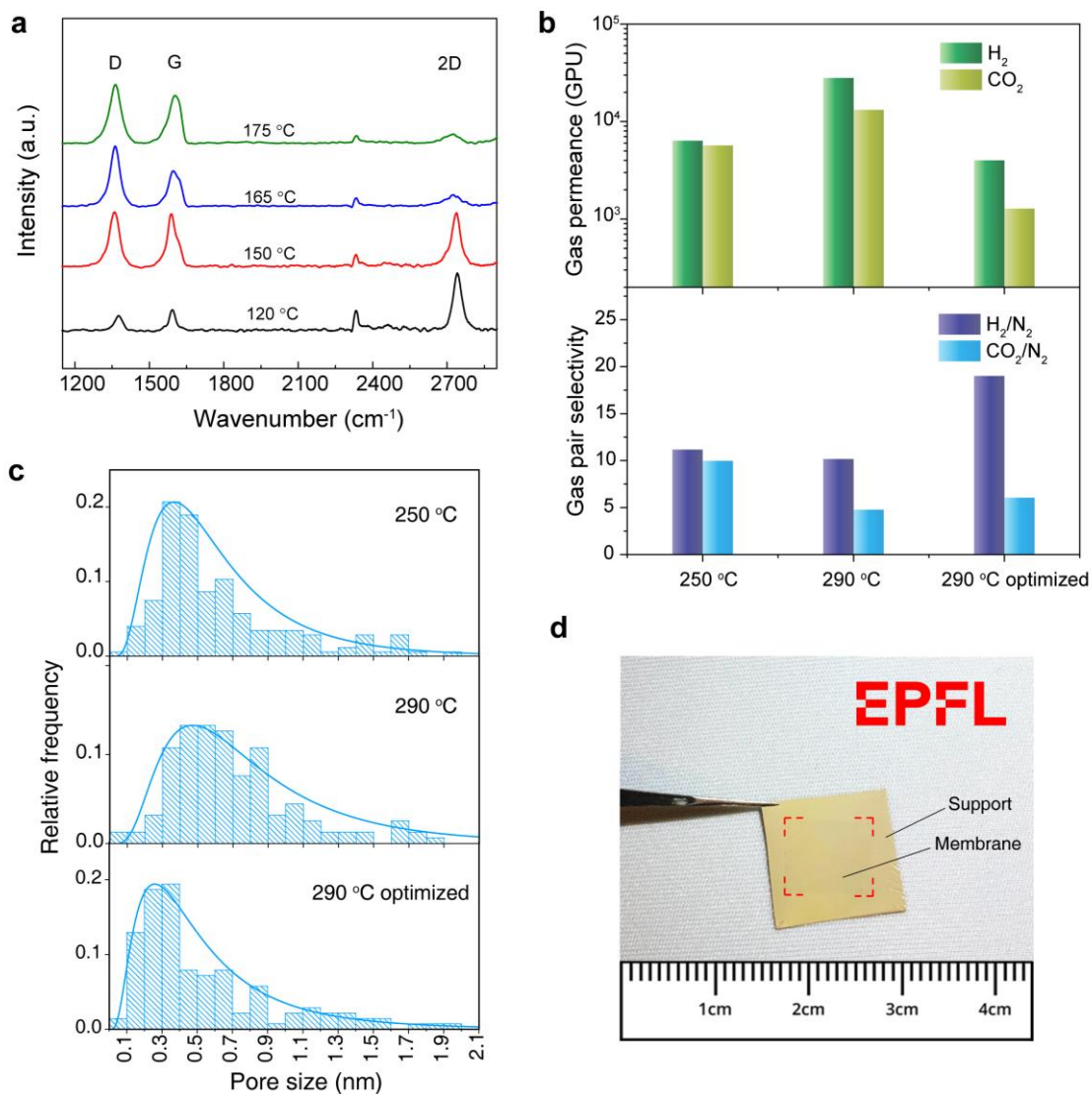
Figure 3.19 a) Raman spectra of N-SLG etched by MGR at 120 – 175 ºC revealing increasing defect density at a function of temperature. CO_2 permeances. Comparison of the gas separation performance of N-SLG etched at 250 and 290 ºC b), and the corresponding PSD extracted from HRTEM (c). t_d was 0.5 s for the 250 and 290 ºC cases (using Ar) and 0.2 s for the optimized 290 ºC case (using the He purge). d) Photograph of the centimeter-scale N-SLG membrane on the smoothened metal-mesh support. Red lines highlight the edges of the membrane.

3.5 Shift molecular cut-off of N-SLG by slow oxygen expansion

Molecular-sieving from N-SLG has a unique advantage that one can adjust the molecular cut-off for a specific separation application. We demonstrate this by expanding vacancy defects using O_2 at 200 ºC in-situ in the membrane module. Briefly, the feed side of N-SLG membrane pre-etched in MGR was pressurized with CO_2/N_2 mixture while the permeate side was swept with Ar, and a steady-state operation was achieved. To initiate the etching, the sweep gas was switched to O_2. Subsequently, the partial pressure of CO_2 and N_2 in the permeate side was tracked as a function of time using an online mass spectrometer. After the reaction, the sweep was switched back to Ar to measure the gas permeance.
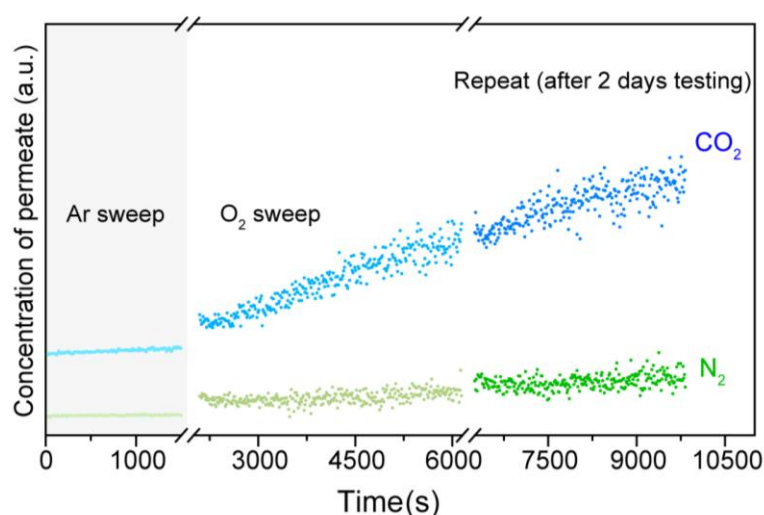
Figure 3.20 Gas separation performance of N-SLG prepared by MGR followed by in-situ O_2 etching at 200 ºC, CO_2 and N_2 evolution in the permeate side during the in-situ etching.

Upon O_2 exposure at 200 ºC, CO_2 and N_2 concentrations in the permeate side increased as a function of time (**Figure 3.20**). However, the increase in the CO_2 concentration was much more rapid which resulted in the improvement of CO_2 permeance as well as CO_2/N_2 selectivity (**Figure 3.21**). The improvement in the performance was permanent and could be observed after several cycles of testing over several days. Repeating O_2-based pore expansion, on the same N-SLG after several days, led to further improvement in permeance while the selectivity did not change considerably (**Figure 3.21**, **Table 3.5**). The pore expansion was confirmed by the reduced apparent activation energy

of all gas molecules (2 kJ mol^{-1} for H_2, and 4 kJ mol^{-1} for other gases, **Figure 3.22**).
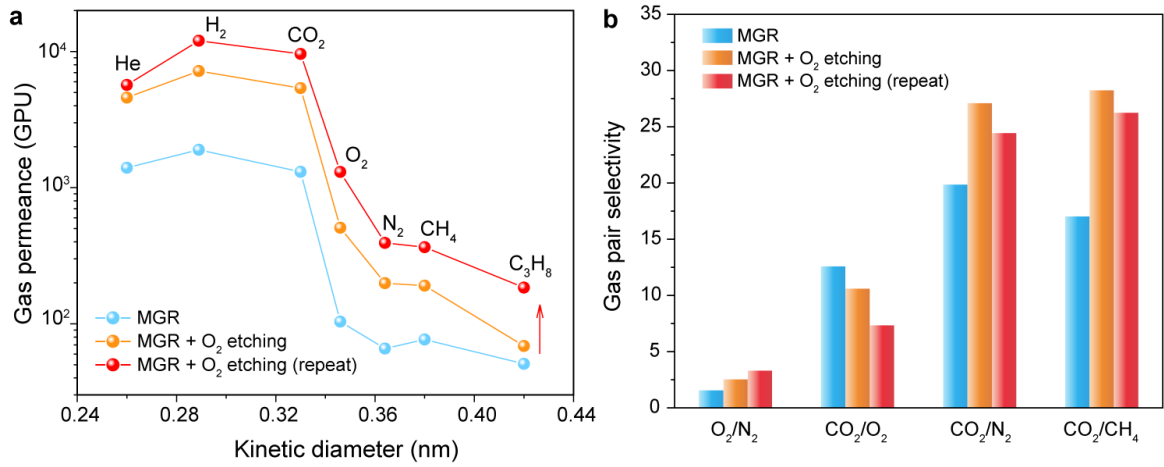
Figure 3.21 Gas permeance as a function of kinetic diameter revealing molecular cut-off a), and the corresponding gas pair selectivities b) before and after the in-situ etching. The term 'repeat' refers to repeating the in-situ etching after two days of gas permeance testing.

The etching rate of graphene with O_2 can be estimated based on the kinetics of oxygen etching on graphite. As known, it is a first-order reaction, the etching rate is proportional to the concentration of O_2[69]. Therefore,

$$\frac{dr}{dt} = k_{O_2} P_{O_2} \tag{3.25}$$

Where k_{O_2} is the rate constant of etching, P_{O_2} is oxygen pressure.

The rate constant of the oxygen etching would follow Arrhenius law, depended on the reaction temperature

$$k_{O_2} = A_{O_2} \exp\left(\frac{-E_{\text{act-}O_2}}{RT}\right) \tag{3.26}$$

Where A_{O_2} is the pre-exponential factor, and $E_{\text{act-}O_2}$ is the activation energy for the oxygen etching reaction. The activation energy could be estimated as 102.4 kJ mol^{-1} by using the temperature-depended data reported by Rabe and co-workers at O_2 pressure of 760 Torr[59].

$$\frac{dr}{dt}\Big|_{T=723K} = 1 \text{ nm min}^{-1} \qquad \frac{dr}{dt}\Big|_{T=643K} = 0.12 \text{ nm min}^{-1}$$

Another set of oxygen data from an independent study was chosen to exam the accuracy of the activation energy and pre-factor. It is reported the etching rate is 6.14 nm min^{-1} at 923 K and P_{O_2} of 0.2 bar in the literature.[180] Consistently, the calculated etching rate based on the estimated activation energy and pre-factor is 7.6 nm min^{-1} for that condiction, indicating the estimation of etching rate is reasonable.
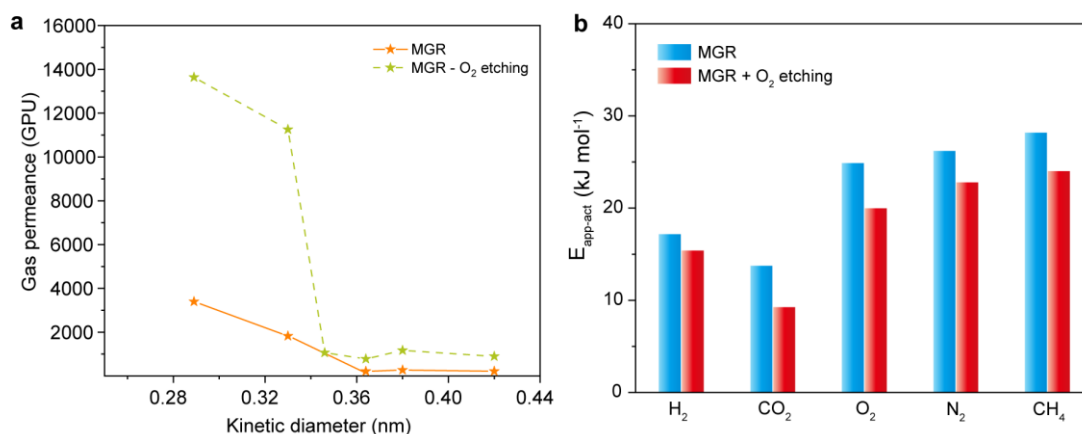
Figure 3.22 a) Gas permeance of N-SLG membrane prepared by MGR at 250 °C and further oxygen etching 1 h at 200 °C, as a function of gas kinetic diameters. b) The apparent activation energy of the N-SLG membrane before and after the in-situ etching for 2 h.

Hence, we predict the pore expansion rate constant 200 °C to be 1.6×10^{-7} nm min^{-1} Torr^{-1} based on the parameters we obtained. As a result, the etching rate at our in-situ oxygen etching experiment would be 0.07 Å h^{-1}. Therefore, for 1 h oxygen post-treatment, the expected pore diameter change is 0.14 Å h^{-1}, consistent with our finding on the adjustment of the molecular cut-off. As a result, the pore expansion for 1-2 h favored O_2 permeation, reducing CO_2/O_2 selectivity from 12.6 to 7.4, and increasing O_2/N_2 selectivity from 1.6 to 3.4 (**Figure 3.21b and Figure 3.22a**). Combined with O_2 permeance of 1300 GPU, it makes N-SLG membranes attractive for the decentralized O_2/N_2 separation for enriching O_2[5]. In the context of post-combustion capture, the shifted cut-off allowed us to realize extremely attractive CO_2/N_2 separation performance with CO_2 permeance and CO_2/N_2 selectivity of 9600 GPU and 24.4, respectively (**Figure 3.23** and **Table 3.6**). Another membrane yielded CO_2 permeance of 11850 GPU and CO_2/N_2 selectivity of 21.7. The attractive separation performance of N-SLG membranes reach the target area of the carbon capture, establishing the nanoporous graphene as a promising membrane for post-

combustion carbon capture.
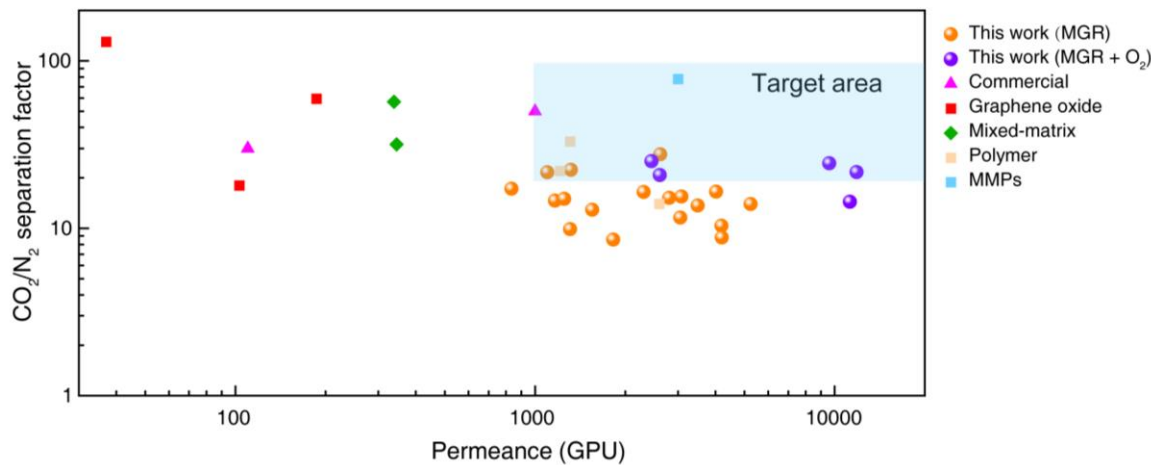
Figure 3.23 Comparison of the CO_2/N_2 mixture separation performance from the N-SLG membranes with that from the state-of-the-art membranes for post-combustion capture. The target area refers to membrane performance needed to surpass the energy-efficiency of amine-based absorption process[1553]. MMPs refers to metal-induced ordered microporous polymers.

Table 3.5-1 Gas permeance of an N-SLG membrane before and after oxygen etching at 200 ºC. Membrane was prepared in MGR using ozone dose of 1.6×10^{17} molecules cm-3 s at 250 °C (τ = 0.1 s, Pup = 3 bar, Ar purge delay = 0.5 s). Slow oxygen etching was carried out after characterizing the membrane by gas permeance.

Gas	As-prepared membrane using MGR			After 1 h O_2 etching
	Permeance (mol m^{-2} s^{-1} Pa^{-1})			Permeance (mol m^{-2} s^{-1} Pa^{-1})
	100 °C	50 °C	25 °C	25 °C
He	3.9×10^{-6}	1.8×10^{-6}	8.3×10^{-7}	2.4×10^{-6}
H_2	4.6×10^{-6}	2.7×10^{-6}	1.1×10^{-6}	4.6×10^{-6}
CO_2	1.9×10^{-6}	1.3×10^{-6}	6.1×10^{-7}	3.8×10^{-6}
O_2				3.6×10^{-7}
N_2	3.0×10^{-7}	1.4×10^{-7}	7.1×10^{-8}	2.6×10^{-7}
CH_4	3.9×10^{-7}	1.9×10^{-7}	9.2×10^{-8}	3.9×10^{-7}
C_3H_8	2.6×10^{-7}	1.3×10^{-7}	7.2×10^{-8}	

Table 3.5-2 Gas permeance of the second N-SLG membrane (prepared in the same way as listed in Table 3.5-1) before and after oxygen etching at 200 ºC.

Gas	As-prepared membrane using MGR			After 2 h O$_2$ etching		
	Permeance (mol m^{-2} s^{-1} Pa^{-1})			Permeance (mol m^{-2} s^{-1} Pa^{-1})		
	100 °C	50 °C	25 °C	100 °C	50 °C	25 °C
He	1.5×10^{-6}	5.7×10^{-7}	2.6×10^{-7}	2.1×10^{-6}	1.0×10^{-6}	4.4×10^{-7}
H$_2$	1.7×10^{-6}	8.7×10^{-7}	4.2×10^{-7}	3.5×10^{-6}	2.0×10^{-6}	9.8×10^{-7}
CO$_2$	8.8×10^{-7}	5.4×10^{-7}	2.8×10^{-7}	1.9×10^{-6}	1.5×10^{-6}	8.7×10^{-7}
O$_2$	2.8×10^{-7}	8.3×10^{-8}	3.6×10^{-8}	5.7×10^{-7}	2.4×10^{-7}	1.1×10^{-7}
N$_2$	1.4×10^{-7}	3.7×10^{-8}	1.6×10^{-8}	2.7×10^{-7}	1.0×10^{-7}	4.2×10^{-8}
CH$_4$	1.8×10^{-7}	5.2×10^{-8}	1.8×10^{-8}	3.3×10^{-7}	1.2×10^{-7}	4.5×10^{-8}

Table 3.5-3 Gas permeance of the third N-SLG membrane (prepared in the same way as listed in Table 3.5-1) before and after oxygen etching at 200 ºC.

Gas	As-prepared membrane using MGR			After 1 h O$_2$ etching
	Permeance (mol m^{-2} s^{-1} Pa^{-1})			Permeance (mol m^{-2} s^{-1} Pa^{-1})
	100 °C	50 °C	25 °C	25 °C
He	3.7×10^{-6}	1.5×10^{-6}	6.2×10^{-7}	1.4×10^{-6}
H$_2$	5.3×10^{-6}	2.2×10^{-6}	8.7×10^{-7}	3.8×10^{-6}
CO$_2$	2.9×10^{-6}	1.5×10^{-6}	7.7×10^{-7}	4.0×10^{-6}
O$_2$	7.8×10^{-7}	2.3×10^{-7}	1.0×10^{-7}	4.1×10^{-7}
N$_2$	4.4×10^{-7}	1.1×10^{-7}	4.7×10^{-8}	1.8×10^{-7}
CH$_4$	6.3×10^{-7}	1.5×10^{-7}	5.3×10^{-8}	2.5×10^{-7}

Table 3.5-4 Gas permeance of the fourth N-SLG membrane (prepared in the same way as listed in Table 3.5-1) before and after oxygen etching at 200 ºC.

Gas	As-prepared membrane using MGR			After 1 h O_2 etching
	Permeance (mol m^{-2} s^{-1} Pa^{-1})			Permeance (mol m^{-2} s^{-1} Pa^{-1})
	100 °C	50 °C	25 °C	25 °C
He	2.2×10^{-6}	6.3×10^{-7}	2.8×10^{-7}	5.7×10^{-7}
H_2	2.8×10^{-6}	1.1×10^{-6}	4.8×10^{-7}	8.9×10^{-7}
CO_2	1.6×10^{-6}	7.1×10^{-7}	3.7×10^{-7}	8.2×10^{-7}
O_2	4.4×10^{-7}	1.1×10^{-7}	4.5×10^{-8}	9.9×10^{-8}
N_2	1.9×10^{-7}	3.7×10^{-8}	1.7×10^{-8}	3.3×10^{-8}
CH_4	2.6×10^{-7}	4.3×10^{-8}	1.6×10^{-8}	3.9×10^{-8}

Table 3.6 Comparison of the CO_2/N_2 mixture separation performance from the N-SLG membranes prepared in this work with the state-of-the-art membranes.

Membrane type	Membrane description	CO_2 Permeance (GPU)	CO_2/N_2 selectivity	Reference
Commercial membrane	Celluose acetate	110	30	[3]
	Polaris®	1000	50	[3]
Graphene oxide (GO) membranes	GO with PEGBA$^{\$}$	186.3	59.4	[181]
	GO with ionic liquid	37	130	[182]
	GO	103	18	[10]
Facilitated transport membranes	Piperazine in GO	1020	680	[183]
	Enzymatic solution	2600	788	[184]
	Polyvinylamine	1827	500	[185]
Mixed matrix membranes	UiO-66-NH$_2$ in PEBAX®	338	57	[186]
	ZIF-8 in PEBAX®	345	31.7	[187]
	GO in thermally-reduced (TR) polymer	1784	17.7*	[188]
Polymeric membranes	PEG/PDMS $^{\$}$	1210	22	[189]
	PEG/NH$_2$-MIL-53 $^{\$}$	2600	14	[190]
	DAmPEG-TMC $^{\$}$	1310	33	[191]
	Pebax2533®/PEG-b-PPFPA $^{\$}$	3330	22*	[192]
	TR polymer	1938	13*	[193]
Hybrid membrane	Metal-induced ordered microporous polymers (MMPs)	3000	78	[194]
N-SLG membranes (MGR at 250 °C)	$\tau = 0.1$ s, $P_{up} = 3$ bar, $t_d = 0.5$ s	2600	27.6	
	$\tau = 0.2$ s, $P_{up} = 3$ bar, $t_d = 0.5$ s	4000	16.5	
	$\tau = 0.1$ s, $P_{up} = 3$ bar, $t_d = 0.5$ s $^{\#}$	1300	9.9	
	$\tau = 0.2$ s, $P_{up} = 5$ bar, $t_d = 0.2$ s	3050	11.6	
	$\tau = 0.1$ s, $P_{up} = 5$ bar, $t_d = 0.5$ s	3100	15.5	

	$\tau = 0.2$ s, $P_{up} = 5$ bar, $t_d = 0$ s	4200	10.4	
	$\tau = 0.1$ s, $P_{up} = 3$ bar, $t_d = 0$ s	2800	15.2	
	$\tau = 0.1$ s, $P_{up} = 3$ bar, $t_d = 0$ s	1150	14.6	
	$\tau = 0.1$ s, $P_{up} = 5$ bar, $t_d = 0$ s	5250	14.0	
	$\tau = 0.05$ s, $P_{up} = 5$ bar, $t_d = 0.5$ s	4200	8.8	
	$\tau = 0.05$ s, $P_{up} = 5$ bar, $t_d = 0.2$ s [§]	1550	12.9	
	$\tau = 0.2$ s, $P_{up} = 3$ bar, $t_d = 0.5$ s	1300	22.4	
	$\tau = 0.1$ s, $P_{up} = 3$ bar, $t_d = 0.5$ s	1800	8.6	
	$\tau = 0.1$ s, $P_{up} = 3$ bar, $t_d = 0.5$ s	850	17.2	This work
	$\tau = 0.1$ s, $P_{up} = 3$ bar, $t_d = 0.5$ s	2300	16.5	
	$\tau = 0.1$ s, $P_{up} = 3$ bar, $t_d = 0.5$ s	1100	21.6	
N-SLG membranes (MGR at 290 °C)	$\tau = 0.05$ s, $P_{up} = 5$ bar, $t_d = 0.5$ s	4200	8.8	
	$\tau = 0.1$ s, $P_{up} = 5$ bar, $t_d = 0.2$ s [§]	3500	13.7	
	$\tau = 0.1$ s, $P_{up} = 5$ bar, $t_d = 0.2$ s [§]	1250	15.0	
N-SLG membranes (MGR at 250 °C + oxygen etching at 200 °C)	MGR ($\tau = 0.2$ s, $P_{up} = 3$ bar, $t_d = 0.5$ s) + O$_2$ etching (2 h)	9600	24.4	
	MGR ($\tau = 0.1$ s, $P_{up} = 3$ bar, $t_d = 0.5$ s) + O$_2$ etching (1 h)	11250	14.4	
	MGR ($\tau = 0.1$ s, $P_{up} = 3$ bar, $t_d = 0.5$ s) + O$_2$ etching (2 h)	2600	20.8	
	MGR ($\tau = 0.1$ s, $P_{up} = 3$ bar, $t_d = 0.5$ s) + O$_2$ etching (1 h)	11850	21.7	
	MGR ($\tau = 0.1$ s, $P_{up} = 3$ bar, $t_d = 0.5$ s) + O$_2$ etching (1 h)	2450	25.2	

[§] PEGBA refers to poly(ethylene glycol) bis(amine). PEG/PDMS refers to poly(ethylene glycol) / polydimethylsiloxane. DAmPEG-TMC refers to diaminopolyethylene glycol - trimesoyl chloride.

[*] Ideal selectivity.

[§] Cooled He purge instead of Ar purge.

[#] Ozone was preheated.

Mixture separation performance revealed the competitive adsorption of the gases on the membrane, displaying the closest performance of the practical separation. In our case, the 20% CO_2 and 80 % N_2 mixture was used as feed to probe the mixture separation performance of N-SLG membrane at different temperatures. At each temperature, then-SLG membrane exhibited similar gas permeance in the mixture and single-component tests. Moreover, CO_2/N_2 separation performance was similar to that from the single component with the mixture separation factor slightly higher than the corresponding ideal selectivity (**Figure 3.24**), which can be attributed to competitive adsorption of CO_2 over N_2.
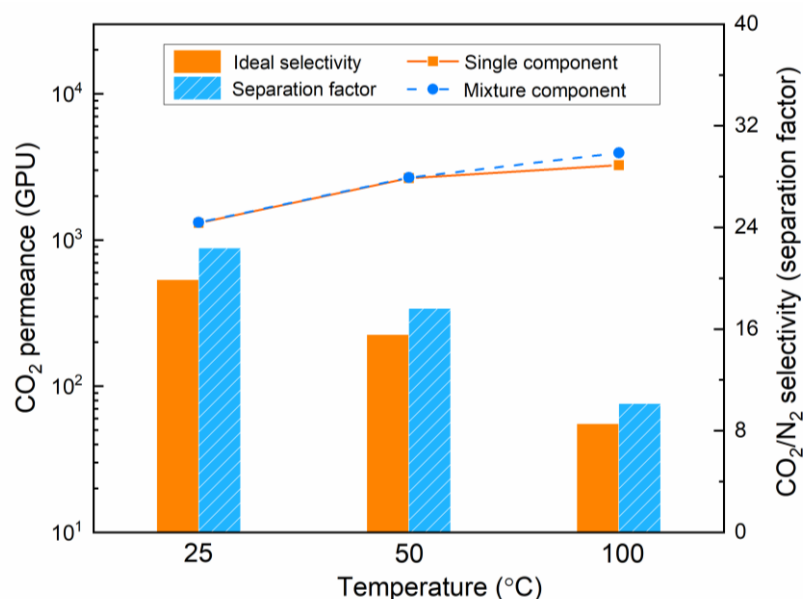
Figure 3.24 Comparison of graphene membrane performance in the single-component and mixed-gas (20% CO_2, 80% N_2) permeation tests.

4. Conclusion

Overall, we report a scalable lattice gasification technique bringing two critical components of the lattice etching kinetics; (i) the use of high temperature to promote rapid chemisorption of O_3 on graphene leading to a high density ($>10^{12}$ cm^{-2}) of functional-oxygen-clusters which eventually nucleate the vacancy defects, and (ii) millisecond reaction time that limits the expansion of vacancy defects to yield CO_2-sieving nanopores with a resolution of 0.2-0.3 Å in molecular differentiation. The in situ pore expansion experiments demonstrate that the graphene nanopore presents a unique opportunity to shift the molecular cutoff by a fraction of angstrom. Both gasification and pore expansion techniques are highly predictable and reproducible, which will pave the way to fabricate nanopores in single-layer graphene for separating several species based on the relative differences in size, even if the size difference is much smaller than 1 Å including isotope purification[99], ion-ion separation[195], and organic solvent nanofiltration.[196] The method demonstrated here takes one to a step closer in achieving the target of incorporating vacancy defects in graphene with the precision of a few atoms, a major goal of material science and chemistry.

Appendix I

Table 3.7 Gas permeance of N-SLG membranes obtained with increasing ozone dose at 250 °C in MGR. No purge was used.

Gas	Ozone dose = 4.8×10^{16} molecules cm^{-3} s * (τ = 0.01 s, P$_{up}$ = 3 bar) Permeance (mol m^{-2} s^{-1} Pa^{-1})			Ozone dose = 1.2×10^{17} molecules cm^{-3} s (τ = 0.05 s, P$_{up}$ = 3 bar) Permeance (mol m^{-2} s^{-1} Pa^{-1})		
	150 °C	**100 °C**	**25 °C**	**100 °C**	**50 °C**	**25 °C**
H$_2$	4.3×10^{-7}	2.5×10^{-7}	5.0×10^{-8}	1.8×10^{-6}	6.4×10^{-7}	3.5×10^{-7}
CO$_2$	1.6×10^{-7}	1.1×10^{-7}	4.0×10^{-8}	1.1×10^{-6}	4.7×10^{-7}	2.8×10^{-7}
CH$_4$	3.3×10^{-8}	1.6×10^{-8}	$2.7\times10^{-9**}$	2.2×10^{-7}	4.3×10^{-8}	1.7×10^{-8}

Gas	Ozone dose = 2.2×10^{17} molecules cm^{-3} s (τ = 0.1 s, P$_{up}$ = 3 bar) Permeance (mol m^{-2} s^{-1} Pa^{-1})			Ozone dose = 3.5×10^{17} molecules cm^{-3} s (τ = 0.2 s, P$_{up}$ = 3 bar) Permeance (mol m^{-2} s^{-1} Pa^{-1})		
	150 °C	**100 °C**	**25 °C**	**100 °C**	**50 °C**	**25 °C**
H$_2$	5.7×10^{-6}	2.4×10^{-6}	1.4×10^{-6}	8.1×10^{-6}	3.4×10^{-6}	1.8×10^{-6}
CO$_2$	2.0×10^{-6}	1.1×10^{-6}	8.5×10^{-7}	3.8×10^{-6}	1.7×10^{-6}	1.1×10^{-6}
CH$_4$	7.2×10^{-7}	2.1×10^{-7}	1.1×10^{-7}	1.4×10^{-6}	3.3×10^{-7}	1.8×10^{-7}

* Data obtained by mixture-component test.

** The permeance of CH$_4$ was based on H$_2$/CH$_4$ mixture, the CH$_4$ permeance based on CO$_2$/CH$_4$ is 2.2×10^{-9} mol m^{-2} s^{-1} Pa^{-1}.

Table 3.8-1 Gas permeance of two N-SLG membranes prepared with ozone dose of 3.2×10^{16} molecules cm^{-3} s at 250 °C with Ar purge (τ = 0.1 s, P_{up} = 3 bar, t_d = 0 s).

Gas	Permeance (mol m^{-2} s^{-1} Pa^{-1})			Permeance (mol m^{-2} s^{-1} Pa^{-1})		
	100 °C	50 °C	25 °C	100 °C	50 °C	25 °C
H_2	4.4×10^{-6}	2.4×10^{-6}	9.6×10^{-7}	2.8×10^{-6}	1.2×10^{-6}	4.4×10^{-7}
CO_2	2.5×10^{-6}	1.8×10^{-6}	9.4×10^{-7}	1.5×10^{-6}	8.7×10^{-7}	3.9×10^{-7}
N_2	3.5×10^{-7}	1.4×10^{-7}	6.2×10^{-8}	2.1×10^{-7}	6.3×10^{-8}	2.7×10^{-8}
CH_4	5.2×10^{-7}	2.2×10^{-7}	8.8×10^{-8}	3.3×10^{-7}	9.5×10^{-8}	3.6×10^{-8}

Table 3.8-2 Gas permeance of three N-SLG membranes prepared with ozone dose of 1.6×10^{17} molecules cm^{-3} s at 250 °C with Ar purge (τ = 0.1 s, P_{up} = 3 bar, t_d = 0.5 s).

Gas	Permeance (mol m^{-2} s^{-1} Pa^{-1})			Permeance (mol m^{-2} s^{-1} Pa^{-1})		
	100 °C	50 °C	25 °C	100 °C	50 °C	25 °C
H_2	1.7×10^{-6}	9.7×10^{-7}	4.0×10^{-7}	6.1×10^{-6}	3.3×10^{-6}	1.6×10^{-6}
CO_2	1.1×10^{-6}	8.3×10^{-7}	4.0×10^{-7}	3.5×10^{-6}	2.7×10^{-6}	1.7×10^{-6}
N_2						
CH_4	1.6×10^{-7}	6.7×10^{-8}	2.1×10^{-8}	8.1×10^{-7}	3.3×10^{-7}	1.4×10^{-7}

Gas	Permeance (mol m^{-2} s^{-1} Pa^{-1})		
	100 °C	50 °C	25 °C
H_2	2.1×10^{-6}	1.2×10^{-6}	5.5×10^{-7}
CO_2	1.9×10^{-6}	1.4×10^{-6}	8.8×10^{-7}
N_2	1.9×10^{-7}	7.7×10^{-8}	3.2×10^{-8}
CH_4	2.7×10^{-7}	1.2×10^{-7}	4.4×10^{-8}

Table 3.8-3 Gas permeance of two N-SLG membranes prepared with ozone dose of 2.0×10^{17} molecules cm^{-3} s at 250 °C with Ar purge (τ = 0.1 s, P_{up} = 3 bar, t_d = 1.0 s).

Gas	Permeance (mol m^{-2} s^{-1} Pa^{-1})			Permeance (mol m^{-2} s^{-1} Pa^{-1})		
	100 °C	50 °C	25 °C	100 °C	50 °C	25 °C
H_2	5.7×10^{-6}	2.8×10^{-6}	1.4×10^{-6}	4.1×10^{-6}	1.4×10^{-6}	6.4×10^{-7}
CO_2	3.0×10^{-6}	1.9×10^{-6}	1.1×10^{-6}	2.0×10^{-6}	8.2×10^{-7}	4.7×10^{-7}
CH_4	5.8×10^{-7}	2.0×10^{-7}	7.5×10^{-8}	6.2×10^{-7}	1.3×10^{-7}	5.0×10^{-8}

Table 3.9 Gas permeance of two N-SLG membranes prepared with ozone dose of 1.8×10^{17} molecules cm^{-3} s at 290 °C with Ar purge ($\tau = 0.05$ s, $P_{up} = 5$ bar, $t_d = 0.5$ s).

Gas	Permeance (mol m^{-2} s^{-1} Pa^{-1})			Permeance (mol m^{-2} s^{-1} Pa^{-1})	
	100 °C	50 °C	25 °C	100 °C	25 °C
H$_2$	9.4×10^{-6}	3.7×10^{-6}	2.2×10^{-6}	6.5×10^{-6}	1.9×10^{-6}
CO$_2$	4.4×10^{-6}	2.1×10^{-6}	1.4×10^{-6}	3.0×10^{-6}	
N$_2$	9.2×10^{-7}	2.5×10^{-7}	1.6×10^{-7}	6.1×10^{-7}	1.4×10^{-7}
CH$_4$	1.4×10^{-6}	3.6×10^{-7}	2.2×10^{-7}	9.3×10^{-7}	1.9×10^{-7}

Table 3.10-1 Gas permeance of an N-SLG membrane prepared by MGR before slow pore expansion by oxygen. MGR was operated using ozone dose of 2.7×10^{17} molecules cm^{-3} s at 250 °C with Ar purge ($\tau = 0.2$ s, $P_{up} = 3$ bar, $t_d = 0.5$ s).

Gas	Permeance (mol m^{-2} s^{-1} Pa^{-1})		
	100 °C	50 °C	25 °C
He	2.4×10^{-6}	1.1×10^{-6}	4.7×10^{-7}
H$_2$	2.8×10^{-6}	1.6×10^{-6}	6.4×10^{-7}
CO$_2$	1.1×10^{-6}	8.9×10^{-7}	4.4×10^{-7}
O$_2$			3.5×10^{-8}
N$_2$	1.3×10^{-7}	5.7×10^{-8}	2.2×10^{-8}
CH$_4$	1.6×10^{-7}	7.1×10^{-8}	2.6×10^{-8}
C$_3$H$_8$	8.9×10^{-8}	4.0×10^{-8}	1.8×10^{-8}

Table 3.10-2 Gas permeance of an N-SLG membrane shown above (Table 3.10-1) after slow oxygen etching at 200 ºC for 1 and 2 h.

Gas	After 1 h O$_2$ etching	After 2 h O$_2$ etching
	Permeance (mol m^{-2} s^{-1} Pa^{-1})	Permeance (mol m^{-2} s^{-1} Pa^{-1})
	25 °C	25 °C
He	1.5×10^{-6}	1.9×10^{-6}
H$_2$	2.4×10^{-6}	4.0×10^{-6}
CO$_2$	1.8×10^{-6}	3.2×10^{-6}
O$_2$	1.7×10^{-7}	4.4×10^{-7}
N$_2$	6.7×10^{-8}	1.3×10^{-7}
CH$_4$	6.4×10^{-8}	1.2×10^{-7}
C$_3$H$_8$	2.3×10^{-8}	6.2×10^{-8}

**Table 3.11** Temporal evolution data from the kinetic model.

Time t_i (s)	Ozone pressure (Torr)	N_i (cm^{-2})	ΔC_i (atom cm^{-2})	$\Delta C_i / \sum N_i$ (atoms/defect)	$v_i^{t_n}$ (atoms/defect)
0.00	0.00	0	0	0.00	0.00
0.11	0.00	0	0	0.00	0.00
0.12	1.81	2.94×10^9	3.03×10^{10}	10.29	35.64
0.13	3.57	8.71×10^9	7.19×10^{10}	6.17	25.34
0.14	5.26	1.43×10^{10}	9.15×10^{10}	3.53	19.17
0.15	6.90	1.97×10^{10}	1.07×10^{11}	2.34	15.64
0.16	8.48	2.49×10^{10}	1.19×10^{11}	1.69	13.31
0.17	10.01	3.00×10^{10}	1.30×10^{11}	1.29	11.62
0.18	11.49	3.48×10^{10}	1.40×10^{11}	1.03	10.32
0.19	12.92	3.96×10^{10}	1.48×10^{11}	0.85	9.29
0.20	14.31	4.41×10^{10}	1.56×10^{11}	0.71	8.44
0.21	15.64	4.85×10^{10}	1.63×10^{11}	0.61	7.73
0.22	15.28	5.01×10^{10}	1.66×10^{11}	0.52	7.12
0.23	14.90	4.89×10^{10}	1.64×10^{11}	0.45	6.60
0.24	14.54	4.77×10^{10}	1.62×10^{11}	0.39	6.15
0.25	14.18	4.65×10^{10}	1.60×10^{11}	0.35	5.76
0.26	13.84	4.54×10^{10}	1.58×10^{11}	0.31	5.41
0.27	13.50	4.43×10^{10}	1.56×10^{11}	0.28	5.10
0.28	13.17	4.32×10^{10}	1.55×10^{11}	0.26	4.82
0.29	12.84	4.21×10^{10}	1.53×10^{11}	0.24	4.56
0.30	12.53	4.11×10^{10}	1.51×10^{11}	0.22	4.32
0.31	12.22	4.01×10^{10}	1.49×10^{11}	0.21	4.09
0.32	11.92	3.91×10^{10}	1.48×10^{11}	0.20	3.88
0.33	11.63	3.82×10^{10}	1.46×10^{11}	0.18	3.69
0.34	11.35	3.72×10^{10}	1.44×10^{11}	0.17	3.50
0.35	11.07	3.63×10^{10}	1.43×10^{11}	0.16	3.33
0.36	10.80	3.54×10^{10}	1.41×10^{11}	0.16	3.17
0.37	10.53	3.46×10^{10}	1.39×10^{11}	0.15	3.01
0.38	10.28	3.37×10^{10}	1.38×10^{11}	0.14	2.86
0.39	10.03	3.29×10^{10}	1.36×10^{11}	0.14	2.72
0.40	9.78	3.21×10^{10}	1.34×10^{11}	0.13	2.59
0.41	9.54	3.13×10^{10}	1.33×10^{11}	0.12	2.46
0.42	9.31	3.05×10^{10}	1.31×10^{11}	0.12	2.33
0.43	9.08	2.98×10^{10}	1.30×10^{11}	0.12	2.21
0.44	8.86	2.91×10^{10}	1.28×10^{11}	0.11	2.10
0.45	8.64	2.83×10^{10}	1.27×10^{11}	0.11	1.99
0.46	8.43	2.77×10^{10}	1.25×10^{11}	0.10	1.88
0.47	8.22	2.70×10^{10}	1.24×10^{11}	0.10	1.78
0.48	8.02	2.63×10^{10}	1.22×10^{11}	0.10	1.68
0.49	7.83	2.57×10^{10}	1.21×10^{11}	0.09	1.58
0.50	7.63	2.50×10^{10}	1.20×10^{11}	0.09	1.49
0.51	7.45	2.44×10^{10}	1.18×10^{11}	0.09	1.39

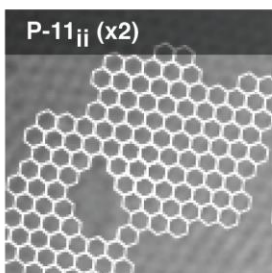| 0.52	7.26	2.38×10^{10}	1.17×10^{11}	0.09	1.31
0.53	7.09	2.33×10^{10}	1.16×10^{11}	0.08	1.22
0.54	6.91	2.27×10^{10}	1.14×10^{11}	0.08	1.14
0.55	6.74	2.21×10^{10}	1.13×10^{11}	0.08	1.06
0.56	6.58	2.16×10^{10}	1.12×10^{11}	0.08	0.98
0.57	6.42	2.11×10^{10}	1.10×10^{11}	0.07	0.90
0.58	6.26	2.05×10^{10}	1.09×10^{11}	0.07	0.83
0.59	6.11	2.00×10^{10}	1.08×10^{11}	0.07	0.75
0.60	5.96	1.95×10^{10}	1.07×10^{11}	0.07	0.68
0.61	5.81	1.91×10^{10}	1.05×10^{11}	0.07	0.61
0.62	5.67	1.86×10^{10}	1.04×10^{11}	0.07	0.55
0.63	5.53	1.81×10^{10}	1.03×10^{11}	0.06	0.48
0.64	5.40	1.77×10^{10}	1.02×10^{11}	0.06	0.41
0.65	5.26	1.73×10^{10}	1.01×10^{11}	0.06	0.35
0.66	5.14	1.68×10^{10}	9.93×10^{10}	0.06	0.29
0.67	5.01	1.64×10^{10}	9.82×10^{10}	0.06	0.23
0.68	4.89	1.60×10^{10}	9.71×10^{10}	0.06	0.17
0.69	4.77	1.56×10^{10}	9.59×10^{10}	0.06	0.11
0.70	4.65	1.53×10^{10}	9.48×10^{10}	0.06	0.06
0.71	4.54	1.49×10^{10}	0	0.00	0.00

Appendix II

Figure 3.25 AC-HRTEM images and lattice fitting based library of the nanopores with 1- 20 missing carbon atoms on N-SLG prepared with O_3 dose of 1.6×10^{17} molecules cm^{-3} s ($\tau = 0.1$ s, $t_d = 0.5$ s) at 250 ºC.
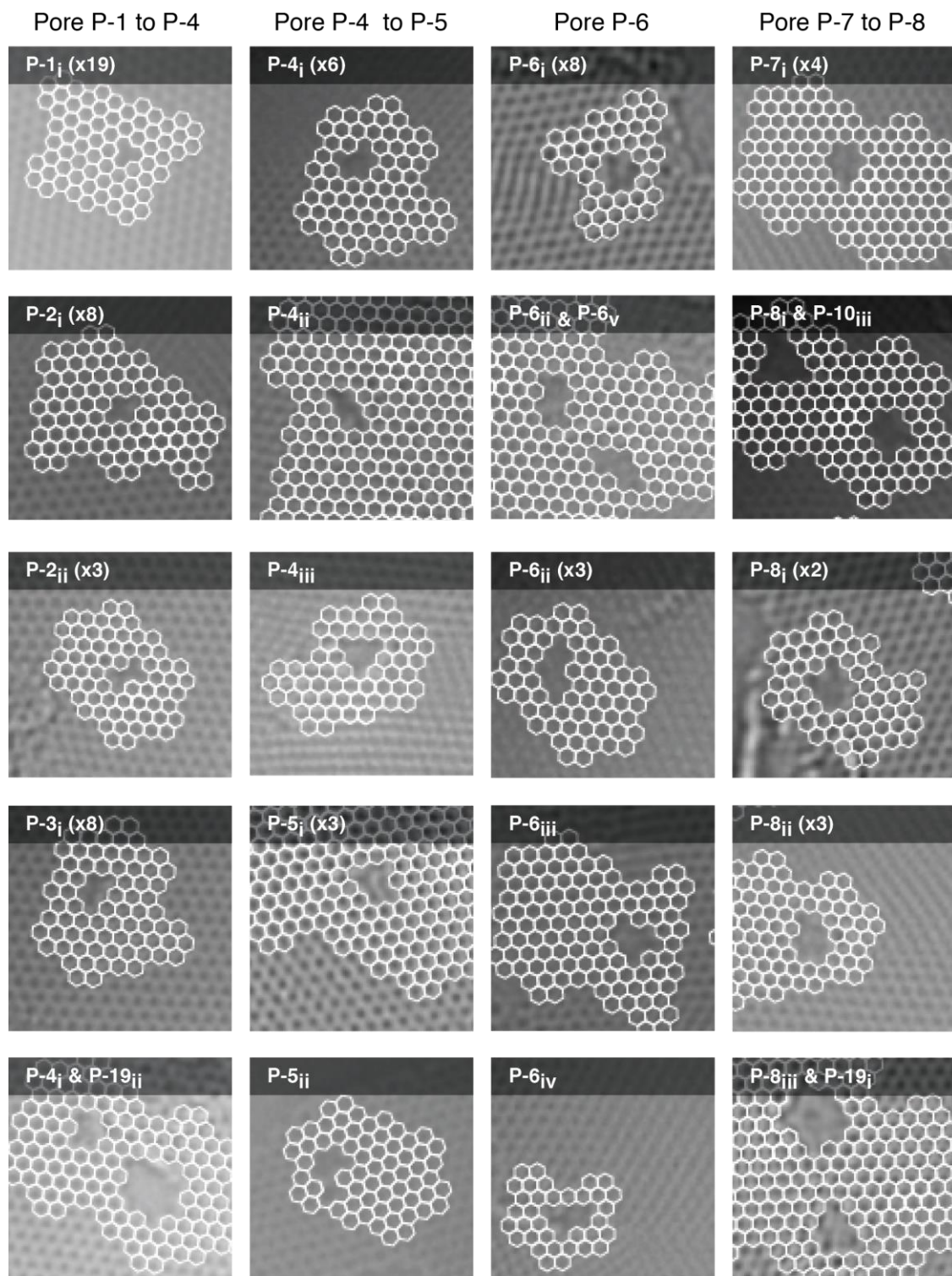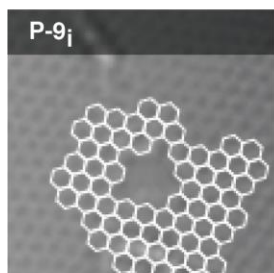
Pore P-9 to P-11	Pore P-11 to P-13	Pore P-13 to P-15	Pore P-16 to P-17
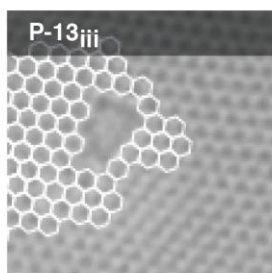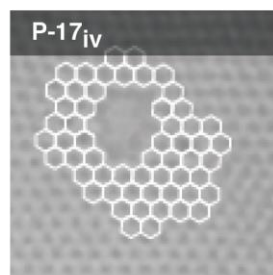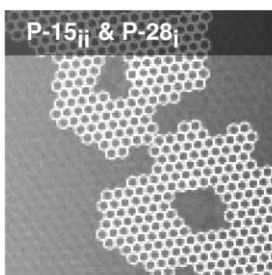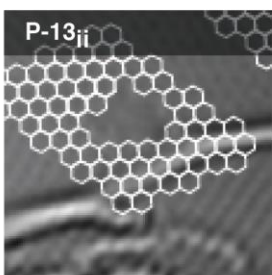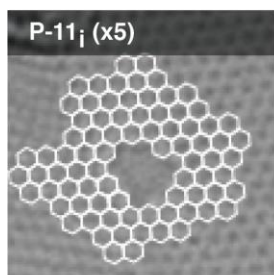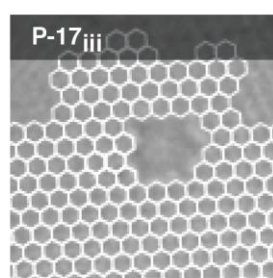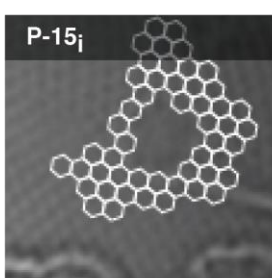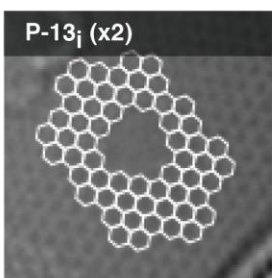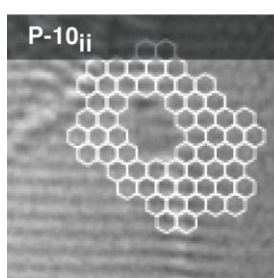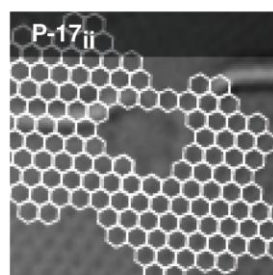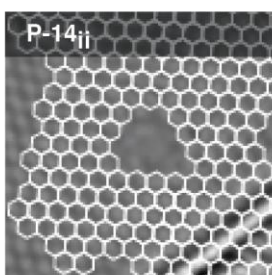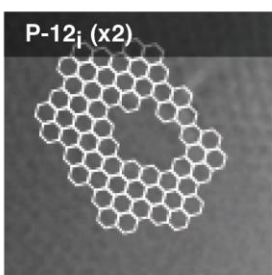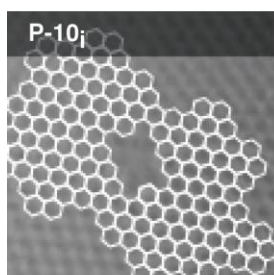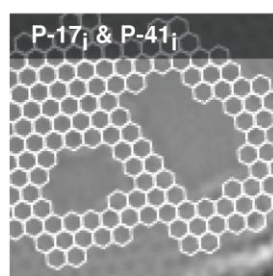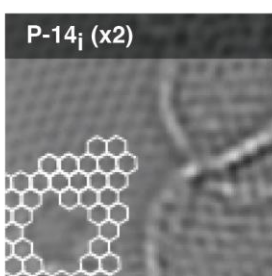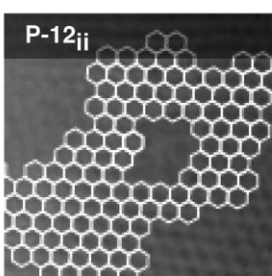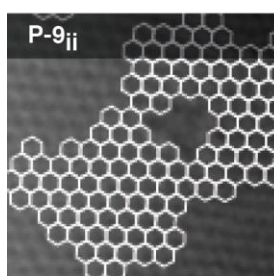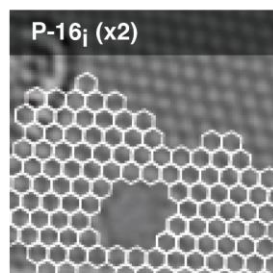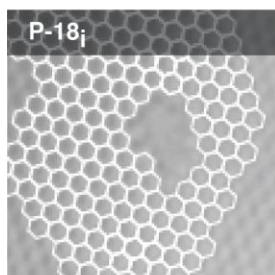
Pore P-18 to P-20   Pore P-20
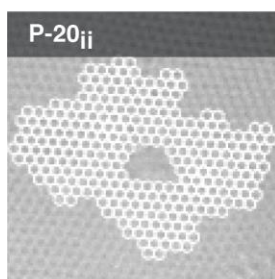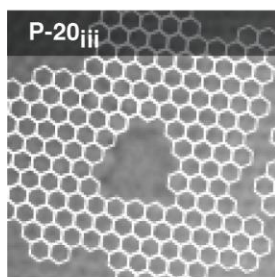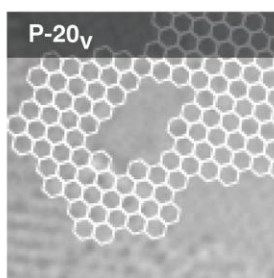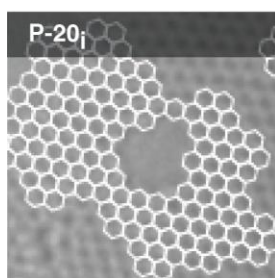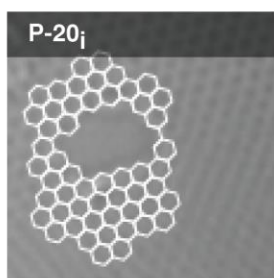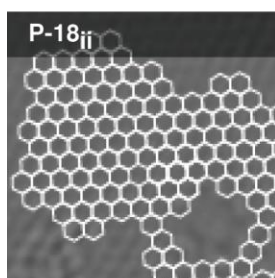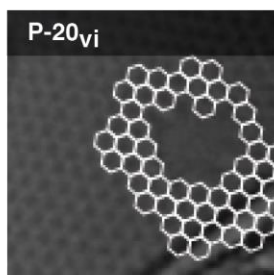
Chapter 4 Ultrathin carbon molecular sieve films and room-temperature oxygen functionalization for gas-sieving

Abstract

Inorganic membranes based on carbon molecular sieve (CMS) films hosting slit-like pores can yield a high molecular selectivity with a sub-angstrom resolution in molecular differentiation, and therefore are highly attractive for energy-efficient separations. However, the selective layer thickness of the state-of-the-art CMS membranes for gas separation is thicker than 1 μm, yielding low gas permeance. Also, there is no room-temperature functionalization route for the modification of the pore-size-distribution of CMS to increase the molecular selectivity. In this context, we report two novel fabrication routes, namely transfer and masking techniques, leading to CMS films with thicknesses as small as 100 nm, yielding attractive gas-sieving performances with H_2 permeance reaching up to 3060 gas permeation units (GPU). Further, a rapid and highly-tunable room temperature ozone treatment based post-synthetic modification is reported, shrinking the electron-density-gap in the nanopores by a fraction of an angstrom, improving gas selectivities by several folds. The optimized membranes yielded H_2 permeance of 507 GPU and H_2/CH_4 selectivity of 50.7.

1. Introduction

Membrane-based gas separation is widely recognized as one of the most energy-efficient processes for the purification of reactants and products in the chemical and the petrochemical industry, stimulating studies in the search and optimization of chemically

and thermally stable materials and films capable of size-sieving.[1,197] Carbon molecular sieves (CMS), hosting slit-like nanopores formed by a disordered packing of aromatic carbon strands driven by volume exclusion effects, have emerged as highly promising membrane materials.[198–200] CMS can be synthesized with a narrow pore-size-distribution (PSD), and as a result, attractive sieving performances have been reported with a sub-angstrom resolution in molecular differentiation, e.g. C_2H_6/C_2H_4,[201,202] and CH_4/N_2[151] separation. The carbon framework displays superior chemical and thermal stability compared to the conventional polymeric material for gas separation.[203,204] The CMS membranes are synthesized by the pyrolysis of precursor polymers such as Matrimid (a commercially available polyimide),[151,201,202,205] 6FDA-based polyimide[206–208], intrinsically microporous polymers (PIMs)[209–212], etc. Although CMS membranes can offer a high selectivity, they typically yield relatively low permeance (molecular flux normalized with transmembrane pressure difference) compared to other nanoporous membranes such as metal-organic frameworks which can be attributed to a relatively higher framework density and the difficulty in engineering thin yet selective films of CMS. The selective layer thickness (SLT) of the state-of-the-art polyimide-derived CMS membranes is of the order of 1 μm. For separations controlled by diffusion, a thinner film reduces the diffusional path length and thereby increases the gas permeance. A challenge with the reduction in the thickness is that the molecular selectivity is often compromised due to the increased contribution of transport from the defective pathways in the film. In this context, it is highly crucial to develop synthetic and processing techniques that can increase the molecular permeance from the CMS membranes while at the same time maintain a high molecular selectivity.

Decreasing SLT is a common approach to increase the permeance from the CMS membranes. For example, CMS hollow-fiber membranes are usually prepared by the pyrolysis of the precursor polymer hollow-fiber. However, the SLT in hollow-fiber is quite thick, of the order of several microns, due to the collapse and densification of the porous support layer during the pyrolysis step. Crosslinking is a common approach to reduce the densification of the support layer. For example, Koros and co-workers added crosslinked silica and silica nanoparticles in the support layer which could reduce SLT to 3 μm. As a result, an increase in the CO_2 permeance to 164 gas permeance unit (GPU, 1 GPU = 3.35 x 10^{-10} mol m^{-2} s^{-1} Pa^{-1}) was reported.[213,214] Lively and co-workers [200] could reduce the

SLT in poly(vinylidene fluoride) or PVDF derived CMS hollow-fibers to less than 100 nm by crosslinking the polymer. This prevented substructure collapse during the pyrolysis and led to an attractive reverse osmosis performance in the separation of xylene isomers. In the case of the planar membranes, CMS films are typically prepared by coating a thin layer of precursor polymer on porous support allowing a more precise control in the thickness and morphology of the CMS films. Infiltration of precursor polymer in support is reduced by using asymmetric supports hosting a relatively dense top layer. For example, Wang and co-workers used the carbon nanotube networks as the top layer on a porous support which substantially reduced the precursor infiltration, leading to a 322-nm-thick, poly(furfuryl alcohol) derived CMS membrane, with a H_2 permeance of 60 GPU and a H_2/CH_4 selectivity of 264.3.[215] Lin and co-workers used a mesoporous γ-alumina layer with 3 nm sized pores as a top layer to prevent precursor infiltration, leading to a 520-nm-thick CMS film yielding a C_3H_6 permeance of 30 GPU and an attractive C_3H_6/C_3H_8 selectivity of 31.[216]

A high molecular selectivity from the CMS films can be obtained by engineering the pyrolysis conditions. Popular approaches include the use of higher temperature or increasing the thermal soaking time which improves the packing of carbon strands, narrowing the pore-size-distribution (PSD).[210,214,217] An alternate approach is chemical functionalization of the carbon framework, e.g. by oxygen during the pyrolysis of the precursor polymer.[198,218,219] For example, Koros and coworkers showed trace amount of oxygen in pyrolysis atmospheres doped the ultramicropore, improving O_2/N_2 selectivity from 5.3 to 9.7.[218] However, such functionalization has been only demonstrated at a high temperature (>500 ºC) increasing the sophistication of the membrane fabrication.

Overall, to the best of our knowledge, ultrathin CMS films with thickness below 300 nm and yielding attractive gas separation performance have not been reported. Herein, we report two novel fabrication techniques (transfer method and support masking) as well as room temperature oxygen functionalization based on a pulsed ozone treatment leading to commercial polyimide (Matrimid 5218)-derived CMS films as thin as 100 nm. A number of membranes were prepared with several attractive combinations of separation performance (for example: H_2 permeance of 3060 GPU with the corresponding H_2/CH_4 selectivity of 18; H_2 permeance of 507 GPU with the corresponding H_2/CH_4 selectivity of

50.7; CO_2 permeance of 497 GPU with the corresponding CO_2/CH_4 selectivity of 14, etc.) While these are the thinnest polyimide-derived CMS membranes ever reported, the selectivity improvement by the room-temperature oxygen functionalization is highly tunable.

2. Materials and methods

2.1 Materials

25 μm-thick Cu foils (99.98%) were purchased from Sigma-Aldrich and annealed at 1000 °C in a H_2 atmosphere to smoothen its surface. Matrimid 5218 (M_w = 88000 g/mol) was purchased from PolyK Technologies, LLC. Anodic aluminum oxide (AAO) supports with 20 nm pore channels were purchased from Smart Membranes GmbH. Macroporous W substrates were fabricated by laser drilling an array of 5 μm holes on a 50 μm-thick W foil. Dichloromethane (99.9%) and ferric chloride ($FeCl_3 \cdot 6H_2O$, 97%, melting point: 304 °C) were purchased from Sigma-Aldrich. Polyvinyl alcohol (MW of 85,000-124,000, 99% hydrolyzed) was purchased from Sigma-Aldrich.

2.2 Membrane fabrication

Transfer technique. Ultrathin CMS membranes were prepared by two routes. In the first route, a thin CMS film was fabricated by spin-coating a polymer precursor on Cu foil, which was followed by pyrolysis and transfer of the CMS film to the macroporous W supports (Figure 1a). Typically, Matrimid 5218 polymer was dissolved in dichloromethane to form the precursor solution. A thin polymer film was prepared by spin coating the precursor solution on the Cu foil. Subsequently, the pyrolysis of the polymer film was conducted at 500 °C for 1 h in an H_2/Ar environment to obtain a CMS film. The Cu foil was subsequently removed by etching in 1 M $FeCl_3$ solution. The freely-floating CMS film was then rinsed with deionized water and placed on top of the W support.

Masking technique. Thin CMS films were directly fabricated on porous anodic aluminum oxide (AAO) support using a masking technique. A 5 wt.% polyvinyl alcohol (PVA) solution in water was spin-coated on the AAO support to mask the pores. Subsequently, thin films of Matrimid were obtained on the masked AAO by spin coating.

During the 500 °C pyrolysis step, the PVA mask was decomposed, leaving a thin CMS layer on the AAO support. To reduce pinhole defects in the CMS membranes, the spin-coating and the pyrolysis steps were repeated.

Room temperature oxygen functionalization. Oxygen functionalization was conducted in-situ in the membrane module at room temperature using ozone. O_3 (10 % in O_2) generated by an ozone generator (Absolute Ozone® Atlas 30) was exposed to the permeate side of membrane, typically for a few minutes. After a certain time, Ar was used to sweep-out the residual ozone.

2.3 Gas permeance test

The gas permeance tests were conducted in a homemade permeation setup. All equipment used in the permeation setup were pre-calibrated. The CMS membranes on W support were sandwiched as a gasket in the Swagelok VCR fittings. The CMS membranes on AAO were sealed using epoxy. The flow rate of the feed gases was regulated by the MFCs, and the feed pressure (1.5 bar) was controlled by adjusting a backpressure regulator installed in the retentate side. The permeate side was swept with an Ar flow (1.0 bar), carrying the permeate to a MS for real-time analysis of the permeate concentration. The measurements were carried out continuously, and the steady-state data was used to calculate permeances and selectivities.

2.4 Characterization

The XPS analysis was performed in an ultrahigh vacuum (UHV) chamber (base pressure 1×10^{-9} mbar) equipped with a Mg Kα (1253.6 eV) X-ray source and PHOIBOS 100 (SPECS GmbH) hemispherical energy analyzer with a multi-channeltron detector. The XPS spectra were recorded in fixed analyzer transmission (FAT) mode using pass energies of 90 eV for the survey and 20 eV for the narrow scans. All the spectra were calibrated using C 1s (C-C bonding) spectra at the binding energy of 284.6 eV (Bonding energy of C–C: 284.6 eV; C–O: 285.6 eV; C–N: 286.2 eV; C=O: 288.3 eV) [220,221]. The XPS spectra were fitted with CasaXPS using Shirley-type background subtraction and Gaussian-Lorentzian line shape.

SEM was carried out by using FEI Teneo scanning electron microscope at 1.0–2.0

kV and working distances of 4.0–9.0 mm.

3. Results and discussion

3.1 Transfer approach for ultrathin CMS membranes

We report a transfer approach for the CMS films, involving the synthesis of ultrathin Matrimid-derived CMS film on a smooth copper foil followed by the transfer of the film to the porous support of choice (**Figure 4.1a**). Freestanding CMS films are mechanically robust, and as a result, they could be directly transferred to a macroporous W support hosting 5 μm pores (**Figure 4.1b**). No mechanically reinforcing layer was needed for the transfer. In this fashion, pinhole-free CMS films with a thickness as small as 100 nm were achieved (**Figure 4.1c-d**). We did not observe any cracks or tears in the transferred film. By optimizing the concentrations of the Matrimid solution and spin coating speed, the thickness of the CMS film could be varied from ca. 30 nm to 1000 nm (**Table 4.1**). We note that although the copper foil was used as a sacrificial substrate in this study, it can be reused to prepare CMS films using electrochemical bubbling based transfer techniques.[222] The transport properties of the 100-nm-thick membranes were investigated using H_2, CO_2, and CH_4 as probe gases. Overall, the gas transport was temperature-activated with gas permeances increasing with temperature (**Figure 4.2**). At room temperature, the membranes exhibited a H_2/CH_4 selectivity of 24 with corresponding H_2 permeance of 761 GPU. The H_2 permeance increased to 3060 GPU at 150 ºC while maintaining a moderate H_2/CH_4 selectivity of 18. An attractive CO_2/CH_4 selectivity of 14 was achieved at room temperature with corresponding CO_2 permeance of 497 GPU.

Table 4.1 Thickness of CMS membranes with different Matrimid concentrations and spin coating speeds.

Spin-coating speed	Concentration (wt.%)		
	5%	2%	1%
1000 (rpm)	1000 nm	300 nm	75 nm
2000 (rpm)		150 nm	40 nm
3000 (rpm)		100 nm	30 nm
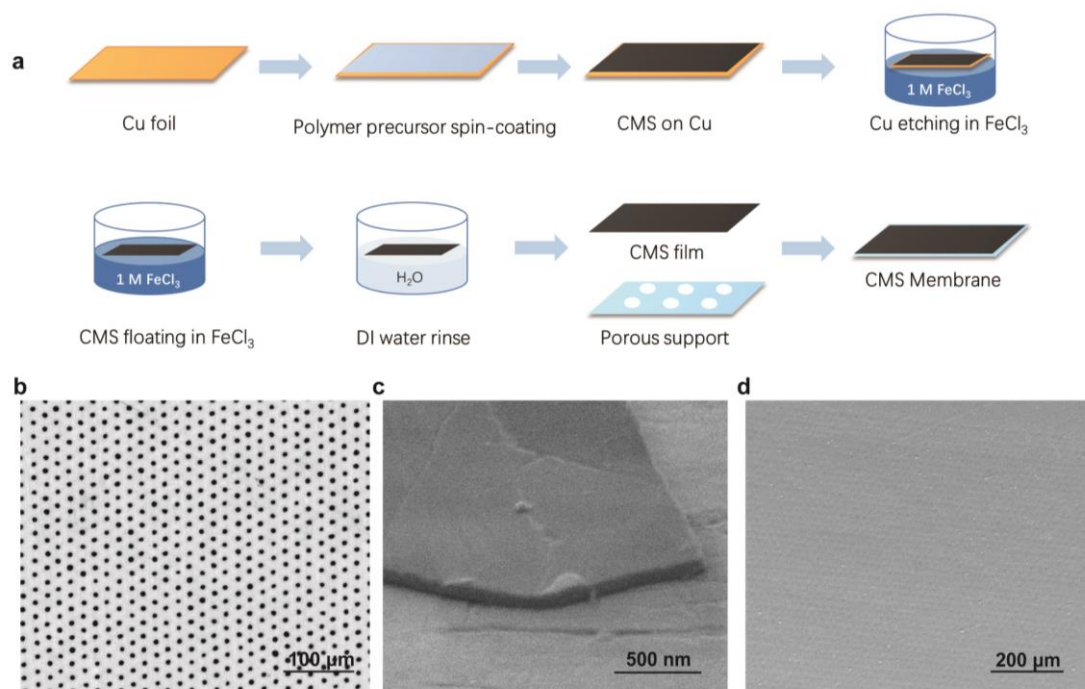
Figure 4.1 Ultrathin CMS film using the transfer approach. a) Schematic of the fabrication of ultrathin CMS membranes by the transfer method. b) SEM image of macroporous W support. c) Cross-section SEM image of a CMS film prepared in this fashion. d) Top-view SEM image of the CMS membranes on macroporous W support. No cracks or pinhole defects were observed.
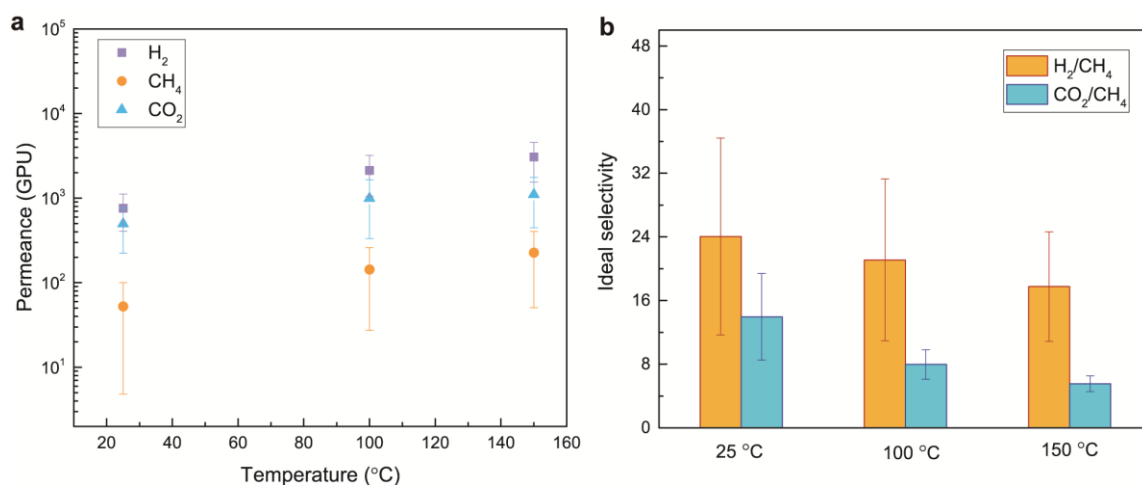
Figure 4.2 Gas separation performance from the 100-nm-thick CMS membranes. a) H_2, CO_2 and CH_4 permeances as a function of temperature using single-component feeds. b) Corresponding ideal selectivities (H_2/CH_4 and CO_2/CH_4) as a function of temperature.

3.2 Masking approach for ultrathin CMS membranes

Using an alternate strategy, involving masking of the support pores, we could fabricate a 200-nm-thick Matrimid-derived CMS film on a commercial porous support (**Figure 4.3a**). Briefly, a sacrificial polyvinyl alcohol (PVA) layer was used to mask 20-nm-sized pores of commercial anodic aluminum oxide (AAO) support (**Figure 4.3b**). The PVA mask efficiently blocked the infiltration of the Matrimid solution in the AAO pores, and as a result, 200-nm-thick CMS films could be prepared (**Figure 4.3c**). The CMS film was uniform and was free from pinhole defects (**Figure 4.3d**, **Figure 4.4a**).
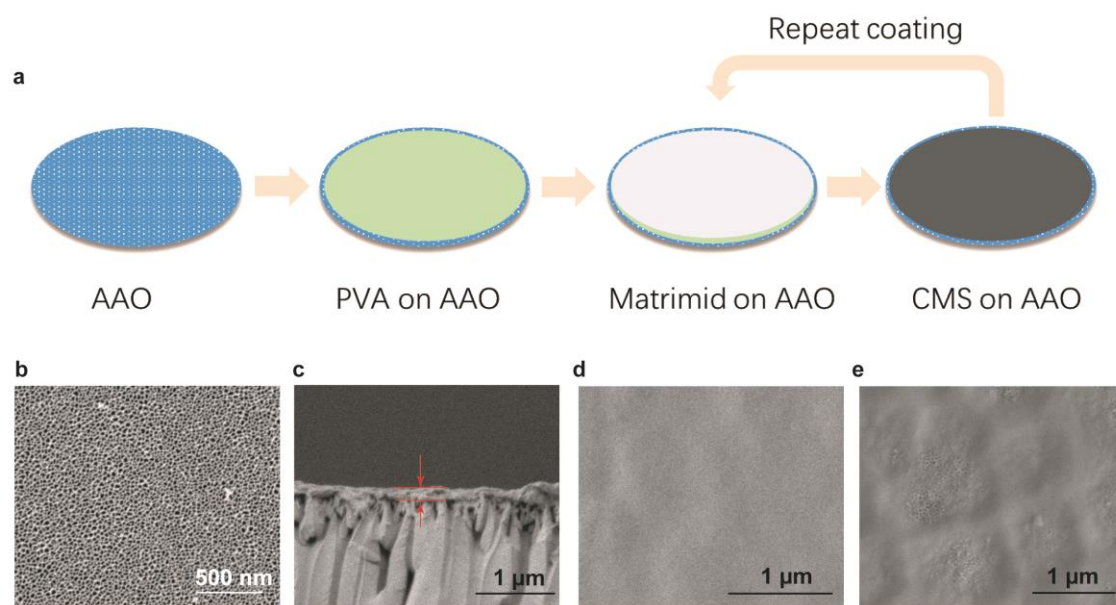
Figure 4.3 Fabrication of ultrathin CMS membranes on a commercial AAO support using the masking approach. a) Schematic of the fabrication process; b) SEM image of the AAO support hosting 20 nm pores. c) Cross-sectional SEM images of CMS film fabricated by the masking approach. Matrimid film was prepared by coating the masked support with 1% solution followed by repeating the coating with 2% solution. d) Top-view SEM image of CMS film fabricated with masking. Matrimid film was prepared by coating the masked support with 2% solution. e) Top-view of CMS film fabricated without masking revealed several pinhole defects. Matrimid film was prepared by coating the support with 2% solution).

Several membranes were made in this way, and gas separation performance was tuned using a repeated coating of the Matrimid solution (**Figure 4.5**). The resulting membranes yielded a high H_2/CH_4 selectivity (106) with attractive H_2 permeance (453

GPU) at 130 ºC. In comparison, the CMS film prepared without masking was rough (**Figure 4.3e**, **Figure 4.5b**), and yielded a lower selectivity (24) as well as H_2 permeance (268 GPU), attributing to the fact that in the absence of a mask, the Matrimid solution infiltrated in the AAO pores leading to an overall thicker film.
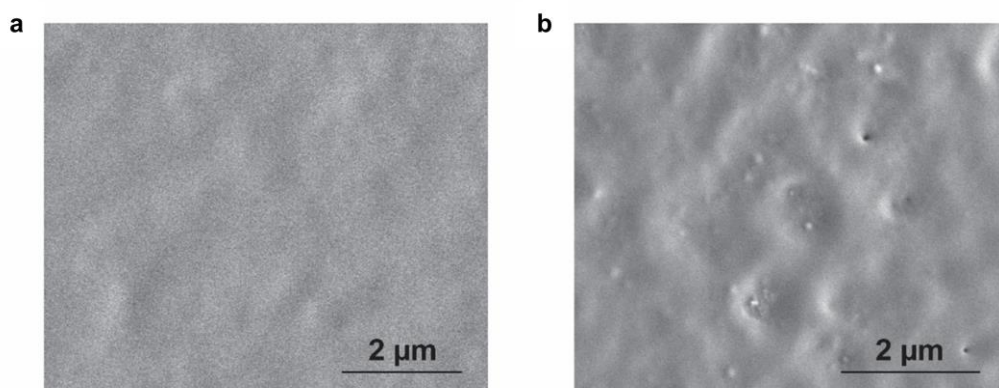
Figure 4.4 Fabrication of ultrathin CMS membranes on a commercial AAO support using the masking approach a) Top-view SEM image of CMS film fabricated with masking. Matrimid coating was prepared by coating two layers (1st layer using 1% Matrimid solution and 2nd layer using 2% Matrimid solution). b) Top-view SEM image of CMS film fabricated without any masking revealing nonuniform defective surface. Matrimid coating was done in two layers, in exactly same manner as that in (a).
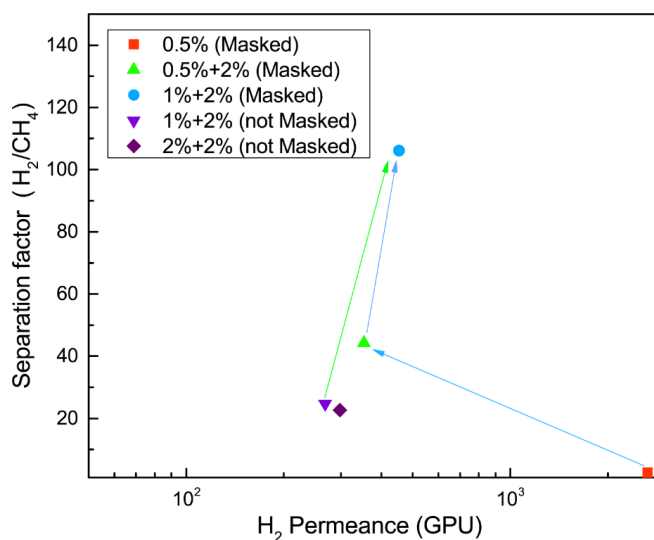
Figure 4.5 Gas separation performance of CMS membranes on AAO support derived from different Matrimid concentrations with and without PVA masking .The masked membrane was masked with 5% PVA solution, then the Matrimid was coated on top of it with different concentrations for 1~2 times; the unmasked one was fabricated by direct coating Matrimid solution without PVA masking.

3.3 Room temperature oxygen functionalization

Unlike crystalline nanoporous materials, CMS has a broad PSD because the carbon strands are packed stochastically during the pyrolysis step. Generally, an oxygen functionalization during pyrolysis is used to modify the CMS pores, where a C-O bond is added to the pore-edge reducing the electron-density-gap in the pore and improving molecular selectivity.[218,219] However, the use of oxygen during the high-temperature pyrolysis increases the complexity of synthesis and restricts the tunability of functionalization. Here, we demonstrate a straightforward and highly tunable oxygen functionalization using a pulsed ozone treatment at room temperature (**Table 4.2**).

Table 4.2 High-performance CMS membranes reported in this study.

Method	SLT (nm)	Permeation temperature (°C)	H_2 permeance (GPU)	H_2/CH_4 selectivity	CO_2 permeance (GPU)	CO_2/CH_4 selectivity
Transfer method	100	25	761	24.1	497	14.0
		150	3060	18		
Oxygen-functionalization on transferred films	100	150	507	50.7	70	7.1
Support masking method	200	130	453	106.1	69	17.4

Ozone is a highly reactive molecule especially towards carbon and has been used to functionalize carbon nanotubes and graphene even at room temperature.[58,160,164,223,224] In the case of CMS, a short (5 min) ozone exposure at room temperature is enough to graft oxygen functional groups as confirmed by X-ray photoelectron spectroscopy (XPS, **Figure 4.6**). The carbonyl groups increased from 6.5% to 40.5% along with the increase of epoxy groups (11.7%).
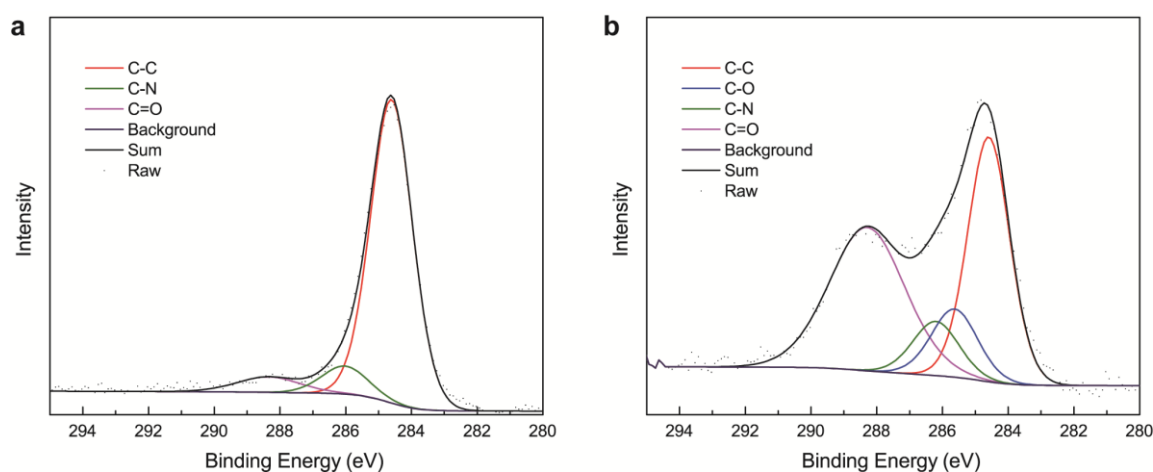
Figure 4.6 XPS spectra from the as-synthesized CMS film a) and from the oxygen functionalized CMS film b).

An in situ ozone treatment was carried out in the gas permeation setup to investigate the effect of functionalization on 100 nm CMS membranes by comparing the separation performance before and after the functionalization. Typically, after testing the gas separation performance of the CMS membrane, ozone was introduced in the permeate side of the membrane for 5 minute. Immediately after this treatment, we observed a decrease in the gas permeances, consistent with the shrinkage in electron-density gap of the pores (**Figure 4.7a**). Remarkably, the ideal gas selectivities increased significantly after the ozone treatment, by several fold, with H_2/CH_4 and H_2/CO_2 selectivities at 150 ºC increasing from 13.3 to 50.7, and from 1.8 to 7.1, respectively (**Figure 4.7b**). Compared with the as-synthesized CMS film, the functionalized film could achieve a more precise molecular differentiation with a smaller difference in kinetic diameter (k.d.), e.g. H_2 (k.d. of 0.289 nm) from CO_2 (k.d. of 0.33 nm). In addition, a 20-fold reduction in CH_4 permeance confirmed that the PSD was narrowed. Interestingly, in contrast to as-synthesized membranes, both the H_2 permeance as well as the H_2/CH_4 selectivity increased with the temperature, leading to an optimized separation performance with a H_2 permeance of 507 GPU and a selectivity of 50.7. **Table 4.2** summarizes the representative CMS membranes in this work. A comparison with the CMS membranes in the literature is shown in **Appendix-I**. The current study reaches the highest H_2 permeance while yielding an attractive gas selectivity.
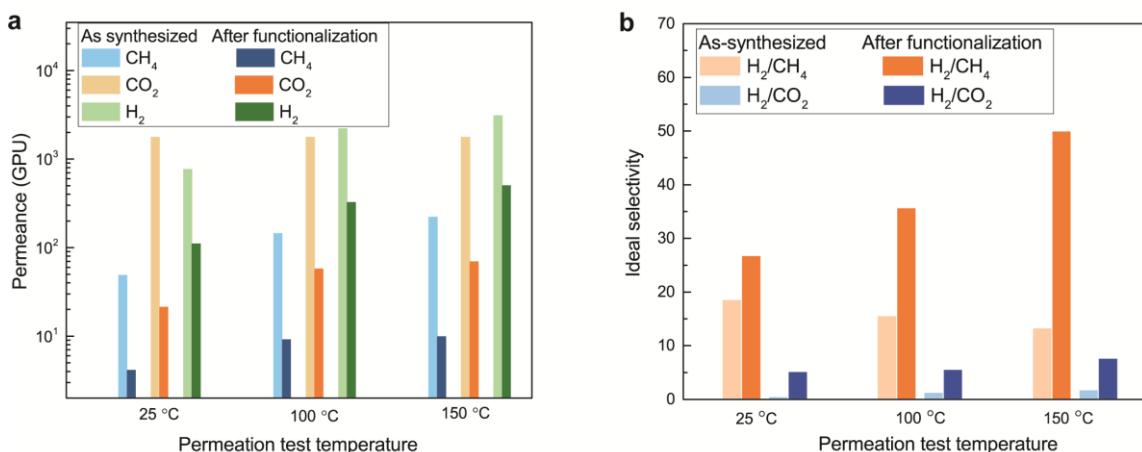
Figure 4.7 Gas separation performance of CMS membranes before and after the oxygen functionalization using ozone treatment. a) gas permeances of H_2, CH_4 and CO_2. b) Ideal selectivity of H_2/CH_4 and H_2/CO_2.

Subsequently, an in situ pulsed ozone treatment was applied to investigate the evolution of the pore-size with the help of separation performance. The gas separation performance of the 100-nm-thick CMS membrane was measured, following which, short ozone treatments (15 s each) were carried out for three times. After each treatment, the ozone was purged out with Ar to stop the reaction and the separation performance was measured. He, H_2, CO_2, and CH_4, with k.d. in the range of 0.26 – 0.38 nm, were used as probe gases to monitor the evolution of PSD (**Figure 4.8a-d**). After the first pulse, the H_2/CH_4 selectivity increased by two-fold, from 15.8 to 32.1, with a near 70% decrease in the CH_4 permeance, indicating that the functionalized pores blocked majority of the pores that allowed the passage of CH_4 (**Figure 4.8e**). With the next two pulses, CO_2 permeance continued to decrease while the CH_4 permeance did not change significantly (**Figure 4.8c and d**). As a result, while the H_2/CH_4 selectivity was maintained around 30, the H_2/CO_2 selectivity increased continuously to 7.7 (**Figure 4.8e**). It appears that oxygen functionalization from a single pulse of ozone treatment reduced the electron-density gap in most of the pores that allowed CH_4 transport, whereas the subsequent pulses continued to shrink pores that allowed CO_2 transport, indicating a stepwise shrinkage of PSD to a smaller pore-size with the number of ozone pulses.

To further understand the evolution of PSD, temperature-dependent gas flux was fitted with an Arrhenius relationship (Equation 1) to extract the apparent activation energy,

$E_{app-act}$ (Equation 4.2), for the gas transport (**Figure 4.8f**) [144145208]:

$$Flux \propto \sigma A \ \exp\left(-\frac{E_{app-act}}{RT}\right) \Delta P \tag{4.1}$$

$$E_{app-act} = \Delta H_{sur} + \ E_{act} \tag{4.2}$$

where E_{act} is the activation energy for the gas molecule to diffuse across the slit-like pore and ΔH_{sur} is the heat of adsorption of the gas molecule on CMS, reflecting the overall transport process involving adsorption of the gas molecule to the pore followed by the diffusion event across the pore. σ is the density of pores per unit area, and A is the pre-exponential factor for the Arrhenius relationship. R is the universal gas constant and T is temperature.

$E_{app-act}$ would be positive when E_{act} is higher than the ΔH_{ads}, making the transport diffusion limited, as it is in the current case (**Figure 4.8f**). Therefore, $E_{app-act}$ indicates the likelihood for the gas to diffuse across a pore, and the higher energy indicates a lower likelihood. Therefore, $E_{app-act}$ is expected to increase as a function of kinetic diameter. Our observation for as-synthesized CMS is consistent with this, except the case for CO_2, which can be explained by much higher ΔH_{ads} for CO_2 (typically 15-30 kJ mole^{-1}) than for He (a nonadsorbing gas especially at room temperature and above), H_2 (weakly adsorbing), and CH_4 (4-10 kJ mole^{-1}). [205,225,226] Based on the E_{act} of He (12 kJ mole^{-1}), the E_{act} of diffusion from as-synthesized CMS is expected to be higher than 12 kJ mole^{-1} for H_2, CO_2, and CH_4.

Table 4.3. Pre-exponential factor, σA, extracted by the Arrhenius relationship model fitting to the observed transport from the CMS membranes with the pulsed ozone treatments.

	He	H_2	CO_2	CH_4
As synthesized CMS film	2.34×10^{-5}	2.10×10^{-5}	1.57×10^{-6}	3.24×10^{-6}
1st O_3 pulse	1.17×10^{-5}	1.49×10^{-5}	9.60×10^{-7}	2.35×10^{-7}
2nd O_3 pulse	1.15×10^{-5}	1.35×10^{-5}	9.85×10^{-7}	6.78×10^{-8}
3rd O_3 pulse	1.02×10^{-5}	1.08×10^{-5}	1.04×10^{-6}	3.29×10^{-8}
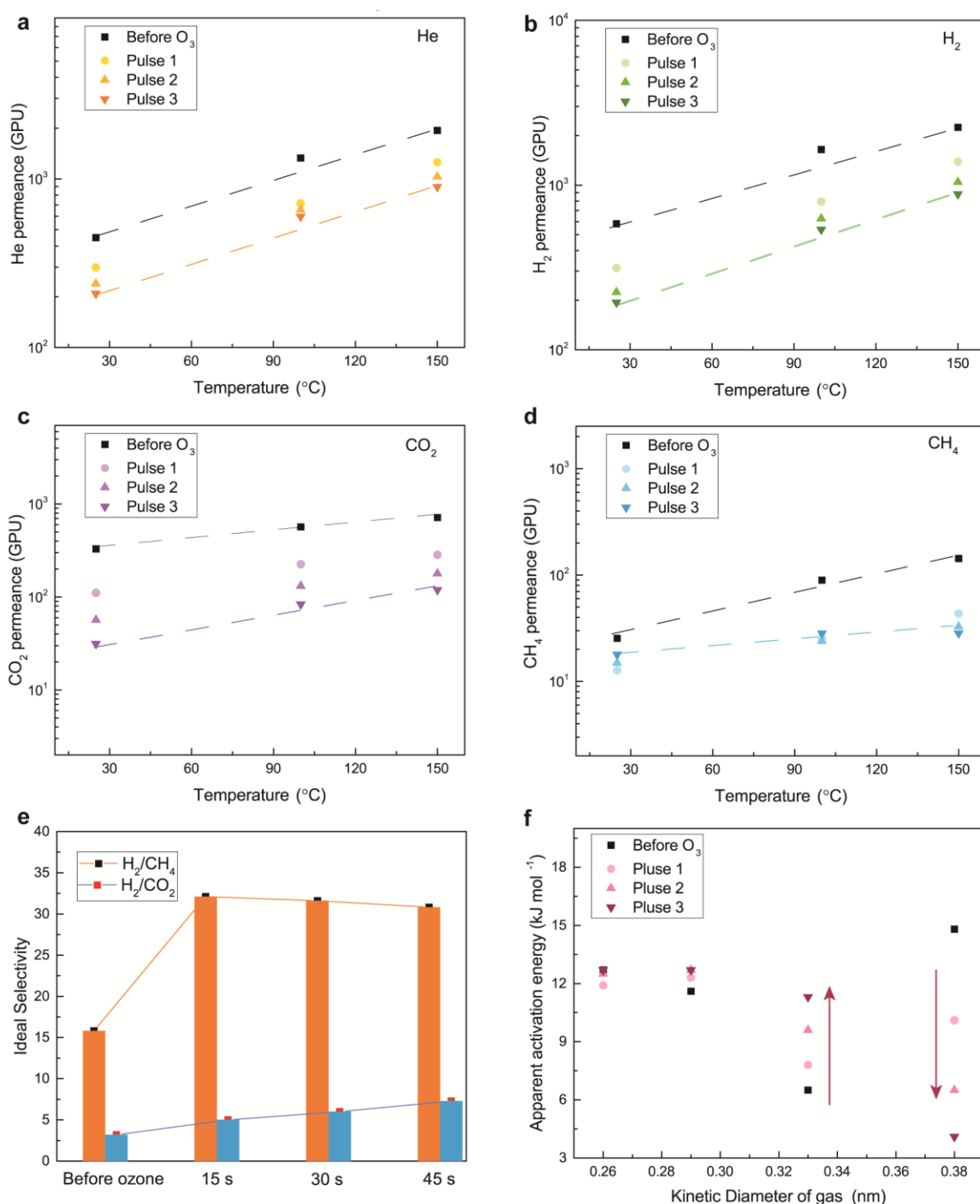
Figure 4.8 Gas separation performance of CMS membranes as a function of temperature before and after the pulsed ozone treatment. Gas permeances as a function of temperature a) He, b) H_2, c) CO_2, and d) CH_4. e) Evolution of H_2/CH_4 and H_2/CO_2 ideal selectivities at 150 ℃ as a function of the ozone pulsing. f) Apparent activation energies before and after the ozone treatment are plotted as a function of the kinetic diameters of the gases.

When the CMS film was functionalized, the $E_{app-act}$ for molecules with k.d. below 0.30 nm (He, H_2) did not change significantly (**Figure 4.8f**), however, $E_{app-act}$ increased

progressively by 1-2 kJ mole^{-1} for CO_2 (k.d. of 0.33 nm) from 6.5 to 11.4 kJ mole^{-1} as the number of ozone treatment was increased. This clearly indicates a progressive pore shrinkage as a result of ozone pulsing, increasing the E_{act} for CO_2, leading to higher H_2/CO_2 selectivities (**Figure 4.8e-f**). The permeance decrease in CO_2 after each treatment was solely due to the pore shrinkage, verified by the constant pre-exponential factor (σA), indicating that the number of pores involved in the transport of CO_2 did not change (**Table 4.3**). In contrast, for CH_4 (k.d. of 0.38 nm), the $E_{app-act}$ decreased by 3-4 kJ mole^{-1} after each ozone pulse (**Figure 4.8f**), leading to an overall decrease from 15 kJ mole^{-1} to 4 kJ mole^{-1} in three pulses. This is indicative of the increasingly smaller contribution from the activated transport from the nanopores as a result of their shrinkage beyond the accessibly of CH_4, and an increasing larger contribution from the Knudsen transport from the defects in the membranes. This blockage of nanopores for CH_4 is verified by ca. 100-fold decrease of the pre-exponential factor, σA, for CH_4 (**Table 4.3**). Although increasing entropic penalty can reduce A, such a large decrease is likely to be from the reduction in σ. Overall, the maintenance of the number of CO_2 transport pathway combined with a large reduction of the number of CH_4 transport pathway establishes that the pulsed ozone treatment based oxygen functionalization is capable of shrinking nanopore size by a fraction of an angstrom, and can help tune the CMS-based sieving for a number of molecular pairs.

4. Conclusion

In summary, we report transfer and masking techniques to fabricate the thinnest (100 to 200-nm-thick) CMS membranes for high-performance gas-sieving. The tunable oxygen functionalization based on ozone treatment could shrink the CMS pores by a fraction of an angstrom, improving H_2/CH_4 and H_2/CO_2 selectivities by several fold. The fact that the treatment was carried out at room temperature and that a short exposure of 15 s was effective in shrinking electron-density-gap in the pores, makes ozone functionalization highly attractive for a number of CMS membranes.

Appendix I

Table 4.4. Comparison of separation performance in this work with that in the literature.

Membrane	Precursor	SLT	Permeance (GPU)			Selectivity or separation factor			References
			H_2	CO_2	He	H_2/CH_4	CO_2/CH_4	He/N_2	
CMS-750°C	Matrimid 5218	33 μm	46	12	15	500	150		[151]
CMS	Matrimid 5218	3 - 4 μm		164			55		[214]
CMS	6FDA-based polyimide	300 nm			657			55	[216]
CMS	poly(furfuryl alcohol) (PFA)	300 nm	134	23		695	116		[215]
CMS	6FDA:BPDA-DAM	3 μm		394			22±2		[227]
	Matrimid	5 μm		216			30		
CMS	PIM-6FDA-OH	not reported		4110 Barrer			20		[210]
CMS-transfer	Matrimid 5218	100 nm	761	497		24.1	14.0		This work
Ozone-treated CMS*	Matrimid 5218	100 nm	507	70		50.7	7.1		This work
CMS-masking method**	Matrimid 5218	200 nm	453	69		106.1	17.4		This work

* Gas permeation test was done at 150 °C

** Gas permeation test was done at 130 °C

Other tests were conducted at either 25 °C or 35 °C

Chapter 5 Summary and Perspective

1. Summary of thesis

Graphene, as a star material in the 21st century, is famous for the one-atom-thick honeycomb lattice. The ultrashort transport path of graphene attracts many researchers to explore its application in the separation field. In 2008, Bunch et al. demonstrated that the single-layer graphene membrane is impermeable to even the smallest gas molecule helium. The dense electron density of graphene lattice constructs an insurmountable energy barrier for the gas molecules. Perforation of graphene lattice would be an essential step to break the energy barrier, creating the transport channel for gas molecules in graphene lattice. Hence, single-layer graphene film, incorporated with high-density narrowly-distributed nanopores, is predicted as the ultimate membrane for gas separation by numerous theoretical calculations.

However, it is not trivial to realize this high-performance nanoporous single-layer graphene membrane experimentally. At least two bottlenecks hinder the development of the nanoporous single-layer graphene membranes: 1) large-area defect-free transfer of single-layer graphene on to the porous substrate. To the best of our knowledge, the diameter of gas-sieving nanoporous single-layer graphene film is limited in 5 μm in 2016. It is far from the realization of practical application or even could not support the solid investigation of gas transport through the film. 2) incorporation of high-density gas-sieving nanopores in graphene lattice. Gas separation requires sub-nanometer pores, with even sub-angstrom resolution, to differentiate the gas molecules with similar gas kinetic diameters. While the existing pore-etching methods are faced with the trade-off between the pore-density and pore-size distribution, leading to broad pore-size distribution. The two issues hindered the development of the nanoporous single-layer graphene membrane for gas separation applications. This dissertation dedicates to develop the strategies to solve the two bottlenecks mentioned above and demonstrates high-performance nanoporous graphene membranes for gas separation.

Firstly, we have developed a novel nanoporous carbon film-assisted transfer method to realize large-area defect-free single-layer graphene transfer on the porous substrate. The conventional PMMA-assisted transfer method has a significant drawback to transferring

graphene on the porous support. The removal of the mechanical reinforcement layer of PMMA would inevitably induce cracks and tears in the graphene film, killing the selectivity of the graphene film. Hence, in this dissertation, the nanoporous carbon comprising of 20 – 30 nm-sized nanopores with high gas permeance was proposed to replace the impermeable PMMA to mitigate the cracks induced by transfer. The 100 nm-thick nanoporous carbon film acts as a reinforcement layer to boost the mechanical strength of the film, ensuring the intactness of the graphene during the transfer. The novel transfer method enables to fabricate crack-free millimeter-scale suspended graphene membrane on a porous support, allowing to observe the gas transport behavior through intrinsic defects of CVD-derived graphene. The single-layer graphene with 0.025% intrinsic defects displayed an attractive H_2/CH_4 separation performance, approaching the state-of-the-art polymeric membrane.

A series of pore-engineering methods were developed to incorporate nanopores with a sub-angstrom resolution in single-layer graphene for gas separation, including rapid ozone etching, ozone-based functionalization, and slow oxygen etching. The ozone-based rapid gasification method was established here to incorporate high-density gas-sieving nanopores on graphene lattice. With the novel design of our custom-made millisecond gasification reactor, the expansion time of vacancy defects could be controlled within milliseconds. The rapid ozone gasification generates narrowly-distributed nanopores with a molecular-sieving resolution of 0.2 Å, achieving CO_2/O_2 and CO_2/N_2 selectivities up to 12.6 and 27.6, respectively. Followed by this, the pore-edge-functionalization chemistry and the slow oxygen etching were developed to shift the molecular cut-off within sub-angstrom for tuning gas-mixture separation performance. Ozone-based pore-edge functionalization chemistry was able to shrink the pore size by a fraction of an angstrom, increasing the diffusion resistance of CH_4 passing and promoting H_2/CH_4 gas selectivity. The slow pore expansion in the presence of oxygen at 200 ºC could shift the molecular cut-off by 0.1 Å, resulting in an attractive O_2/N_2 separation performance with a selectivity of 3.4 and corresponding O_2 permeance of 1300 gas permeation units (GPU), and CO_2/N_2 selectivity of 21.7 with corresponding CO_2 permeance of 11850 GPU. The etching method and functionalization chemistry developed here would pave the way to fabricate nanopores in single-layer graphene for separating several species based on the relative differences in size.

The methods mentioned above are also universal to fabricate other carbon-based membranes. A sub-200 nm carbon molecular sieve membrane was successfully fabricated with the tunable pore-size distribution by the implementation of the transfer method and ozone-based pore-edge functionalization method. The resulting CMS film displayed attractive H_2 permeance and H_2/CH_4 or H_2/CO_2 separation factors.

In this thesis, for the first time, we realized a scalable nanoporous single-layer graphene membrane with high gas mixture separation performance. These films hold an atomic thickness with 1% porosity of narrowly-distributed nanopores, displayed an attractive gas separation performance, reaching the DOE target area of carbon capture. However, this is not the ending of the exploration of the single-layer graphene membrane. This study will become a new starting point to realize the enormous potential of the magic one-atom-thick graphene in the separation field.

2. Perspective

The one-atom-thick graphene exhibits exceptional thermal and mechanical properties, making it an excellent fit for pressure-driven membrane separations. In our work, the graphene membrane with only 1% porosity has already shown attractive separation performance. According to the previous experimental work and theoretical studies, the nanoporous graphene with 5% porosity could still withstand 100 bar trans-membrane pressure.[115,116] Therefore, the future work will push the limit of nanoporous graphene to further increase the nanoporous graphene porosity. Ozone etching would be a promising approach to achieve it based on our previous research. However, some fundamental understanding of ozone etching is missing to guide us to reach higher porosity. Revealing the mechanism of the ozone etching would be an essential step for our future study. In this field, another future direction is developing an economic-feasible and efficient method to scale up the membrane for industrial applications.

In this thesis, we have already established a mathematical model, based on the ozone-etching kinetics, to predict the pore density and pore-size distribution of the incorporated nanopores in the graphene. The model prediction was consistent with the observation in the HRTEM and STM. However, the mechanism of the ozone etching from nucleation to expansion is still under-discovered. Such as, what is the relationship between the content

of the O-containing functional groups and the nucleation density? What is the evolution from the epoxy group to the vacancy defect?

As most of the simulation work demonstrated,[147,148] the ozone etching starts with epoxy formation by overcoming 0.74 eV barrier,[75] followed by epoxy group diffusion to form a cluster with ether or lactone group (0.73 – 0.76 eV).[76] Eventually, a carbon atom will be cleaved because of the lattice strain induced by bucking of the lattice. The proposed mechanism was partially consistent with our STM, and HRTEM observation that there was some elongated pores generation after ozone treatment. But still, this could not clearly explain the relationship between the morphology of the nanopore and the functional group cluster, as well as the evolution from nucleated functional groups to the vacancy defect. To answer these questions, we need a system in which the pore nucleation and expansion are decoupled so that we could investigate the nucleation and expansion stages separately. The decoupled system would allow the observation of the different carbon etching chemistry on the basal plane of graphene and defective site. Also, it would contribute to understanding the relationship between the nucleated functional groups and the final properties of nanopores, such as pore density and pore size distribution.

We have constructed a strategy that nucleates the epoxy groups at low temperatures to initialize high-density sp^3 active sites and expand the pre-nucleating sites in the following step. We have conducted some preliminary experiments to understand the chemisorption of ozone (forming the O-containing functional group) on graphene lattice at different temperatures. The samples were treated at different reaction temperatures to gain the temperature-dependent information of the O-containing functional groups formed by ozone. All the reaction temperatures were under 60 °C, to avoid the cleavage of the carbon atoms from the graphene lattice by ozone (**Figure 5.1**). The XPS measurement analysis displayed the functional groups induced by ozone were a mixture of the C-O and the C=O, indicating there were multiple reactions involved in the ozone reaction rather than the only epoxy formation. The preliminary results also demonstrated we could gain high-density O-containing functional groups on graphene; the low-temperature treatment coverage could reach 30%. Subsequently, we fitted the reaction rate of forming O-containing functional groups and reaction temperatures. The obtained apparent activation energy to form O-containing functional groups on graphene is 64 kJ mol^{-1}. Considering

the adsorption energy of ozone on graphene lattice is 24 kJ mol^{-1}, the real chemisorption energy of ozone to form the O-containing functional groups on graphene lattice is around 88 kJ mol^{-1}, higher than the chemisorption energy of epoxy group reported in the literature (0.74 eV).
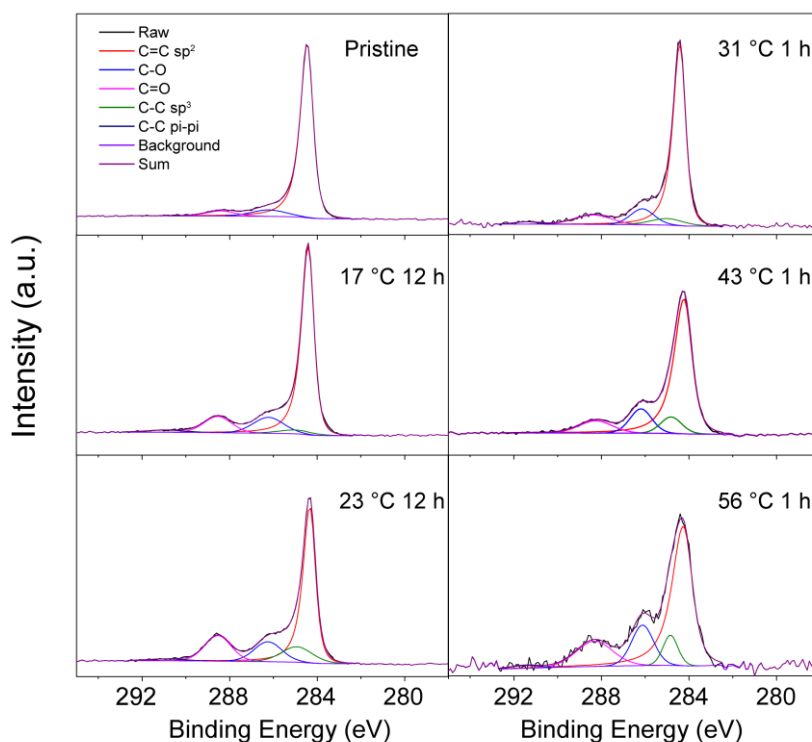
Figure 5.1 XPS spectra of ozone-treated graphene with different reaction temperatures and time.

The work demonstrates the feasibility of high-density sp^3 active sites pre-nucleating on graphene lattice and provides a promising approach to decouple the nucleation and expansion. Now we are dedicated to developing a strategy to observe the evolution of carbon atom removing from the pre-nucleating site by STM. Then the next step is constructing a decoupled pore expansion system with a controllable etching approach, improving the resolution of the nanopores. We believe the future study of this topic would reveal more fundamental observation of the ozone etching process, which would accelerate the process of achieving the nanoporous single-layer graphene membrane with higher porosity and more attractive performance.
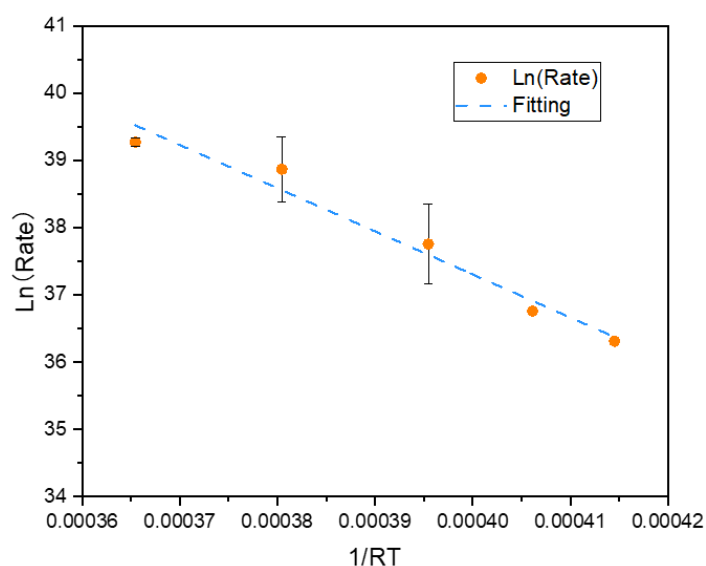
Figure 5.2 Temperature dependence of the reaction rate of the O-functional group on graphene lattice.

Another future direction of the nanoporous single-layer graphene membrane is to scale up the membrane for real industrial applications. The ultimate goal of membrane research is to apply them in the real industrial world. As I mentioned in the previous notes, the gas-sieving single-layer graphene film was 5 μm in 2016. At the end of my thesis, the membrane area becomes 1 mm^2, and we could manage to handle with centimeter-scale nanoporous single-layer graphene membrane.

However, this scale is still far from the real meter-scale membrane in the industrial application. As suggested by Grossman's calculation,[116] the pore size on the membrane substrate would greatly influence the mechanical strength of the suspended nanoporous graphene. The failure pressure would decrease when graphene is suspended on a big pore of the membrane support. Nowadays, scaling up the single-layer graphene membrane by roll-to-roll synthesis and casting is becoming a hot topic, and most of the scale-up focuses on nanoporous polyethersulfone (PES) support. The aromatic structure of PES would increase the affinity of graphene lattice and membrane support. However, the nanoporous PES membrane support formed by the current NIPS casting method is not perfect for the suspended graphene. One issue is the macrovoid formation in PES support; most of the

PES support inevitably contains the macrovoids in the layer attached to the single-layer graphene, increasing the possibility of generating cracks in graphene during transfer or under pressure. The membranes for gas separation has no tolerance to even a nanometer size defect. As a result, most of the nanoporous graphene membrane needs an additional layer to plug the defects generated during the fabrication process, such as PDMS. This extra layer increases the membrane's transport resistance, diminishing the advantage of the single-layer graphene. Hence, high-flux porous membrane support with the uniform nanoporous structure would be ideal for nanoporous graphene membrane fabrication. The ideal membrane support would improve the quality of the nanoporous graphene membrane and enhance the success rate of the large-area membrane fabrication, putting a step closer to realize the energy-efficient membrane separation.

At last, I should say that I am happy on the journey of exploring the secrets of the nanoporous graphene. I do hope more interesting findings would come up after this work, and I will always be inspired by this magic material.

References

1. Sholl, D. S. & Lively, R. P. Seven chemical separations to change the world. *Nature* **532**, 435–437 (2016).

2. National Academies of Sciences. *A Research Agenda for Transforming Separation Science*. (The National Academies Press, 2019).

3. Merkel, T. C., Lin, H., Wei, X. & Baker, R. Power plant post-combustion carbon dioxide capture: An opportunity for membranes. *J. Memb. Sci.* **359**, 126–139 (2010).

4. Rochelle Gary T. Amine Scrubbing for CO_2 Capture. *Science* **325**, 17–52 (2009).

5. Robeson, L. M. The upper bound revisited. *J. Memb. Sci.* **320**, 390–400 (2008).

6. Wang, S. *et al.* Two-dimensional nanochannel membranes for molecular and ionic separations. *Chem. Soc. Rev.* 1071–1089 (2020).

7. Liu, G., Jin, W. & Xu, N. Two-Dimensional-Material Membranes: A New Family of High-Performance Separation Membranes. *Angew. Chemie - Int. Ed.* **55**, 13384–13397 (2016).

8. Agrawal, K. V. Towards the Ultimate Membranes: Two-dimensional Nanoporous Materials and Films. *Chimia* **72**, 313–321 (2018).

9. Li, H. *et al.* Ultrathin, Molecular-Sieving Graphene Oxide Membranes for Selective Hydrogen Separation. *Science* **342**, 95–98 (2013).

10. Kim, H. W. *et al.* Selective gas transport through few-layered graphene and graphene oxide membranes. *Science* **342**, 91–96 (2013).

11. Chen, L. *et al.* Ion sieving in graphene oxide membranes via cationic control of interlayer spacing. *Nature* **550**, 1–4 (2017).

12. Ding, L. *et al.* MXene molecular sieving membranes for highly efficient gas separation. *Nat. Commun.* **9**, 1–7 (2018).

13. Ding, L. *et al.* A Two-Dimensional Lamellar Membrane: MXene Nanosheet Stacks. *Angew. Chemie - Int. Ed.* **56**, 1825–1829 (2017).

14. Shen, J. *et al.* 2D MXene Nanofilms with Tunable Gas Transport Channels. *Adv. Funct. Mater.* **28**, 1–13 (2018).

15. Jeon, M. Y. *et al.* Ultra-selective high-flux membranes from directly synthesized zeolite nanosheets. *Nature* **543**, 690–694 (2017).

16. Varoon, K. *et al.* Dispersible Exfoliated Zeolite Nanosheets and Their Application as a Selective Membrane. *Science* **754**, 72–76 (2012).

17. Agrawal, K. V. *et al.* Oriented MFI membranes by gel-less secondary growth of sub-100 nm MFI-nanosheet seed layers. *Adv. Mater.* **27**, 3243–3249 (2015).

18. Rodenas, T. *et al.* Metal-organic framework nanosheets in polymer composite materials for gas separation. *Nat. Mater.* **14**, 48–55 (2015).

19. Peng, Y. *et al.* Metal-organic framework nanosheets as building blocks for molecular sieving membranes. *Science* **346**, (2014).

20. Geim, A. K. Nobel Lecture: Random walk to graphene. *Rev. Mod. Phys.* **83**, 851–862 (2011).

21. K. S. Novoselov, A. K. Geim, S. V. Morozov, D. Jiang, Y. Zhang, S. V. Dubonos, I. V. G. and A. A. F. Electric Field Effect in Atomically Thin Carbon Films. *Science* **306**, 666–669 (2016).

22. Geim, A. K. & Novoselov, K. S. The rise of graphene. *Nat. Mater.* **6**, 183–191 (2007).

23. Ye, R. & Tour, J. M. Graphene at fifteen. *ACS Nano* **13**, 10872–10878 (2019).

24. Kong, W. *et al.* Path towards graphene commercialization from lab to market. *Nat. Nanotechnol.* **14**, 927–938 (2019).

25. De, N. Quelques propriétés typiques des corps solides. **3**, 177–222 (1935).

26. Galashev, A. E. & Rakhmanova, O. R. Mechanical and thermal stability of graphene and graphene-based materials. *Physics-Uspekhi* **57**, 970–989 (2014).

27. Frank, I. W., Tanenbaum, D. M., Van Der Zande, A. M. & McEuen, P. L. Mechanical properties of suspended graphene sheets. *J. Vac. Sci. Technol. B Microelectron. Nanom. Struct.* **25**, 2558–2561 (2007).

28. Lee, C., Wei, X., Kysar, J. W. & Hone, J. Measurement of the Elastic Properties and Intrinsic Strength of Monolayer Graphene. *Science* **321**, 385–388 (2008).

29. Balandin, A. A. Thermal properties of graphene and nanostructured carbon materials. *Nat. Mater.* **10**, 569–581 (2011).

30. Prasher, R. Graphene spreads the heat. *Science* **328**, 185–186 (2010).

31. Kim, K. *et al.* High-temperature stability of suspended single-layer graphene. *Phys. Status Solidi - Rapid Res. Lett.* **4**, 302–304 (2010).

32. Robertson, A. W. *et al.* Spatial control of defect creation in graphene at the nanoscale. *Nat. Commun.* **3**, (2012).

33. Li, G., Luican, A. & Andrei, E. Y. Scanning tunneling spectroscopy of graphene on graphite. *Phys. Rev. Lett.* **102**, 1–4 (2009).

34. Li, X. *et al.* Large-area synthesis of high-quality and uniform graphene films on copper foils. *Science* **324**, 1312–1314 (2009).

35. Bae, S. *et al.* Roll-to-roll production of 30-inch graphene films for transparent electrodes. *Nat. Nanotechnol.* **5**, 1–5 (2009).

36. Polsen, E. S., McNerny, D. Q., Viswanath, B., Pattinson, S. W. & John Hart, A. High-speed roll-to-roll manufacturing of graphene using a concentric tube CVD reactor. *Sci. Rep.* **5**, 10257 (2015).

37. Hsieh, Y. P., Shih, C. H., Chiu, Y. J. & Hofmann, M. High-Throughput Graphene Synthesis in Gapless Stacks. *Chem. Mater.* **28**, 40–43 (2016).

38. Bunch, J. S. *et al.* Impermeable Atomic Membranes from Graphene Sheets. *Nano Lett.* **8**, 2458–2462 (2008).

39. Sun, P. Z. *et al.* Limits on gas impermeability of graphene. *Nature* **579**, 229–232 (2020).

40. Safron, N. S., Kim, M., Gopalan, P. & Arnold, M. S. Barrier-guided growth of micro- and nano-structured graphene. *Adv. Mater.* **24**, 1041–1045 (2012).

41. Yi, J., Lee, D. H., Lee, W. W. & Park, W. Il. Direct synthesis of graphene meshes and semipermanent electrical doping. *J. Phys. Chem. Lett.* **4**, 2099–2104 (2013).

42. Choi, K., Droudian, A., Wyss, R. M., Schlichting, K.-P. & Park, H. G. Multifunctional wafer-scale graphene membranes for fast ultrafiltration and high permeation gas separation. *Sci. Adv.* **4**, eaau0476 (2018).

43. Moreno, C. *et al.* Bottom-up synthesis of multifunctional nanoporous graphene. *Science* **360**, 199–203 (2018).

44. Smith, B. W. & Luzzi, D. E. Electron irradiation effects in single wall carbon nanotubes. *J. Appl. Phys.* **90**, 3509–3515 (2001).

45. Warner, J. H. *et al.* Structural transformations in graphene studied with high spatial and temporal resolution. *Nat. Nanotechnol.* **4**, 500–504 (2009).

46. Garaj, S. *et al.* Graphene as a subnanometre trans-electrode membrane. *Nature* **467**, 190–193 (2010).

47. Schneider, G. F. *et al.* DNA translocation through graphene nanopores. *Nano Lett.* **10**, 3163–3167

(2010).

48. Crespi, V. H., Chopra, N. G., Cohen, M. L., Zettl, A. & Louie, S. G. Anisotropic electron-beam damage and the collapse of carbon nanotubes. *Phys. Rev. B - Condens. Matter Mater. Phys.* **54**, 5927–5931 (1996).

49. El-Barbary, A., Telling, H., Ewels, P., Heggie, I. & Briddon, R. Structure and energetics of the vacancy in graphite. *Phys. Rev. B - Condens. Matter Mater. Phys.* **68**, 1–7 (2003).

50. Banhart, F., Kotakoski, J. & Krasheninnikov, A. V. Structural defects in graphene. *ACS Nano* **5**, 26–41 (2011).

51. Girit, Ç. Ö. *et al.* Graphene at the Edge: Stability and Dynamics. *Science* **323**, 1705–1708 (2009).

52. Lehtinen, O. *et al.* Effects of ion bombardment on a two-dimensional target: Atomistic simulations of graphene irradiation. *Phys. Rev. B - Condens. Matter Mater. Phys.* **81**, 1–4 (2010).

53. Russo, C. J. & Golovchenko, J. A. Atom-by-atom nucleation and growth of graphene nanopores. *Proc. Natl. Acad. Sci.* **109**, 5953–5957 (2012).

54. Deng, Y. *et al.* Precise fabrication of a 5 nm graphene nanopore with a helium ion microscope for biomolecule detection. *Nanotechnology* **28**, (2017).

55. Celebi, K. *et al.* Ultimate Permeation Across Atomically Thin Porous Graphene. *Science* **344**, 289–292 (2014).

56. Surwade, S. P. *et al.* Water desalination using nanoporous single-layer graphene. *Nat. Nanotechnol.* **10**, 459–464 (2015).

57. Mulyana, Y., Uenuma, M., Ishikawa, Y. & Uraoka, Y. Reversible Oxidation of Graphene Through Ultraviolet/Ozone Treatment and Its Nonthermal Reduction through Ultraviolet Irradiation. *J. Phys. Chem. C* **118**, 27372–27381 (2014).

58. Cheng, Y. C., Kaloni, T. P., Zhu, Z. Y. & Schwingenschlögl, U. Oxidation of graphene in ozone under ultraviolet light. *Appl. Phys. Lett.* **101**, (2012).

59. Tracz, A., Wegner, G. & Rabe, J. P. Scanning tunneling microscopy study of graphite oxidation in ozone-air mixtures. *Langmuir* **19**, 6807–6812 (2003).

60. Koizumi, K., Boero, M., Shigeta, Y. & Oshiyama, A. Atom-scale reaction pathways and free-energy landscapes in oxygen plasma etching of graphene. *J. Phys. Chem. Lett.* **4**, 1592–1596 (2013).

61. Bai, J., Zhong, X., Jiang, S., Huang, Y. & Duan, X. Graphene nanomesh. *Nat. Nanotechnol.* **5**, 190–4 (2010).

62. Luo, D. *et al.* Adlayer-Free Large-Area Single Crystal Graphene Grown on a Cu(111) Foil. *Adv. Mater.* **1903615**, 1903615 (2019).

63. Solís-Fernández, P., Paredes, J. I., Cosío, A., Martínez-Alonso, A. & Tascón, J. M. D. A comparison between physically and chemically driven etching in the oxidation of graphite surfaces. *J. Colloid Interface Sci.* **344**, 451–459 (2010).

64. Paredes, J. I., Martínez-Alonso, A. & Tascón, J. M. D. Early stages of plasma oxidation of graphite: Nanoscale physicochemical changes as detected by scanning probe microscopies. *Langmuir* **18**, 4314–4323 (2002).

65. Al-Mumen, H., Rao, F., Li, W. & Dong, L. Singular Sheet Etching of Graphene with Oxygen Plasma. *Nano-Micro Lett.* **6**, 116–124 (2014).

66. Seah, C. M., Vigolo, B., Chai, S. P. & Mohamed, A. R. Mechanisms of graphene fabrication through plasma-induced layer-by-layer thinning. *Carbon N. Y.* **105**, 496–509 (2016).

67. Hennig, G. R. Anisotropic reactivities of graphite-I. Reactions of ozone and graphite. *Carbon N. Y.* **3**, 107–114 (1965).

68. Chang, H. & Bard, A. J. Scanning Tunneling Microscopy Studies of Carbon-Oxygen Reactions on Highly Oriented Pyrolytic Graphite. *J. Am. Chem. Soc.* **113**, 5588–5596 (1991).

69. Chu, X. & Schmidt, L. D. Reactions of NO, O_2, H_2O, and CO_2 with the basal plane of graphite. *Surf. Sci.* **268**, 325–332 (1992).

70. Chu, X. & Schmidt, L. D. Gasification of graphite studied by scanning tunneling microscopy. *Carbon N. Y.* **29**, 1251–1255 (1991).

71. Chu, X. & Schmidt, L. D. Intrinsic Rates of NOx-Carbon Reactions. *Ind. Eng. Chem. Res.* **32**, 1359–1366 (1993).

72. Koenig, S. P., Wang, L., Pellegrino, J. & Bunch, J. S. Selective molecular sieving through porous graphene. *Nat. Nanotechnol.* **7**, 728–32 (2012).

73. Alzina, F. *et al.* Probing the electron-phonon coupling in ozone-doped graphene by Raman spectroscopy. *Phys. Rev. B - Condens. Matter Mater. Phys.* **82**, 1–6 (2010).

74. Marsh, H., O'Hair, T. E. & Wynne-Jones. The carbon-atomic oxygen reaction: surface-oxide formation on paracrystalline carbon and graphite. *Carbon N. Y.* **7**, 555–566 (1969).

75. Lee, G., Lee, B., Kim, J. & Cho, K. Ozone adsorption on graphene : Ab initio study and experimental validation. *J. Phys. Chem. C* **113**, 14225–14229 (2009).

76. Suarez, A. M., Radovic, L. R., Bar-Ziv, E. & Sofo, J. O. Gate-voltage control of oxygen diffusion on graphene. *Phys. Rev. Lett.* **106**, 146802 (2011).

77. Yuan, J. *et al.* Tuning the Electrical and Optical Properties of Graphene by Ozone Treatment for Patterning Monolithic. *ACS Nano* **7**, 4233–4241 (2013).

78. Sun, T. & Fabris, S. Mechanisms for oxidative unzipping and cutting of graphene. *Nano Lett.* **12**, 17–21 (2012).

79. Merchant, C. A. *et al.* DNA translocation through graphene nanopores. *Nano Lett.* **10**, 2915–2921 (2010).

80. Yang, Y., Yang, X., Liang, L., Yuyuan, G. & Cheng, H. Large-area graphene-nanomesh/ carbon-nanotube hybrid membranes for ionic and molecular nanofiltration. *Science* **364**, 1057–1062 (2019).

81. O'Hern, S. C. *et al.* Selective ionic transport through tunable subnanometer pores in single-layer graphene membranes. *Nano Lett.* **14**, 1234–1241 (2014).

82. Jang, D., Idrobo, J. C., Laoui, T. & Karnik, R. Water and Solute Transport Governed by Tunable Pore Size Distributions in Nanoporous Graphene Membranes. *ACS Nano* **11**, 10042–10052 (2017).

83. He, Z., Zhou, J., Lu, X. & Corry, B. Bioinspired graphene nanopores with voltage-tunable ion selectivity for Na^+ and K^+. *ACS Nano* **7**, 10148–10157 (2013).

84. Kang, Y. *et al.* Na^+ and K^+ ion selectivity by size-controlled biomimetic graphene nanopores. *Nanoscale* **6**, 10666–10672 (2014).

85. Sahu, S., Di Ventra, M. & Zwolak, M. Dehydration as a Universal Mechanism for Ion Selectivity in Graphene and Other Atomically Thin Pores. *Nano Lett.* **17**, 4719–4724 (2017).

86. Jain, T. *et al.* Heterogeneous sub-continuum ionic transport in statistically isolated graphene nanopores. *Nat. Nanotechnol.* **10**, 1–6 (2015).

87. Rollings, R. C., Kuan, A. T. & Golovchenko, J. A. Ion selectivity of graphene nanopores. *Nat. Commun.* **7**, (2016).

88. O'Hern, S. C. *et al.* Nanofiltration across defect-sealed nanoporous monolayer graphene. *Nano Lett.* **15**, 3254–3260 (2015).

89. Yuan, Z., Misra, R. P., Rajan, A. G., Strano, M. S. & Blankschtein, D. Analytical prediction of gas permeation through graphene nanopores of varying sizes: Understanding transitions across multiple transport regimes. *ACS Nano* **13**, 11825–11833 (2019).

90. Yuan, Z. *et al.* Mechanism and prediction of gas permeation through sub-nanometer graphene pores: comparison of theory and simulation. *ACS Nano* **11**, 7974–7987 (2017).

91. Lee W. Drahushuk and Michael S. Strano. Mechanisms of Gas Permeation through Single Layer

Graphene Membranes. *Langmuir* **28**, 16671–16678 (2012).

92. Sun, C. *et al.* Mechanisms of molecular permeation through nanoporous graphene membranes. *Langmuir* **30**, 675–682 (2014).

93. Wang, L. *et al.* Fundamental transport mechanisms, fabrication and potential applications of nanoporous atomically thin membranes. *Nat. Nanotechnol.* **12**, 509–522 (2017).

94. Sun, C. & Bai, B. Fast mass transport across two-dimensional graphene nanopores : Nonlinear pressure-dependent gas permeation flux. *Chem. Eng. Sci.* **165**, 186–191 (2017).

95. He, G. *et al.* Synergistic CO_2-sieving from polymer with intrinsic microporosity masking nanoporous single-layer graphene. *Adv. Funct. Mater.* **2003979**, 1–10 (2020).

96. Jiang, D.-E., Cooper, V. R. & Dai, S. Porous graphene as the ultimate membrane for gas separation. *Nano Lett.* **9**, 4019–4024 (2009).

97. Liu, H., Dai, S. & Jiang, D. E. Permeance of H_2 through porous graphene from molecular dynamics. *Solid State Commun.* **175**–**176**, 101–105 (2013).

98. Liu, H., Dai, S. & Jiang, D. E. Insights into CO2/N2 separation through nanoporous graphene from molecular dynamics. *Nanoscale* **5**, 9984–9987 (2013).

99. Hauser, A. W., Schrier, J. & Schwerdtfeger, P. Helium tunneling through nitrogen-functionalized graphene pores: Pressure- and temperature-driven approaches to isotope separation. *J. Phys. Chem. C* **116**, 10819–10827 (2012).

100. Schrier, J. Helium separation using porous graphene membranes. *J. Phys. Chem. Lett.* **1**, 2284–2287 (2010).

101. Schrier, J. & McClain, J. Thermally-driven isotope separation across nanoporous graphene. *Chem. Phys. Lett.* **521**, 118–124 (2012).

102. Schrier, J. Fluorinated and nanoporous graphene materials as sorbents for gas separations. *ACS Appl. Mater. Interfaces* **3**, 4451–4458 (2011).

103. Tian, Z., Mahurin, S. M., Dai, S. & Jiang, D. en. Ion-Gated Gas Separation through Porous Graphene. *Nano Lett.* **17**, 1802–1807 (2017).

104. Boutilier, M. S. H. *et al.* Molecular Sieving Across Centimeter-Scale Single-Layer Nanoporous Graphene Membranes. *ACS Nano* **11**, 5726–5736 (2017).

105. Yuan, Z., Benck, J. D., Eatmon, Y., Blankschtein, D. & Strano, M. S. Stable, Temperature-Dependent Gas Mixture Permeation and Separation through Suspended Nanoporous Single-Layer Graphene Membranes. *Nano Lett.* **18**, 5057–5069 (2018).

106. Lee, C. K. *et al.* Monatomic chemical-vapor-deposited graphene membranes bridge a half-millimeter-scale gap. *ACS Nano* **8**, 2336–2344 (2014).

107. Qin, Y. *et al.* Ultrafast Nanofiltration through Large-Area Single-Layered Graphene Membranes. *ACS Appl. Mater. Interfaces* **9**, 9239–9244 (2017).

108. Kidambi, P. R. *et al.* A Scalable Route to Nanoporous Large-Area Atomically Thin Graphene Membranes by Roll-to-Roll Chemical Vapor Deposition and Polymer Support Casting. *Appl. Mater. Interfaces* **10**, 10369–10378 (2018).

109. Kidambi, P. R. *et al.* Selective Nanoscale Mass Transport across Atomically Thin Single Crystalline Graphene Membranes. *Adv. Mater.* **1605896**, 1–6 (2017).

110. Sun, C., Wen, B. & Bai, B. Application of nanoporous graphene membranes in natural gas processing: Molecular simulations of CH4/CO2, CH4/H2S and CH4/N2separation. *Chem. Eng. Sci.* **138**, 616–621 (2015).

111. Shan, M. *et al.* Influence of chemical functionalization on the CO_2/N2 separation performance of porous graphene membranes. *Nanoscale* **4**, 5477–5482 (2012).

112. Blankenburg, S. *et al.* Porous graphene as an atmospheric nanofilter. *Small* **6**, 2266–2271 (2010).

113. Du, H. *et al.* Separation of hydrogen and nitrogen gases with porous graphene membrane. *J. Phys. Chem. C* **115**, 23261–23266 (2011).

114. Schrier, J. Carbon dioxide separation with a two-dimensional polymer membrane. *ACS Appl. Mater. Interfaces* **4**, 3745–3752 (2012).

115. Wang, L., Williams, C. M., Boutilier, M. S. H., Kidambi, P. R. & Karnik, R. Single-Layer Graphene Membranes Withstand Ultrahigh Applied Pressure. *Nano Lett.* **17**, 3081–3088 (2017).

116. Cohen-Tanugi, D. & Grossman, J. C. Mechanical strength of nanoporous graphene as a desalination membrane. *Nano Lett.* **14**, 6171–6178 (2014).

117. Boutilier, M. S. H. *et al.* Implications of permeation through intrinsic defects in graphene on the design of defect-tolerant membranes for gas separation. *ACS Nano* **8**, 841–849 (2014).

118. Strudwick, A. J. *et al.* Chemical vapor deposition of high quality graphene films from carbon dioxide atmospheres. *ACS Nano* **9**, 31–42 (2015).

119. K. V. Agrawal, M. Dakachoune, S. Huang, G. He, N. D. "Ultrahigh Flux Gas -selective Nanoporous Carbon Membrane and Manufacturing Method Thereof",. *Application PCT/EP2017/057684.*

120. Reina, A. *et al.* Large area, few-layer graphene films on arbitrary substrates by chemical vapor deposition. *Nano Lett.* **9**, 30–35 (2009).

121. Suk, J. W. *et al.* Transfer of CVD-grown monolayer graphene onto arbitrary substrates. *ACS Nano* **5**, 6916–6924 (2011).

122. Agrawal, K. V. *et al.* Fabrication, Pressure Testing and Nanopore Formation of Single Layer Graphene Membranes. *J. Phys. Chem. C* **121**, 14312–14321 (2017).

123. Zhang, J. *et al.* Clean Transfer of Large Graphene Single Crystals for High-Intactness Suspended Membranes and Liquid Cells. *Adv. Mater.* **29**, 1–7 (2017).

124. Kang, J., Shin, D., Bae, S. & Hong, B. H. Graphene transfer: key for applications. *Nanoscale* **4**, 5527 (2012).

125. Lin, Y. C. *et al.* Clean transfer of graphene for isolation and suspension. *ACS Nano* **5**, 2362–2368 (2011).

126. Lee, C.-K. *et al.* Monatomic Chemical-Vapor- Deposited Graphene Membranes. *ACS Nano* **8**, 2336–2344 (2014).

127. Rodriguez, A. T., Li, X., Wang, J., Steen, W. A. & Fan, H. Facile Synthesis of Nanostructured Carbon through Self-Assembly between Block Copolymers and Carbohydrates. *Adv. Funct. Mater.* **17**, 2710–2716 (2007).

128. Meyer, J. C. *et al.* The structure of suspended graphene sheets. *Nature* **446**, 60–63 (2007).

129. Song, J. *et al.* A general method for transferring graphene onto soft surfaces. *Nat. Nanotechnol.* **8**, 356–362 (2013).

130. Cancado, L. G. *et al.* Quantifying defects in graphene via Raman spectroscopy at different excitation energies. *Nano Lett.* **11**, 3190–3196 (2011).

131. He, G., Dakhchoune, M., Zhao, J., Huang, S. & Agrawal, K. V. Electrophoretic Nuclei Assembly for Crystallization of High Performance Membranes on Unmodified Supports. *Adv. Funct. Mater.* **28**, 1707427 (2018).

132. Castricum, H. L., Qureshi, H. F., Nijmeijer, A. & Winnubst, L. Hybrid silica membranes with enhanced hydrogen and CO2 separation properties. *J. Memb. Sci.* **488**, 121–128 (2015).

133. Qureshi, H. F., Nijmeijer, A. & Winnubst, L. Influence of sol-gel process parameters on the micro-structure and performance of hybrid silica membranes. *J. Memb. Sci.* **446**, 19–25 (2013).

134. Vos, R. M. De & Verweij, H. High-Selectivity , High-Flux Silica Membranes for Gas Separation. *Science* **279**, 1710–1712 (1998).

135. Ahn, S. J., Yun, G. N., Takagaki, A., Kikuchi, R. & Oyama, S. T. Synthesis and characterization of

hydrogen selective silica membranes prepared by chemical vapor deposition of vinyltriethoxysilane. *J. Memb. Sci.* **550**, 1–8 (2018).

136. Lee, D., Zhang, L., Oyama, S. T., Niu, S. & Saraf, R. F. Synthesis, characterization, and gas permeation properties of a hydrogen permeable silica membrane supported on porous alumina. *J. Memb. Sci.* **231**, 117–126 (2004).

137. Gu, Y., Hacarlioglu, P. & Oyama, S. T. Hydrothermally stable silica-alumina composite membranes for hydrogen separation. *J. Memb. Sci.* **310**, 28–37 (2008).

138. Ahn, S. J., Takagaki, A., Sugawara, T., Kikuchi, R. & Oyama, S. T. Permeation properties of silica-zirconia composite membranes supported on porous alumina substrates. *J. Memb. Sci.* **526**, 409–416 (2017).

139. Kosinov, N., Auffret, C., Borghuis, G. J., Sripathi, V. G. P. & Hensen, E. J. M. Influence of the Si/Al ratio on the separation properties of SSZ-13 zeolite membranes. *J. Memb. Sci.* **484**, 140–145 (2015).

140. Wang, B., Hu, N., Wang, H., Zheng, Y. & Zhou, R. Improved AlPO-18 membranes for light gas separation. *J. Mater. Chem. A* **3**, 12205–12212 (2015).

141. Himeno, S. *et al.* Synthesis and permeation properties of a DDR-type zeolite membrane for separation of CO_2/CH_4 gaseous mixtures. *Ind. Eng. Chem. Res.* **46**, 6989–6997 (2007).

142. Huang, A., Wang, N. & Caro, J. Synthesis of multi-layer zeolite LTA membranes with enhanced gas separation performance by using 3-aminopropyltriethoxysilane as interlayer. *Microporous Mesoporous Mater.* **164**, 294–301 (2012).

143. Kida, K., Maeta, Y. & Yogo, K. Pure silica CHA-type zeolite membranes for dry and humidified CO_2/CH_4 mixtures separation. *Sep. Purif. Technol.* **197**, 116–121 (2018).

144. Barrer, R. M. Porous crystal membranes. *J. Chem. Soc. Faraday Trans.* **86**, 1123–1130 (1990).

145. de Lange, R. S. A., Keizer, K. & Burggraaf, A. J. Analysis and Theory of Gas Transport in Micropouros Sol-Gel Derived Ceramic Membranes. *J. Memb. Sci.* **104**, 81–100 (1995).

146. Huh, S. *et al.* UV/Ozone-Oxidized Large-Scale Graphene Platform with Large Chemical Enhancement in Surface-Enhanced Raman Scattering. *ACS Nano* **5**, 9799–9806 (2011).

147. Li, J. L. *et al.* Oxygen-driven unzipping of graphitic materials. *Phys. Rev. Lett.* **96**, 5–8 (2006).

148. Li, Z., Zhang, W., Luo, Y., Yang, J. & Hou, J. G. How graphene is cut upon oxidation? *J. Am. Chem. Soc.* **131**, 6320–6321 (2009).

149. Carlsson, J. M., Hanke, F., Linic, S. & Scheffler, M. Two-Step Mechanism for Low-Temperature Oxidation of Vacancies in Graphene. *Phys. Rev. Lett.* **102**, 1–4 (2009).

150. Ferrari, A. & Basko, D. Raman spectroscopy as a versatile tool for studying the properties of graphene. *Nat. Nanotechnol.* **8**, 235–46 (2013).

151. Zhang, C. & Koros, W. J. Ultraselective Carbon Molecular Sieve Membranes with Tailored Synergistic Sorption Selective Properties. *Adv. Mater.* **29**, 1–6 (2017).

152. Ma, X. *et al.* Zeolitic imidazolate framework membranes made by ligand-induced permselectivation. *Science* **361**, 1008–1011 (2018).

153. Zhou, S. *et al.* Paralyzed membrane: Current-driven synthesis of a metal-organic framework with sharpened propene/propane separation. *Sci. Adv.* **4**, 1–9 (2018).

154. Lozada-Hidalgo, M. *et al.* Sieving hydrogen isotopes through two-dimensional crystals. *Science* **351**, 68–70 (2016).

155. Roussanaly, S., Anantharaman, R., Lindqvist, K., Zhai, H. & Rubin, E. Membrane properties required for post-combustion CO_2 capture at coal-fired power plants. *J. Memb. Sci.* **511**, 250–264 (2016).

156. Yamada, Y. *et al.* Subnanometer vacancy defects introduced on graphene by oxygen gas. *J. Am. Chem. Soc.* **136**, 2232–2235 (2014).

157. Lee, G. Do *et al.* Diffusion, coalescence, and reconstruction of vacancy defects in graphene layers. *Phys. Rev. Lett.* **95**, 1–4 (2005).

158. Liu, H., Chen, Z., Dai, S. & Jiang, D. Journal of Solid State Chemistry Selectivity trend of gas separation through nanoporous graphene. *J. Solid State Chem.* **224**, 2–6 (2015).

159. Vallejos-burgos, F., Coudert, F.-X. & Kaneko, K. Air separation with graphene mediated by nanowindow-rim concerted motion. *Nat. Commun.* 1812 (2018).

160. Zhao, J. *et al.* Etching gas-sieving nanopores in single-layer graphene with an angstrom precision for high-performance gas mixture separation. *Sci. Adv.* **5**, eaav1851 (2019).

161. Buchheim, J., Wyss, R. M., Shorubalko, I. & Park, H. G. Understanding the interaction between energetic ions and freestanding graphene towards practical 2D perforation. *Nanoscale* **8**, 8345–8354 (2016).

162. Ajayan, P. M., Ebbesen, T. W. & Williams, J. S. Reports on Progress in Physics Related content Irradiation effects in carbon nanostructures Irradiation effects in carbon nanostructures. *Reports Prog. Phys. Irradiat.* **62**, (1999).

163. Wang, X. & Dai, H. Etching and narrowing of graphene from the edges. *Nat. Chem.* **2**, 661–665 (2010).

164. Huang, S. *et al.* Single-layer graphene membranes by crack-free transfer for gas mixture separation. *Nat. Commun.* **9**, 2632 (2018).

165. He, G. *et al.* High-permeance polymer-functionalized single-layer graphene membranes that surpass the postcombustion carbon capture target. *Energy Environ. Sci.* **12**, 3305–3312 (2019).

166. Gong, C. *et al.* Rapid selective etching of PMMA residues from transferred graphene by carbon dioxide. *J. Phys. Chem. C* **117**, 23000–23008 (2013).

167. Giannozzi, P. *et al.* QUANTUM ESPRESSO: A modular and open-source software project for quantum simulations of materials. *J. Phys. Condens. Matter* **21**, 395502 (2009).

168. Giannozzi, P. *et al.* Advanced capabilities for materials modelling with Quantum {ESPRESSO}. *J. Phys. Condens. Matter* **29**, 465901 (2017).

169. Lejaeghere, K. *et al.* Reproducibility in density functional theory calculations of solids. *Science* **351**, 1415 (2016).

170. Prandini, G., Marrazzo, A., Castelli, I. E., Mounet, N. & Marzari, N. Precision and efficiency in solid-state pseudopotential calculations. *npj Comput. Mater.* **4**, 72 (2018).

171. Lee, K., Murray, É. D., Kong, L., Lundqvist, B. I. & Langreth, D. C. Higher-accuracy van der Waals density functional. *Phys. Rev. B - Condens. Matter Mater. Phys.* **82**, 3–6 (2010).

172. Ding, F. *et al.* Colossal grain growth yields single-crystal metal foils by contact-free annealing. *Science* **362**, 1021–1025 (2018).

173. Eckmann, A. *et al.* Probing the nature of defects in graphene by Raman spectroscopy. *Nano Lett.* **12**, 3925–3930 (2012).

174. Govind Rajan, A. *et al.* Addressing the isomer cataloguing problem for nanopores in two-dimensional materials. *Nat. Mater.* **18**, 129–135 (2019).

175. Hollins, P. & Pritchard, J. Interactions of CO molecules adsorbed on Cu(111). *Surf. Sci.* **89**, 486–495 (1979).

176. Marsh, H., O'Hair, E., Reed, R. & Wynne-Jones, W. F. Reaction of atomic oxygen with Carbon. *Nature* **198**, 1195–1196 (1963).

177. Xu, K. & Ye, P. D. Theoretical study on the oxidation mechanism and dynamics of the zigzag graphene nanoribbon edge by oxygen and ozone. *J. Phys. Chem. C* **118**, 10400–10407 (2014).

178. Nagai, K., Masuda, T., Nakagawa, T., Freeman, B. D. & Pinnau, I. Poly[1-(trimethylsilyl)-1-propyne] and related polymers: Synthesis, properties and functions. *Prog. Polym. Sci.* **26**, 721–798 (2001).

179. Lau, C. H. *et al.* Ending aging in super glassy polymer membranes. *Angew. Chemie - Int. Ed.* **53**, 5322–5326 (2014).

180. Yang, R. T. & Wong, C. Kinetics and mechanism of oxidation of basal plane on graphite. *J. Chem. Phys.* **75**, 4471–4476 (1981).

181. Wang, S. *et al.* Graphene oxide membranes with heterogeneous nanodomains for efficient CO_2 separations. *Angew. Chemie - Int. Ed.* **56**, 14246–14251 (2017).

182. Karunakaran, M. *et al.* Graphene oxide doped ionic liquid ultrathin composite membranes for efficient CO_2 capture. *J. Mater. Chem. A* **5**, 649–656 (2017).

183. Zhou, F. *et al.* Ultrathin graphene oxide-based hollow fiber membranes with brush-like CO_2-philic agent for highly efficient CO_2 capture. *Nat. Commun.* **8**, 2107 (2017).

184. Fu, Y. *et al.* Ultra-thin enzymatic liquid membrane for CO_2 separation and capture. *Nat. Commun.* **9**, 990 (2018).

185. Kim, T. J., Vrålstad, H., Sandru, M. & Hägg, M. B. Separation performance of PVAm composite membrane for CO2 capture at various pH levels. *J. Memb. Sci.* **428**, 218–224 (2013).

186. Sutrisna, P. D. *et al.* Surface functionalized UiO-66/Pebax-based ultrathin composite hollow fiber gas separation membranes. *J. Mater. Chem. A* **6**, 918–931 (2018).

187. Sutrisna, P. D., Hou, J., Li, H., Zhang, Y. & Chen, V. Improved operational stability of Pebax-based gas separation membranes with ZIF-8: A comparative study of flat sheet and composite hollow fibre membranes. *J. Memb. Sci.* **524**, 266–279 (2017).

188. Kim, S. *et al.* Highly permeable thermally rearranged polymer composite membranes with a graphene oxide scaffold for gas separation. *J. Mater. Chem. A* **6**, 7668–7674 (2018).

189. Fu, Q. *et al.* A novel cross-linked nano-coating for carbon dioxide capture. *Energy Environ. Sci.* **9**, 434–440 (2016).

190. Xie, K. *et al.* Continuous assembly of a polymer on a metal-organic framework (CAP on MOF): A 30 nm thick polymeric gas separation membrane. *Energy Environ. Sci.* **11**, 544–550 (2018).

191. Li, S. *et al.* Interfacially polymerized thin film composite membranes containing ethylene oxide groups for CO_2 separation. *J. Memb. Sci.* **436**, 121–131 (2013).

192. Scofield, J. M. P. *et al.* Development of novel fluorinated additives for high performance CO_2 separation thin-film composite membranes. *J. Memb. Sci.* **499**, 191–200 (2016).

193. Kim, S., Han, S. H. & Lee, Y. M. Thermally rearranged (TR) polybenzoxazole hollow fiber membranes for CO_2 capture. *J. Memb. Sci.* **403–404**, 169–178 (2012).

194. Qiao, Z. *et al.* Metal-induced ordered microporous polymers for fabricating large-area gas separation membranes. *Nat. Mater.* **18**, 163–168 (2019).

195. Razmjou, A., Asadnia, M., Hosseini, E., Habibnejad Korayem, A. & Chen, V. Design principles of ion selective nanostructured membranes for the extraction of lithium ions. *Nat. Commun.* **10**, 1–15 (2019).

196. Thompson, K. A. *et al.* N-Aryl–linked spirocyclic polymers for membrane separations of complex hydrocarbon mixtures. *Science* **369**, 310–315 (2020).

197. Park, H. B., Kamcev, J., Robeson, L. M., Elimelech, M. & Freeman, B. D. Maximizing the right stuff: The trade-offbetween membrane permeability and selectivity. *Science* **0530**, 1137 (2017).

198. Rungta, M. *et al.* Carbon molecular sieve structure development and membrane performance relationships. *Carbon N. Y.* **115**, 237–248 (2017).

199. Adams, J. S. *et al.* New insights into structural evolution in carbon molecular sieve membranes during pyrolysis. *Carbon N. Y.* (2018). doi:10.1016/j.carbon.2018.09.039

200. Koh, D.-Y., McCool, B. A., Harry W., D. & Ryan P., L. Reverse osmosis molecular differentiation of organic liquids using carbon molecular sieve membranes. *Science* **353**, (2016).

201. Xu, L., Rungta, M. & Koros, W. J. Matrimid® derived carbon molecular sieve hollow fiber membranes for ethylene/ethane separation. *J. Memb. Sci.* **380**, 138–147 (2011).

202. Rungta, M., Xu, L. & Koros, W. J. Carbon molecular sieve dense film membranes derived from Matrimid® for ethylene/ethane separation. *Carbon N. Y.* **50**, 1488–1502 (2012).

203. Koros, W. J. & Zhang, C. Materials for next-generation molecularly selective synthetic membranes. *Nat. Mater.* **16**, 289–297 (2017).

204. Sanyal, O. *et al.* Next generation membranes —using tailored carbon. *Carbon N. Y.* **127**, 688–698 (2018).

205. Ning, X. & Koros, W. J. Carbon molecular sieve membranes derived from Matrimid® polyimide for nitrogen/methane separation. *Carbon N. Y.* **66**, 511–522 (2014).

206. Vu, D. Q., Koros, W. J. & Miller, S. J. High Pressure CO_2 /CH_4 Separation Using Carbon Molecular Sieve Hollow Fiber Membranes. *Ind. Eng. Chem. Res.* **41**, 367–380 (2002).

207. Fu, S., Sanders, E. S., Kulkarni, S. S., Wenz, G. B. & Koros, W. J. Temperature dependence of gas transport and sorption in carbon molecular sieve membranes derived from four 6FDA based polyimides: Entropic selectivity evaluation. *Carbon N. Y.* **95**, 995–1006 (2015).

208. Fu, S. *et al.* The significance of entropic selectivity in carbon molecular sieve membranes derived from 6FDA/DETDA:DABA(3:2) polyimide. *J. Memb. Sci.* **539**, 329–343 (2017).

209. Swaidan, R., Ma, X., Litwiller, E. & Pinnau, I. High pressure pure- and mixed-gas separation of CO2/CH4by thermally-rearranged and carbon molecular sieve membranes derived from a polyimide of intrinsic microporosity. *J. Memb. Sci.* **447**, 387–394 (2013).

210. Ma, X. *et al.* Carbon molecular sieve gas separation membranes based on an intrinsically microporous polyimide precursor. *Carbon N. Y.* **62**, 88–96 (2013).

211. Salinas, O., Ma, X., Litwiller, E. & Pinnau, I. High-performance carbon molecular sieve membranes for ethylene/ethane separation derived from an intrinsically microporous polyimide. *J. Memb. Sci.* **500**, 115–123 (2016).

212. Salinas, O., Ma, X., Litwiller, E. & Pinnau, I. Ethylene/ethane permeation, diffusion and gas sorption properties of carbon molecular sieve membranes derived from the prototype ladder polymer of intrinsic microporosity (PIM-1). *J. Memb. Sci.* **504**, 133–140 (2016).

213. Bhuwania, N. *et al.* Engineering substructure morphology of asymmetric carbon molecular sieve hollow fiber membranes. *Carbon N. Y.* **76**, 417–434 (2014).

214. Zhang, C., Zhang, K., Cao, Y. & Koros, W. J. Composite Carbon Molecular Sieve Hollow Fiber Membranes: Resisting Support Densification via Silica Particle Stabilization. *Ind. Eng. Chem. Res.* 16051–16058 (2018).

215. Hou, J. *et al.* Carbon Nanotube Networks as Nanosca ff olds for Fabricating Ultrathin Carbon Molecular Sieve Membranes. *ACS Appl. Mater. Interfaces* **10**, 20182−20188 (2018).

216. Xiaoli Ma, Y.S. Lin, X. W. and J. K. Ultrathin Carbon Molecular Sieve Membrane for Propylene/Propane Separation. *AIChE J.* **62**, 3–194 (2003).

217. Liao, K. S. *et al.* Development of the asymmetric microstructure of carbon molecular sieve membranes as probed by positron annihilation spectroscopy. *J. Phys. Chem. C* **117**, 3556–3562 (2013).

218. Singh, R. & Koros, W. J. Carbon molecular sieve membrane performance tuning by dual temperature secondary oxygen doping (DTSOD). *J. Memb. Sci.* **427**, 472–478 (2013).

219. Kiyono, M., Williams, P. J. & Koros, W. J. Effect of pyrolysis atmosphere on separation performance of carbon molecular sieve membranes. *J. Memb. Sci.* **359**, 2–10 (2010).

220. Vandencasteele, N. & Reniers, F. Plasma-modified polymer surfaces: Characterization using XPS. *J. Electron Spectros. Relat. Phenomena* **178**–**179**, 394–408 (2010).

221. Matienzo, L. J. & Egitto, F. D. Polymer oxidation downstream from oxygen microwave plasmas.

Polym. Degrad. Stab. **35**, 181–192 (1992).

222. Wang, Y. *et al.* Electrochemical delamination of CVD-grown graphene film: Toward the recyclable use of copper catalyst. *ACS Nano* 9927–9933 (2011).

223. Sham, M. L. & Kim, J. K. Surface functionalities of multi-wall carbon nanotubes after UV/Ozone and TETA treatments. *Carbon N. Y.* **44**, 768–777 (2006).

224. Chang, C. M. & Liu, Y. L. Functionalization of multi-walled carbon nanotubes with non-reactive polymers through an ozone-mediated process for the preparation of a wide range of high performance polymer/carbon nanotube composites. *Carbon N. Y.* **48**, 1289–1297 (2010).

225. Bae, Y. S., Moon, J. H., Ahn, H. & Lee, C. H. Effects of adsorbate properties on adsorption mechanism in a carbon molecular sieve. *Korean J. Chem. Eng.* **21**, 712–720 (2004).

226. Reid, C. R. & Thomas, K. M. Adsorption of gases on a carbon molecular sieve used for air separation: Linear adsorptives as probes for kinetic selectivity. *Langmuir* **15**, 3206–3218 (1999).

227. Sanyal, O. *et al.* Cause and effects of hyperskin features on carbon molecular sieve (CMS) membranes. *J. Memb. Sci.* **551**, 113–122 (2018).

Curriculum Vitae

Shiqi Huang

Date of Birth: May 29th, 1991

E-mail: shiqi.huang@epfl.ch   Tel: +41 762041253

Address: Rue de Condemines 30, Sion, Switzerland

Education

Ph. D. in Chemistry and Chemical Engineering   2016/08 – 2020/10

École Polytechnique Fédérale de Lausanne (EPFL), Switzerland

Advisor: Prof. Kumar Varoon Agrawal

Thesis: Etching nanopores in single-layer graphene with a sub-angstrom resolution in molecular sieving

M. Sc. in Chemical Engineering   2013/09 – 2016/06

Dalian University of Technology, P. R. China   GPA Rank: 1/40

Advisor: Prof. Gaohong He, Prof. Xuemei Wu

Thesis: Bilateral electrochemical hydrogen pump reactor for coupling dehydrogenation and hydrogenation

B. Eng. in Chemical Engineering   2009/09 – 2013/06

Dalian University of Technology, P. R. China   GPA Rank: 3/60

Research Experience

École Polytechnique Fédérale de Lausanne (EPFL)   2016 – 2020

High-performance gas-sieving single-layer graphene membrane with sub-angstrom resolution

- Investigated ozone-based etching kinetics and designed millisecond gasification reactor
- Fabricated gas-sieving nanopore on graphene lattice with sub-angstrom resolution
- Innovated method to scale-up single-layer graphene membrane while avoiding cracks
- Developed a mathematical model to describe the gas transport through nanoporous graphene

Ultrathin carbon molecular sieve (CMS) membrane for gas separation

- Developed a room-temperature functionalization method to tune pore-size distribution of CMS
- Fabricated 100-nm thick CMS membranes with a record high hydrogen flux

Dalian University of Technology   2013 – 2016

Fuel-cell membrane reactor for biomass conversion and gas purification

- Integrate multiple processes in a single membrane reactor
- Investigated the kinetics and mechanism of the biomass conversion in the membrane reactor

PEI-PDMS hollow fiber composite membrane for gas separation

- Fabricated PEI-PDMS hollow fiber membrane by dry-jet wet spinning for industrial application

Publications

1. **<u>S. Huang</u>**, L. F. Villalobos, D. J. Babu, S. Li, M. T. Vahdat, E. Oveisi, K. V. Agrawal*, "Millisecond lattice gasification for high-density CO_2- and O_2-sieving nanopores in single-layer graphene", **Submitted**.

2. **<u>S. Huang</u>**, M. Dakhchoune, W. Luo, E. Oveisi, G. He, M. Rezaei, J. Zhao, A. Züttel, M. S. Strano, K. V. Agrawal*, "Single-layer graphene membranes by crack-free transfer for gas mixture separation", **Nature Communications**, 2018, 9, 2632.

3. **<u>S. Huang</u>**, L. F. Villalobos, D. J. Babu, G. He, M. Li, A. Züttel, K. V. Agrawal*, "Ultrathin carbon molecular sieve films and room-temperature oxygen functionalization for gas-sieving", **ACS Applied Materials & Interfaces**, 2019, 11, 16729-16736.

4. G. He, **<u>S. Huang</u>**, L. F. Villalobos, J. Zhao, M. Mensi, E. Oveisi, M. Rezaei, K. V. Agrawal*, "High-permeance polymer-functionalized single-layer graphene membranes that surpass the postcombustion carbon capture target", **Energy & Environmental Science**, 2019, 12, 3305.

5. G. He, **<u>S. Huang</u>**, L. F. Villalobos, M. T. Vahdat, M. D. Guiver, J. Zhao, W.-C. Lee, M. Mensi, K. V. Agrawal*, "Synergistic CO_2-sieving from polymer with intrinsic microporosity masking nanoporous single-layer graphene", **Advanced Functional Materials**, 2020, 30, 2003979. (Back cover)

6. J. Zhao, G. He, **<u>S. Huang</u>**, L. F. Villalobos, M. Dakhchoune, H. Bassas, K. V. Agrawal*, "Etching nanopores in single-layer graphene with an angstrom precision for high-performance gas separation", **Science Advances**, 2019, 5, eaav1851.

7. G. He, M. Dakhchoune, J. Zhao, **<u>S. Huang</u>**, K. V. Agrawal*, "Electrophoretic nuclei assembly for crystallization of high-performance membranes on unmodified supports", **Advanced Functional Materials**, 2018, 28, 1707427.

8. M. H. Khan, M. Dakhchoune, M. Rezaei, **<u>S. Huang</u>**, J. Zhao, K. V. Agrawal*, "Hydrogen sieving from intrinsic defects of benzene-derived single-layer graphene", **Carbon**, 153, 458-466, 2019.

9. M. Rezaei, S. Li, **<u>S. Huang</u>**, K. V. Agrawal*, "Crystallographic and morphological optimization of catalytic copper foil for high-quality single-layer graphene membranes", **Journal of Membrane Science**, 2020, 612, 118406.

10. W. Lee, L. Bondaz, **<u>S. Huang</u>**, G. He, M. Dakhchoune, K. V. Agrawal*, "Centimeter-scale gas-sieving single-layer nanoporous graphene membrane", **Journal of Membrane Science**, Just accepted.

11. L. F. Villalobos, **<u>S. Huang</u>**, M. Dakhchoune W. Lee, K. V. Agrawal*, "Polybenzimidazole copolymer derived lacey carbon film for graphene transfer and contamination removal strategies for imaging graphene nanopores", **Submitted.**

12. **<u>S. Huang</u>**, X. Wu,* W. Chen, T. Wang, Y. Wu, G. He*, "Bilateral electrochemical hydrogen pump reactor for 2-propanol dehydrogenation and phenol hydrogenation", **Green Chemistry**, 2016, 18, 2353-2362. (Back cover)

13. **<u>S. Huang</u>**†, T. Wang†, X. Wu, W. Xiao, M. Yu, W. Chen, F. Zhang, G. He*, "Coupling hydrogen separation with butanone hydrogenation in an electrochemical hydrogen pump with sulfonated poly (phthalazinone ether sulfone ketone) membrane", **Journal of Power Sources**, 2016, 327, 178-186.

14. **<u>S. Huang</u>**, X. Wu*, W. Chen, L. Ma, S. Liu, G. He*, "Electrocatalytic dehydrogenation of 2-propanol in electrochemical hydrogen pump reactor", **Catalysis Today**, 2016, 276, 128-132.

15. W. Chen, X. Yan, X. Wu*, **<u>S. Huang</u>**, Y. Luo, X. Gong, G. He*, "Tri-quaternized poly (ether sulfone) anion exchange membranes with improved hydroxide conductivity", **Journal of Membrane Science**, 2016, 514, 613-621.

16. S. Liu, W. Xiao, S. Zhang, X. Wu*, **<u>S. Huang</u>**, L. Ma, G He*, "Elimination of product inhibition by ethanol competitive adsorption on carbon catalyst support in maleic acid electrochemical hydrogen pump hydrogenation reactor", **ACS Sustainable Chemistry & Engineering**, 2017, 5, 8738–8746.

17. L. Ma, S. Fan, D. Zhen, X. Wu*, S. Liu, J. Lin, **<u>S. Huang</u>**, G He*, "Electrochemical reduction of CO_2 in proton exchange membrane reactor: the function of buffer layer", **Industrial & Engineering**

Chemistry Research, 2017, 56, 10242–10250.

18. X. Gong, X. Yan, T. Li, X. Wu*, W. Chen, **S. Huang**, Y. Wu, D. Zhen, G. He*, "Design of pendent imidazolium side chain with flexible ether-containing spacer for alkaline anion exchange membrane", *Journal of Membrane Science,* 2017*,* 523, 216–224.

Patents

1. K. V. Agrawal, **S. Huang**, "New process for graphene membranes lattice engineering and uses thereof," Application EP20166877

2. K. V. Agrawal, **S. Huang**, "Graphene membrane filter for gas separation," WO2019/175162 A1

3. K. V. Agrawal, M. Dakachoune, **S. Huang**, G. He, N. Dudani, "Ultrahigh flux gas-selective nanoporous carbon membrane and manufacturing method thereof," WO2018/177533A1.

4. G. He, X. Wu, **S. Huang**, et al., "Electrochemical hydrogen pump reactor of coupling organics dehydrogenation and biomass hydrogenation," ZL 201510641954.5

Conferences

1. AIChE Annual Meeting, USA, 2020 (Oral presentation)

2. International Congress on Membranes & Membrane Processes, UK, 2020 (Oral presentation)

3. Swiss Chemical Society Fall Meeting 2020, Switzerland (Poster presentation)

4. North American Membrane Society 29th Annual Meeting, USA, 2019 (Poster presentation)

5. AIChE Annual Meeting, 2019, Orlando, USA, 2019 (Oral presentation)

6. Swiss Chemical Society Fall Meeting 2019, Zurich, Switzerland, 2019 (Poster presentation)

7. North American Membrane Society 28th Annual Meeting, Pittsburgh, USA, 2019 (Oral presentation)

8. Swiss Chemical Society Fall Meeting 2018, Lausanne, Switzerland, 2018 (Poster presentation)

9. Gordon Research Conference on Membranes: Materials and Processes, New London, USA, 2018 (Poster presentation)

10. Gordon Research Seminar on Membranes: Materials and Processes, New London, USA, 2018 (Oral presentation)

11. The 27th World Gas Conference, Washington D.C., USA, 2018 (Oral presentation)

12. Challenges & Opportunities in Energy Research, Crans-Montana, Switzerland, 2018 (Oral presentation)

13. The 8th Sino-US Joint Conference of Chemical Engineering, Shanghai, China, 2015 (Poster presentation)

Awards

• AIChE Separations Division Graduate Student Research Award, 2020

• Chinese Government Award for Outstanding Self-financed Students Abroad, 2019

• North American Membrane Society (NAMS) Student Fellowship Award, 2019

• AIChE Inorganic Material Division Graduate Student Award, 2019

• Chemistry Travel Award by Swiss Academy of Sciences and Swiss Chemical Society, 2019

• Selected Oral Presentation at "Challenges and Opportunities in Energy Research", 2018

• Outstanding Thesis Award of Liaoning Province, 2016

• Excellent Graduate Award of Liaoning Province, 2015

- Scholarship Winner, Infineum Co., 2014
- Outstanding Graduate Award, DUT, 2013
- Special Award of National Chemical Engineering Design Competition (Top 1%), 2012
- Scholarship Winner, Mitsubishi Chemical Co., 2011